

JURASSIC NAVAJO SANDSTONE OF COYOTE BUTTES,  
UTAH/ARIZONA: COLORATION AND DIAGENETIC  
HISTORY, PRESERVATION OF A DINOSAUR  
TRAMPLE SURFACE, AND TERRESTRIAL  
ANALOGS TO MARS

by

Winston Marmion Seiler

A thesis submitted to the faculty of  
The University of Utah  
in partial fulfillment of the requirements for the degree of

Master of Science

in

Geology

Department of Geology and Geophysics

The University of Utah

August 2008

Copyright © Winston Marmion Seiler 2008

All Rights Reserved

THE UNIVERSITY OF UTAH GRADUATE SCHOOL

## SUPERVISORY COMMITTEE APPROVAL

of a thesis submitted by

Winston Marmion Seiler

This thesis has been read by each member of the following supervisory committee and by majority vote has been found to be satisfactory.

May 19, 2008

---

  
Chair: Marjorie A. Chan

May 19, 2008

---

  
John R. Bowman

May 19, 2008

---

  
Erich U. Petersen

THE UNIVERSITY OF UTAH GRADUATE SCHOOL

**FINAL READING APPROVAL**

To the Graduate Council of the University of Utah:


I have read the thesis of Winston Marmion Seiler in its final form and have found that (1) its format, citations, and bibliographic style are consistent and acceptable; (2) its illustrative materials including figures, tables, and charts are in place; and (3) the final manuscript is satisfactory to the supervisory committee and is ready for submission to The Graduate School.

May 19, 2008


Date

  
Marjorie A. Chan  
Chair: Supervisory Committee

Approved for the Major Department

  
Erich U. Petersen  
Chair/Dean

Approved for the Graduate Council

  
David S. Chapman  
Dean of The Graduate School



## ABSTRACT

The Coyote Buttes, in Jurassic Navajo Sandstone, straddles the Utah-Arizona border at the northwest margin of Vermilion Cliffs National Monument. Its spectacular geology—cyclic eolian cross strata, striking coloration, and sculpted geomorphology—makes the area one of the most popular on the Colorado Plateau. Field and laboratory techniques document three geologic features of the Coyote Buttes: sandstone diagenesis, a dinosaur trample surface, and modern iron oxide micro-concretion eolian ripples analogous to Mars.

The range of red, orange, pink, and purple sandstone hues is largely due to iron oxide—hematite and lesser goethite grain-coatings and cement. Six diagenetic color facies (10's m thick) document paleofluid interactions and both advective fluid flow and diffusive iron mobilization in the host rock. Bleaching patterns (cm-10's m scale) indicate advective, upward migration and accumulation of a buoyant, chemically reducing fluid (likely hydrocarbons). Liesegang bands record diffusive mass transfer across redox boundaries between a fluid enriched in mobile, ferrous iron and oxygen-rich groundwater. Coloration developed during a narrow timeframe concurrent with Laramide-aged faulting; paleofluid flow is eastward.

A well-preserved dinosaur trample surface in a wet interdune interval exhibits multiple overlapping track types and sizes, high track density, footprint features, and rare tail drag marks. At least three distinct ichnogenera are present – *Eubrontes*,

*Anchisauripus*, and *Grallator*, along with tracks of an unidentified Sauropodomorph.

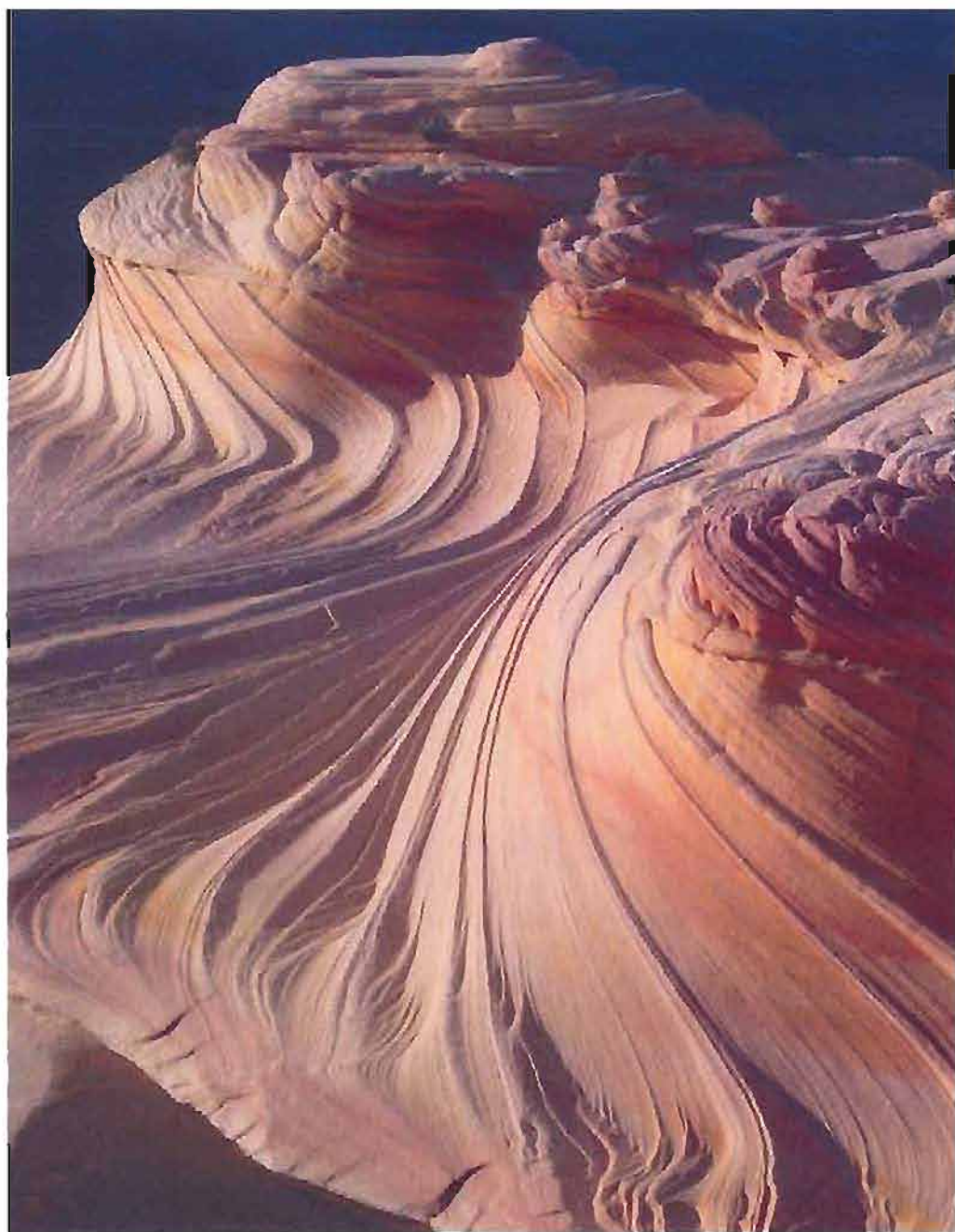
The trample surface refines ecologic and climatic conditions recorded in Early Jurassic eolian deposits.

Complex, coarse-grained ripples of iron oxide micro-concretions derived from redox fronts are terrestrial analogs to Martian features. The ripples illuminate the history of host rock diagenesis (similar to Liesegang banding), weathering stages, and modern wind processes. These events may be scaled to Martian conditions where similar ripples are widespread and formed in a lower-density atmosphere under higher winds.

The Coyote Buttes annually draw thousands of wilderness enthusiasts and photographers. This study contributes a better understanding of the area's intense diagenetic coloration and fluid history, the paleoecology of the Navajo erg, and wind-dominated Martian processes. The Coyote Buttes is a valuable geologic feature for the scientific community, and an exceptional aesthetic landscape for resource management in the Vermilion Cliffs National Monument.

To those who inspire others, use their powers for good, and wander the desert.

There never comes an end to good work that you have done.



Despite the best efforts of a small army of writers, painters, photographers, scientists, explorers, Indians, cowboys, and wilderness guides, the landscape of the Colorado Plateau lies still beyond the reach of reasonable words. Or unreasonable representation. This is a landscape that has to be seen to be believed, and even then, confronted directly by the senses, it strains credulity.

Here you may yet find the elemental freedom to breathe deep of unpoisoned air, to experiment with solitude and stillness, to graze through a hundred miles of untrammelled atmosphere, across redrock canyons, beyond blue mesas, toward the snow-covered peaks of the most distant mountains—to make the discovery of the self in its proud sufficiency which is not isolation but an irreplaceable part of the mystery of the whole.

Come on in. The earth, like the sun, like the air, belongs to everyone - and to no one.

—Edward Abbey, 1995

## TABLE OF CONTENTS

ABSTRACT .....	iv
LIST OF TABLES .....	xi
LIST OF FIGURES .....	xiv
ACKNOWLEDGMENTS .....	xviii
Chapter	
1. INTRODUCTION.....	1
The Coyote Buttes .....	1
Navajo Sandstone .....	4
Chapter Summaries.....	7
References .....	9
2. COLORATION AND DIAGENETIC HISTORY OF JURASSIC NAVAJO SANDSTONE AT COYOTE BUTTES, PARIA CANYON/VERMILION CLIFFS WILDERNESS, UTAH AND ARIZONA .....	11
Abstract .....	11
Introduction .....	12
Location and Geologic Setting .....	13
Previous Work .....	19
Methods .....	23
Diagenetic Descriptions and Interpretations.....	27
Discussion .....	57
Implications .....	67
Conclusions .....	69
Acknowledgments .....	70
References .....	70

3. A WET INTERDUNE DINOSAUR TRAMPLE SURFACE IN THE JURASSIC NAVAJO SANDSTONE, COYOTE BUTTES, ARIZONA: RARE PRESERVATION OF MULTIPLE TRACK TYPES AND TAIL DRAG MARKS .....	78
Abstract .....	78
Introduction .....	79
Location, Geologic Setting and Stratigraphy .....	80
Methods .....	83
Results .....	86
Interpretations .....	92
Discussion .....	101
Conclusions .....	106
Acknowledgments .....	107
References .....	108
4. HEMATITE “MICROBERRY” WIND RIPPLES: EOLIAN CONDITIONS FOR A TERRESTRIAL MARTIAN ANALOG FROM THE JURASSIC NAVAJO SANDSTON, UTAH-ARIZONA .....	113
Abstract .....	113
Introduction .....	114
Observations and Results .....	114
Discussion .....	120
Conclusions .....	121
Acknowledgments .....	121
References .....	122
5. A COMPARISON OF MINERAL IDENTIFICATION BY REFLECTANCE SPECTROSCOPY AND POWDERED X-RAY DIFFRACTION.....	123
Abstract .....	123
Introduction and Objectives .....	123
Methods .....	125
Results .....	126
Discussion .....	132
Conclusions .....	141
References .....	142
APPENDICES	
A. SUPPORTING DATA AND FIGURES .....	144
B. DATA IN DIGITAL FORMAT (CD) .....	237

## LIST OF TABLES

<u>Table</u>	<u>Page</u>
2.1 Coyote Buttes Diagenetic Facies .....	29
3.1 Trample Surface Data from Ten Plots .....	91
3.2 Tridactyl Impressions Identified from Plots in Table 3.1 .....	96
3.3 Ovate Impressions with Clear Middle (III) Impressions Identified from Plots in Table 3.1 .....	97
3.4 Sauropodomorph Impressions .....	98
5.1 Band Minima (nm) for Measured Reflectance (R <sub>m</sub> ) Spectra .....	128
5.2 Band Minima (nm) for Continuum Removed (R <sub>m</sub> /R <sub>c</sub> ) Spectra .....	130
A.1 Sample Facies, Locality and Analyses .....	145
A.2. EDAX Analysis, Sample CBN 7.20.06#1 Location A .....	159
A.3 EDAX Analysis, Sample CBN 7.20.06#1 Location B .....	159
A.4 EDAX Analysis, Sample CBN 7.20.06#1 Location C .....	159
A.5 EDAX Analysis, Sample CBN 7.20.06#1 Location D .....	160
A.6 EDAX Analysis, Sample CBN 7.20.06#1 Location E .....	160
A.7 EDAX Analysis, Sample CBN 7.20.06#1 Location F .....	160
A.8 EDAX Analysis, Sample CBN 7.22.06#2 Location A .....	161
A.9 EDAX Analysis, Sample CBN 7.22.06#2 Location B .....	161
A.10 EDAX Analysis, Sample CBN 7.22.06#2 Location C .....	161



A.11 EDAX Analysis, Sample CBN 7.22.06#2 Location D .....	162
A.12 EDAX Analysis, Sample CBN 7.22.06#2 Location E .....	162
A.13 EDAX Analysis, Sample CBN 7.22.06#2 Bulk Count .....	162
A.14 EDAX Analysis, Sample CBN 12.18.06#9 Location A .....	163
A.15 EDAX Analysis, Sample CBN 12.18.06#9 Location B .....	163
A.16 EDAX Analysis, Sample CBN 12.18.06#9 Location C .....	163
A.17 EDAX Analysis, Sample CBN 12.21.06#6 Location A .....	164
A.18 EDAX Analysis, Sample CBN 12.21.06#6 Location B .....	164
A.19 EDAX Analysis, Sample CBN 12.21.06#3 Bulk Count .....	165
A.20 EDAX Analysis, Sample CBN 12.21.06#3 Bulk Count .....	165
A.21 EDAX Analysis, Sample CBN 12.21.06#3 Bulk Count .....	165
A.22 EDAX Analysis, Sample CBN 12.21.06#3 Single Grain .....	166
A.23 Trample Surface Plot 1, Impression Dimensions and Orientation .....	196
A.24 Trample Surface Plot 2, Impression Dimensions and Orientation .....	198
A.25 Trample Surface Plot 3, Impression Dimensions and Orientation .....	200
A.26 Trample Surface Plot 4, Impression Dimensions and Orientation .....	203
A.27 Trample Surface Plot 5, Impression Dimensions and Orientation .....	205
A.28 Trample Surface Plot 6, Impression Dimensions and Orientation .....	208
A.29 Trample Surface Plot 7, Impression Dimensions and Orientation .....	209
A.30 Trample Surface Plot 8, Impression Dimensions and Orientation .....	212
A.31 Trample Surface Plot 9, Impression Dimensions and Orientation .....	214
A.32 Trample Surface Plot 10, Impression Dimensions and Orientation .....	217
A.33 Sieved Fractions of Micro-concretion Bearing Sand .....	219

A.34	Characterization of Micro-concretion Site 1 .....	220
A.35	Characterization of Micro-concretion Site 2 .....	221
A.36	Characterization of Micro-concretion Site 3A .....	222
A.37	Wind Ripple Index of Micro-concretion Site 3A .....	223
A.38	Wind Ripple Index of Site 3B .....	224
A.39	Wind Ripple Index of Sand Ripple Site 3C .....	225
A.40	Wind Ripple Index of Micro-concretion Site 3D .....	226
A.41	Intersection Angles and Analysis of Polygonal Fractures Measured from Wopmay Rock, Meridiani Planum, Mars .....	227
A.42	Intersection Angles and Fracture Lengths of Large (> 2.0 m dia.) Polygonal Fractures Measured from Navajo Sandstone .....	228
A.43	Intersection Angles of Small (< 2.0 m dia.) Polygonal Fractures Measured from Navajo Sandstone .....	229
A.44	Bulbous Polygonal Weathering Fractures .....	230
A.45	Vertical Faces Accompanying Polygonal Weathering Fractures .....	231
A.46	Checkerboard Weathering Fractures .....	232
A.47	Step and Riser Orientation and Inferred Wind Direction at The Wave ..	233
A.48	Wind Velocity Measured at The Wave .....	234

## LIST OF FIGURES

<u>Figure</u>	<u>Page</u>
1.1 The Coyote Buttes and Paria Plateau .....	2
1.2 Extent of Navajo Sandstone and equivalent units .....	5
2.1 Paria Plateau, Vermilion Cliffs National Monument, and Coyote Buttes study area .....	14
2.2 Aerial photo and mapped color facies of Coyote Buttes .....	17
2.3 Stratigraphic sections along a N-S transect of Coyote Buttes .....	24
2.4 Diagenetic facies of Coyote Buttes .....	30
2.5 Increased potassium feldspar in Coyote Buttes thin sections .....	31
2.6 Representative petrography and reflectance spectra for Coyote Buttes diagenetic facies .....	32
2.7 Upward migration and pooling of a buoyant, reducing fluid .....	38
2.8 Panoramics of Coyote Buttes (Top Rock) .....	47
2.9 Mottled coloration indicative of invertebrate burrowing .....	50
2.10 Horizontal red staining in wet interdune intervals .....	51
2.11 Cataclastic deformation bands .....	53
2.12 HFO staining against cataclastic deformation bands .....	54
2.13 Coloration associated with synsedimentary faulting in Sand Cove .....	58
2.14 Diagenetic, sedimentary, and geomorphic evolution of the Wave .....	64

3.1	Top Rock trample surface and representative impressions .....	81
3.2	Ten individual measured plots delineated by dashed line .....	84
3.3	Stratigraphic column including the Top Rock trample surface .....	87
3.4	Schematic of the Top Rock trample surface .....	89
3.5	Representative tracks and impressions .....	90
3.6	Southwest track orientation showing direction of travel perpendicular to northwesterly paleowind .....	93
4.1	Depositional context of micro-concretion ripples.....	115
4.2	Representative micro-concretion ripples.....	116
4.3	Petrographic thin section of spheroidal micro-concretions .....	118
4.4	Grain size distribution of quartz sand and micro-concretions from sieved samples .....	118
4.5	Navajo Sandstone micro-concretion ripples .....	119
5.1	Reflectance spectra of samples with varying quartz content .....	129
5.2	X-ray powder diffraction patterns of hematite, goethite, and quartz standards .....	131
5.3	X-ray powder diffraction patterns for 99 Qtz:1 HFO <sub>mix</sub> weight percent mixtures .....	133
5.4	X-ray powder diffraction patterns of 50 Hm:50 Go HFO <sub>mix</sub> mixtures combined with quartz sand at various weight percent ratios .....	134
5.5	750-1300 nm absorption features for various hematite:goethite mixtures .....	136
5.6	Reflectance spectra for 99 Qtz:1 HFO <sub>mix</sub> weight percent mixtures .....	138
5.7	Average band minima of 34 Hm:Go mixtures .....	140
A.1	Common coloration of Coyote Buttes diagenetic facies .....	149
A.2	SEM image of sample CBN 7.20.06#1 .....	150

A.3 SEM image of carbon-rich fibers in sample CBN 7.20.06#1 .....	151
A.4 SEM image of sample CBN 7.22.06#2 .....	152
A.5 SEM image of sample CBN 7.22.06#2 .....	153
A.6 SEM image of bleached sample CBN 12.18.06#9 .....	154
A.7 SEM image variable Liesegang atop red and white banded sample CBN 12.21.06#6 .....	155
A.8 SEM image of sample CBN 12.21.06#3 .....	156
A.9 SEM image of orange hematite and micro-concretion facies sample CBN 8.22.06#4 .....	157
A.10 SEM image of orange hematite and micro-concretion facies sample CBN 8.22.06#4 .....	158
A.11 Reflectance spectra transect across sample CBN 8.22.06#5 .....	168
A.12 Reflectance spectra transect across sample CBN 7.22.06#2 .....	169
A.13 Reflectance spectra transect across sample CBN 7.22.06#1 .....	170
A.14 Reflectance spectra transect across sample CBN 8.22.06#3 .....	171
A.15 Reflectance spectra transect across sample CBN 12.20.06#5 .....	172
A.16 Reflectance spectra transect across sample CBN 12.20.06#5 .....	173
A.17 Reflectance spectra transect across sample CBN 12.20.06#4 .....	174
A.18 Reflectance spectra transect across sample CBN 12.21.06#2 .....	175
A.19 Reflectance spectra transect across sample CBN 12.21.06#6 .....	176
A.20 Reflectance spectra transect across sample CBN 5.1.07#1 .....	177
A.21 Reflectance spectra transect across sample CBN 7.15.06#9 .....	178
A.22 Reflectance spectra transect across sample CBN 12.18.06#10 .....	179
A.23 Reflectance spectra transect across sample CBN 7.19.06#2 .....	180

A.24	Reflectance spectra transect across sample CBN 4.26.07#2 .....	181
A.25	Reflectance spectra transect across sample CBN 7.20.06#4 .....	182
A.26	Reflectance spectra transect across sample CBN 12.21.06#5 .....	183
A.27	Reflectance spectra transect across sample CBN 7.14.06#2 .....	184
A.28	Reflectance spectra transect across sample CBN 5.2.07#2 .....	185
A.29	Photomicrographs of basal red facies .....	186
A.30	Photomicrographs of red and white banded facies sample CBN 12.18.06#10 .....	187
A.31	Photomicrographs of a micro-concretion in the bleached facies .....	188
A.32	Photomicrographs of bleached facies samples CBN 12.18.06#5 .....	189
A.33	Photomicrographs of variable Liesegang facies sample CBN 6.25.06#2 .....	190
A.34	Photomicrographs of iron oxide crystal growth in variable Liesegang facies .....	191
A.35	Photomicrographs of orange hematite and micro-concretion facies .....	192
A.36	Photomicrographs of upper red facies sample CBN 12.20.06#6 .....	193
A.37	Photomicrograph of basal red facies showing high (20-30%) porosity ..	194

## ACKNOWLEDGMENTS

This research has been realized through the support of many individuals. In particular, my Supervisory Committee—Marjorie Chan, John Bowman, William Parry, and Erich Petersen—has guided me with insight, patience, and encouragement. My officemate Sally Potter has offered invaluable ideas, humor, and enthusiasm. Jessica Allen, Travis Potter, Vaughn and Victoria Thompson, Mara Dale, Hugh Sakols, Brian Parnham, and Sara Hanner endured shadeless days as field assistants. Tony Ekdale at the University of Utah and Jim Kirkland at the Utah Geological Survey provided dinosaur track expertise. Special thanks to Rody Cox, Mike Salamacha, and the Bureau of Land Management, Arizona Strip and Kanab Field Offices for permitting and logistical support. Critical review of the trample surface manuscript was given by David Gillette and Loïc Costeur. Quintin Sahratian prepared high-quality thin sections and Matthew DeLong assisted with the SEM. Funding was received through the NSF GK-12 Program and the NASA Mars Fundamental Research Program grant number NNG06GI10G to M.A. Chan. Certainly, my experience at the University of Utah would not have been nearly as enjoyable or productive without the friendship of my fellow graduate students. Thanks to Erica Tucker, Matt Baxter, and Jake Brenner for the inspiration to explore the desert. Finally, little in my life would have been possible without the loving guidance of my family. For all your ongoing support, I am forever grateful.

## CHAPTER 1

### INTRODUCTION

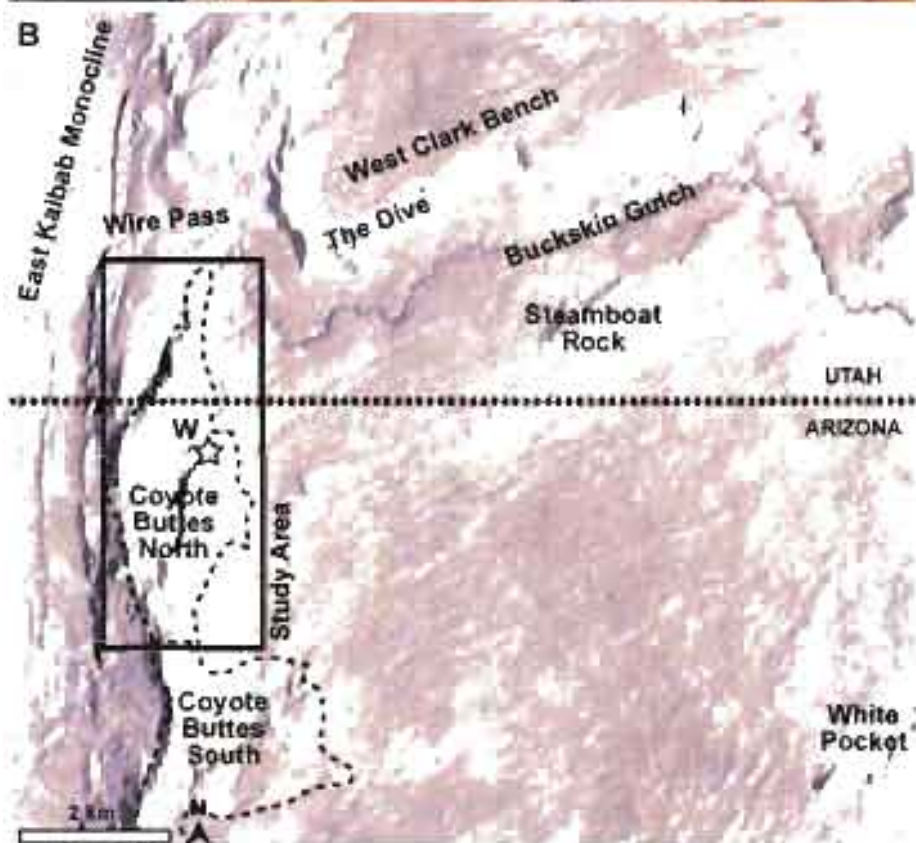
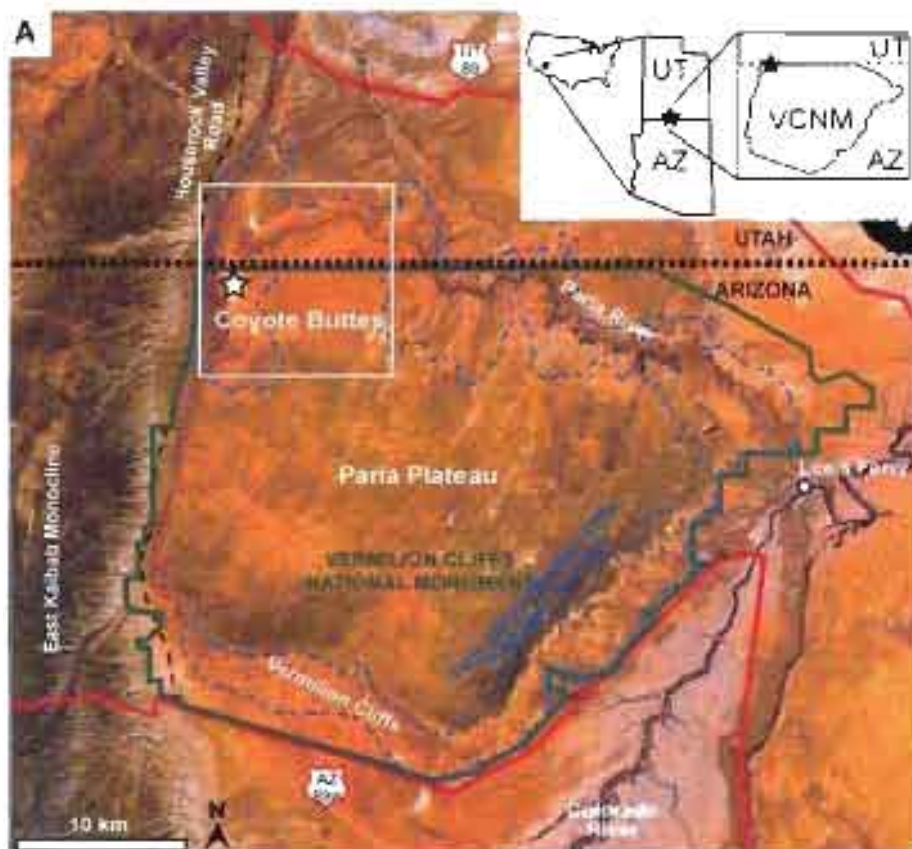
#### The Coyote Buttes

The Colorado Plateau occupies much of the southwestern United States including portions of Arizona, Colorado, Utah, and New Mexico. This region presents unobstructed views from mesa tops, rocks and soils the colors of an artist's palette, lone standing buttes, and canyons cut thousands of feet deep. Straddling the Utah and Arizona borders, situated west of center on the Colorado Plateau, is a wilderness upland—the Paria Plateau (Figure 1.1A). The plateau forms the bulk of the Vermilion Cliffs National Monument (VCNM).

On the Paria's western margin, along a narrow ridge of upturned strata, lie the Coyote Buttes. Here, visitors wander through wind-sculpted bowls of Navajo Sandstone deposited in a vast and ancient erg. The spectacular geology draws thousands of wilderness enthusiasts and photographers each year. Most venture to discover "The Wave," where vivid colors accent cross-strata resembling a cresting ocean wave. In 2005, more than 6,600 visitors registered at trailheads entering the Coyote Buttes (Salamacha, 2006). The area's popularity necessitates special permitting regulations; the Coyote Buttes Permit Area is divided into north and south sections to allow maximum visitation with minimum impact (Figure 1.1B).



Figure 1.1. The Coyote Buttes and Paria Plateau. A) The Coyote Buttes is located within the Paria Canyon/Vermilion Cliffs Wilderness, NW corner of VCNM, UT/AZ (image courtesy NASA Worldwind). B) The study area encompasses the Coyote Buttes North Permit Area and is bound to the west by the ~N-S trending East Kaibab monocline (image courtesy Google Earth). W = The Wave.



The Coyote Buttes has a unique combination of stratigraphy, coloration, and exposure that provides insight into the sedimentary, geomorphic, and diagenetic evolution of eolian deposits on the Colorado Plateau. Red, purple, pink, orange, and yellow hues paint the landscape and preserve in fine detail the migration and chemical reaction fronts of fluids and gases through the sandstone. The exquisite preservation of numerous dinosaur ichnogenera in both interdune and dune settings allows insight into ecology of the Navajo erg. Modern surface processes—producing micro-concretion ripples and polygonal weathering patterns—have proved useful terrestrial analogs to process thought to have occurred on Mars.

Despite the Coyote Butte's spectacular geology, relatively little work has been done to understand its history. This study uses both field and laboratory techniques to document and interpret the spectacular geology preserved at the Coyote Buttes. Field techniques were primarily used at the macro scale: geologic mapping of diagenetic facies, measured sections, sample collection, and outcrop observations. Laboratory analyses were predominately performed at the micro-scale: thin section analysis and the use of reflectance spectra to determine the mineralogy associated with coloration patterns. This study focuses upon the Coyote Buttes North Permit Area, which is herein referred to as the Coyote Buttes.

### Navajo Sandstone

Distinguished by its large-scale, eolian cross bedded foresets, the Navajo Sandstone and its equivalent formations (Aztec and Nugget Sandstones) cover an area of over 350,000 km<sup>2</sup> in Arizona, Colorado, Nevada, New Mexico, and Utah (Kocurek and Dott, 1983; Figure 1.2). In Utah, the Navajo Sandstone can form sandstone cliffs over

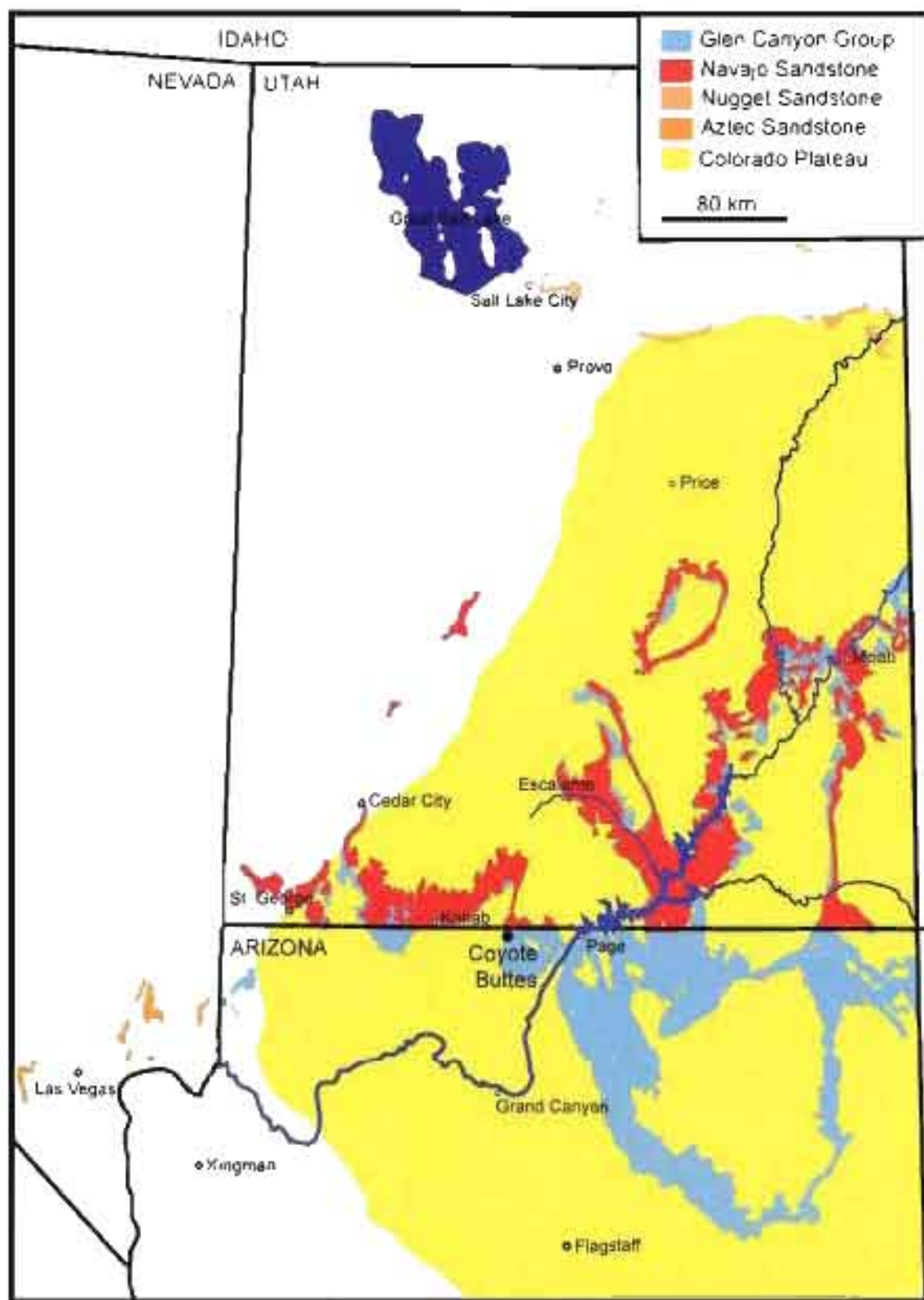


Figure 1.2. Extent of Navajo Sandstone and equivalent units compiled after Stewart and Carlson, 1978; Hirschberg and Pitts, 2000, and Hintze et al., 2002

600 m tall and extends from the Vermilion Cliffs, through Glen Canyon, to Arches National Park. On the Paria Plateau, the Navajo Sandstone forms the sculpted rock of the Coyote Buttes.

The Navajo Sandstone was deposited 190 million years ago (Loope and Rowe, 2003) as a giant, arid, eolian erg. It has been estimated that the volume of sand deposited by the Navajo erg was between 60,000 - 140,000 km<sup>3</sup>, the equivalent of 6 - 14 million years of continuous deposition at the mouth of the Mississippi River (Kocurek, 2003). In recreating the geography of the Navajo erg, Rahl et al. (2003) envision that most of the Navajo sands were derived from the erosion of the ancestral Appalachian Mountains. They propose rivers carrying sediment from their headwaters in the ancient Appalachians to the western shores of Pangea, flowing north of the Ancestral Rockies. From here, the rivers' sand was blown to the south to form the Navajo erg.

The Early Jurassic Navajo Sandstone is the youngest unit of the Glen Canyon Group (e.g., Olsen and Galton, 1977; Clark and Fastovsky, 1986; Biek et al., 2000; Irmis, 2005). On the Paria Plateau, the Navajo Sandstone overlies the Permian Kaibab Formation, the Triassic Moenkopi and Chinle Formations, and the Jurassic Moenave and Kayenta Formations (Blakey 1989; Blakey et al., 1993; Caputo, 2003; Doelling et al., 2003). The Navajo lies beneath the Jurassic Carmel Formation and Page Sandstone (Blakey et al., 1988; Caputo, 2003; Doelling et al., 2003). This stratigraphic sequence records the transition from shallow marine limestones (Kaibab and Moenkopi) to terrestrial muds and siltstones (Moenkopi, Chinle, Moenave) to fluvial muds and eolian sands (Kayenta) to large eolian dunes (Navajo) to near shore sands and siltstones

(Carmel) to near shore eolian sands (Page Sandstone; Blakey et al., 1988; Jones and Blakey, 1997; Biek, 2002).

On the Paria Plateau, the Navajo Sandstone is a fine to medium-grained, rounded, well-sorted quartz to feldspathic arenite. It is colored in a combination of whites, yellows, purples, oranges, and reds. The Navajo Sandstone is the sculpted rock of the Coyote Buttes and forms the prominent cliffs of The Dive, Steamboat Rock, and White Pocket on the Paria Plateau.

### Chapter Summaries

The following three chapters each deal with significant components that make the Coyote Buttes a unique geologic resource. The first chapter, and main focus of this thesis, “Coloration and Diagenetic History of Jurassic Navajo Sandstone at Coyote Buttes, Paria Canyon/Vermilion Cliffs Wilderness, Utah and Arizona,” investigates the occurrence of numerous diagenetic events that stain the sandstone with vividly hued iron oxide mineralogies. Stratigraphic constraints on fluid flow are gleaned from coloration patterns, while the relationship between coloration and tectonic structures allows for a relative time constraint on fluid flow. Laboratory analyses identify coloration as due to iron oxide mineralogies—primarily hematite.

“Wet Interdune Dinosaur Trample Bed in the Jurassic Navajo Sandstone, Coyote Buttes, Arizona: Rare Preservation of Multiple Track Types and Tail Drag Marks,” documents the spectacular occurrence of thousands of vertebrate tracks. These prints are assigned to the ichnogenera *Eubrontes*, *Anchisauripus*, *Grallator* and to an unidentified Sauropodomorph. This presence of this large trample bed allows for insights into

climatic and ecologic dynamics during the early Jurassic. This trample surface was discovered while conducting diagenetic studies.

“Hematite ‘Microberry’ Wind Ripples: Eolian Conditions for a Terrestrial Martian Analog from the Jurassic Navajo Sandstone, Utah-Arizona,” investigates the unique set of conditions that create complex, coarse-grained wind ripples that include mm-scale iron oxide micro concretions. The micro-concretions occur within the several diagenetic facies of the Navajo Sandstone. These terrestrial ripples hold remarkable similarity to widespread ripples revealed by the Mars Exploration Rover Opportunity. Study of their occurrence at the Coyote Buttes may be scaled to atmospheric and geologic processes on Mars.

Finally, “A Comparison of Mineral Identification by Reflectance Spectroscopy and Powder X-ray Diffraction,” utilizes laboratory techniques to discriminate between iron oxide mineral identification using both reflectance spectroscopy and powder x-ray diffraction (XRD). Samples obtained from the University of Utah, Geology and Geophysics mineral collection were used as standards to create sand samples of known iron oxide mineralogy and abundance. Results highlight the utility of reflectance spectroscopy in reliably identifying iron oxide mineralogies at concentrations too low to be detected by XRD and establish a ratio for discriminating relative abundances of hematite and goethite from samples containing a mixture of the two oxides. This is used as a type of calibration to understand analyses of field sandstone samples.

## References

- BIEK, R.F., 2002, Interim geologic map of the Kolob Reservoir quadrangle, Washington and Iron Counties, Utah: Utah Geological Survey Open-File Report 387, scale 1:24,000.
- BIEK, R.F., WILLIS, G.C., HYLLAND, M.D., AND DOELLING, H.H., 2000, Geology of Zion National Park, Utah, *in* Sprinkel, D.A., Chidsey, T.C., and Anderson, P.B., eds., Geology of Utah's Parks and Monuments, Utah Geological Association, Publication 28, p. 107-135.
- BLAKEY, R.C., 1989, Triassic and Jurassic geology of southern Colorado Plateau, *in* Jenney, J.P. and Reynolds, S.J., eds., Geologic Evolution of Arizona, Arizona Geological Society, Digest 17, p. 369-396.
- BLAKEY, R.C., BASHAM, E.L., AND COOK, M.J., 1993, Early and Middle Triassic paleogeography, Colorado Plateau and vicinity, *in* Morales, M., ed., Aspects of Mesozoic Geology and Paleontology of the Colorado Plateau, Museum of Northern Arizona, Bulletin 59, p.13-26.
- BLAKEY, R.C., PETERSON, F., AND KOCUREK, G., 1988, Late Paleozoic and Mesozoic eolian deposits of the Western Interior of the United States: Sedimentary Geology, vol. 56, p. 3-125.
- CAPUTO, M.V., 2003, Geology of the Paria Canyon—Vermilion Cliffs Wilderness, Utah and Arizona, *in* Sprinkel, D.A., Chidsey, T.C., Jr., and Anderson, P.B. eds., Geology of Utah's Parks and Monuments, Utah Geological Association, Publication 28, p. 535-561.
- CLARK, J.M. AND FASTOVSKY, D.E., 1986, Vertebrate biostratigraphy of the Glen Canyon Group in northern Arizona, *in* Padian, K. ed., The Beginning of the Age of Dinosaurs: Faunal Changes Across the Triassic-Jurassic Boundary: New York, Cambridge University Press, p. 285-301.
- DOELLING, H.H., BLACKETT, R.E., HAMBLIN, A.H., POWELL, J.D., AND POLLOCK, G.L., 2003, Geology of Grand Staircase-Escalante National Monument, Utah, *in* Sprinkel, D.A., Chidsey, T.C., Jr., and Anderson, P.B. eds., Geology of Utah's Parks and Monuments, Utah Geological Association, Publication 28, p. 535-561.
- HINTZE, L.F., WILLIS, G.C., LAES, D.Y.M., SPRINKEL, D.A., AND BROWN, K.D., 2002, Digital geologic map of Utah: Utah Geologic Survey Map 179DM.
- HIRSCHBERG, D.M., AND PITTS, G.S., 2000, Digital geologic map of Arizona: a digital database derived from the 1983 printing of the Wilson, Moore, and Cooper 1:500,000-scale map: United States Geological Survey Open-file Report 00-409.



- IRMIS, R.B., 2005, A review of the vertebrate fauna of the Lower Jurassic Navajo Sandstone in Arizona, *in* McCord, R.D. eds., *Vertebrate Paleontology of Arizona*, Mesa Southwest Museum, Bulletin 11, p. 55-71.
- JONES, L. S., AND BLAKEY, R. C., 1997, Eolian-fluvial interaction in the Page Sandstone (Middle Jurassic) in south-central Utah, USA: a case study of erg-margin processes: *Sedimentary Geology*, v. 109, p. 181-198.
- KOCUREK, G., 2003, Limits on extreme eolian systems; Sahara of Mauritania and Jurassic Navajo Sandstone examples, *in* Chan, M.A., and Archer, A., eds., *Extreme Depositional Environments: Mega End Members in Geologic Time*, Geological Society of America, Special Paper 370, p. 43-52.
- KOCUREK, G., AND DOTT, R.H., JR., 1983, Jurassic paleogeography and paleoclimate of the central and southern Rocky Mountains regions, *in* Reynolds, M.W., and Dolly, E.D., eds., *Mesozoic Paleogeography of the West-Central United States*: Denver, SEPM, Rocky Mountain Section, p. 101-116.
- LOOPE, D.B., AND ROWE, C.M., 2003, Long-lived pluvial episodes during deposition of the Navajo Sandstone: *Journal of Geology*, v. 111, p. 223-232.
- OLSEN, P.E. AND GALTON, P.M., 1977, Triassic-Jurassic tetrapod extinctions: are they real?: *Science*, v. 197, p. 983-986.
- RAHL, J., REINERS, P., CAMPBELL I., NICOLESCU, S., AND ALLEN, C., 2003, Combined single-grain (U/Th)/He and U/Pb dating of detrital zircons from the Navajo Sandstone, Utah: *Geology*, v. 31, p. 761-764.
- STEWART, J.H. AND CARLSON, J.F., 1978, *Geologic Map of Nevada: United States Geological Survey*, 1:500,000 scale.
- SALAMACHA, M., 2006, Email to the author, 4 May.

## CHAPTER 2

# COLORATION AND DIAGENETIC HISTORY OF JURASSIC NAVAJO SANDSTONE AT COYOTE BUTTES, PARIA CANYON/VERMILION CLIFFS WILDERNESS, UTAH AND ARIZONA

### Abstract

The Coyote Buttes, in Jurassic Navajo Sandstone at the northwestern margin of the Vermilion Cliffs National Monument, AZ, is renowned for its stunning diagenetic coloration of delicately sculpted, cyclic eolian cross-strata. The location draws thousands of wilderness enthusiasts and photographers each year primarily to a unique geomorphic feature – “The Wave” – where vivid colors accent cross-strata resembling a cresting ocean wave. The wide range of red, orange, pink, and purple sandstone hues is due to predominately hematite grain coatings and cement. Yellow to brown coloration is indicative of goethite. White (bleached) color occurs where iron oxide coatings have been removed. Coloration is influenced by both sedimentary and tectonic structures at microscopic to outcrop to regional scales.

Sandstone coloration is categorized into six main (10's m thick) diagenetic facies: (1) a basal, primary red facies; (2) a red and white banded transition facies; (3) a bleached upper facies; (4) an upper, primary red facies; (5) an overprinting facies of numerous,

variably colored iron oxide Liesegang bands; and (6) an overprinting orange Liesegang band and micro-concretion facies composed of multiple reaction fronts. Stratigraphic relationships show that large-scale diagenetic facies (1-4) are due primarily to advective fluid flow and iron mobilization within the host rock. Small (cm-scale) and large (10's-m scale) bleaching patterns indicate the upward migration and accumulation of a buoyant, chemically reducing and bleaching fluid. Cm to m scale, Liesegang-type reaction fronts are due to diffusive mass transfer causing the chemical precipitation of iron oxide mineralogies.

Relative timing of diagenetic episodes is constrained by cross-cutting relationships at outcrop to microscopic scales. Primary coloration is an even synsedimentary red. Bleaching is followed by the introduction of variable Liesegang coloration and the orange Liesegang overprinting events. Bleaching and Liesegang coloration occur concurrently with Laramide-aged faulting along the East Kaibab monocline. Localized, synsedimentary faulting suggests that some white windripple strata may be primary. No fewer than four diagenetic episodes are recorded at The Wave where the importance of wind as the stand-alone force of contemporary erosion is highlighted. This study contributes a better understanding of the intense diagenetic coloration and fluid flow history that distinguish the Coyote Buttes as an exceptional geologic resource.

### Introduction

The Jurassic Navajo Sandstone is well exposed at the Coyote Buttes along the Utah/Arizona border on the western margin of the Paria Plateau in Vermilion Cliffs

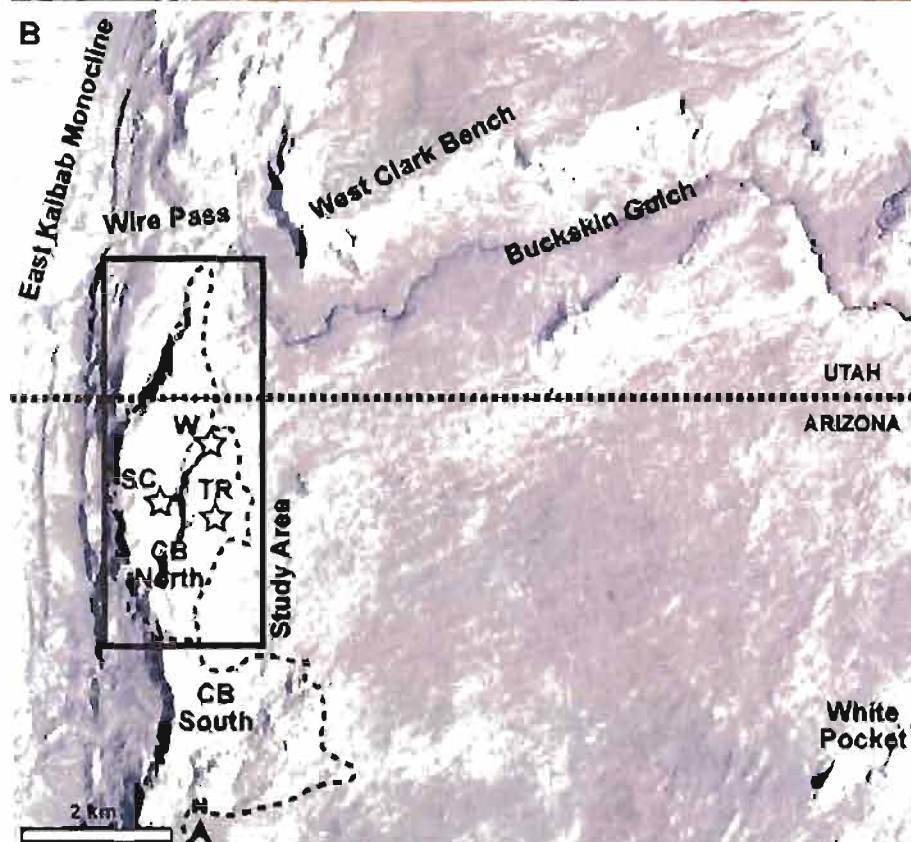
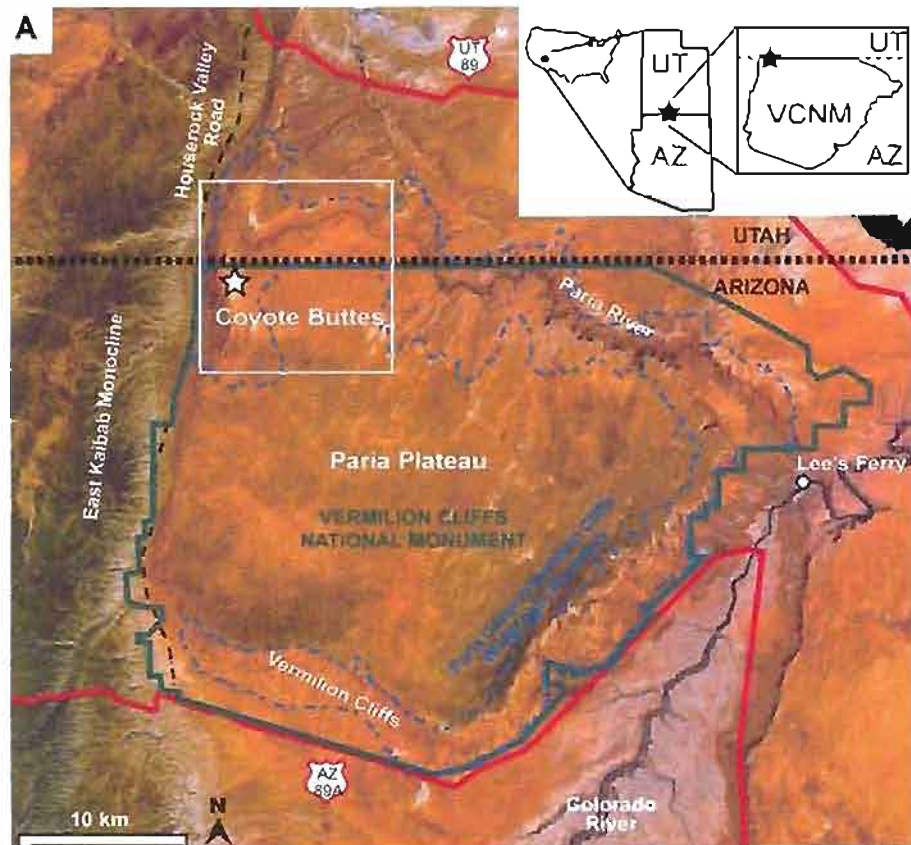
National Monument (Figure 2.1). The site is renowned for its stunning diagenetic coloration, climatically induced cyclic eolian stratification (Chan and Archer, 2000; Loope et al., 2001), dinosaur tracks, (Loope, 2006; Seiler and Chan, 2008), erosional sculpting by wind (Loope et al., 2008), and analogs to Mars (Chan et al., 2007; Seiler et al., 2007). The aesthetic combination of sandstone coloration and modern eolian sculpting makes the Coyote Buttes a major attraction for outdoor enthusiasts.

This study has seven goals: (1) identify and describe the diagenetic color facies at Coyote Buttes; (2) map these facies; (3) determine the relationship between coloration and fluid interactions; (4) identify stratigraphic constraints on coloration; (5) identify structural influences on coloration; (6) identify iron oxide (herein referred to as HFO, hydrous ferric oxide) mineralogies associated with the various colors; and (7) establish the relative timing of fluid interactions. The study utilizes detailed field technique, thin section petrography and visible and near infrared reflectance spectroscopy. Work presented here has important implications for understanding diagenesis and fluid flow patterns in a major oil-producing reservoir and important aquifer. In addition, mobility of iron and the occurrence of HFO concretions can be a terrestrial analog to the red planet Mars.

### Location and Geologic Setting

The Coyote Buttes Permit Area (N36° 59' 45" W 112° 00' 22") occupies 112,500 acres of the Paria Canyon/Vermilion Cliffs Wilderness Area, UT/AZ, on the western margin of the Paria Plateau (Bureau of Land Management, 2007; Figure 2.1). The

Figure 2.1. Paria Plateau, Vermilion Cliffs National Monument, and Coyote Buttes study area. A) The Coyote Buttes is located within the Paria Canyon/Vermilion Cliffs Wilderness, NW corner of Vermilion Cliffs National Monument, UT/AZ (image courtesy NASA Worldwind). B) The study area encompasses the Coyote Buttes North Permit Area and is bound to the west by the ~N-S trending East Kaibab monocline (image courtesy Google Earth). The Butte fault is implicated by Tindall and Davis (1999) and Tindall (2000) as the mechanism for monocline development. CB North = Coyote Buttes North Permit Area; CB South = Coyote Buttes South Permit Area; SC = Sand Cove; W = The Wave.



Coyote Buttes derive their name from a series of Navajo Sandstone spires and lie ~3 km east and parallel to the N-S trending, East Kaibab monocline. The study area encompasses the whole of the Coyote Buttes North Permit area, ~5 km N-S by ~2 km E-W and is herein referred to as Coyote Buttes. Thickness of the Navajo Sandstone on the Paria Plateau is ~600 m (Loope and Rowe, 2003; Loope, 2006); exposure exceeds 200 m at Coyote Buttes. Locally, the Navajo Sandstone strikes  $355^{\circ}$  and dips  $5^{\circ}$ E. This corresponds to the Laramide reactivation (50-80 Ma) of the basement-rooted, west-dipping, high angle reverse Butte Fault whose development led to the eastward dipping East Kaibab monocline (Tindall and Davis, 1999; Tindall, 2000). Navajo Sandstone dip decreases to roughly horizontal eastward from the monocline.

Associated with the Butte Fault are a series of near vertical, m-10 m spaced joints trending  $345$ - $355^{\circ}$  along the western margin of the field area (Figure 2.2). Subparallel to the joints is a complex system of cataclastic deformation bands that likely formed in the damage zone ahead of the propagating fault tip (Fossen et al., 2007). A second set of Laramide-aged, widely spaced ( $>100$  m), near vertical joints trend NE and are likely due to Laramide E-W regional shortening (Pederson, 2008). On the Paria Plateau, these joints have been exploited by Colorado River (Miocene to recent; Pederson et al., 2002) tributary incision to form Buckskin Wash.

Regionally, the Navajo Sandstone is a well-sorted, fine- to medium-grained quartz arenite of eolian origin composed of ~90% quartz, ~5% potassium feldspar, and ~5% clays and subsidiary minerals (Beitler et al., 2005; Chan et al., 2005). At Coyote Buttes, Navajo Sandstone is more feldspar-rich and is classified as a feldspathic arenite (see Diagenetic Descriptions and Interpretations). The Navajo Sandstone and equivalent units



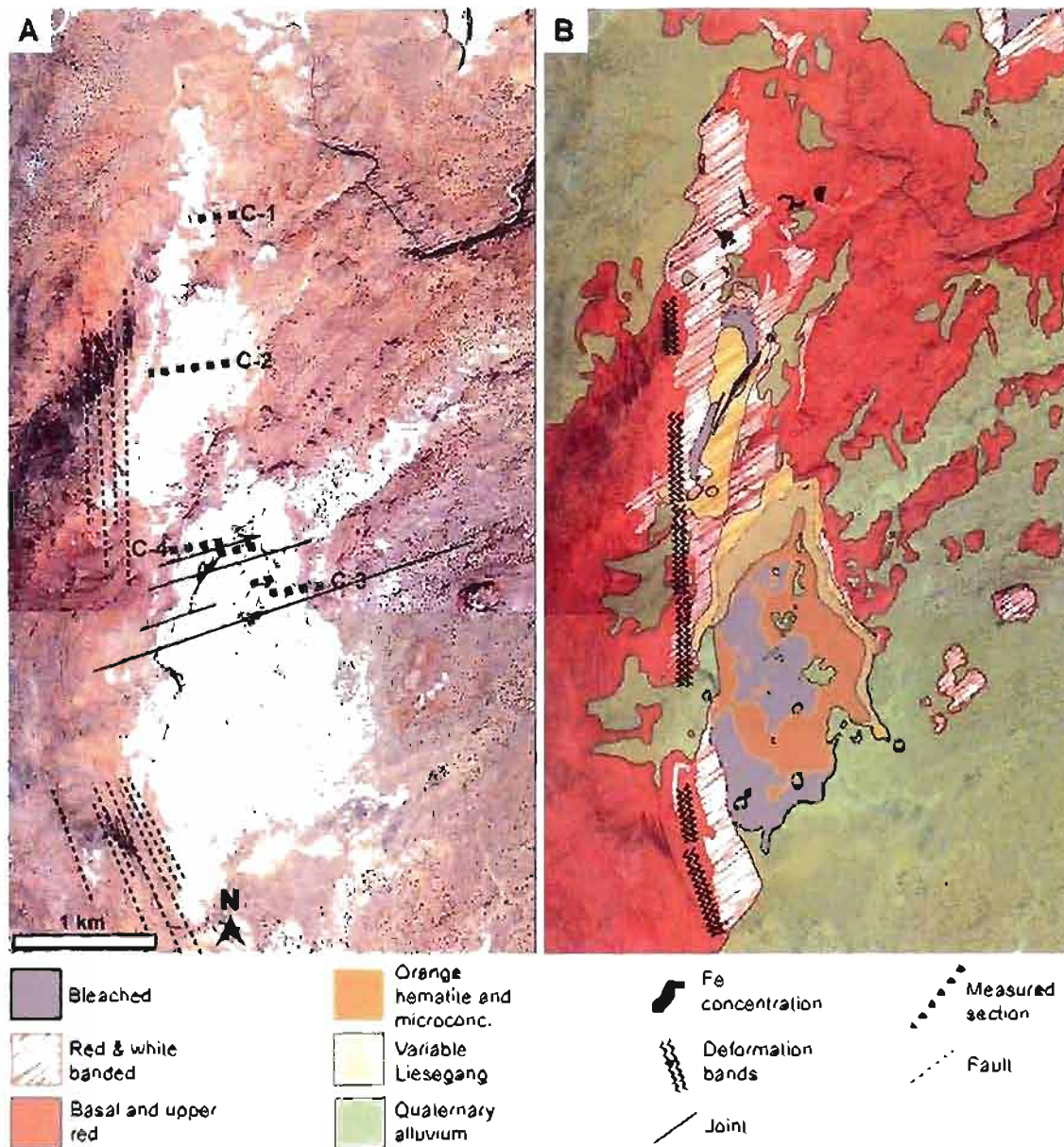


Figure 2.2. Aerial photo and mapped color facies of Coyote Buttes. Bleached and secondary colored sandstone E and NE of the study area is eroded. Stratigraphic sections C-1 to C-4 indicated. Aerial photo courtesy Bureau of Land Management.



(Aztec and Nugget Sandstones) occupy a basinal area  $>350,000 \text{ km}^2$  though its original extent may have been two and a half times that preserved in the rock record (Kocurek and Dott, 1983; Blakey et al., 1988; Kocurek, 2003). These deposits represent the largest erg (sand-sea) deposits known (Blakey et al., 1988; Peterson and Tuner-Peterson, 1989).

Navajo Sandstone provenance is from the Ancestral Appalachians and Rocky Mountains (Dickinson and Gehrels, 2003; Rahl et al., 2003; Reiners et al., 2005) with deposition occurring  $\sim 10^\circ \text{ N}$  latitude on the western edge of the Pangaea Supercontinent (Blakey, 2001; Loope et al., 2004). Jurassic paleoclimate and paleogeography is summarized by Kocurek and Dott (1983), Parrish and Peterson (1988), Parrish (1993), Loope et al. (2001, 2004), Loope and Rowe (2003), Parish and Falcon-Lang (2007), and Rowe et al. (2007). A vast literature exists on the sedimentology and stratigraphy of the Navajo Sandstone (e.g., Blakey et al., 1988; Peterson, 1988; Sampson, 1992; Verlander, 1995; Chan et al., 2000; Eisenberg, 2003).

The Navajo Sandstone (and equivalent Nugget Sandstone) is a significant modern petroleum reservoir in the Sevier Fold and Thrust Belt (Chidsey and Morgan, 2005; Chidsey, 2007; Dalrymple and Morris 2007). Production occurs in the Anschutz Ranch Field, WY, and Pineview Field, UT with discoveries of 75-200 million BBL made in 2004 at the central Utah Covenant Field (Brown, 2005; Moulton and Pinnell, 2005; Bowen et al, 2007). Coloration investigated by this study elaborates upon intraformational interactions of multiple fluids—likely both hydrocarbons and groundwater.

## Previous Work

### Navajo Sandstone Diagenesis

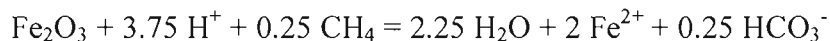
Iron oxides have long been recognized as causing color variations in the Navajo Sandstone and related units (Berner, 1969). Recent investigations have identified specific mechanisms of Navajo Sandstone diagenesis and HFO concretion formation (Chan et al., 2000, 2004, 2005, 2006; Chan and Parry, 2002; Beitler et al., 2003, 2005; Eichhubl et al., 2004; Parry et al., 2004; Eichhubl and Flodin, 2005; Bowen et al., 2007).

Chan et al. (2005) identify three phases responsible for overall coloration events in a complex and open chemical system:

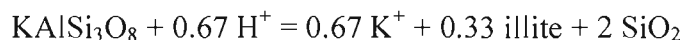
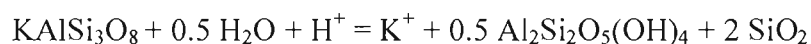
- 1) Primary sandstone reddening due to HFO grain coats derived from the syndepositional to synsedimentary breakdown of iron bearing, detrital mineral grains (Berner, 1969). HFO grain coats represent a minor whole rock percentage—between 0.18 and 1.25 wt %—but cause the even primary (original) pink to orange to red coloration of the sandstone and are commonly encapsulated within early hematite quartz overgrowths (Chan et al., 2005).
- 2) Advective, chemically reducing fluids (likely hydrocarbons) mobilize Fe and bleach the sandstone towards white, leaving < 0.5 wt % HFO in the rock (Chan et al., 2000; Beitler et al., 2005).
- 3) The interaction of iron-bearing reducing fluids with oxidizing groundwater precipitates HFO and produces secondary coloration by diffusion across the redox front between the two fluids (van Gunten and Schneider, 1991).

Bowen et al. (2007) identify the common Navajo Sandstone chemical reactions responsible for events 2 and 3 described above:

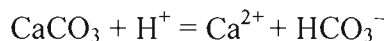
Iron is reduced by a hydrocarbon agent, which bleaches the sandstone and places HFO into solution:



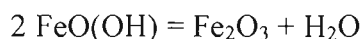
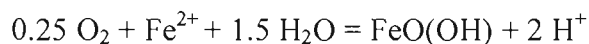
Potassium feldspar alters to kaolinite and illite clays:



Carbonate cement is precipitated and dissolved:



Oxidation by molecular oxygen and the precipitation of HFO from solution produces secondary coloration and iron concretions. The  $\text{H}^+$  produced during the chemical reaction forming goethite may drive the alteration of potassium feldspar to kaolinite and illite and the dissolution of carbonate cements:



Coloration and HFO concretion formation has been investigated from local to regional scales in the Navajo Sandstone and its equivalent Aztec Sandstone (Beitler et al.,

2003, 2004, 2005; Eichhubl et al., 2004; Bowen et al., 2007). General Navajo Sandstone diagenetic facies were identified by Beitler et al. (2005). These facies resulted from groundwater chemical changes that allowed advective iron transport but diffusive mineralization.

Faults act as conduits for fluid flow and HFO mineralization (Chan et al., 2000). Beitler et al. (2003) constrain the most significant regional-scale bleaching on the Colorado Plateau to eroded crests of Laramide highs. These monoclinal uplifts are underlain by blind thrust faults that act as conduits for buoyant, hydrocarbon, reducing fluids which mobilize primary iron in the sandstone (Beitler et al., 2003). Using reflectance spectroscopy, Bowen et al. (2007) map and analyze diagenetic patterns and fluid migration pathways along the East Kaibab monocline ~30 km north of the Coyote Buttes study area.

Parry et al. (2004) utilize deformation bands as timing indicators of diagenetic coloration events. Deformation bands in Navajo Sandstone can form low permeability barriers that compartmentalize the unit (Taylor and Pollard, 2000; Fossen et al., 2007). However, they can also serve as fluid conduits during early, dilatant phases of formation (Parry et al., 2004).

### Reservoir Porosity, Permeability, and Transport

Porosity and permeability studies of core from the equivalent Nugget Sandstone by Lindquist (1988) can be applied to the Navajo Sandstone. Lindquist documents porosity ranging from a few to 25% with permeability spanning five orders of magnitude, from hundredths of milliDarcies to Darcies. Porosity and permeability is closely related

to eolian stratal characteristics and diagenetic history. Porosity and permeability are generally lower towards the base of the Navajo (Lindquist, 1988). Grainflow cross strata has porosity as high as 25% (average 12-13%) and horizontal permeability to one Darcy (Lindquist, 1988). Windripple strata porosity can be as low as 3%, (average 7-8%), with horizontal permeability typically less than 1 milliDarcy (ranging from hundredths to tens of milliDarcies [Lindquist, 1988]). Connate fluids can be displaced to <10% irreducible water in grainflow, but are not as easily displaced in windripple cross strata (Lindquist, 1988). Wet interdune deposits have porosity as low as 2%, permeability of hundredths of milliDarcies, and can contain 60-70% irreducible connate water (Lindquist, 1988). As such, wet interdune deposits can form barriers to fluid flow.

Within the Navajo Sandstone reservoir, mass transport can occur by either advection or diffusion. Advective transport involves the movement of molecules in response to a force and is influenced by eolian stratification (under the conditions described above). Fluids flow preferentially along higher permeability strata, and may be constrained by low permeability eolian laminae.

Diffusive transport—the movement of molecules in response to a concentration gradient across a certain distance—requires no force. Liesegang-type reaction fronts are caused by diffusive mass transfer and chemical precipitation across redox boundaries (Ortoleva, 1984; Barge et al., 2008). Liesegang band formation requires that a large gradient exist between reduced iron and oxygen (Dee, 1986; Barge et al., 2008). Diffusion patterns can be influenced by numerous variables including sedimentary properties, relative reactant concentrations, and biomediation (Ortoleva, 1984; Ortoleva et al., 1987a, b; Barge et al., 2008).

## Methods

### Fieldwork

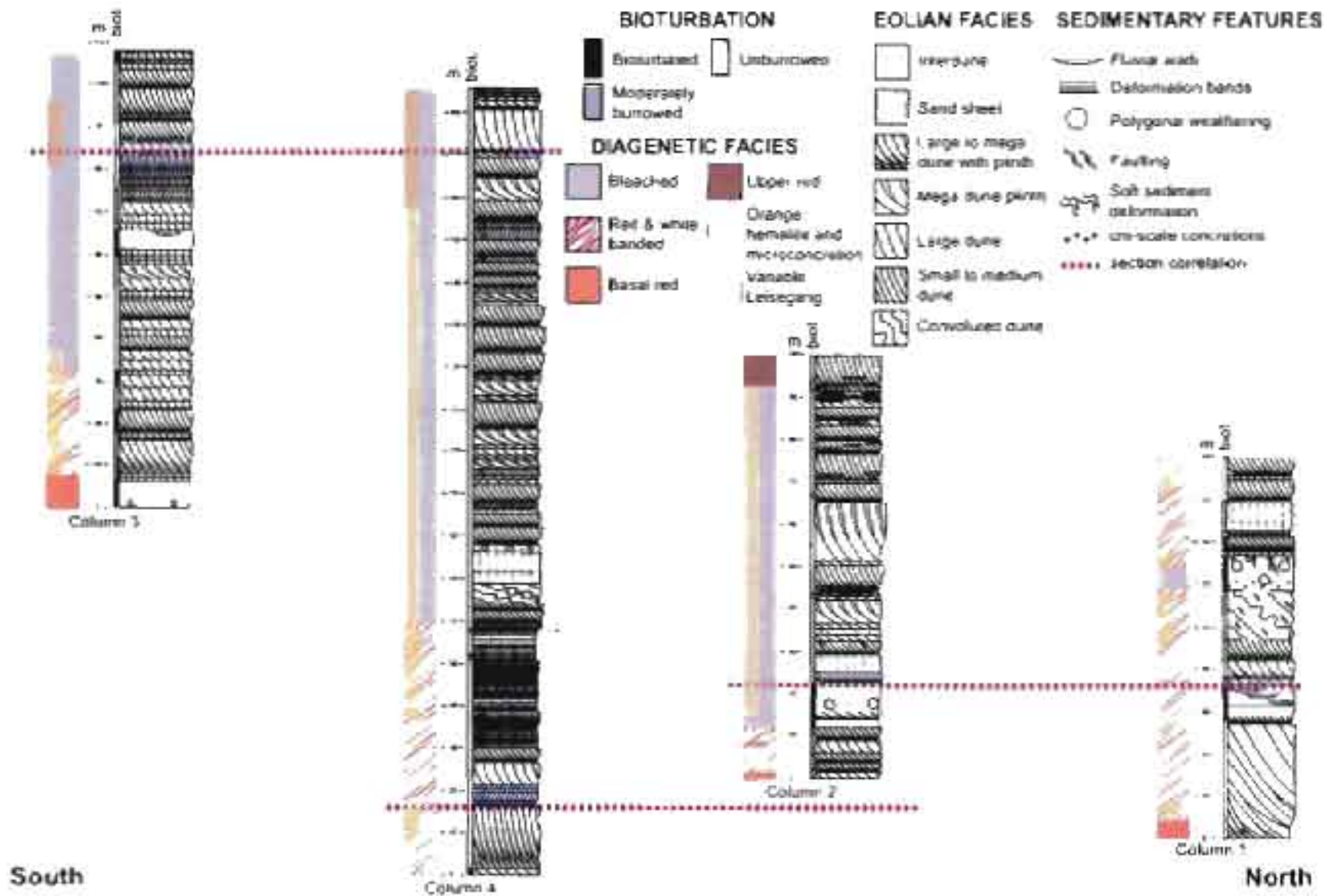
Diagenetic patterns were observed in the field and divided into six diagenetic facies based on coloration, mineralogy, and stratigraphic position. The contacts between these six facies were walked out and mapped over the Coyote Buttes field area (Figure 2.2). Color hue, value, and chroma were quantified against standard Munsell Soil Color Charts (1975). Four detailed stratigraphic sections were measured along a north-south transect of Coyote Buttes and record eolian facies, bioturbation, sedimentary structures, and diagenetic facies (Figure 2.3). The field area was extensively photographed to capture characteristic coloration patterns in context with sedimentary (bedding and synsedimentary faults) and tectonic (joints, tectonic faults, and deformation bands) structures. A focused study incorporating the aforementioned components was performed at The Wave. One hundred twenty three samples were gathered with special attention paid to ensure that sampling did not leave visible outcrop scars.

### Laboratory Analyses

#### Petrography

Thirty-eight thin sections were created, selected from each of the mapped diagenetic facies (minimum five thin sections per facies). Twenty samples were impregnated with blue epoxy to aid in porosity determination. Thin sections were stained for potassium feldspar identification and analyzed using transmitted light. Grain sorting

Figure 2.3. Stratigraphic sections along a N-S transect of Coyote Buttes. Sections record color facies and sedimentary structures. Upper red facies occurs stratigraphically at the top of the section and to the west of N-S trending, Laramide-aged joints and deformation bands.





and visual percentage estimation were performed using comparison charts after Pettijohn et al. (1972) and Terry and Chilingar (1955), respectively.

### Visible and Near Infrared Reflectance Spectroscopy

Samples were analyzed for visible (VIS), near infrared (NIR), and shortwave infrared (SWIR) reflectance spectra using an Analytical Spectral Devices Inc. FieldSpec Spectroradiometer (Model FSP350-2500P), analytical spectral device (ASD). The ASD measures reflectance spectra on 2151 channels from 350-2500 nm. Measurements were made using calibrated artificial illumination and bare fiber foreoptic optimized to a standardized white reference plate. White referencing was repeated between multiple sample batches. Gross sampling was performed with the foreoptic 6 cm from the sample with a constrained 3 cm field of view. Fine-scale ASD transects were performed with the foreoptic mounted 0.5-1 cm from the sample to create a 0.15-0.30 cm field of view.

Reflectance spectroscopy after Bowen et al. (2007) was used to identify diagenetic facies mineralogy. Spectral mineral identification is possible in the eolianites studied because quartz and feldspar lack descriptive spectral signatures over the spectral range analyzed (350-2500 nm; Bowen et al., 2007). Reflectance spectra that depart from this baseline can be attributed to diagenetic mineralization (Bowen et al., 2007). Hematite, goethite and water/hydroxyl have defining band minima in the NIR range (650-2000 nm) whereas kaolinite, illite, and carbonate possess defining band minima in the SWIR spectrum (2000-2500 nm) (Morris 1985; Townsend, 1987; Deaton and Balsam, 1991; Clark, 1995; Vincent 1997; Bowen et al., 2007). Hematite and goethite produce an absorption trough between 750 and 1100 nm; hematite band minima occur at

~855 nm whereas goethite band minima occur at ~930 nm (Deaton and Balsam, 1991; Bowen et al., 2007). Departures from these end members can be due to the inclusion of metals other than Fe into the mineral structure (Ji et al., 2002) and to mixtures of hematite and goethite (Townsend, 1987). When occurring together, hematite has been shown experimentally to have a greater influence on the position of band minima than does goethite (Seiler, 2008). Water and/or hydroxyl ions display band minima at 1400 and 1900 nm (Clark, 1995). Kaolinite exhibits an absorption wavelength doublet at 2200 nm and a relatively pointed trough whereas illite displays a more rounded trough centered around 2200 nm, lacks a doublet, and shows additional absorption bands at 2350 and 2450 nm (Clark, 1995; Vincent, 1997; Bowen et al., 2007). Carbonate displays band minima at 1900, 2350 and 2550 nm (Gaffey, 1985), but is not noted in Coyote Buttes samples.

### Diagenetic Descriptions and Interpretations

Beitler et al. (2005) identify six general diagenetic facies in the Navajo Sandstone at outcrop to microscopic scale in southern Utah (mainly Grand Staircase-Escalante National Monument): red, bleached, diffuse reddish-brown with HFO cement, diffuse yellowish-orange with HFO cement, brownish HFO concretion, and carbonate facies. Though the coloration observed in this study can be placed within these gross categories, six unique diagenetic facies were defined based upon the mappable color patterns of Coyote Buttes (Figure 2.2). Although fine coloration detail preserved at Coyote Buttes allows nearly infinite subcategorization, the facies defined are based upon stratigraphic position, outcrop color patterns, mineralogic, and petrographic criteria that exist at the m-

10's m scale. Descriptions of each diagenetic facies is followed by an interpretation; a summary is presented in Table 2.1.

## Basal Red Facies

### Description

The basal red facies is a generally uniformly colored dark red to red (Munsell color 2.5YR 3/6 to 2.5YR 4/7; Figure 2.4). The facies extends downwards (>100 m) through the lower Navajo Sandstone to basal sections exposed in Buckskin Gulch and Wire Pass (Figure 2.1). On the Paria Plateau, the facies extends laterally >10 km. HFO (predominately hematite) Liesegang bands and hematite micro-concretions (<2 mm diameter) occur in limited distribution and appear to decrease down section. The transition into the red and white banded facies is gradual.

In thin section, the basal red facies is a texturally mature, feldspathic arenite. Samples are moderately to well-sorted, display subrounded to well-rounded grains and 20-30% interparticle primary porosity. Cements are primarily due to pressure solution and quartz overgrowth, with limited clay cements. Clays are generally a minor component (<3%) and fill pore spaces in isolated patches. Illite grain rims are absent. Feldspars range from 10% to 30% in samples (Figure 2.5). Hematite is dispersed throughout samples. Primary hematite flakes and thin crusts on quartz grains are overlain by subhedral to euhedral quartz overgrowths (Figure 2.6). Where not encapsulated within quartz overgrowths, hematite forms thin, specular, colloform accumulations of anhedral platelets. Hematite appears reddish brown in transmitted light and is generally not opaque.

Table 2.1

## Coyote Buttes Diagenetic Facies

Facies	Description	Interpretation
Basal Red	Uniformly colored red (2.5YR 3/6 to 2.5YR 4/7). >100 m thick. extends laterally >10 km. Limited Liesegang bands and hematite microconcretions (< 2mm diameter). Thin, primary hematite grain coats. Both kaolinite and illite are present. No carbonate noted.	Primary red coloration originally pervasive from thin hematite grain coatings - derived from early diagenetic breakdown of Fe-rich, detrital sand constituents. Liesegang bands, microconcretions and secondary hematite growth indicate localized Fe-enrichment.
Red and White Banded	Overall red (2.5YR 3/6 to 2.5 YR 4/7) with lesser bleaching (5YR 8/4) following crossbeds. 10's m thick. Bleaching constrained by low permeability laminae and within windripple strata. Deep red color from secondary goethite precipitation. Spectra and petrographic descriptions match those of the red and bleached facies respectively.	Lowest extent of bleaching, where partially saturated with reducing fluid. Advective flow along permeable laminae forms limited bleaching bands and shows upward migration/pooling of buoyant reducing fluid.
Bleached	Bleached white with minor color variations (7.5YR 7.5/2 to 10YR 8/2). 10's - 100 m thick. Limited, thin hematite grain coats preserved (trapped) by quartz overgrowths. Bleaching extends to low permeability cataclastic deformation bands. Predominately kaolinite clays.	Fe mobilization due to advective fluid flow and pooling of a buoyant reducing fluid (Beitler et al., 2003; 2005). Preserved hematite grain coats underneath quartz overgrowths indicate red coloration predates bleaching. Multiple bleaching events possible.
Variable Liesegang Band	Multiple, cm-m scale Fe- enriched Liesegang bands of variable coloration (10YR 7/8; 5R 2.5/3; 10R 6/8). 10's m thick. Individual bands can extend >30 m. Liesegang bands due to hematite, goethite and mixtures of both. Bands cross-cut all eolian laminae. Kaolinite, illite, or no clay may be present.	Fe diffusion across fluid interface between reducing, buoyant fluid, overlying an oxidizing water table. Cross-cutting relationships show multiple Liesegang band episodes and variable diffusion directions.
Orange Hematite and Micro-Concretion	Multiple, 1-5 m scale orange Liesegang bands with hematite microconcretions (< 2 mm). 10's m thick, in upper 25m of bleached facies. Cyclic color transition in bands (10YR 7.5/3; 10YR 7/6; 5YR 5.5/8). Hematite cement fills pore space at reaction front boundary. Bands cross-cut all eolian laminae. Kaolinite present, illite absent.	Fe diffusion across the upper boundary of a reducing and oxidizing fluid. Reaction fronts may mark the interface between the Fe-saturated bleaching fluid and meteoric water, perched groundwater, a rising groundwater level, or the fluid/air interface.
Upper Red	Uniformly colored red (2.5YR 5.5/4 to 2.5YR 4.5/6) with localized 1-2 cm FeO concretions. 10's m thick. Thin, early diagenetic hematite grain coats. Basal and upper red facies appear as a continuous unit in western portion of field area. Both kaolinite and illite present.	Basal and upper red facies similarities suggest primary/early coloration extended vertically throughout section prior to bleaching. Larger concretions (> 2mm) and carbonate concretions indicate diagenetic style on W side of deformation bands is different from E side.

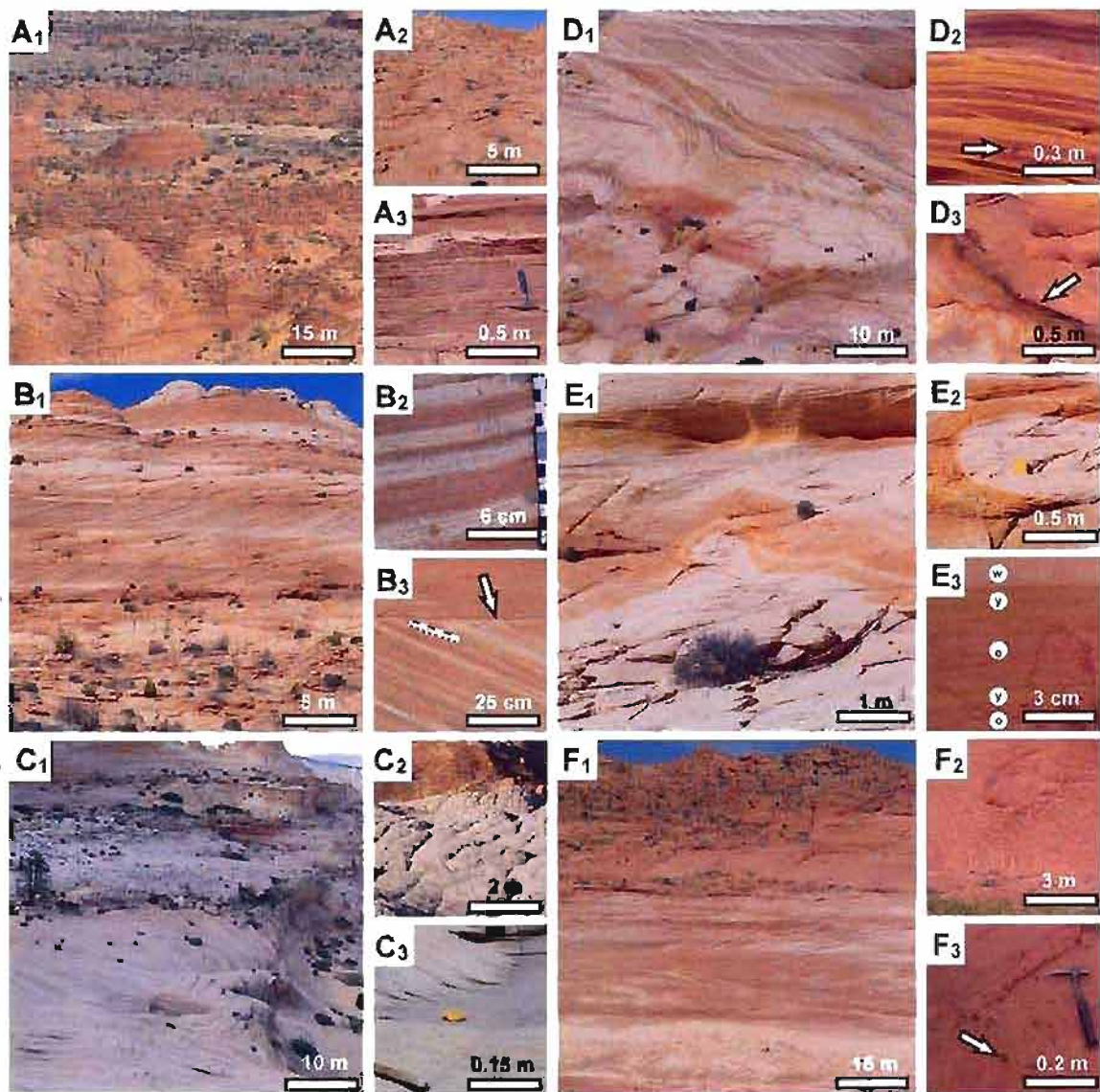


Figure 2.4. Diagenetic facies of Coyote Buttes. A) Basal red facies. B) Red and white banded facies. Regularly alternating red and white coloration in windripple plinth shown in B<sub>2</sub>. Red coloration is traceable along crossbedding to red grainflow strata. Pooling by buoyant reducing fluid occurs beneath upper bounding surface (arrow) in B<sub>3</sub>. C) Bleached facies. Polygonal weathering fractures visible in C<sub>2</sub>. D) Variable Liesegang facies. Late-stage HFO circles (arrow) overprint secondary coloration in D<sub>2</sub> and may be predecessors to well-formed HFO concretions. Arrow in D<sub>3</sub> points to dark, cohesive, HFO rich Liesegang band. E) Orange hematite and micro-concretion facies at various scales. Notation in E<sub>3</sub> corresponds to reflectance spectra in Figure 5E. F) Upper red facies. Possible fluid escape structure at top of F<sub>2</sub>. Well-cemented HFO concretions (arrow) in F<sub>3</sub>.

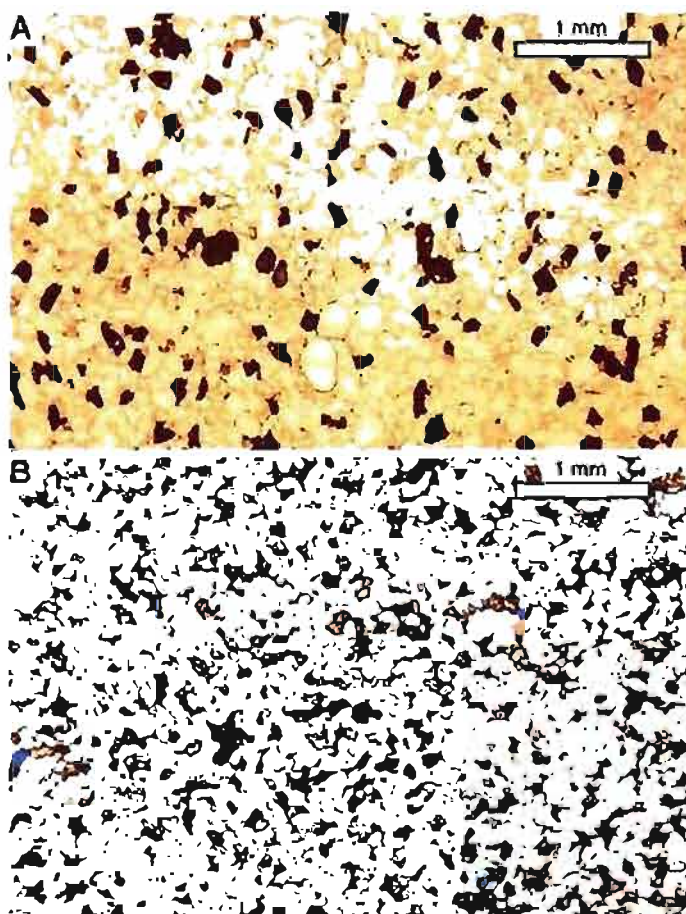
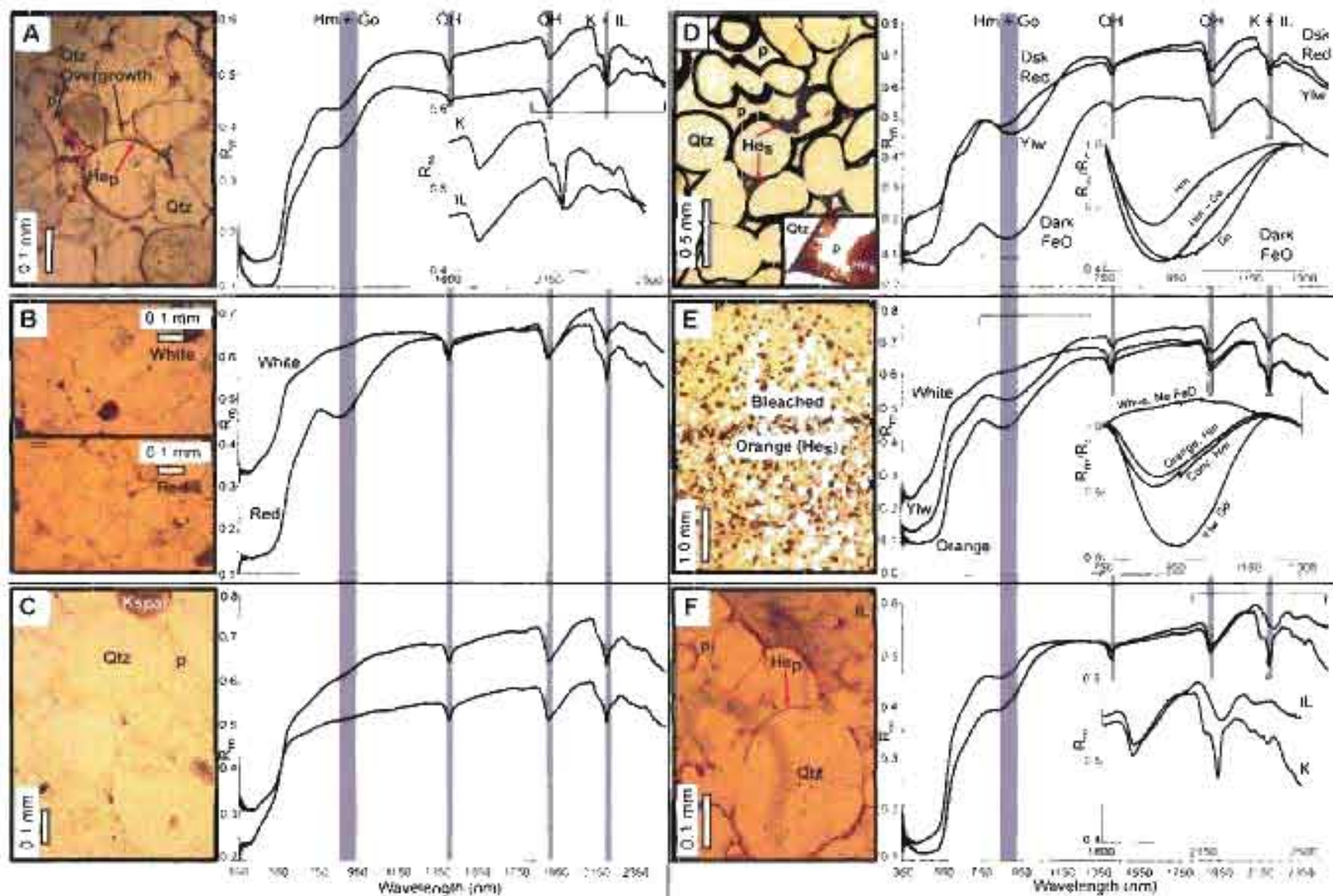


Figure 2.5. Increased potassium feldspar in Coyote Buttes thin sections. Thin sections are stained for potassium feldspar (brown grains). Navajo Sandstone is typically a quartz arenite with ~5% potassium feldspar, while Coyote Buttes samples can display up to 30% potassium feldspar. Estimation of potassium feldspar in thin section was performed visually by comparison to charts after Terry and Chilgar (1955). A) Potassium feldspar estimated at ~10%. B) Potassium feldspar estimated at ~25%; porosity shown with blue epoxy. Both photomicrographs from the basal red facies.

Figure 2.6. Representative petrography and reflectance spectra for Coyote Buttes diagenetic facies. Gray bands indicate positions of diagnostic absorption band minima. Brackets indicate wavelength intervals of inset spectra. He=hematite; He<sub>s</sub>=secondary hematite; He<sub>p</sub>=primary hematite; Go=goethite; Qtz=quartz; OH=hydroxyl/water; K=kaolinite; IL=illite; Kspar=potassium feldspar; p=pore space. All photomicrographs in plane-polarized light. A) Basal red facies display primary hematite grain coats beneath quartz overgrowths. Spectra reveals hematite accounts for red coloration. Facies possesses both kaolinite and illite clays (inset). B) Red and white banded facies possesses spectral and petrographic characteristics of both basal red and bleached facies. Quartz grains are outlined by primary hematite grain coats in red section but are less distinct in white portions where hematite is absent. Spectra display hematite band minima (~850 nm) in red samples, but no absorption is recorded over the same interval in white strata. C) Bleached facies lack HFO grain coats and band minima. D) Secondary hematite growth in the variable Liesegang facies is clearly visible. Reflectance spectra reveal hematite, goethite, and mixtures of the two in variably colored bands (Dsk Red=dusky red bands; Ylw=yellow bands). In dark HFO bands, clays are absent and fine scale spectral transects reveal varying mineralogy in continuum removed spectra ( $R_m/R_c$ ; inset). E) Orange hematite and micro-concretion facies possesses significant potassium feldspar (stained). An opaque band of hematite cement marks the boundary between bleached and orange zones. Continuum removed spectra (inset) show yellow banding is due to goethite while orange banding and concretions (conc.) are due to hematite. White bands lack HFO. F) Upper red facies shares characteristics of basal red facies including primary hematite grain coats and both illite and kaolinite clays (inset).







Basal red reflectance spectra display a decrease towards VIS (400-650 nm) at ~700 nm. Slope steepens at 600 nm and then the signal bottoms out between ~530 and ~430 nm with an erratic signal return around 350 nm (Figure 2.5A). A noticeable slope inflection and absorption trough occurs between 750 – 1100 nm indicative of HFO mineralogies. Band minima centered around 855 nm indicates nearly pure hematite. Water/hydroxyl band minima at both 1400 and 1900 nm indicate hematite and not limonite (Gupta, 2003; Bowen et al., 2007). Strong diagnostic clay absorption features indicate the presence of kaolinite and illite are equally abundant.

### Interpretation

The basal red facies preserves the primary red coloration that was originally pervasive throughout the Navajo Sandstone. The color derives from thin hematite grain coatings—developed from the early diagenetic breakdown of Fe-rich, detrital sand constituents (Chan et al., 2000; Beitler et al., 2003, 2005). Limited Liesegang bands, micro-concretions and secondary hematite growth indicate localized iron enrichment (see variable Liesegang facies description and interpretation). This enrichment occurred across the redox boundary formed between oxidizing ground waters (occupying this zone) and the overlying reducing fluids (occupying the bleached zone).

## Red and White Banded Facies

### Description

The red and white banded facies separates the basal red from the bleached facies (Figure 2.4B). Overall the unit is dark red to red (2.5YR 3/6 to 2.5 YR 4/7) with lesser

white to pink coloration (5YR 8/4) following crossbedding. Facies thickness can vary locally. The facies is thickest (~90 m) in the northern portion of Coyote Buttes, but generally is 10's m thick.

Within this interval, white coloration has two occurrences: (1) in grainflow strata beneath low permeability laminae including pinstripes, bounding surfaces, and windripple laminae (Figure 2.4B<sub>3</sub>); and (2) constrained to windripple strata. In some windripple strata, well-constrained red and white coloration regularly alternates in plinths and is traceable along crossbeds to red grainflow and white windripple laminae (Figure 2.4B<sub>2</sub>). Windripple strata commonly display a mottled color appearance at the mm-cm scale. Horizontal, cyclic, ~0.5 m thick, parallel red stains (2.5YR 4/5) occur in wet interdune deposits; these bands typically correspond to bedding planes that display excellent preservation of both vertical and horizontal burrows (*Planolites*, *Palaeophycus*, *Entradichmus*; after Ekdale et al., 2007), as well as scattered wood impressions. Finally, where overprinted by the variable Liesegang facies, red coloration can be deepened to a dark red (2.5YR 3/6 to 10R 4/6).

Petrographically, unaltered (not diagenetically overprinted) red and white intervals share the respective descriptions for the basal red and bleached facies (Figure 2.5B). Samples selected for thin section focus on red and white transitional areas that corresponded closely to grainflow-windripple lamina boundaries. Within these respective coarse and fine-grained intervals, grains were moderately to well-sorted. Coarse grains are rounded to well-rounded, while fine grains are subrounded to rounded. Primary porosity in grainflow deposits is generally ~25%, but is ~5-10% in windripple lamina and can approach 0% in individual pinstripe lamina. Pressure solution forms

primary cements, though in several examples, thorough quartz overgrowth cement inundate the sandstone and reduce porosity by ~75%. Feldspars comprise ~10% of the sandstone. Clays are generally 3% or less, but can be more concentrated in narrow, discrete bands where clays fill pore space. In red and white grainflow strata, red portions display anhedral, reddish-brown, flakey to specular HFO coats that uniformly coat a majority of the grains. Within these grainflow strata, a relatively abrupt transition leads to bleached areas where HFO occurs as flakey to specular HFO coats located only at grain contacts, where pore space is restricted. Windripple deposits generally overlie upper bounding surfaces. The bounding surface is marked by a definitive line of increased clay content and better developed quartz cement. Small-scale, but abrupt changes in HFO concentration exist across the bounding surface. Alternating, uniform, red and white coloration constrained to windripple strata show primary specular to flakey HFO grain coats in red intervals. However, HFO coats are rare and never appear on more than a small fraction of an individual grain in the white intervals. HFO grain coats are not located at grain contacts as in bleached grainflow samples.

Red bands display NIR reflectance minima indicative of predominantly hematite whereas bleached portions lack hematite/goethite troughs (see spectral descriptions for respective basal red and bleached facies; Figure 2.5B). The spectral transition between red and bleached areas is abrupt. Distinct changes in spectral character can be recorded at the mm-scale and correspond precisely with coloration trends viewed with the naked eye. The red and white banded facies is commonly overprinted with a yellow stain that will be addressed in the variable Liesegang facies section.

## Interpretation

Overall, the red and white banded facies represents the lowest extent of bleaching, where reducing fluids only partially saturated the sandstone. Advective flow along permeable laminae formed areas of limited bleaching. These areas display the upward migration and pooling of a buoyant reducing fluid (Figure 2.7). This bleaching fluid, in limited quantities within this transitional zone, remove most HFO grain coats, but leaves HFO at narrow pore throats at grain contacts—possibly by not displacing all water at the scale of individual pores. Thorough overprinting by variable Liesegang bands in this zone documents the boundary interaction of oxidizing and reducing fluids. White, low porosity/permeability wind ripple strata interspersed amongst high porosity/permeability grainflow strata is enigmatic and may be due to original fluid irreducibility in the windripple strata preventing primary hematite reddening. This is discussed in detail under “Faulting and Red and White Banding.”

## Bleached Facies

### Description

The bleached facies is white with minor, color variations (7.5YR 7.5/2 to 10YR 8/2; Figure 2.4C). Thickness varies between 10's – 100 m with the thickest occurrence at Top Rock. Within its main extent, white coloration has overwhelmingly replaced all red coloration, but at its margins with the red and white banded facies, bleaching can occur in m-scale, isolated patches. Regionally the bleached facies can be traced eastward from the East Kaibab monocline up to 10 km. Where the full upper section of Navajo Sandstone is observed along West Clark Bench, the bleached facies is at the top of the section and

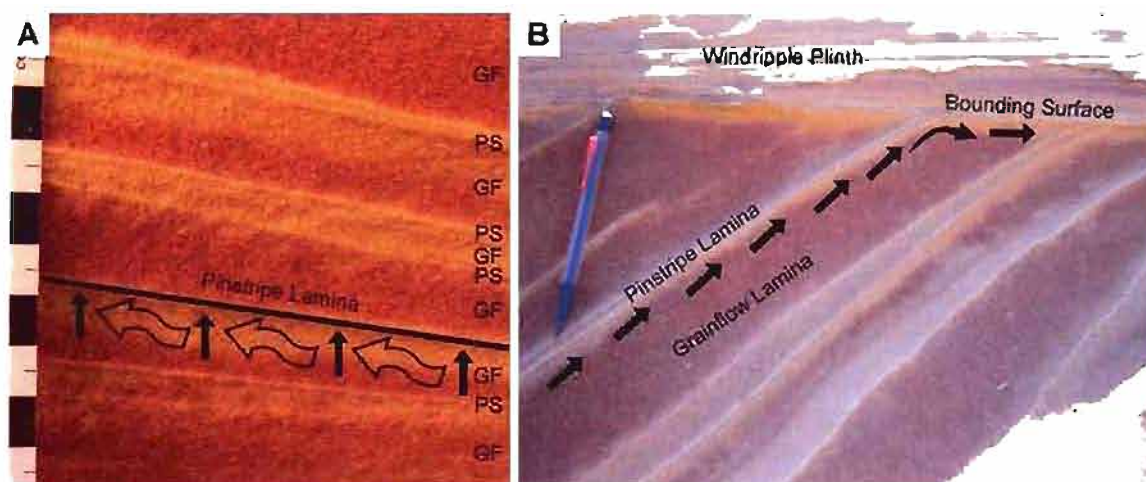


Figure 2.7. Upward migration and pooling of a buoyant, reducing fluid. A) Buoyant fluids pool beneath (solid arrows) pinstripe laminae (PS), but flow laterally up-dip (open arrows) along grainflow strata (GF). B) Reducing fluids move upwards within grainflow strata and pool along upper bounding surfaces, beneath overlying, low permeability, windripple plinths.

appears to thin eastward. Prominent buttes at White Pocket likewise display the bleached facies and imply that the facies was originally continuous (before erosion) and laterally extensive. Limited areas display HFO micro-concretions within entirely bleached intervals. Micro-concretions occur in the upper 10 m. The facies' westward extent roughly corresponds with the N-S trending joints associated with the Butte Fault.

Bleached facies samples are a texturally mature feldspathic arenite. Samples are moderately to well sorted, subrounded to well-rounded, with interparticle primary porosity to 30%. Feldspar ranges from 5-10%, with very limited clays (<3%). Cements are primarily quartz and pressure solution. HFO is largely absent; thin, uniform hematite grain coats exist only where preserved (trapped) in quartz overgrowths (Figure 2.5C). Overall, the facies shows little remnant hematite. Micro-concretions are not present in all bleached samples, but occur as opaque to dark brown, isolated anhedral pore-filling masses. Individual micro-concretions may be best formed in their centers, but generally appear uniform from edge to center and do not show signs of significant HFO removal from bleaching.

Bleached facies spectra display a steep drop towards VIS wavelengths at 600 nm without the plateau at ~530 nm observed in the red facies (Figure 2.5C). Generally, neither hematite nor goethite feature exist, however a slight inflection at ~750 nm may relate to trace HFO remnants. In no cases was a true HFO absorption trough observed. Both water/hydroxyl troughs are present. Clays are predominantly kaolinite with minor illite (10 vs. 2 samples).

## Interpretation

Iron mobilization due to advective fluid flow and pooling of a buoyant, hydrocarbon, reducing fluid (Beitler et al., 2003; 2005) accounts for the bleached facies. The pooled bleaching fluid reduces hematite grain coats to mobile  $\text{Fe}^{2+}$ . Preserved hematite grain coats protected beneath quartz overgrowths indicate red coloration predates bleaching. The limited occurrence of HFO micro-concretions within otherwise bleached intervals suggests that the unit experienced HFO enrichment followed by an episode of bleaching which may have been sufficient to remove Liesegang bands associated with the concretions, but not the concretions themselves. Likewise, the presence of isolated bleaching spots overprinting the banding associated with the variable Liesegang facies suggests a history of multiple, including late-stage, bleaching events of varying scale. Petroleum production from the Navajo and Nugget Sandstones in central and northern Utah and Wyoming indicates hydrocarbon availability in the reservoir.

### Variable Liesegang Facies

#### Description

The variable Liesegang facies forms a 10's m thick zone of multiple, cm-m scale, secondary, Fe-enriched Liesegang bands (Figure 2.4D). The facies is most pervasive in the lower bleached and red and white banded facies with some incursions into the basal red zone. Best outcrop display occurs on the northern and eastern portions of Top Rock. Coloration is variable (e.g., yellow 10YR 7/8; very dusky red 5R 2.5/3; and light red 10R 6/8 with further variations) with crosscutting indicating multiple Liesegang events. Liesegang bands can trace laterally > 30 m. Banding crosscuts all eolian laminae.

Liesegang bands display variable HFO abundance, from faint, sweeping coloration, to well-developed, well-cemented HFO concretions.

Bands occur in quartz and feldspathic arenites with high interparticle porosity (to 30%). Samples are moderately to well-sorted, subrounded to rounded. Feldspar abundance varies from <3% to 20%; clays abundance varies from 0-10%. Cements include pressure solution, quartz overgrowth, and polycrystalline quartz. HFO exhibits varied occurrence within the facies. Diffuse Liesegang bands display faint, specular grain coats of anhedral to subhedral platlets. Darker bands hold similar character, with platelets forming colloform grain coats. Other bands display opaque, subhedral to euhedral, pore-filling colloform masses. These isolated and irregular masses show possible self-organized spacing, and may represent HFO proto-concretions. Best-developed, dark, HFO-rich bands display relatively thick, deep red to opaque, secondary HFO mineral growth on all grains and an overall increased HFO abundance. HFO grain coats occur as euhedral, fibrous needles radiating into void pore space (Figure 2.5D), and as colloform assemblages of euhedral, rosette hematite platelets.

The variable Liesegang facies displays NIR reflectance spectra of both hematite and goethite (Figure 2.5D). Clay abundance is highly variable. Dark, deeply colored HFO bands (reddish black 5R 2.5/1) display the strongest HFO absorption feature of all facies. Gross spectral readings are dominated by hematite band minima. However, fine scale spectral transects indicate a significant goethite component. Within these dark Liesegang bands, yellow portions display band minima of primarily goethite; band minima where colors approach black (5R 2.5/1) indicate a roughly equal mixture of hematite and goethite. These Liesegang bands can contain either kaolinite, illite, or lack



clay entirely. Dusky red to diffuse Liesegang banding is predominantly hematite with uniform spectral signatures observed across multiple fine scale bands. A slight hematite signature in the bleached portion of samples matches that where HFO banding is well developed. Kaolinite is observed, illite is absent. The yellow coloration commonly overprinting the red and white banded facies has the net effect of deepening the red color (from 2.5 YR 4.5/8 to 10R 4/6) and is primarily due to a hematite/goethite mixture (865-877 nm band minima).

### Interpretation

Liesegang-type reaction fronts record the chemical precipitation of hematite and goethite across reduction-oxidation boundaries (Ortoleva, 1984; Dee, 1986; Ortoleva et al., 1987a, b; Barge et al., 2008). The variable Liesegang facies documents iron diffusion across a fluid interface between a reducing, buoyant fluid enriched in  $\text{Fe}^{2+}$  overlying an iron-depleted, oxygen-rich, oxidizing fluid, likely groundwater (von Gunten and Schneider, 1991; Bowen et al., 2007; Barge et al., 2008). Cross cutting relationships indicate that the variable Liesegang facies formed after the main bleaching event, and encompassed multiple band-forming episodes (Figure 2.4D). The occurrence of these events at multiple stratigraphic levels and in variable diffusion directions may be due to a shifting groundwater/hydrocarbon interface through time, and/or the repeated infusion of fresh reactant fluids.

## Orange Hematite and Micro-concretion Facies

### Description

Multiple, large-scale (1-5 m) orange Liesegang bands with associated micro-concretions overprint the upper ~25 m of the bleached facies (Figure 2.4E). Overall, the orange hematite and micro-concretion facies is 10's m thick. The Liesegang bands display a reaction front that transitions cyclically (into the reaction direction) from bleached, to yellow, to orange (pinkish white to very pale brown 7.5 YR 8/3 to 10YR 7.5/3; yellow 10YR 7/6; yellowish red 5YR 5.5/8 respectively) with micro-concretions (<2 mm; yellowish red 5YR 4.5/6) located in the orange portion of the front. Reaction fronts cross eolian lamination without deflection and display a lobe and cusp appearance. The facies occurs primarily on Top Rock, with best exposure towards Top Rock's southern flank.

Orange Liesegang bands and micro-concretions occur in well to very well-sorted, subrounded to rounded, feldspathic arenites. Interparticle porosity is between 20-30%; cements are primarily due to pressure solution, and to quartz and clays to a minor degree. Samples appear to have ~20% feldspar. Clays are more abundant than in other facies, generally 5-10%. Within bleached portions, HFO is not present. The transition into Liesegang bands is abrupt and marked by narrow, dark brown to opaque, anhedral to euhedral HFO grain coats that fill porosity in thin (1-5 sand grains thick), subparallel bands (Figure 2.5E). Euhedral platelets form colloform aggregates. These bands do not correspond with bedding. Colored areas between narrow, pore-filling bands show thin and irregular, less abundant, reddish brown HFO grain coats. Irregular colloform aggregates commonly grow from grain coats into pores. Micro-concretions appear as

masses of porosity-filling, colloform growths of subhedral to euhedral HFO crystals and are generally opaque at center, but reddish brown translucent at edges. Clays are colored brown in the orange portion of the reaction front.

Reflectance spectra display a drop towards VIS at ~750 nm, steepening at 600 nm, without a plateau ~530 nm. Yellow and orange portions of reaction fronts display goethite and hematite spectral patterns respectively. White portions of the reaction front lack HFO and match characteristics of the bleached facies (Figure 2.5E). Water/hydroxyl features are observed at both 1400 and 1900 nm. Kaolinite occurs in all samples; illite appears absent. At the mm-scale, yellow banding within the reaction front is indicative of exclusively goethite (band minima between 900-924 nm). Likewise, mm-scale transects of orange bands reveal exclusively hematite (band minima between 850-866 nm). Transitions from white to yellow to orange appear abrupt and do not suggest mixing across hematite/goethite/HFO depleted zones. Micro-concretions display hematite absorption features.

### Interpretation

Iron diffusion across the upper boundary between a reducing and oxidizing fluid is represented by the orange hematite and micro-concretion facies. Reaction fronts may mark the upper interface between the  $\text{Fe}^{2+}$  enriched bleaching fluid and meteoric water, perched groundwater, a rising groundwater table (accompanied by hydrocarbon displacement), or a fluid/air interface. A static interface with meteoric water would require sandstone lamination to slow downward percolating meteoric water sufficiently so that advection does not overwhelm diffusive mass transport at the redox boundary.

Perched groundwater atop the hydrocarbon boundary would require stratigraphic traps that are not observed at outcrop and may be an unlikely explanation (Schneider, 2008). However, a falling fluid column may allow diffusion across a boundary between the hydrocarbon body and atmospherically derived oxygen (Potter, 2008). Likewise, should the trap overlying the Navajo Sandstone be breached, it is possible that escaping hydrocarbons be replaced by oxidizing fluids. The final interactions of the rising water column with the last remnants of the reducing fluids may be recorded in the orange Liesegang zone.

### Upper Red Facies

#### Description

The upper red facies is located stratigraphically above and to the west of the bleached facies (Figure 2.4F). It is generally uniformly colored light reddish brown to red (2.5YR 5.5/4 to 2.5YR 4.5/6) with 1-2 cm diameter HFO micro-concretions present locally. However, areas of large (1-3 cm diameter) HFO concretions, as well as carbonate concretions (~1 cm diameter) exist to the west of N-S trending cataclastic deformation bands. Large HFO and carbonate concretions occur only in this upper red facies and appear limited to the west of the deformation bands. The basal and upper red facies are mapped as separate units due to spatial (vertical) separation in the main extent of the Coyote Buttes, however, to the west of the field area, basal and upper red facies appear as a continuous, indistinguishable unit.

Upper red samples are moderately to well-sorted, subrounded to well-rounded, feldspathic arenites with interparticle porosity to 30% in grainflow units. Secondary

porosity in some pinstripe lamina approaches 0% due to quartz overgrowth. Cementation is due to pressure solution and quartz overgrowth. HFO grain coats are evenly dispersed as anhedral, uneven, flakey to specular crusts. Limited pore-filling HFO growth may indicate secondary hematite. Primary hematite coats are preserved within quartz overgrowth (Figure 2.5F). Clays and accessory minerals are minor constituents (<3%). Overall the unit appears the same as the basal red facies.

The upper red facies possesses the same reflectance spectral characteristics as the basal red facies (Figure 2.5F). HFO mineralogy appears to be exclusively hematite. Both kaolinite and illite exist in an equal number of samples.

### Interpretation

Similarities between the basal and upper red facies suggest primary red coloration extended vertically throughout the section prior to bleaching. Based on this primary diagenetic classification, basal and upper red facies may be synonymous. However, larger HFO concretions (> 2 mm and up to 7 cm diameter) to the west of the deformation bands indicate differing late-stage Fe enrichment styles on opposing sides of the Laramide structures. Likewise, limited (~1 cm diameter) carbonate concretions occur only to the west of the deformation bands. These differing, late-stage diagenetic patterns suggest reservoir compartmentalization by the Laramide deformation bands.

### Distribution of Diagenetic Facies

Diagenetic facies display distinct aerial distribution (Figures 2.2 and 2.8). The basal red facies forms the lower red coloration of the Navajo Sandstone on a regional

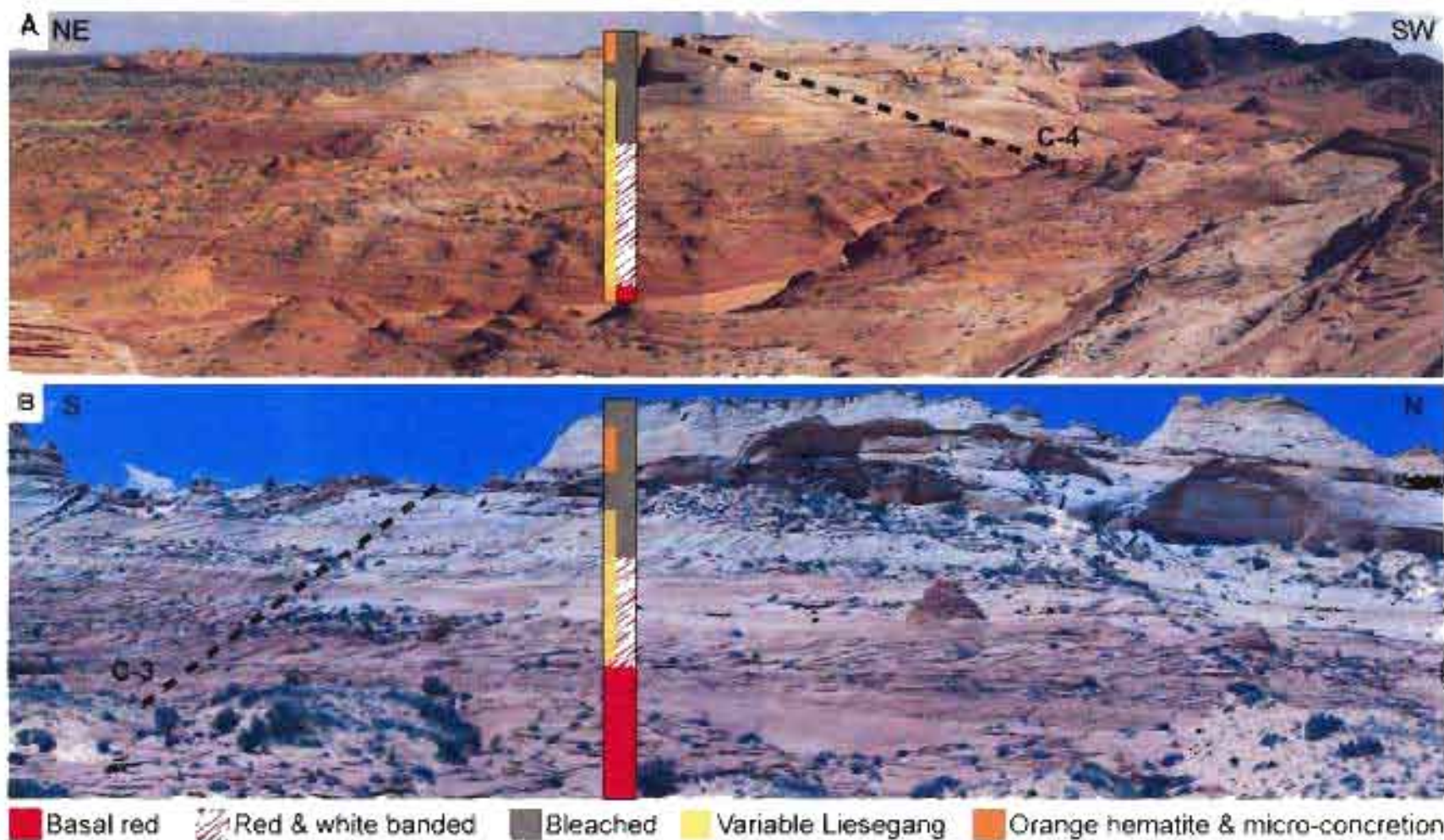


Figure 2.8: Panoramics of Coyote Buttes (Top Rock). Generic stratigraphic columns show diagenetic facies. A) Top Rock viewed to the SE. Measured section C-4=dashed line. B) Top Rock viewed to the W. Measured section C-3 (0-60m)=dashed line.

scale (throughout the Coyote Buttes and Paria Plateau, corresponding to overall trends on the Colorado Plateau [Beitler et al., 2005]). The transition between basal red and upper red facies on the western margin of the Coyote Buttes is indistinguishable; it appears that red, primary coloration exists throughout the western Navajo section (Figures 2.2 and 2.8).

The bleached facies is concentrated around the Top Rock topographic high. Towards the north and the south, thoroughly bleached sandstone tapers into the red and white banded facies within 1-2 km from Top Rock (Figure 2.2). Viewed at a large scale, the western boundary of bleaching is sharp and corresponds approximately with the zone of deformation bands and N-S joints. Stratigraphy to the east of Top Rock has been removed, but large-scale color trends on the Paria Plateau show that bleaching extends eastward  $\geq 10$  km.

Liesegang banding occurs in all facies, but is most easily viewed where it overprints bleached rock. The variable Liesegang facies appears in the lower portion of the bleached zone, and extends downward into the red and white banded facies and basal red facies. Diffuse coloration makes viewing fine-scale banding difficult from a distance, however large Liesegang-type reaction fronts are visible on West Clark Bench (Figure 2.1B), suggesting that this facies may be regionally extensive. The orange Liesegang and micro-concretion facies is limited to the upper extent of the bleached facies and is concentrated only on Top Rock. In comparison to studies by Beitler et al. (2005) and Bowen et al. (2007) Navajo Sandstone at Coyote Buttes has overall increased potassium feldspar (Figure 2.6), no carbonate (with the exception of carbonate concretions in the upper red facies), and lacks illite rims around quartz grains. These characteristics may

influence the chemical reactions responsible for diagenetic patterns, may explain the intensity of coloration at the Coyote Buttes, and warrant further study.

### Localized Diagenetic Patterns

#### Mottled Coloration and Burrowing

Mottled coloration patterns occur throughout Coyote Buttes colored intervals, particularly in windripple laminae and plinths (Figure 2.9). This mottled pattern corresponds with areas of burrowing, even in cases where burrow traces are no longer preserved. Invertebrate trace fossils including *Planolites*, *Palaeophycus*, *Skolithos*, *Arenicolites*, *Entradichnus*, *Taenidium*, and *Digitichnus* display shallow burrowing by Jurassic beetles and arachnids (Ekdale et al., 2007). Though traces are most prevalent in grainflow, they are best preserved in windripple laminae (Loope and Rowe, 2003). Organic matter concentrated by the burrowing organisms (fecal matter, burrow lining secretion, remnant food, etc.) may facilitate the small-scale bleaching of these mottled intervals. Conversely, the interruption of lower permeability windripple laminae by burrows facilitates the introduction of reducing fluids along burrow traces. Mottling is traceable laterally from areas where it corresponds to burrowing patterns, to areas where burrow preservation gradually decreases but mottled color remains (Figure 2.9).

#### Coloration of Interdune Areas

Horizontal red stains (2.5 YR 4/5) occurring only in wet interdune intervals may indicate areas of syndimentary, paleowater table derived iron staining (Figure 2.10). Cyclic iron staining corresponds to bedding surfaces of exceptional trace fossil



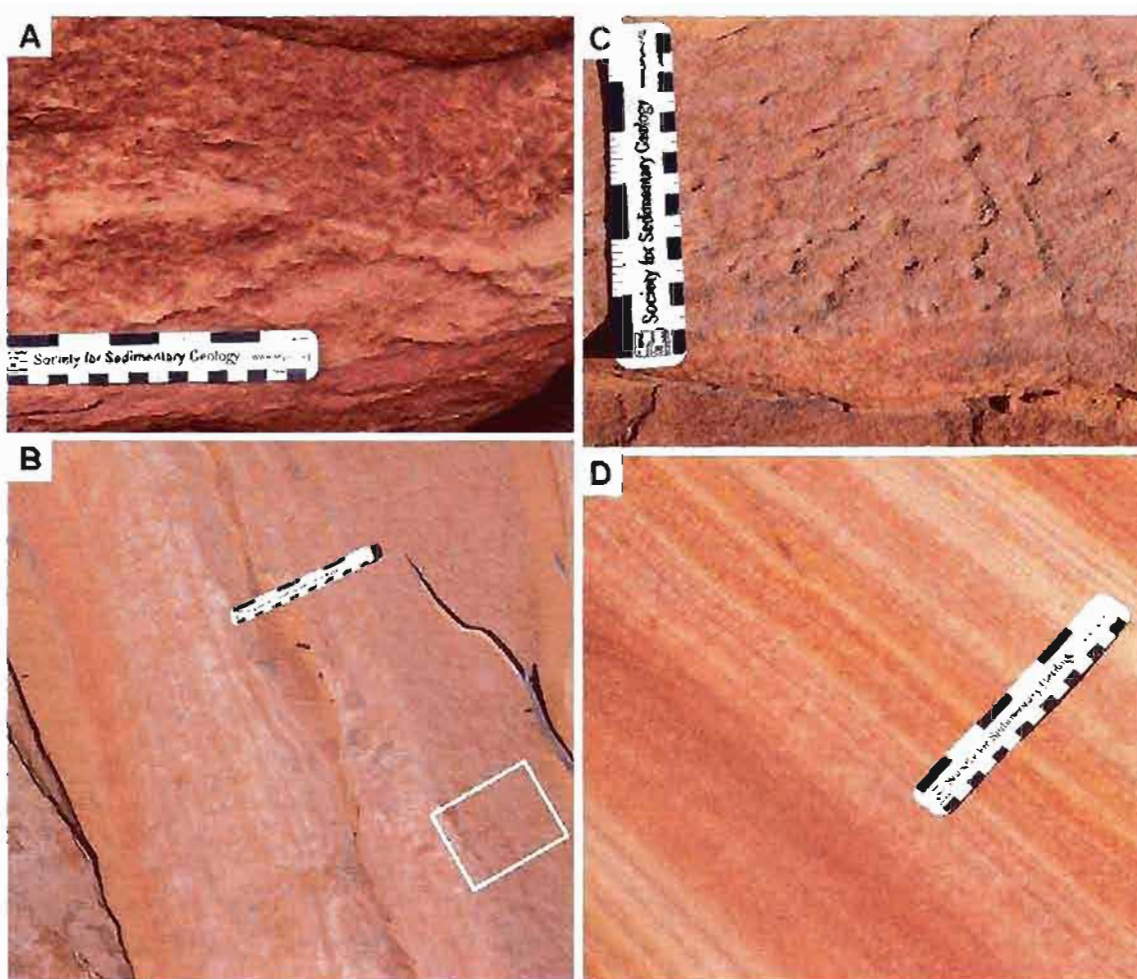


Figure 2.9. Mottled coloration indicative of invertebrate burrowing. A) Mottled coloration corresponding to well preserved burrows (*Planolites* isp.?). B) Mottled coloration in windripple strata where burrows are less obvious, but still present. Box indicates location of Figure 8C. C) Vertical burrows (*Skolithos* isp.?) along top surface of well cemented windripple laminae. Burrows are easily viewed in map view of windripple laminae, but do not disrupt lamina in cross-section view. D) Mottled coloration in windripple strata where burrowing is not visible in cross-section.

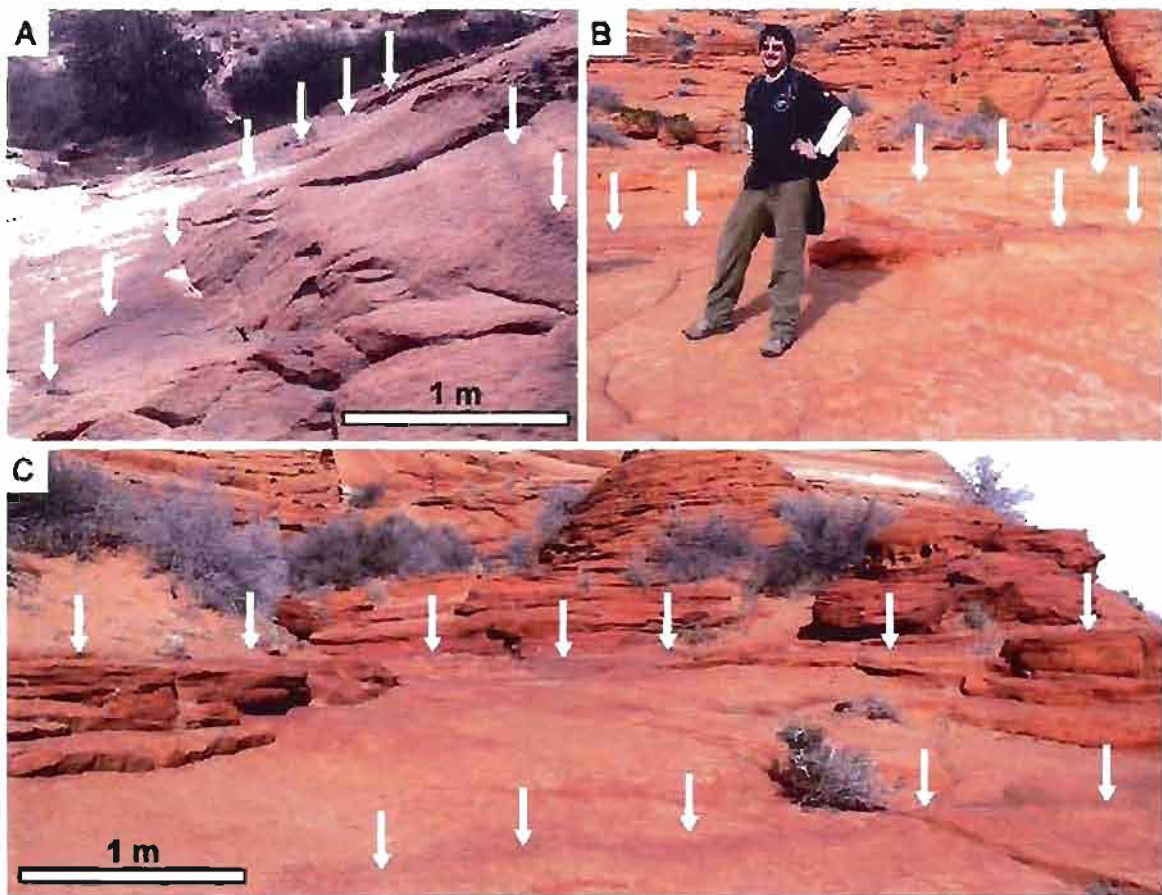


Figure 2.10. Horizontal red staining in wet interdune intervals. Stained bands are marked by white arrows and correspond to bedding planes with well-preserved burrows in map view.

preservation; increased preservation along these bedding surfaces is likely due to wet sand deposition. The occurrence of iron staining on these bedding planes suggests a syngenetic origin, perhaps indicating original water table levels. The preservation of multiple bands is interpreted as the expression of changing paleowater table levels.

## Structural Influences

### Deformation Bands

A generally N-S trending, ~150 m wide zone of well developed cataclastic deformation bands appear along the entire western margin of the Coyote Buttes (Figures 2.11 and 2.12). Orientation of major bands shift from ~122° in the south to ~173° in the north. Dip varies from ~30°W to near vertical. Minor bands intersect major sets at ~30°. Minor bands average 1-2 mm thick; better-developed bands average 3-10 mm thick (averaging ~5 mm); some bands can be up to 20 cm thick and appear as an amalgamation of smaller deformation bands. Well-formed bands extend >150 m. Deformation bands appear best developed in grainflow strata and upwards in the section. Where crossing diagenetic facies, deformation bands change color corresponding to facies coloration. Band offset is minor, in few cases up to 1 cm.

### Joints and Faults

Two major fracture sets occur at the Coyote Buttes. One is closely spaced, N/S trending, and focused along the area's western ridge. The second is ~NE-SW trending (average ~60°), widely spaced (50 m to > 180 m), and distributed regionally.



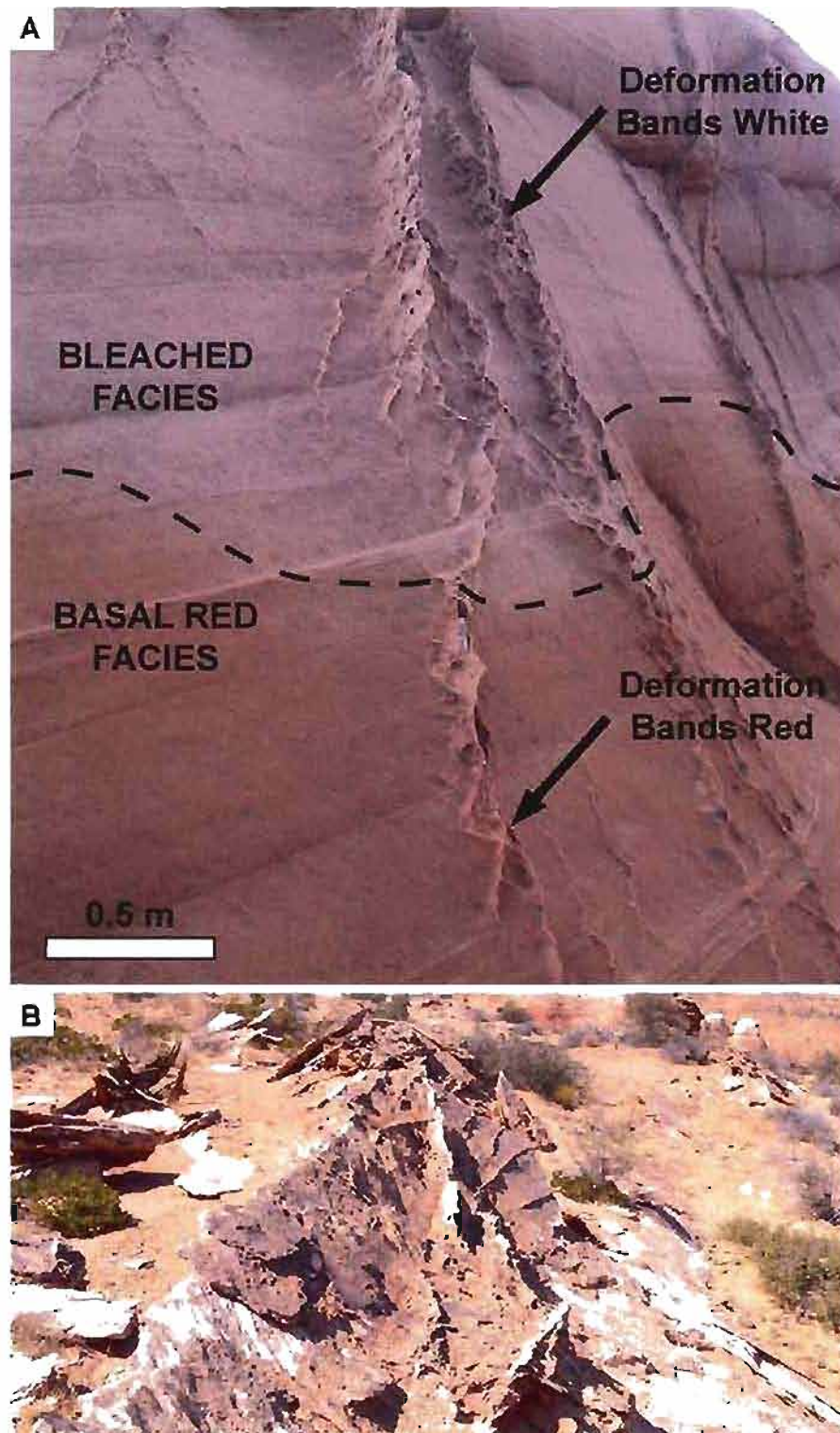
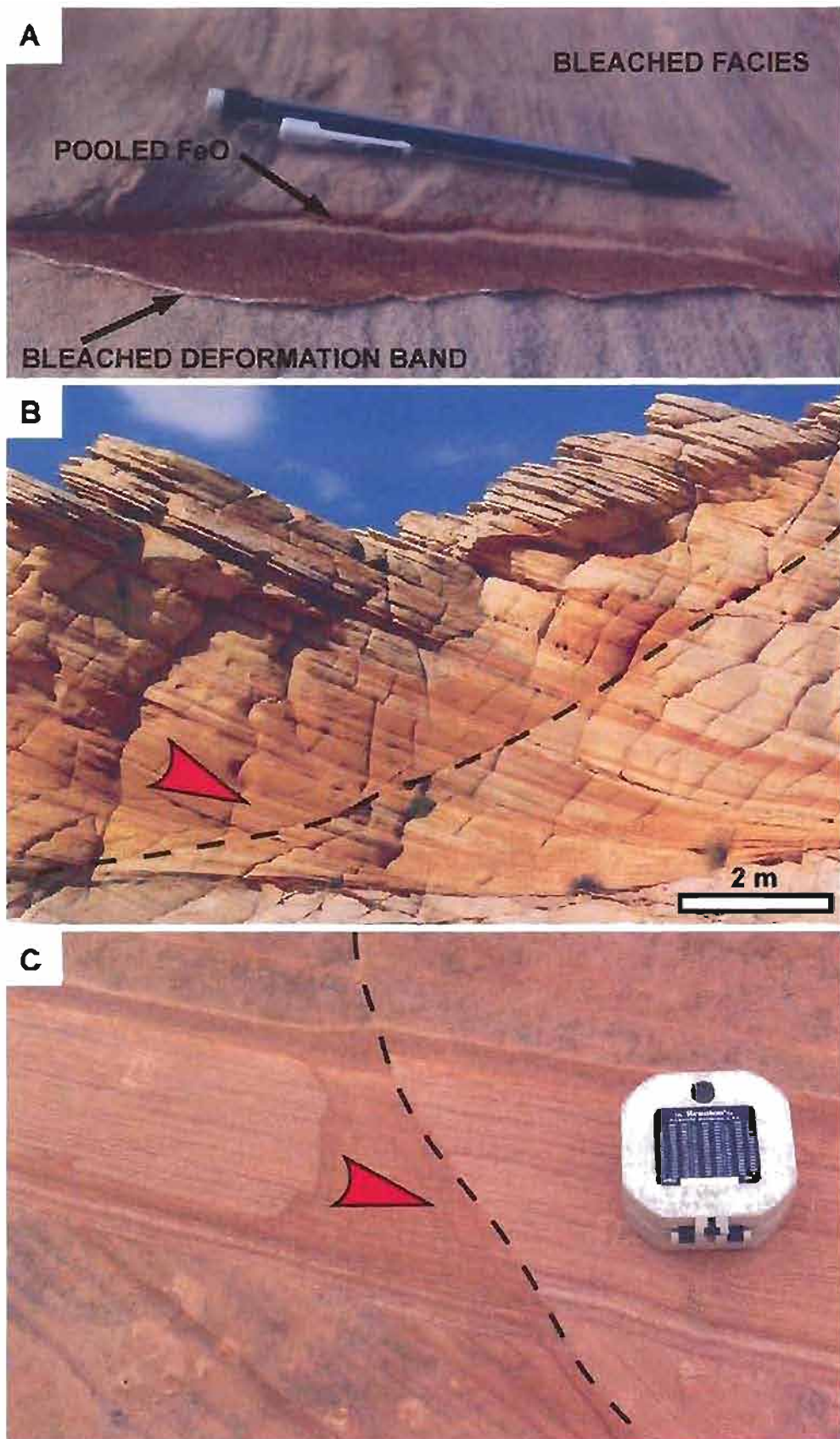


Figure 2.11. Cataclastic deformation bands. A) Color of Laramide-aged deformation bands corresponds to the diagenetic facies they cross. B) Following a dilatant phase, cataclastic deformation bands are impermeable to flow and compartmentalize the reservoir.

Figure 2.12. HFO staining against cataclastic deformation bands. In each case, paleoflow is from the west. A) Pooling of an HFO precipitating fluid against a bleached deformation band. White color of deformation band indicates the incorporation of bleached facies coloration during formation and subsequent impermeability to later fluids. B) Sandstone compartmentalization and HFO staining against well-formed deformation band (dashed line). Arrow indicates paleoflow direction. C) Pooling of HFO precipitating fluid against deformation band (dashed line) with minor offset (lower right). Deep staining indicates advective fluid flow preferentially along coarser-grained lamina. Arrow indicates paleoflow direction.



North-South trending fractures dissect the Coyote Buttes western ridgeline, are near vertical and subparallel to the overall trend of deformation bands (Figure 2.2). The fractured zone is ~400 m wide, E-W. Where most intense, fracture spacing averages between 1-5 m. Fracture orientation varies from  $335^{\circ}$ - $345^{\circ}$  in the south to  $\sim 360^{\circ}$  in the north. In most regards, the fractures appear without offset. In the few cases where present, slickenlines indicate a high-angle reverse, right lateral sense of movement. Offset is on the cm to m-scale. It is difficult to conclusively trace eolian bounding surfaces across the most intensely fractured zone, however the lack of gouge and breccia intervals suggests minimal displacement. The fractures are likely high-angle reverse faults similar to those described by Roznovsky and Aydin (2001) at Waterpocket Fold. The fractures trend primarily through the red diagenetic facies. Limited, m-scale pockets of bleaching exist within, and to the west of the fractured zone. Cross cutting relationships show fractures occur after deformation bands, overprinting deformation bands as the fault tip propagates up-section.

NE-SW fractures are widely spaced (up to 200 m, average ~75 m), near vertical, and laterally extensive (in cases >2 km) and are interpreted to be joints. Major joints cut the entire section, though minor examples can taper vertically. Unlike modern joints, NE-SW joints do not follow topography. Joints show no influence on coloration.

### Synsedimentary Faulting

Small normal faults exist at numerous localities and occur entirely within beds, indicating their synsedimentary nature. Of these, three instances were identified where normal faults offset eolian sets, abruptly truncate at upper bounding surfaces, and offset

red grainflow and white windripple laminae (Figure 2.13). White laminae terminate abruptly at the fault surface; white coloration does not bleed across the fault trace. Fault offset is on the cm-m scale. Likewise, secondary bleaching pooled beneath pinstripes is offset by these faults. Liesegang bands cross faults without offset; Fe-rich concretion-type deposits line one fault and indicate paleofluid flow to the east. Intra-stratal iron staining preferentially follows coarser grained, higher permeability laminae and cross the fault traces without precise offset. Fault truncation against upper bounding surfaces provides enigmatic timing constraints on the offset coloration which will be considered in the Discussion section.

## Discussion

### Deformation Bands and the Butte Fault

The Butte Fault beneath the East Kaibab monocline is implicated as a pathway for upward flow of reduced fluid (Bowen et al., 2007). Tindall and Davis (1999) argue that the reverse, Laramide-aged (Late Cretaceous/Early Tertiary; ~80-50 Ma.) Butte Fault is a reactivation of a Precambrian-aged basement normal fault. During Laramide fault growth, cataclastic deformation bands lead fault tip propagation ahead of the slip plane (Antonellini and Aydin, 1994; Roznovsky and Aydin, 2001). During growth, deformation bands experience a dilatent phase and act as conduits for fluid flow, but once well-developed, form flow barriers (Sigda et al., 1999; Sigda and Wilson, 2003; Parry et al., 2004). At the Coyote Buttes, diagenetic coloration patterns are incorporated into deformation bands, indicating that the sandstone was colored (bleached and Liesegang facies) before deformation band propagation (Figure 2.11).



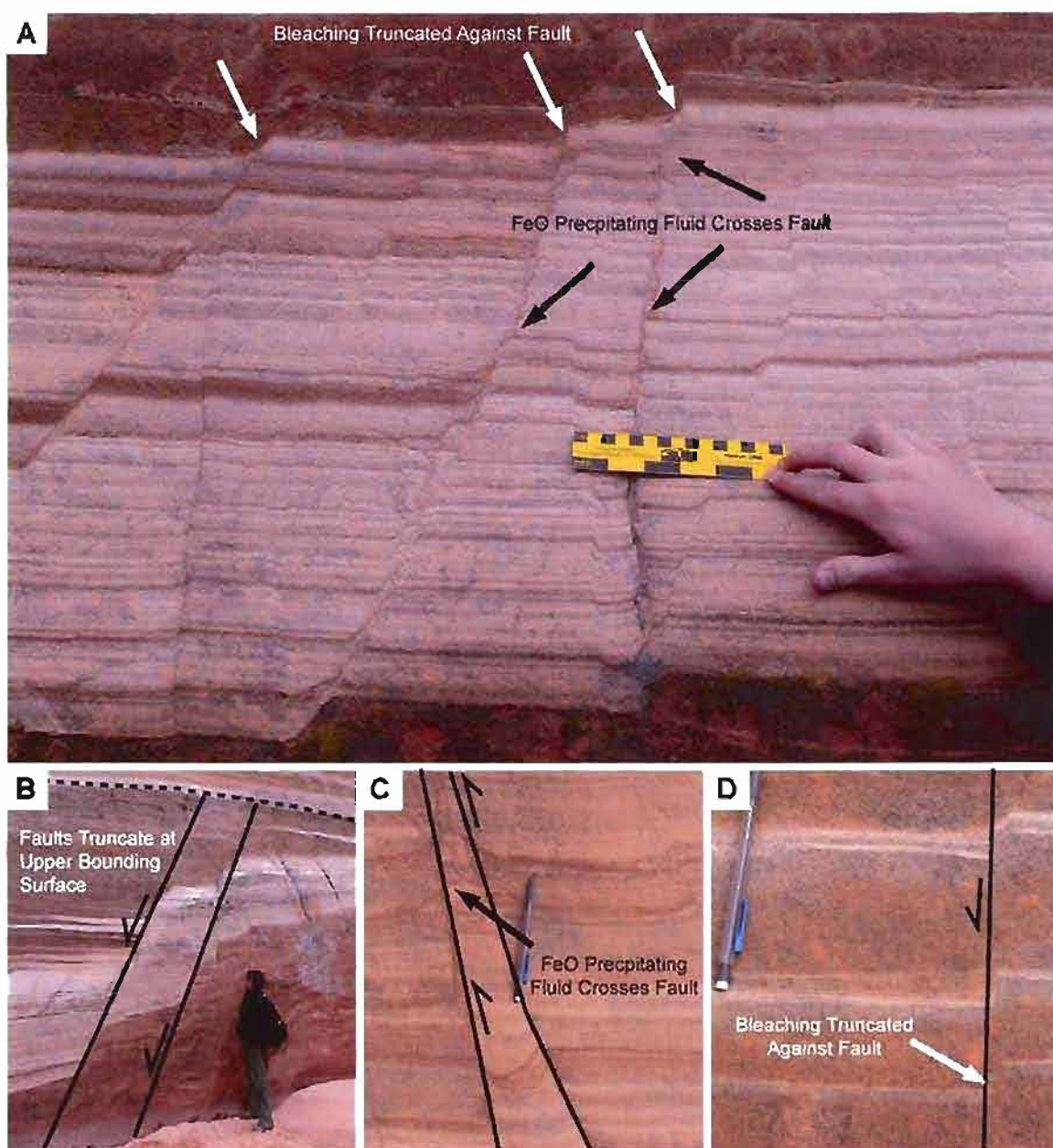


Figure 2.13. Coloration associated with synsedimentary faulting in Sand Cove.

A) Well-developed package of bleached windripple lamina offset by syndepositional normal faults. White laminae are offset by the fault without bleaching crossing the fault trace. B) Faults truncate at upper bounding surface (dashed line), suggesting a synsedimentary origin. C) Fluid that precipitates FeO staining crosses fault traces advectively (indicating a permeable fault trace) and without the precise offset observed in bleached intervals. D) Wave-type bleaching pools beneath offset pinstripe lamina.

The incorporation of diagenetic coloration into deformation bands suggests two timing scenarios: 1) fluid migration predates Laramide-aged reverse faulting; or 2) coloration (bleaching and variable Liesegang banding) occurs concurrently with Laramide faulting and is captured by incremental deformation band propagation at the fault tip. This second scenario agrees with the findings of Beitler et al. (2003) that fluid migration follows Laramide highs associated with basement fault-derived monoclines. In this context, bleaching and variable Liesegang events are constrained to a narrow timeframe—coloration occurs after the initiation of Laramide structures (fluids collect in Laramide-derived traps), but ends before the termination of fault growth. In any case, major diagenetic events occurred in a Navajo reservoir that, at the time, was not compartmentalized by deformation bands. The distribution of bleaching indicates an eastward paleoflow.

Pooling of a minor, late-phase iron oxidizing fluid occurs against the western edge of fully developed deformation bands (Figure 2.12). This implies that once formed, deformation bands acted as flow barriers. Postdeformation fluids appear to flow under hydraulic head from the west. Fluid collection against deformation bands indicates post-Laramide reservoir compartmentalization.

### Timing of Coloration Events

Diagenetic, stratigraphic, and structural variables allow for the relative timing of major events at the Coyote Buttes:

1. Early Jurassic eolian deposition of Navajo Sandstone.
2. Synsedimentary faulting of dune sets.

3. Syndepositional to early diagenetic reddening of sandstone via hematite grain coats (e.g., basal and upper red facies).
4. Initiation of Laramide-age faulting along the reactivated Butte Fault and development of the East Kaibab monocline.
5. Buoyant, chemically reducing fluid introduced to reservoir along fault. Advective  $\text{Fe}^{2+}$  mobilization and bleaching occurs (possibly as multiple events).  
Development of bleached facies.
6. Diffusive overprinting by variable Liesegang facies.
7. Laramide-aged development of cataclastic deformation bands associated with the East Kaibab monocline.
8. Pooling of late-stage HFO against deformation bands indicates post-Laramide, limited iron mobilization and hydraulic head from the west. Differing diagenetic regimes develop on opposing sides of deformation bands (e.g., large HFO concretions and  $\text{CaCO}_3$  concretions on west side).
9. Postdeformation band faulting associated with the East Kaibab monocline.
10. Unconstrained timing of diffusive overprinting by orange hematite and micro-concretion facies, and isolated, late-stage bleaching (crosscutting relationships with tectonic structures do not exist; an upper-end constraint of timing is not available).

### Synsedimentary Faulting and Red and White Banding

Nonreddened, low angle windripple deposits within hematite colored dune foresets were noted by Lindquist (1988) in Nugget Sandstone core from the Anschutz

Ranch East Field, UT/WY. Similar color patterns (white windripple and red grainflow laminae) occur in the red and white banded facies at Coyote Buttes and offer intriguing questions regarding diagenetic evolution when viewed in association with synsedimentary faulting.

Synsedimentary faulting was likely due to dune collapse or slumping. Fault traces terminate at upper eolian bounding surfaces, indicating that faulting occurred before burial—the upper fault trace planed-off by erosion to the upper bounding surface (Figure 2.13B). Offset of red grainflow and white windripple strata implies one of four possibilities: (1) red and white coloration predates faulting, and exists at the time of deposition; (2) later reducing fluids preferentially bleached windripple strata; (3) the entire deposit was bleached—secondary hematite grain coatings are then added to only grainflow cross strata; (4) Faulting is not synsedimentary and terminates at upper bounding surfaces based on layer isotropy.

Cross-cutting relationships suggest windripple and grainflow strata were colored white and red prior to faulting. Such early coloration, before deposition of the next dune, implies that each eolian set underwent unique coloration episodes (color added before the next successive dune was deposited). In any case, very early coloration is implied. This could be accomplished by a differential sand source for the individual strata (white vs. red) without later reddening, or by irreducible connate water in windripple strata preventing the introduction of primary hematite reddening fluids.

The second explanation holds that white windripple laminae were bleached after faulting. However, precise and preferential bleaching of only lower permeability windripple strata is problematic. Advective reducing fluids should favor movement

along higher permeability grainflow strata. In addition, some bleeding from the bleached windripple laminae into adjacent grainflow strata should occur especially where the two members are offset across the fault trace (late stage iron coloration indicates a permeable fault trace; Figure 2.13A and C).

To preserve bleached windripple strata that appear to be colored syndepositionally, it may require the entire unit to be bleached. Red may then be reintroduced preferentially to coarse-grained grainflow deposits. This explanation requires bleaching and recoloration to have occurred over larger portions of the Navajo. Evidence for such diagenetic events are neither supported by large-scale outcrop coloration patterns nor micro-scale petrographic observations.

Finally, it is possible that the faults are not syndimentary, but occurred under burial conditions. In this case, faults would have behaved much like deformation bands that are best defined in coarse-grained grainflow units, but terminate at fine-grained windripple plinths (Fossen et al., 2007). Abrupt termination of faults with offset  $>0.5\text{m}$  make this explanation unlikely.

Field observations suggest coloration patterns predate faulting (Figure 2.13). Isolated bleaching beneath pinstripes appears offset by the faults, however this may be an apparent effect more closely related to the time required for reducing fluids to bleach the rock (bleaching may only occur where fluids pool beneath low permeability lamina for a given time—if the lamina are offset, then the location of bleaching will be offset as well; Figure 2.13D). Red and white banding of windripple lamina is offset perfectly and without bleeding across the fault surface (Figure 2.13A and B), whereas postfault red staining indicates that fluids are able to freely migrate across the syndimentary faults

(Figure 2.13A and C). The lack of bleeding of bleaching fluids across the fault from windripple strata argues that coloration occurred before offset. Irreducible connate waters may be a plausible explanation (connate waters may prevent the introduction of primary red). This explanation would hold that white windripple lamina never received primary HFO graincoats. Synsedimentary, active bleaching of windripple laminae contradicts regional diagenetic patterns that establish a convincing diagenetic framework under burial conditions and certainly long after lithification (Chan et al., 2000; Beitler, et al., 2003, 2005; Bowen et al., 2007). In any case, bounding surface terminating faults that offset coloration are enigmatic and warrant further investigation.

### Geomorphic and Diagenetic Evolution of The Wave

The unique combination of stratigraphy, coloration, and exposure at “The Wave” provides insight into the sedimentary, geomorphic and diagenetic evolution of many of the unique features at the Coyote Buttes (Figure 2.14). Diagenetically, the Wave is located at the overlap of the variable Liesegang facies atop the red and white banded facies. No fewer than four diagenetic events are recorded after initial sandstone reddening. Cross cutting relationships between nearby synsedimentary faults and similarly colored grainflow and windripple strata (discussed earlier) suggest that grainflow strata were originally red (2.5YR 4/8) and windripple strata originally pinkish white (7.5YR 8/2; Figure 2.14F). Once the sandstone was saturated by groundwater, a small volume of buoyant, reducing fluid was introduced. This fluid bleached the rock (to 10YR 7.5/3) and pooled in grainflow strata under three conditions: (1) beneath fine-grained and well-cemented grainflow delineating pinstripes; (2) beneath fine-grained



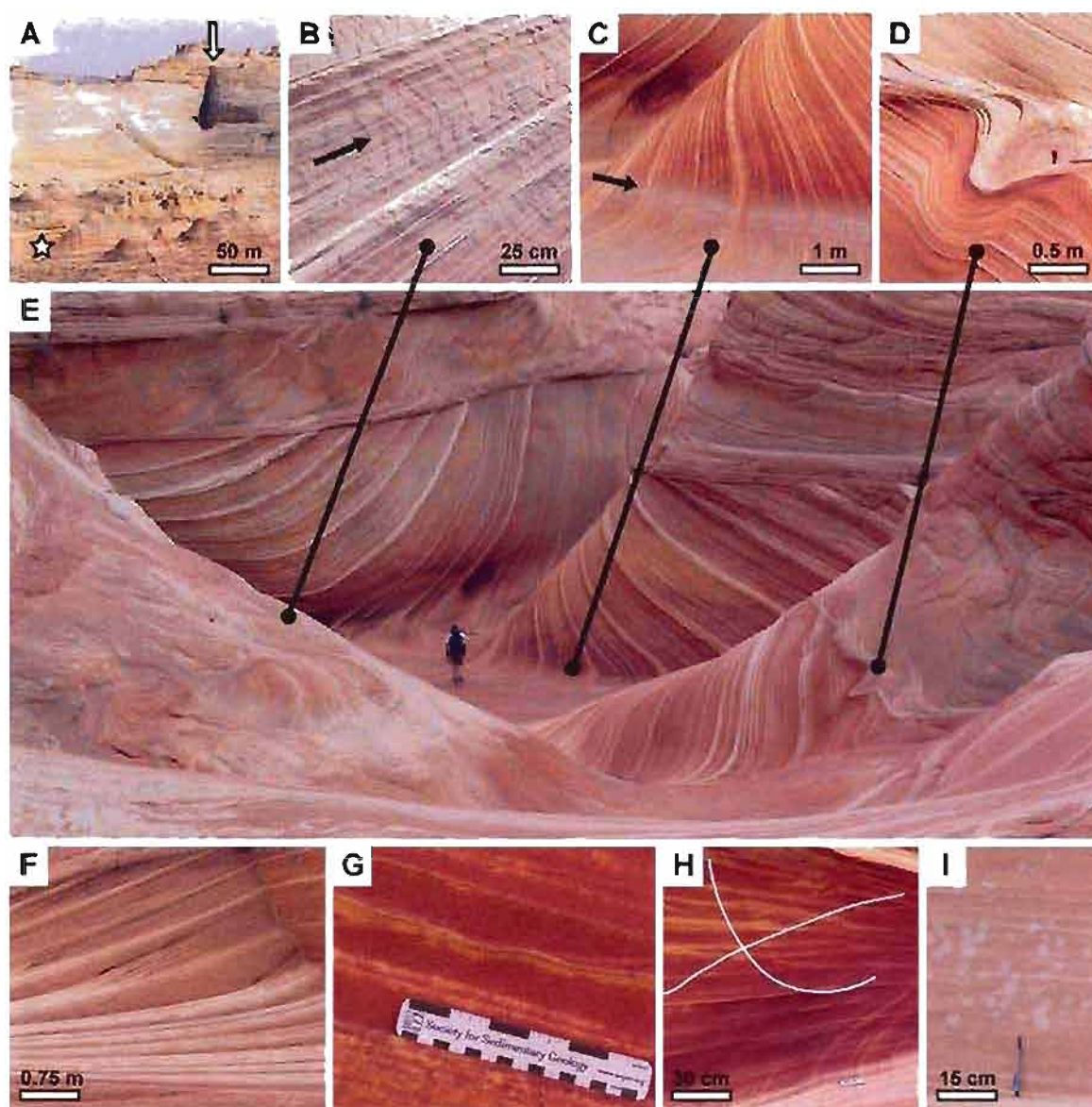


Figure 2.14. Diagenetic, sedimentary, and geomorphic evolution of the Wave. A) The Wave (star) is situated beneath a large, N-S trending joint. B) Modern erosion is attributed to wind and is evidenced by eolian steps and risers on steep trough walls (arrow=wind direction). C) Rainfall pools to a depth of 1 m and is not a significant force of modern erosion. A series of parallel, horizontal scour marks correspond to the maximum water depth (arrow), but no fluvial erosion chutes and pools exist. D) The Wave with locations of described geomorphic features. E) Soft sediment deformation may record dinosaur footprints. F) Cyclic eolian cross strata with red (grainflow) and white (windripple) coloration. G) A buoyant reducing fluid bleaches areas beneath pinstripe lamina and bounding surfaces. H) Multiple, concurrent Liesegang events overprint both red and white coloration and bleaching. White lines trace cross-cutting events. I) Bleaching atop secondary coloration indicates a localized, late-stage reducing event.

wedges of windripple laminae; and (3) where the upper bounding surface is overlain by windripple cross strata (Figure 2.14G). These patterns represent the limited, boundary mixing of a hydrocarbon, reducing fluid into a groundwater-saturated zone. The reducing fluid flowed advectively through high porosity/permeability grainflow strata. Sandstone was bleached only in the isolated areas where fluid movement was constrained by low permeability pinstripes and windripple laminae—where trapped reducing fluids had sufficient time to dissolve HFO grain coats.

Following localized bleaching, the unit is overprinted by the variable Liesegang facies. Multiple, cross cutting events are recorded by yellow (10YR 7.5/6), Fe-rich brown to yellow (avg. 10YR 6.5/8), and deep purple to reddish black (avg. 5R 2.5/1) Liesegang bands (Figure 2.14H). In some cases, coloration at the distal edges of the yellow bands transition into an iron-rich Liesegang band. In other examples, Fe-rich banding overprints the yellow. Variable Liesegang facies relationships appear conflicting, display an “interfingering” of multiple events, and indicate an overlapping timeframe for Liesegang emplacement. The overall effect of the yellow banding is to deepen the primary red from 2.5YR 4.5/8 to 10R 4/6. In places at the Wave, Fe-rich bands protrude as erosionally resistant fins, but predominantly show little evidence of sandstone case hardening. Fe-rich circles averaging 1 cm in diameter (but up to 4 cm diameter) are superimposed on Liesegang events. A final, late phase reducing event is indicated by cm-scale bleached patches that overprint secondary coloration (Figure 2.14I).

Geomorphically, the Wave marks the convergence of two wind-scoured troughs (Loope et al., 2008; Figure 2.14A). The N-S oriented feature is approximately 96 m in



length—the wider, U-shaped trough is 19 m wide by 36 m long. The narrower trough measures 16 m in length by ~2 m in width (Loope et al., 2008). These troughs expose large foresets of rhythmic and cyclic alternating grainflow and windripple laminae reflecting Jurassic paleoclimate conditions (Chan and Archer, 2000; Loope et al., 2001; Figure 2.14F). The troughs expose a 10.2 m thick eolian set with a mean cyclic foreset thickness of 0.78 m. Well defined, m to sub-m scale, downward plunging soft sediment deformation on the southern flanks of the Wave may represent fluid escape structures, however, the size, spacing, and presence of dinosaur footprints in the area, suggest that these soft sediment deformation features may be vertebrate in origin (Figure 2.14E).

Fluvial processes likely initialed the Wave along near vertical, Laramide-aged joints during Late Miocene to Pliocene Colorado River incision (Pederson, 2008; Figure 14B). However, during its geomorphic evolution, the upstream drainage area was diminished to its current ~0.05 km<sup>2</sup> (Loope et al., 2008)—too small to attribute modern, active trough scouring by water. A series of horizontal scour marks at the Wave's base indicates water pooling to 1.0 m (Figure 2.14D), but the preservation of protruding ribs of windripple laminae along the trough floor are not cut by water channels. Chutes and pools common in water-sculpted sandstone are absent. Water does little to actively shape the Wave (Loope et al., 2008). Modern erosion is nearly exclusively by wind, as evidenced by eolian steps and risers along steep trough walls and is discussed in detail by Loope et al. (2008; Figure 2.14C). Eolian steps and risers are oriented at 134° along surfaces oblique to the dominant wind and are consistent with wind entering The Wave from the S and exiting to the N. The Wave acts as a natural venturi, increasing wind velocity with constricted flow in its central passage.

The Wave's combination of features provides insight into the geomorphic and diagenetic evolution of eolian deposits at the Coyote Buttes and the larger Colorado Plateau. Events can be organized sequentially: (1) Jurassic deposition of Navajo Erg; (2) dinosaur tracks emplaced in dune cross strata; (3) original red and white banding (cm-scale); (4) bleaching fluid introduced (cm to m scale); (5) yellow precipitating fluid introduced (mm to m scale); (6) multiple Fe-rich Liesegang bands emplaced (mm to cm scale); (7) minor addition of late-stage reducing fluid; (8) water driven erosion follows regional joints; (9) wind scouring drives modern erosion; and (10) contemporary pooling of water after intense, localized precipitation events.

### Implications

This study reveals reservoir fluid dynamics that illustrate fluid emplacement rates, timing, and reservoir anisotropies due to eolian stratification. Furthermore, this example holds implications to HFO concretion formation in the Navajo Sandstone and on Mars. Beitler et al. (2003), estimate the volume of the Navajo reservoir within the East Kaibab structure at  $5.8 \times 10^3 \text{ km}^3$ . Following their assumed 15% porosity, fluid volume in the East Kaibab uplift would approach  $0.9 \times 10^3 \text{ km}^3$  ( $\sim 5.9 \times 10^{12}$  barrels). If the extent of bleaching on only the Paria Plateau is used as an indicator of hydrocarbon residence, rough calculations produce hydrocarbon volumes of  $\sim 0.75 \text{ km}^3$  ( $\sim 5.0 \times 10^9$  barrels). Likewise, in performing mass-balance calculations on bleached deformation bands, Parry et al. (2004) establish that 1500 pore volumes of fluid are required to remove 0.1 wt% Fe. Tremendous fluid volumes follow the Butte Fault to accumulate in the Kaibab structure over a relatively narrow timeframe—between the initiation and termination of faulting

(~80-50 Ma.; Tindall and Davis, 2003). However, the paleoflow at Coyote Buttes (to the east) is opposite that described by Bowen et al. (2007) along the East Kaibab monocline, ~30 km to the north. Likewise, the Coyote Buttes lack carbonate as observed by Bowen et al. (2007) in bleached areas to the North. The combination of differing paleoflow and mineralogy suggests that fluid introduction along the monocline was not uniform along its length. The wide-range of diagenetic variations observed at the Coyote Buttes, in close proximity to the fault, suggests that various fluids, both reducing and oxidizing, were supplied to the system along the fault trace.

At the outcrop scale, the study provides evidence for fine-scale interactions between fluids and eolian lamina. Viewed as a whole, the Navajo Sandstone possesses ideal reservoir characteristics: high porosity and permeability in a homogeneous sand. However, bleaching patterns indicate that advective fluid migration at the outcrop scale is directed and compartmentalized by eolian stratification.

The Navajo Sandstone has been investigated as a suitable terrestrial analog to Mars (Beitler et al., 2004; Chan et al., 2004, 2005, 2006, 2008; Seiler et al., 2007). In particular, attention has been given to Martian “blueberries,” hematite concretions that show remarkable similarity to those in the Navajo. Some Liesegang bands at Coyote Buttes appear as self-organized micro-concretions at the microscopic scale and may represent the first stages of larger concretion growth (had there been an additional Fe supply).

The Coyote Buttes display a complex history of fluid interactions and show that multiple HFO enrichment and depletion episodes can be superimposed within an area. Fine-scale reflectance spectra transects through variably colored areas (Liesegang facies)

give detailed mineralogic characterizations that may refine remotely sensed spectral characterizations of Mars. Finally, of general interest, this study interprets the coloration patterns at one of the most photographed locations on the Colorado Plateau.

### Conclusions

Coloration patterns observed at Coyote Buttes record a dynamic fluid and diagenetic history in the Navajo Sandstone. Six diagenetic facies in Jurassic Navajo Sandstone are recognized, mapped and analyzed by thin section and reflectance spectroscopy. Stratigraphic relationships and reaction front mapping shows that diagenetic facies are due to both advective fluid flow and diffusive Fe mobilization within the host rock. Small (cm-scale) and large (10's-m scale) bleaching patterns clearly indicate advective, upward migration and accumulation of a buoyant, chemically reducing fluid (likely hydrocarbons). Small (cm-scale) and large (m-scale) Liesegang bands commonly cross low permeability eolian strata without deflection and indicate diffusive mass transfer. This likely occurred (without advective flow) across the reaction boundary between a fluid enriched in mobile and reduced iron ( $\text{Fe}^{2+}$ ) and an iron-depleted, oxygen-rich, oxidizing fluid.

Coyote Buttes coloration is due primarily to hematite and to goethite in a lesser degree. Reflectance spectroscopy indicates red, to orange, to dark purple coloration is due to hematite; yellow Liesegang bands are due to goethite. Bleached (white) areas lack HFO. Coloration events occurred over a narrow timeframe concurrent with Laramide-aged faulting along the East Kaibab monocline. Outcrop and regional-scale patterns indicate a paleoflow to the east. The emplacement of cataclastic deformation bands

compartmentalized the Navajo Sandstone reservoir. Large HFO and carbonate concretions occur only to the west of the bands and suggest differing late-stage diagenetic evolutions east and west of the deformation bands. This study provides insight into eolian petroleum reserves in central UT and southern WY and holds application to interpreting HFO concretions that serve as terrestrial analogs to “blueberry” HFO concretions discovered on Mars. The Coyote Buttes is a valuable geologic resource for the scientific community, and an exceptional aesthetic landscape feature for resource management in the Vermilion Cliffs National Monument.

#### Acknowledgments

Special thanks to John Bowman, Bill Parry, Erich Petersen, Sally Potter, Vaughn Thompson, and Jessica Allen at the University of Utah and to Linda Price, Mike Salamacha and Rody Cox at the Bureau of Land Management. This work is supported by the National Aeronautics and Space Administration (to M.A. Chan) under grant number NNG06GI10G issued through the Mars Fundamental Research Program. Additional research support was received from the British Broadcasting Corporation and the Chevron Corporation.

#### References

- ANTONELLINI, M. AND AYDIN, A., 1994, Effect of faulting on fluid flow in porous sandstones; petrophysical properties: AAPG Bulletin, v. 78, p. 355-377.
- BARGE, L.M., JARRETT, D., NEALSON, K., AND PETRUSKA, J., 2008, Generation of ordered mineral structures in diffusion-controlled systems: in preparation.

- BEITLER, B., CHAN, M.A., AND PARRY, W.T., 2003, Bleaching of Jurassic Navajo Sandstone on Colorado Plateau Laramide highs: evidence of exhumed hydrocarbon supergiants?: *Geology*, v. 31, p. 1041-1044.
- BEITLER, B. , CHAN, M.A., PARRY, W.T., ORMÖ, J., AND, KOMATSU, G., 2004, Diagenetic analogs to hematite regions on Mars: examples from Jurassic sandstones of Southern Utah, USA (Invited Paper), *in* Hoover, R.B., Levin, G.V., and Rozanov, A.Y., eds., *Proceedings of SPIE Volume 5555, Instruments, Methods, and Missions for Astrobiology VIII*, SPIE, Bellingham, Washington, p. 162-169
- BEITLER, B. , PARRY, W.T., AND CHAN, M.A., 2005, Fingerprints of fluid flow: chemical diagenetic History of the Jurassic Navajo Sandstone, southern Utah: *Journal of Sedimentary Research*, v. 75, p. 545-559.
- BERNER, R.A., 1969, Migration of iron and sulfur within anaerobic sediments during early diagenesis: *American Journal of Science*, v. 267, p. 19-42.
- BIEK, R.F., 2002, Interim geologic map of the Kolob Reservoir quadrangle, Washington and Iron Counties, Utah: *Utah Geological Survey Open-File Report 387*, scale 1:24,000.
- BIEK, R.F., WILLIS, G.C., HYLLAND, M.D., AND DOELLING, H.H., 2000, Geology of Zion National Park, Utah, *in* Sprinkel, D.A., Chidsey, T.C., and Anderson, P.B., eds., *Geology of Utah's Parks and Monuments*, Utah Geological Association, Publication 28, p. 107-135.
- BLAKEY, R.C., 2001, Paleogeography through geologic time, updated June 10, 2002, [http://jan.ucc.nau.edu/~rcb7/global\\_history.html](http://jan.ucc.nau.edu/~rcb7/global_history.html). Checked December, 2006.
- BLAKEY, R.C., PETERSON, F., AND KOCUREK, G., 1988, Synthesis of Late Paleozoic and Mesozoic eolian deposits of the Western Interior of the United States, *in* Kocurek, G., ed., *Late Paleozoic and Mesozoic Aeolian Deposits of the Western Interior of the United States: Sedimentary Geology*, v. 56, p. 3-125.
- BOWEN, B.B., MARTINI, B.A., CHAN, M.A., AND PARRY, W.T., 2007, Reflectance spectroscopic mapping of diagenetic heterogeneities and fluid-flow pathways in the Jurassic Navajo Sandstone: *AAPG Bulletin*, v. 91, p. 173-190.
- BROWN, D., 2005, Covenant field keeping promises, Utah play makes lots of headlines: *AAPG Explorer*, v. 25, p. 4-8.
- BUREAU OF LAND MANAGEMENT, 2007, Paria Canyon/Vermilion Cliffs Wilderness, Paria Canyon Permit Area: <https://www.blm.gov/az/asfo/paria/index.htm>, website accessed 14 February.

- CAPUTO, M.V., 2003, Geology of the Paria Canyon - Vermilion Cliffs Wilderness, Utah and Arizona, *in* Sprinkel, D.A., Chidsey, T.C., Jr., and Anderson, P.B. eds., Geology of Utah's Parks and Monuments, Utah Geological Association, Publication 28, 2nd edition, p. 535-561.
- CHAN, M.A., AND ARCHER, A.W., 2000, Cyclic eolian stratification on the Jurassic Navajo Sandstone, Zion National Park; periodicities and implications for paleoclimate, *in* Sprinkel, D.A., Chidsey, T.A., Jr., and Anderson, P.B., eds., Geology of Utah's Parks and Monuments, Utah Geological Association, Publication 28, p. 606-617.
- CHAN, M.A., AND PARRY, W.T., 2002, Rainbow of Rocks: Mysteries of Sandstone Colors and Concretions in Colorado: Salt Lake City, Utah Geological Survey, 17 p.
- CHAN, M.A., PARRY, W. T., AND BOWMAN, J. R., 2000, Diagenetic hematite and manganese oxides and fault-related fluid flow in Jurassic sandstones, southeastern Utah: AAPG Bulletin, v. 84, p. 1281-1310 (with cover photo on v. 84).
- CHAN, M.A., BEITLER, B., PARRY, W.T., ORMÖ, J, AND KOMATSU, G., 2004, A possible terrestrial analogue for haematite concretions on Mars: Nature, v. 429, p. 731-734.
- CHAN, M.A., BOWEN, B.B., PARRY, W.T. ORMÖ, J, AND KOMATSU, G., 2005, Red rock and red planet diagenesis: Comparisons of Earth and Mars concretions: GSA Today, v. 15, p. 4-10.
- CHAN, M. A., JOHNSON, C. M., BEARD, B.L., BOWMAN, J.R., AND PARRY, W.T., 2006, Iron isotopes constrain the pathways and formation mechanisms of terrestrial oxide concretions: a tool for tracing iron cycling on Mars?: Geosphere, v. 2, p. 324-332.
- CHAN, M.A., YONKEE, W.A., NETOFF, D.I., SEILER, W.M., AND FORD, R.L., 2008, Polygonal cracks in bedrock on Earth and Mars: Implications for weathering: Icarus, v.194, p. 65-71.
- CHIDSEY, T.C. AND MORGAN, C.D., 2005, Major oil plays in Utah and vicinity: Quarterly Technical Progress Report 2005, Utah Geological Survey, Salt Lake City, 64 p.
- CHIDSEY, T.C., 2007, Major oil plays in Utah and vicinity: Quarterly Technical Progress Report for the period October 1 to December 31, 2006: U.S. Department of Energy, DE-FC26-02NT15133, 19 p.
- CLARK, R.N., 1995, Reflectance spectra: AGU Handbook of Physical Constants: Washington, D.C., p. 178-188.
- CLARK, J.M. AND FASTOVSKY, D.E., 1986, Vertebrate biostratigraphy of the Glen Canyon Group in northern Arizona, *in* Padian, K. ed., The Beginning of the Age

of Dinosaurs: Faunal Changes Across the Triassic-Jurassic Boundary: Cambridge University Press, New York, p. 285-301.

- DALRYMPLE, A. AND MORRIS, T.H., 2007, Facies analysis and reservoir characterization of outcrop analogs to the Navajo Sandstone in the central Utah thrust belt exploration play, *in* Willis, G.C., Hylland, M.D., Clark, D.L., and Chidsey, T.C. Jr., eds., Central Utah - Diverse Geology of a Dynamic Landscape, Utah Geological Association, Publication 38, p. 311-322.
- DEATON, B.C. AND BALSAM, W.L., 1991, Visible spectroscopy - a rapid method for determining hematite and goethite concentration in geological materials: *Journal of Sedimentary Petrology*, v. 61, p.628-632.
- DEE, G.T., 1986, Patterns produced by precipitation at a moving reaction front: *Physical Review Letters*, v. 57, p. 275-278.
- DICKINSON, W.R. AND GEHRELS, G.E., 2003, U-Pb ages of detrital zircons from Permian and Jurassic eolian sandstones of the Colorado Plateau, USA: paleogeographic implications: *Sedimentary Geology*, v. 163, p. 29-66.
- EICHHUBL, P., AND FLODIN, E., 2005, Brittle deformation, fluid flow, and diagenesis in sandstone at Valley of Fire State Park, Nevada, *in* Pederson, J., and Dehler, C. M., eds., Interior Western United States: Geological Society of America Field Guide, vol. 6, p. 151-167.
- EICHHUBL, P., TAYLOR, W. L., POLLARD, D. D. AND AYDIN, A., 2004, Paleo-fluid flow and deformation in the Aztec Sandstone at the Valley of Fire, Nevada - evidence for the coupling of hydrogeologic, diagenetic, and tectonic processes: *GSA Bulletin*, vol. 116, p 1120-1136.
- EISENBERG, L., 2003, Giant stromatolites and a supersurface in the Navajo Sandstone, Capitol Reef National Park, Utah: *Geology*, v. 31, p. 111-114.
- EKDALE, A.A., BROMLEY, R.G., AND LOOPE, D.B., 2007, Ichnofacies of an ancient erg: a climatically influenced trace fossil association in the Jurassic Navajo Sandstone, southern Utah, U.S.A., *in* Miller III, W., ed., Trace Fossils, Concepts, Problems, Concepts: Amsterdam, Elsevier, 632 p.
- FOSSEN, H., SCHULTZ, R.A., SHIPTON, Z.K., AND MAIR, K., 2007, Deformation bands in sandstone: a review: *Journal of the Geological Society of London*, v. 164, p. 755-769.
- GAFFEY, S.J., 1985, Reflectance spectroscopy in the visible and near infrared (0.35-2.55  $\mu\text{m}$ ): applications in carbonate petrology: *Geology*, v.13 p. 270-273.



- GUPTA, R.P., 2003, Remote Sensing Geology, 2<sup>nd</sup> edition: Heidelberg, Germany, Springer, 655 p.
- IRMIS, R.B., 2005, A review of the vertebrate fauna of the Lower Jurassic Navajo Sandstone in Arizona, *in* McCord, R.D. eds., Vertebrate Paleontology of Arizona, Mesa Southwest Museum, Bulletin 11, p. 55-71.
- Ji, J., BALSAM, W., CHEN, J., AND LIU, L., 2002, Rapid and quantitative measurement of hematite and goethite in the Chinese loess-paleosol sequence by diffuse reflectance spectroscopy: Clays and Clay Minerals, v. 50, p. 208-216.
- KOCUREK, G., 2003, Limits on extreme eolian systems; Sahara of Mauritania and Jurassic Navajo Sandstone examples, *in* Chan, M.A., and Archer, A., eds., Extreme Depositional Environments: Mega End Members in Geologic Time, Geological Society of America, Special Paper 370, p. 43-52.
- KOCUREK, G., AND DOTT, R.H., JR., 1983, Jurassic paleogeography and paleoclimate of the central and southern Rocky Mountains regions, *in* Reynolds, M.W., and Dolly, E.D., eds., Mesozoic Paleogeography of the West-Central United States, SEPM, Rocky Mountain Section, Rocky Mountain Paleogeography Symposium 2, p. 101-116.
- LINDQUIST, S.J., 1988, Practical characterization of eolian reservoirs for development: Nugget Sandstone, Utah-Wyoming thrust belt: Sedimentary Geology, v. 56, p. 315-339.
- LOOPE, D.B., 2006, Dry-season tracks in dinosaur-triggered grainflows: Palaios, v. 21, p. 132-142.
- LOOPE, D.B., AND ROWE, C.M., 2003, Long-lived pluvial episodes during deposition of the Navajo Sandstone: Journal of Geology, v. 111, p. 223-232.
- LOOPE, D.B., ROWE, C.M., AND JOECKEL, R.M., 2001, Annual monsoon rains recorded by Jurassic dunes: Nature, v. 412, p. 64-66.
- LOOPE, D.B., STEINER, M.B., ROWE, C.M., AND LANCASTER, N., 2004, Tropical westerlies over Pangaeian sand seas: Sedimentology, v. 51, p. 315-322.
- LOOPE, D.B., SEILER, W.M., MASON, J.A., AND CHAN, M.A., 2008, Wind scour of Navajo Sandstone at the Wave (central Colorado Plateau, U.S.A.): Journal of Geology, v. 116, p. 173-183.
- MORRIS, R.V., 1985, Spectral and other physiochemical properties of submicron powders of hematite, maghemite, magnetite, goethite, and lepidocrite: Journal of Geophysical Research, v. 90, p. 3126-3144.

- MOULTON, F.C. AND PINNELL, M.L., 2005, Stunning Utah oil, gas discovery focuses spotlight on Hingeline: *Oil and Gas Journal*, v. 103, p. 42-49.
- MUNSELL, A.H., 1975, *Munsell Soil Color Charts*: Baltimore, Munsell Color, 23 p.
- OLSEN, P.E. AND GALTON, P.M., 1977, Triassic-Jurassic tetrapod extinctions: are they real?: *Science*, v. 197, p. 983-986.
- ORTOLEVA, P., 1984, The self organization of Liesegang bands and other precipitate patterns, *in* Nicolis, G. and Baras, F., eds., *Chemical Instabilities: Applications in Chemistry, Engineering, Geology, and Materials Science*: Amsterdam, Riedel, 289-297.
- ORTOLEVA, P. T., E. MERINO, C. MOORE, AND J. CHADAM, 1987a, Geochemical self-organization I: reaction-transport feedbacks and modeling approach: *American Journal of Science*, v. 287, p. 979-1007.
- ORTOLEVA, P. T., J. CHADAM, E. MERINO, AND A. SEN, 1987b, Geochemical self-organization II: the reactive-infiltration instability: *American Journal of Science*, v. 287, p. 1008-1040.
- PARRISH, J.T., 1993, Climate of the supercontinent Pangea: *Journal of Geology*, v. 101, p. 215-233.
- PARRISH, J.T. AND FALCON-LANG, H.J., 2007, Coniferous trees associated with interdune deposits in the Jurassic Navajo Sandstone Formation, Utah, USA: *Palaeontology*, v. 50, p. 829-843.
- PARRISH, J.T., AND PETERSON, F., 1988, Wind directions predicted from global circulation models and wind directions determined from eolian sandstones of the western United States – a comparison: *Sedimentary Geology*, v. 56, p. 261-282.
- PARRY, W.T., CHAN M.A., AND BEITLER, B., 2004, Chemical bleaching indicates episodes of fluid flow in deformation bands in sandstone: *AAPG Bulletin*, v. 88, p. 175-191.
- PEDERSON, J., 2008, Personal communication, 31 January.
- PETERSON, F., 1988, Pennsylvanian to Jurassic eolian transportation systems in the western United States: *Sedimentary Geology*, v. 56, p. 207-260.
- PETERSON, F. AND TUNER-PETERSON, C., 1989, Geology of the Colorado Plateau, *in* Hanshaw, P.M., ed., 28<sup>th</sup> International Geological Congress Field Trip Guidebook T130, American Geophysical Union, v. 1, p. 1-65.

- PETTIJOHN, F.J., POTTER, P.E., AND SIEVER, R., 1972, *Sand and Sandstone*: New York, Springer-Verlag, 618 p.
- POTTER, S.L., 2008, Personal communication, University of Utah, 15 January.
- RAHL, J., REINERS, P., CAMPBELL I., NICOLESCU, S., AND ALLEN, C., 2003, Combined single-grain (U/Th)/He and U/Pb dating of detrital zircons from the Navajo Sandstone, Utah: *Geology*, v. 31, p. 761-764.
- REINERS, P.W., CAMPBELL, I.H., NICOLESCU, S., ALLEN, C.M., HOURIGAN, J.K., GARVER, J.I., MATTINSON, J.M., AND COWAN, D.S., 2005, (U-Th)/(He-Pb) double dating of detrital zircons: *American Journal of Science*, v. 305, p. 259-311.
- ROWE, C.M., LOOPE, D.B., OGLESBY, R.J., VANDER VOO, R., AND BROADWATER, C.E., 2007, Inconsistencies between Pangean reconstructions and basic climate controls: *Science*, v. 318, p. 1284-1286.
- ROZNOVSKY, T.A. AND AYDIN, A., 2001, Concentration of shearing deformation related to changes in strike of a monoclinial fold axes: the Waterpocket monocline, Utah: *Journal of Structural Geology*, v. 23, p. 1567-1579.
- SAMPSON, P.J., 1992, *Sedimentology of the Navajo Sandstone, southern Utah, USA*: Unpublished Ph.D. dissertation, University of Oxford, 291 p.
- SCHNEIDER, F.W., 2008, Personal communication, University of Utah, 23 January.
- SEILER, W.M., 2008, *Unique geologic characteristics of the Coyote Buttes, Utah-Arizona*: Unpublished M.S. thesis, University of Utah, 150 p.
- SEILER, W.M., AND CHAN, M.A., 2008, A wet interdune dinosaur trample bed in the Jurassic Navajo Sandstone, Coyote Buttes, Arizona: rare preservation of multiple track types and tail drag marks: *Palaios*, in review.
- SEILER, W.M., CHAN, M.A., AND SULLIVAN, R.J., 2007, Hematite “microberry” wind ripples: eolian conditions for a terrestrial Martian analog from the Jurassic Navajo Sandstone, Utah-Arizona: 38th Lunar and Planetary Science Conference, May 12-16, 2007, Paper # 2076.
- SIGDA, J.M., GOODWIN, L.B., MOZLEY, P.S., AND WILSON, J.L., 1999, Permeability alteration in small displacement faults in poorly lithified sediments: Rio Grande Rift, central New Mexico: *Faults and Subsurface Fluid Flow in the Shallow Crust* v.113, American Geophysical Union, p. 51-68.
- SIGDA, J.M. AND WILSON, J.L., 2003, Are faults preferential flow paths through semiarid and arid vadose zones?: *Water Resources Research*, v.39, p. 1225.

- TAYLOR, W.L. AND POLLARD, D.D., 2000, Estimation of in situ permeability of deformation bands in porous sandstone, Valley of Fire, Nevada: *Water Resources Research*, v. 36, p. 2595-2606.
- TERRY, R.D., AND CHILINGAR, G.V., 1955, Summary of "Concerning some additional aids in studying sedimentary formation," by M.S. Shvetsov: *Journal of Sedimentary Petrology*, v. 25, p. 229-234.
- TINDALL, S.E., 2000, The Cockscomb segment of the East Kaibab Monocline: taking the structural plunge, *in* D.A. Sprinkel, T.C. Chidsey, Jr., and P.B. Anderson, eds., *Geology of Utah's Parks and Monuments*, Utah Geological Association, Publication 28, p. 629-643.
- TINDALL, S.E. AND DAVIS, G.H., 1999, Monocline development by oblique-slip fault-propagation folding: the East Kaibab monocline, Colorado Plateau, Utah: *Journal of Structural Geology*, v. 21, p. 1203-1230.
- TOWNSEND, T.E., 1987, Discrimination of iron alteration minerals in visible and near-infrared reflectance data: *Journal of Geophysical Research*, v. 92, p. 1441-1454.
- VON GUNTEN, U. AND SCHNEIDER, W., 1991, Primary products of oxygenation of iron (II) at an oxic/anoxic boundary; nucleation, agglomeration, and aging: *Journal of Colloid and Interface Science*, v. 145, p. 127-139.
- VERLANDER, J.E., 1995, Basin-scale stratigraphy of the Navajo Sandstone: southern Utah, U.S.A.: Unpublished Ph.D. dissertation, University of Oxford, 159 p.
- VINCENT, R.K., 1997, *Fundamentals of Geological and Environmental Remote Sensing: Upper Saddle River, New Jersey*, Prentice Hall, 366 p.

## CHAPTER 3

# A WET INTERDUNE DINOSAUR TRAMPLE SURFACE IN THE JURASSIC NAVAJO SANDSTONE, COYOTE BUTTES, ARIZONA: RARE PRESERVATION OF MULTIPLE TRACK TYPES AND TAIL DRAG MARKS

### Abstract

A well-preserved dinosaur trample surface in a wet interdune interval of Jurassic Navajo Sandstone at the Coyote Buttes along the Arizona/Utah border exhibits an unusual combination of multiple overlapping track types and sizes, high track density, striking footprint features including claws and toes, and rare tail drag marks. The trample surface covers an ~3000 m<sup>2</sup> area, with an average density of about 12 impressions/m<sup>2</sup> in its main extent. At least three distinct ichnogenera—*Eubrontes*, *Anchisauripus*, *Grallator*—and the tracks attributed to a sauropodomorph appear as regular to asymmetric penetrations into the substrate with digitate features, commonly accompanied by soft-sediment mounds of upturned sand preserved in the sandstone. The trample surface provides paleoecologic and paleoclimatologic proxies suggesting a pluvial climate shift that likely induced subaerial groundwater saturation in an eolian interdune

that attracted dinosaurs to the area. The trample surface provides valuable data for refining ecologic and climatic sensitivities recorded in Early Jurassic eolian deposits.

### Introduction

Well-preserved dinosaur tracksites have been described at numerous localities in the Western United States. These tracksites occur in many continental formations from the Late Triassic through Late Cretaceous, represent a wide range of depositional environments, and provide valuable paleoenvironmental and paleobiological information (Lockley and Conrad, 1989). This paper documents the initial survey of a disturbed-bedding surface that is herein interpreted to be a dinoturbated, interdune trample surface in the Navajo Sandstone. The number of impressions at this trample surface may exceed those of the large trackway sites of the Morrison Formation (Lockley et al., 1986). This unusual surface lends significant climatic and ecologic insight into conditions in western Pangaea during the Early Jurassic.

More than 60 tracksites have been documented in the Jurassic Navajo Sandstone (Faull and Roberts, 1951; Clark and Fastovsky, 1986; Winkler et al., 1991; Rainforth, 1997; Lockley, 1998; Hamblin and Foster, 2000; Irmis, 2005; Loope, 2006). Most of these tracks were originally interpreted to have formed in wet eolian sands, although Loope (2006) argues that many Navajo Sandstone tracks can be attributed to a dry-sand origin.

The Jurassic Navajo Sandstone is well exposed at the Coyote Buttes along the Utah-Arizona border on the western margin of the Paria Plateau. The locale is notable for its unique diagenetic coloration of FeO mineralogies, climatically induced cyclic

eolian stratification (Chan and Archer, 2000; Loope et al., 2001), dry season dinosaur tracks, (Loope, 2006), and erosional sculpting by wind (Loope et al., 2007). Although a vast literature exists on the sedimentology and stratigraphy of the Navajo Sandstone (e.g., Blakey et al., 1988; Peterson, 1988; Sampson, 1992; Verlander, 1995; Chan et al., 2000; Eisenberg, 2003), this study focuses on one unusual, and important trample surface.

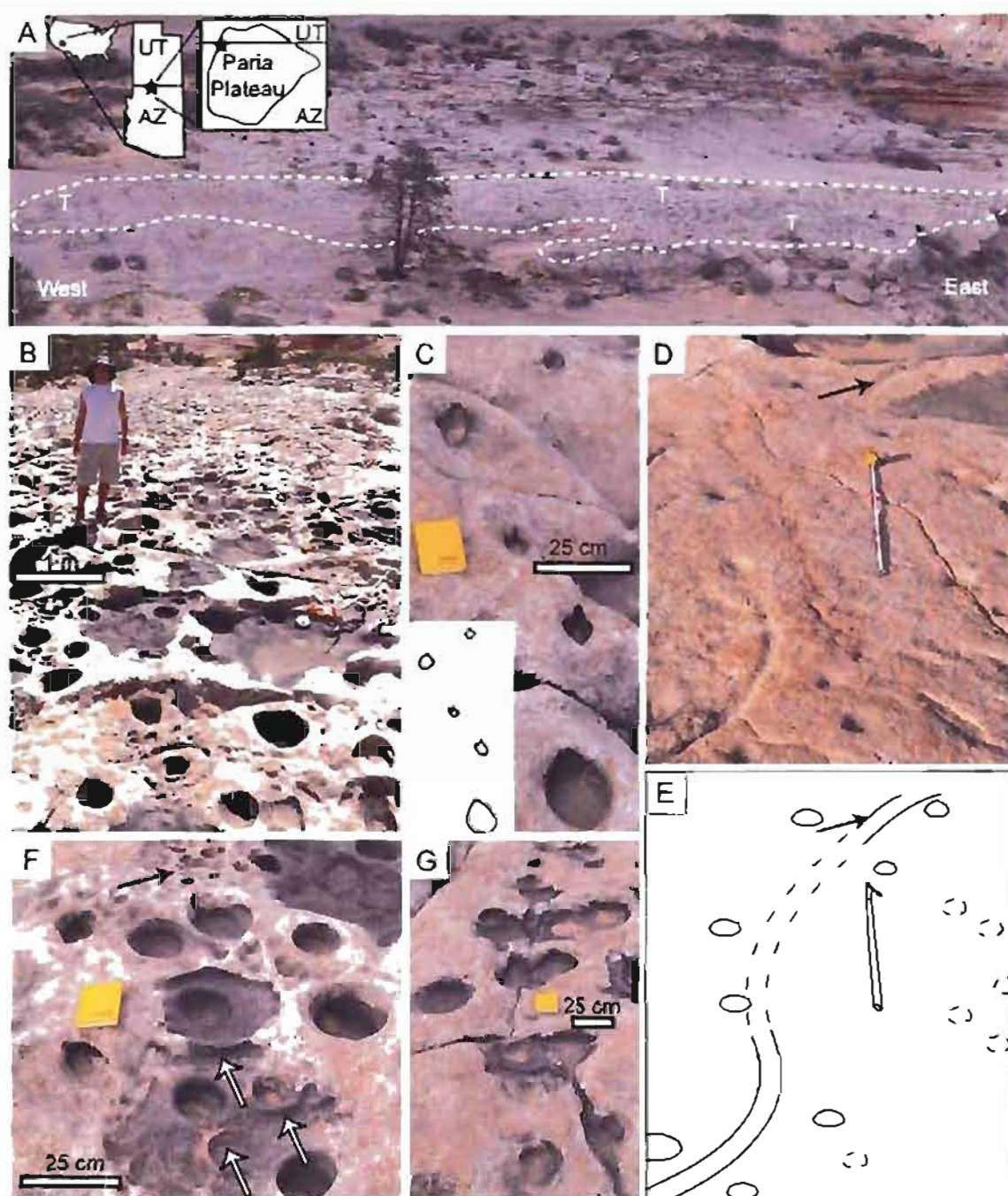
### Location, Geologic Setting and Stratigraphy

The Coyote Buttes (N36° 59' 45" W 112° 00' 22") are raised buttes of Jurassic Navajo Sandstone crossing the Arizona/Utah border ~50 km west of Page, AZ (Figure 3.1). The trample surface (Figure 3.1B) is located in the central portion of the Bureau of Land Management Coyote Buttes North Special Permit Area, on the eastern flank of the north trending Top Rock topographic high. The surface will be first described as a disturbed-bedding plane and then interpreted and informally referred to as the Top Rock trample surface.

The Navajo Sandstone and its equivalent deposits occupy a basinal area of >265,000 km<sup>2</sup>, though its original extent may have been two and a half times what is preserved in the geologic record (Kocurek and Dott, 1983; Blakey et al., 1988; Kocurek, 2003). The eolian Navajo Sandstone preserves the deposits of an ancient erg and is the youngest unit of the Glen Canyon Group (e.g., Olsen and Galton, 1977; Clark and Fastovsky, 1986; Irmis, 2005). Deposition is estimated to have occurred ~10° N latitude on the western edge of the Pangaea Supercontinent (Blakey, 2001; Loope et al., 2004); the generalized Jurassic paleoclimate setting is summarized by Parrish (1993) and Parrish and Peterson (1988).

Figure 3.1. Top Rock trample surface and representative impressions A) The Coyote Buttes study area along the Arizona/Utah border. Oblique downward, NNW view of the trample surface outlined by dashed line. Footprints provide the primary structures that give rise to small rainwater catchments that promote the growth of modern, black bacterial mats during wet-dry cycles. T = tail drag location. B) Characteristic impression distribution within the central portion of the trample surface. C) Track way of three-toed *Grallator*. D) Sinuous, curved tail-drag impression straddled by shallow (1-2 cm ), circular (7.7 cm diameter) footprints. Note the mound of sediment formed by the tail at the upper right (arrow). Tape extended to 1 m. E) Diagram of photograph D features. Solid line = known tail-drag; dashed line = inferred tail-drag path; solid ellipses = footprints belonging to tail-dragging organism; broken ellipses = footprints not associated with tail-drag. F) Syntsedimentary soft sediment mounds upturned around imprints (white arrows), smaller impressions overprinted atop larger impressions (black arrow). G) Impression forming a possible trackway (into the frame).



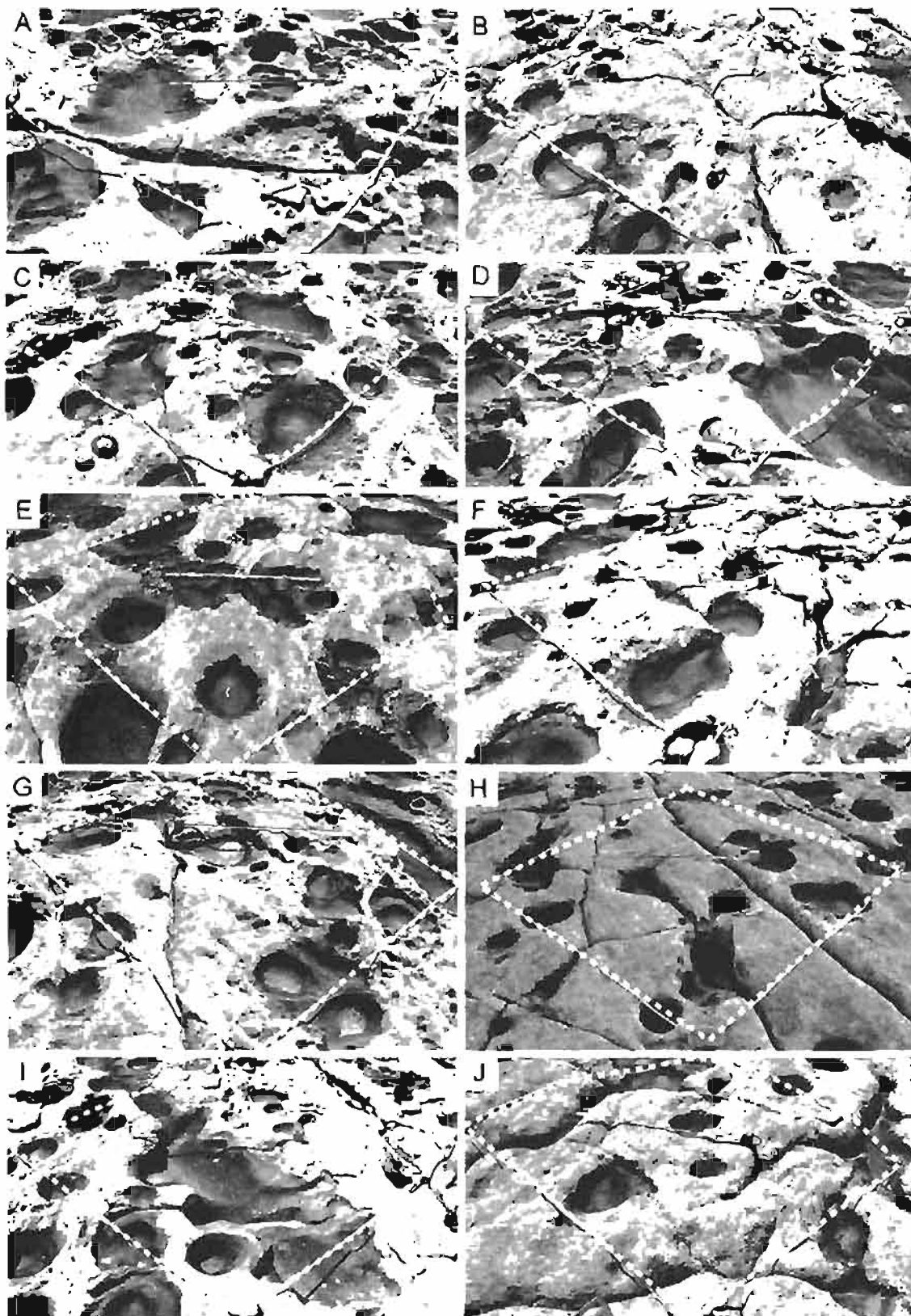


Locally, the Navajo Sandstone strikes  $355^{\circ}$  and dips  $5^{\circ}\text{E}$  corresponding to tilting associated with the Laramide uplift of the East Kaibab Monocline. Thickness of the Navajo Sandstone on the Paria Plateau is  $\sim 600$  m (Loope and Rowe, 2003; Loope, 2006) and exposure exceeds 200 m at the Coyote Buttes.

### Methods

The disturbed bedding plane surface of this study is  $\sim 1$  m thick, and covers a relatively large area ( $\sim 3000$  m<sup>2</sup>) that can only be viewed at a low, oblique angle from above (Figure 3.1A). Unlike other trackways that may have several to dozens of footprint impressions, this particular surface has  $>1000$  individual prints that exceed our ability to measure each individually for this pilot study. To document the significance of this surface, ten field plots ( $2 \times 2$  m) totaling 40 m<sup>2</sup> were surveyed in the main extent (the eastern 60 m =  $\sim 1320$  m<sup>2</sup>) of the trample surface as a preliminary means to assess the occurrence of impressions (aerial documentation of the surface was not feasible in this initial study; Figure 3.2). Plots were chosen randomly (to avoid bias towards the larger, more unusual, or visually exciting impressions), with the stipulation that plots not overlap. In randomly selecting ten plots from within the main trample area, a representative initial characterization could be made of the trample surface as a whole, including impression type, dimension, morphology, and density. Each plot was photographed along with individual tracks of interest. Impressions were measured as discrete, individual events. Larger trackways were not defined because impressions of the Top Rock trample surface are superimposed and of such a high density that it is difficult to assign individual tracks to larger trackways. All impressions within a plot

Figure 3.2. Ten individual measured plots delineated by dashed line (2 m/side). Scale = 1 m at each plot's center. A = plot 1; B = plot 2; C = plot 3; D = plot 4; E = plot 5; F = plot 6; G = plot 7; H = plot 8; I = plot 9; J= plot 10. These representative plots are used to characterize the trample surface.



were measured, inclusive of those only partially entering a given plot. Measurements included impression length, width and depth, the width and height of surrounding soft-sediment mounds, impression orientation, and any notable features (shape, overprinting, toe and claw prints).

Tail drags were photographed and measured for length, width, depth, mound height and width, orientation, and association with surrounding tracks. A 108 m stratigraphic section was measured adjacent to the trample surface to record eolian facies, sedimentary structures, bounding surfaces, and bioturbation (Figure 3.3). Track data were analyzed for impression density, size distribution, and predominant orientation.

## Results

### Description of Disturbed Bedding Plane and Impressions

The Top Rock measured section provides stratigraphic context for the disturbed surface (Figure 3.3). The section includes 51 crossbedded cosets of small (<3 m) to mega (>20 m) eolian dunes. Three distinct, heavily bioturbated, interdune deposits are located in interdune troughs between larger dunes at 0 - 7 m, 61 - 66 m, and 107 - 108 m (Figure 3.3). Eolian interdune deposits can be distinguished by a combination of factors that may include an association to lacustrine or fluvial deposits, root traces, sabkah-type laminations, mudcracks, and a high degree of burrowing and bioturbation. In each of the measured interdune intervals, intense burrowing has destroyed original eolian stratification.

The focus of this study is an ~1 m thick, massive, white sandstone bed that occurs at 64 m in the measured section, in the middle interdune deposit. This interval is

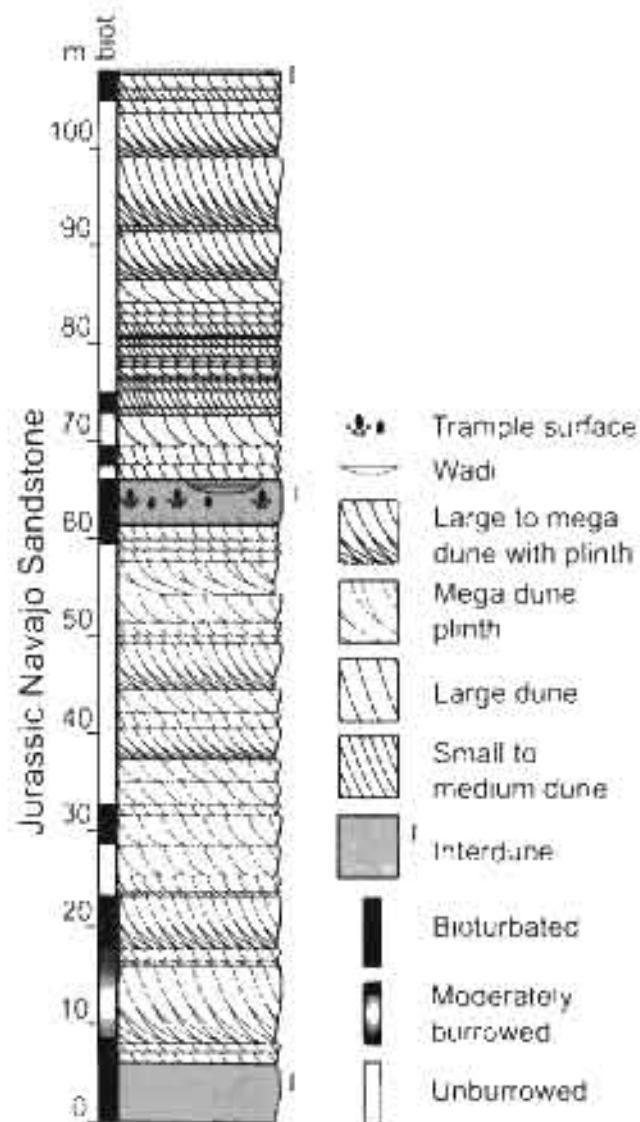


Figure 3.3 Stratigraphic column including the Top Rock trample surface. The trample surface is in the middle interdune deposit with a high degree of bioturbation surrounded by medium-sized dune sets.

distinguished by its proximity to a fluvial (wadi) channel, its high degree of burrowing/bioturbation, the presence of mudcracks, and the absence of cross-bedded, eolian dune deposits. This interdune deposit is superimposed over the underlying dune deposits such that the boundary is partially gradational. Impressions penetrate an interdune deflation surface that caps an eolian dune whose original crossbedding has been nearly obliterated by burrowing (Figure 3.4). The density of impressions can obscure the deflation plane. Horizontal and vertical, unlined burrows increase upwards in this stratigraphic interval. Interdune deposits up to 1 m thick occur above and adjacent to the imprinted surface. These interdune bedding planes display branching, unlined, horizontal burrows lacking meniscate backfill, unlined vertical burrows and occasional mudcracks. A lens-shaped, fluvial channel (~4 m thick with normally graded, fine to medium-grained sand, and bed thickness averaging between 0.15 m and 0.8 m) occurs laterally adjacent to the interdune deposit and stratigraphically above the trample surface.

The Top Rock disturbed surface extends east/west over an area ~3,000 m<sup>2</sup> (~100 m long x ~30 m wide) and contains a high density of circular to irregular impressions that at first glance appear as steep-walled potholes or weathering pits lined with a dark-colored bacterial mat. (Figures 3.1, 3.5). The densest concentration of impressions is in the easternmost 60 m (Figure 3.1A). Penetration is commonly at an angle into the substrate, with impressions ringed or surrounded by symmetric to asymmetric mounds.

The survey records 473 impressions in 10 plots totaling 40 m<sup>2</sup> (Table 3.1). An average density of 12 impressions/m<sup>2</sup> is calculated. Roughly one-third (152) of the impressions are rimmed by lithified soft-sediment mounds of upturned sand (Figure 3.1F, 3.5F, H). Mounds average 4 cm wide and 2 cm tall. Fine-scale soft sediment

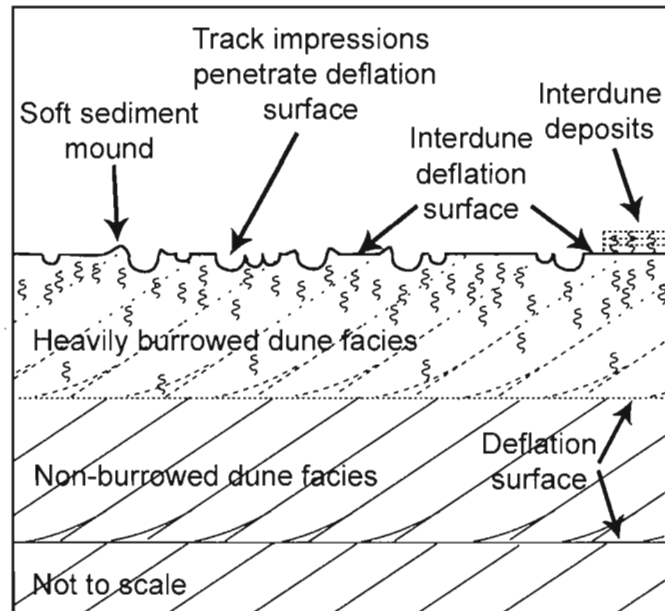


Figure 3.4. Schematic of the Top Rock trample surface. Impressions penetrate the wetted interdune deflation surface of a heavily burrowed eolian dune. Interdune deposits directly overly the trampled deflation surface. Burrowing increases upwards in the bioturbated dune.



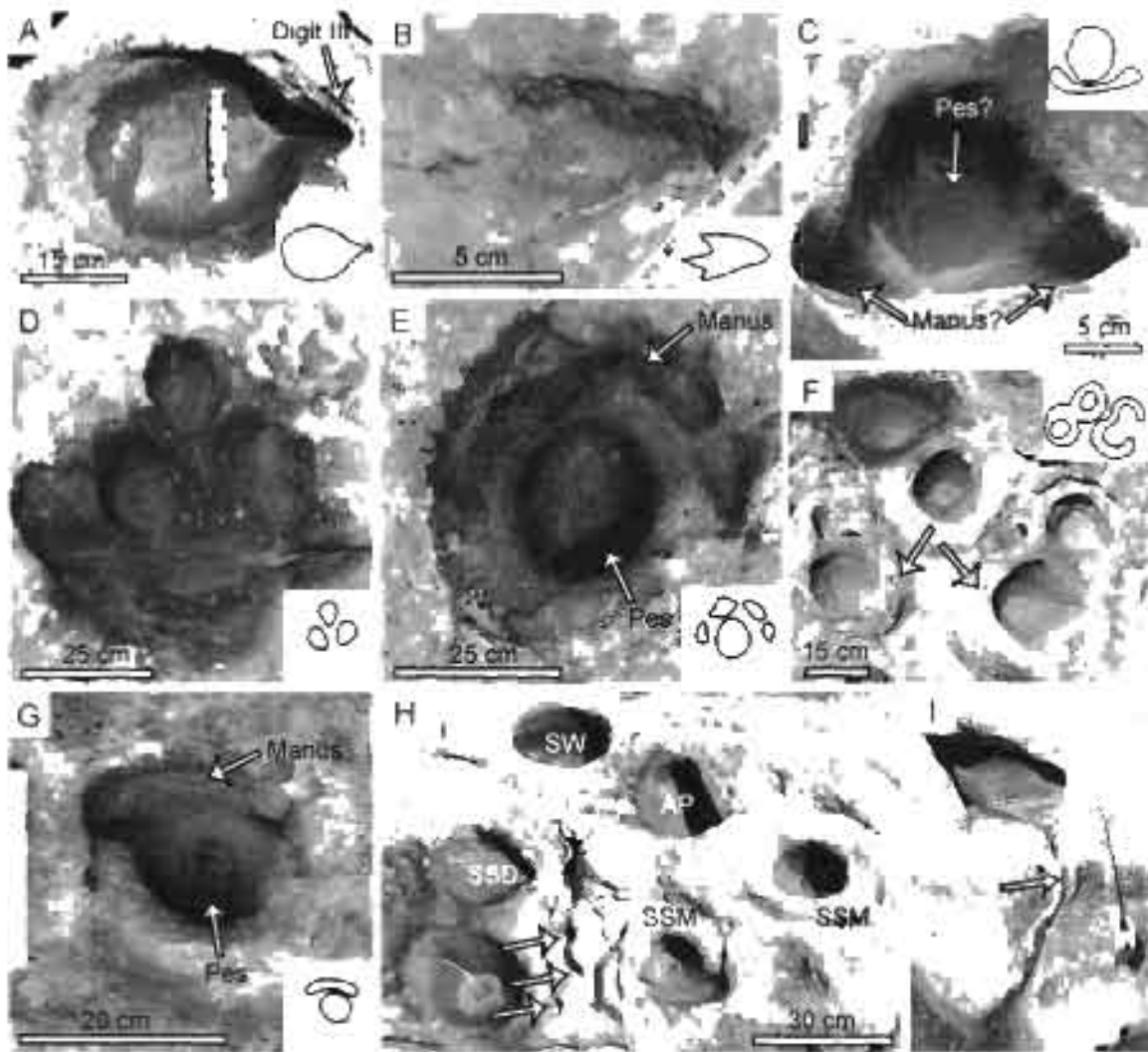


Figure 3.5. Representative tracks and impressions - specified as length x width x depth (where known). Inset diagram interpreted features. A) Ovate print 42 x 29 x 11.5 cm. Mound 3 cm wide x 2 cm tall. Digit III deformation (arrow) 8 cm long. B) Grallator track 11 x 5.5 x 2.5 cm. C) Possible Sauropodomorph track 18 x 20.5 x 12 cm. Note preservation of fine-scale soft-sediment deformation at distal edges of manus. D) Eubrontes print ~42 x ~38 cm. E) Sauropodomorph track 36 x 44 cm. The ovate pes is 23 cm x 20 cm and is imprinted significantly deeper than manus. F) Tracks displaying asymmetric soft-sediment mounds. Inset diagrams the soft sediment mound configuration. G) Sauropodomorph, 15 x 18 cm displaying manus, pes, and asymmetric mound. H) Well-developed primary structures that distinguish the tracks. SW = steep walled; AP = angular penetration; SSM = soft sediment mound, SSD = soft sediment mound at digit tip; arrows point to possible toe impressions. I) Rivulet channel (arrow) drains from higher (top) to lower (bottom) impression.

Table 3.1

## Trample Surface Data from Ten Plots

	Plot 1	Plot 2	Plot 3	Plot 4	Plot 5	Plot 6	Plot 7	Plot 8	Plot 9	Plot 10	Total
Impressions	43	34	67	50	80	20	61	34	66	18	473
Circular	38	21	38	18	13	1	11	6	10	2	158
Ovate	0	4	10	10	29	13	33	20	33	12	164
Elongate	0	0	0	3	17	2	4	3	9	1	39
Irregular	5	9	19	19	21	4	13	4	13	1	108
Tails	0	0	0	0	0	0	0	1	1	2	4
Mounds	6	14	20	20	29	5	19	12	22	5	152
Overprints	21	0	5	3	15	1	7	2	5	1	60
Oriented	8	7	9	7	10	7	8	3	10	2	71
Tridactyl	5	2	3	4	5	1	6	2	5	0	33
Ovate with digit III	0	3	4	0	5	1	3	2	4	4	26
Sauropodomorph	0	0	2	2	2	0	1	0	0	0	7
Total with definitive print morphology	5	5	9	6	12	2	10	4	9	4	66

Plots correspond to those shown in Figure 3.2.

deformation is typically noted at the tip of asymmetric impressions (Figure 3.5A). Where impressions penetrate the substrate at an angle, mounds are commonly best developed along the leading edge of penetration. Sixty-two impressions exhibit overprinting.

Impressions have an average length of 18.5 cm, with a range spanning from 1.5 - 140 cm. In several instances, impressions larger than 100 cm are likely the combination or merging of two imprints. Average impression depth is 4.9 cm with a range between 0.5 cm and 30 cm. Impressions possess both sloped and flat bases. Average mound width is 4.2 cm (ranging between 1 - 18 cm); mean mound height is 2.2 cm (ranging between 0.5 - 11 cm). Seventy-one impressions provide a penetration orientation primarily to the west-southwest (Figure 3.6).

Elongate, curvilinear traces up to 7.3 m in length and rimmed by parallel, soft sediment mounds were noted at several locations within the trample surface. The impressions display a mildly sinuous course, with the most easily distinguishable specimen (Figure 3.1D, E) in the southwest extent of the trample surface. These elongate impressions are 6 cm wide. Their displaced, soft sediment mounds stand 10 cm wide by 3-4 cm tall.

### Interpretations

#### Track Occurrence and Preservation

The impressions are interpreted as dinosaur tracks due to several important and distinguishing criteria that follow those of Martinell et al. (2001):

1. 66 (14%) of the impressions possess identifiable foot morphologies.

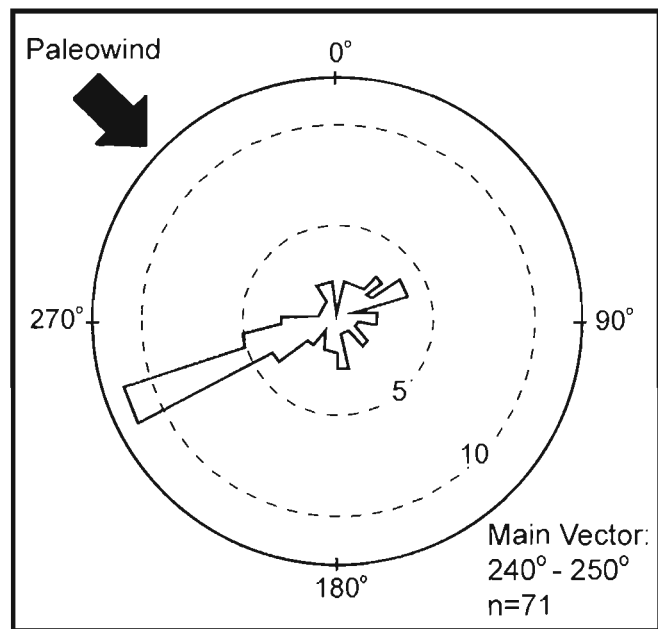


Figure 3.6. Southwest track orientation showing direction of travel perpendicular to northwesterly paleowind.

2. Thirty-two percent of impressions (152) show primary plastic sediment deformation features formed prior to lithification—fine, cm-scale deformation mounds rimming impressions and observed at digit tips (Figure 3.5A, G).

3. Asymmetric soft sediment mounds and penetration angles indicate a clear direction of west-southwest travel (Figure 3.6).

4. Thirteen percent of the impressions (61) display overprinting.

5. The impressions are constrained within one major bed.

6. Other documented dinosaur tracks occur in the same area (Loope, 2006).

The disturbed bedding plane surface is herein interpreted as a trample surface that was tracked by numerous footprint impressions made while the sediment was soft. Further justification for the trample surface is given in the discussion section.

The preservation of small (<5cm) prints along with larger prints indicates the impressions are true tracks as opposed to undertracks; the smaller trace maker would have insufficient mass to deform underlying beds. Additionally, well preserved mounds and fine scale deformation surrounding the end of track digits (Figure 3.5A, F, H) implies that little denudation has occurred to the trample surface (Lockley, 1986). Based on the scale of Lockley and Conrad (1989), the trample surface displays moderate dinoturbation. The high density and abundance of impressions of various sizes (2 cm - >50 cm) allows for the likelihood that all impressions (particularly the smaller ones) may not be individual footprints (i.e., some may be partial toe imprints or sediment splatters associated with foot removal from the substrate). However, all impressions are related to the same track-forming episode.

### Three Distinct Ichnogenera

Impressions are assigned to three distinct ichnogenera—*Eubrontes*, *Anchisauripus*, *Grallator*—and to an unidentified sauropodomorph (J. Kirkland, personal communication, 2006); others may be discovered in the trample surface (Figure 3.5). *Grallator*, *Anchisauripus*, and *Eubrontes* tracks are common in the Navajo Sandstone and are identified as bipedal, tridactyl impressions with less than 40° divarication between digits II and IV (Hitchcock, 1845, 1858; Rainforth, 1997; Olsen et al., 1998; Irmis, 2005). *Grallator* impressions (Figures 3.1D, 3.2D) are less than 18 cm long, *Anchisauripus* are between 18 - 25 cm long, and *Eubrontes* tracks (Figure 3.5B) are classified when greater than 25cm (Rainforth, 1997). Thirty-three tracks were assigned to these ichnospecies (Tables 3.2, 3.3). In each case, digits are well defined, typically with clear pads and claw marks. In this study, impressions are assigned to either *Grallator*, *Anchisauripus*, or *Eubrontes* based on their known occurrence and documented characteristics in Navajo Sandstone, tridactyl character, low divarication angle, and dimension.

Tracks displaying manus and pes impressions (Figure 3.5C, E, G), hold closest affinity to sauropod tracks, but possess notable differences and are thus assigned to a sauropodomorph. The impressions share the sauropod characteristic U-shaped manus with a sub-circular pes overprinted atop the manus (Table 3.4) (Wilson and Carrano, 1999). The interpreted sauropodomorph tracks are quadrupedal with both manus and pes impressions visible. Two basic morphologies can be described, one in which the manus displays four toe or claw impressions (Figure 3.5E), and the second in which individual toes/claws are not clearly defined in the manus (Figure 3.5C, G). In both cases, the pes is

Table 3.2

Tridactyl Impressions Identified From Plots in Table 3.1

Ichnospecies		Length	Width	Depth	Mound Width	Mound Height
<i>Grallator</i> n=20	Average	10.3	8.8	3.0	3.4	1.6
	Range	5 to 17	4.5 to 17	1 to 10	1.5 to 9	0.5 to 4
<i>Anchisauripus</i> n=3	Average	21.0	18.3	6.5	1.5	1.0
	Range	20 to 23	15 to 24	3.5 to 11	1.5	1.0
<i>Eubrontes</i> n=10	Average	41.6	34.9	7.5	3.3	2.6
	Range	25 to 78	10 to 78	3 to 15	1.5 to 5	1 to 6
All measurements in cm.						

Table 3.3

Ovate Impressions with Clear Middle (III) Impressions Identified From Plots in Table 3.1

Ichnospecies		Length	Width	Depth	Mound Width	Mound Height
<i>Grallator</i> n=6	Average	13.0	8.8	6.4	1.8	1.0
	Range	6 to 17	6 to 13	4 to 10.5	1 to 2.5	0.5 to 1.5
<i>Anchisauripus</i> n=7	Average	21.5	17.1	6.5	4.4	2.2
	Range	19 to 23	14 to 23	5 to 8	2.5 to 9	1 to 3
<i>Eubrontes</i> n=13	Average	35.9	24.3	10.0	4.6	1.7
	Range	25 to 52	18 to 39	6 to 20	2.5 to 8	1 to 2.5

All measurements in cm.



Table 3.4

## Sauropodomorph Impressions

	Pes Length	Pes Width	Pes Depth	Manus Length	Manus Width	Manus Depth
Small Sauropodomorph Impressions				n=6		
Average	14.3	12.8	8.0	20.9	3.7	4.9
Range	12 to 16	10 to 15	4 to 12	20 to 24	3 to 5	2 to 12
Large Sauropodomorph Impressions				n=4		
Average	24.3	18.5	5.5	33.5	7.5	3.3
Range	23 to 27	14 to 23	4 to 6.5	28 to 44	5 to 10	2.75 to 4
Overall Sauropodomorph Impressions				n=10		
Average	19.3	15.6	6.5	26.0	5.2	4.2
Range	12 to 27	10 to 23	4 to 12	20 to 44	3 to 10	2 to 12

Three distinct, well-preserved sauropodomorph impressions (2 small, 1 large) that occur adjacent to, but outside of measured plots, were included in this characterization. All measurements in cm.

ovate and symmetrical along its short and long axes. Generally, sauropods show pes impressions that are larger than manus, however the specimens observed at Top Rock show an ovate pes that is significantly smaller than the manus (J. Kirkland, personal communication, 2006). This direct registry of manus and pes prints at various scales (Figure 3.5C, E, G) may indicate trace-makers of the same genera at different ages. These sauropodomorph impressions require further study and formal description.

Another common morphology is an ovate impression with a clear, middle (III) claw deforming the sand (Figure 3.5A and Tables 3.2, 3.3). In some cases, marks corresponding with digit II and IV occur on the walls of the ovate impressions. These are interpreted as a tridactyl prints that have lost all but the distinct trace of the longest digit during trace making or preservation.

### Tail Drag Impressions

Elongate, curvilinear impressions extend up to 7.3 m and are rimmed along their length by parallel soft sediment mounds. These impressions are interpreted as the tail drags of a quadruped dinosaur based on their occurrence along the trampled surface in association with other dinosaur footprints. In areas of high impression density, it was not possible to assign individual, footprint-type impressions to the tail drags. However in an area of lower track density at the southwestern portion of the trampled surface, individual quadruped tracks straddle the elongate impression (Figure 3.1D, E). This tail drag mark extends for ~4 m, is 6 cm wide and 1.5 cm deep. Soft-sediment mounds are present along the impression's length on both sides. Associated quadruped footprints are circular, averaging 7.7 cm in diameter, and comparatively shallow, only 1-2 cm deep.

Track width is ~0.4 m; track gait is ~0.5 m. Since tail drag impressions are rarely preserved (Irby and Albright, 2002), their presence makes the Top Rock trample surface all the more unique.

### Track Size Distribution

Tracks do not yield clear and distinct size groupings, but rather show a gradational transition from small to large (Tables 3.2, 3.3). This can be attributed to five factors: (1) the presence of species of roughly overlapping size (distinct foot impressions imply the existence of at least four different species); (2) the presence of juvenile to adult individuals of a particular species; (3) preservation method; (4) partial footprint impression; and (5) a combination of the above. Regardless, numerous ichnogenera and print sizes in the interdune shows that a diversity of taxa was supported within the Navajo erg.

Some discussion has been made over whether tracks of a particular size can be generalized to a certain depositional facies (small tracks constrained to crossbedded dune foresets; large tracks constrained to interdune deposits) or whether such occurrence is merely a bias in preservation (Rainforth, 1997; Irmis, 2005). In this case, tracks of both large and small fauna are preserved in the interdune setting. The abundance of both large and small tracks indicates that, at the least, the habitat of small track bearing organisms (i.e., *Grallator* trace makers) extended from crossbedded, dune sands, into an interdune setting occupied with large track producing animals. Thus, the Top Rock trample surface supports that correlating track sizes to eolian facies reflects a bias in preservation.

## Discussion

### A Vertebrate Origin vs. Alternate Interpretations

The Top Rock trample surface is a bedding surface modified by large vertebrates (dinosaurs) to produce tracks that are weathered to expose the original, steep-walled, footprint impressions. The impressions are not merely an exposure of modern weathering pits or potholes because of their distinct geometry, morphology, and their relationship to syndepositional soft-sediment deformed laminae. Potholes, or weathering pits, are relatively recent surficial features generally occurring as broad, shallow, flat-bottomed depressions on flat to gently sloping outcrops (Netoff et al., 1995). Chan and others (2005) identify pothole occurrence along three genetic surfaces: (1) at the exposed top of a formation; (2) on exposed regional supersurfaces (Kocurek, 1996); and (3) on exposed first-order eolian bounding surfaces, where interdune deposits are common. Netoff and others (1995) identify physical, chemical, and biological forces that account for pothole formation. These include water and wind dependent weathering, granular disintegration induced by mineral crystallization, clay desiccation and hydration, freeze and thaw cycles, carbonation, dissolution, hydrolysis, and biological activity. Potholes and pits have gently sloping borders when located on open surfaces, where bedding lacks joints and regular water flow. By any account, potholes are weathering features that post-date deposition and develop after a substrate has been lithified.

In contrast to potholes or weathering pits, the impressions at the Top Rock surface are distinct in seven regards (Figure 3.5F): (1) impression floors are rarely flat and are typically oriented at an angle into the sandstone; (2) the impressions are steep-sided but lack the hydraulic mechanism or abrading tool required for carving steep-sided potholes;

(3) well-formed lichens on impression walls suggest the features are not being actively scoured; (4) imprint population density far exceeds that of potholes; (5) impressions are superimposed and do not display the self-organized, nearest-neighbor type spacing common of weathering pits (Chan et al., 2005); (6) repeated impression morphologies occur that would be anomalous in a weathering regime (but are consistent with a vertebrate origin); and (7) most importantly, many impressions (32%) are surrounded by symmetric to asymmetric mounds of soft-sediment deformation, penecontemporaneous with impression formation. Minor, modern weathering with water accumulation and black bacterial mats is superimposed on the trample surface simply because it is exposed and the depressions act as catchments. However, it is clear that the origin of impressions is distinctly primary (syndepositional) and that they are not simply a modern weathering phenomenon.

A key to the track interpretations are the soft sediment mounds related to the impressions that indicate these are primary and syndepositional features and not modern, late-stage, surficial weathering phenomena. The vertical relief and asymmetric character of the mounds suggest they were formed by the angular penetration of an object and the displacement of adjacent sand. Based on cross-cutting relationships and similarities between impressions with soft-sediment mounds and those without, impressions lacking mounds are considered to be original, soft-sediment features. Although some modern potholes occur in a few scattered areas and on different exposure surfaces at the Coyote Buttes, the widespread occurrence and concentration of soft-sediment mounds surrounding asymmetric impressions—specific to this one interdune bed—argues for a Jurassic, vertebrate origin of the Top Rock trample surface.

Other possible symsedimentary processes leading to the formation of the impressions could include burrowing or some type of dewatering event. However, the impressions lack burrow structures such as burrow lining, branching, or tiering. Likewise, the surface does not display any vertical pillar structures expected from a symsedimentary, dewatering origin.

### Paleobiologic Implications

Winkler et al. (1991) suggests that the existence of both body and trace fossils at numerous interdune deposits in the Navajo Sandstone supports the presence of a well-developed food chain requiring significant time for establishment. The food web implied by the abundant and varied interdune track types at Top Rock speaks to the long-lived nature of interdunes in the Navajo erg. The resources required to support a complex food web of large organisms implies that interdunes did not exist in ecologic isolation of one another. Organisms may have traveled significant distances through the erg between interdunes.

The orientation of tracks (Figure 3.6) to the west-southwest ( $240^{\circ}$  -  $250^{\circ}$ ) lies perpendicular to the predominant northwest paleowind (Parrish and Petersen, 1988; Chan and Archer, 2000; Loope et al., 2001) and parallel to dune crests (striking  $39^{\circ}$ ). This implies that travel through the trample surface was directed by the orientation of surrounding dunes. Subordinate orientations may indicate wandering within the interdune area or behavioral dynamics.

Finally, dinosaur tracks in the Navajo Sandstone are significantly more abundant than body fossils, which are rarely preserved if not entirely absent (Irmis, 2005; D.D.

Gillette, personal communication, 2007). Gillette (2007) further asserts that little is known of dinosaurs in North America until later in the Mesozoic when a diversity of megafauna suddenly appears in the Late Jurassic Morrison Formation (Winkler et al., 1991). The discovery of the Top Rock trample surface may extend a window to species distribution and dynamics deeper into the Early Jurassic.

### Paleoclimatic Implications

Although the Navajo Sandstone records predominantly arid conditions, the Top Rock trample surface's well-defined angular penetrations and mounded soft-sediment deformation (Figures 3.1F, 3.5H) argue for the existence of a wet interdune paleoenvironment. Any tracks penetrating dry interdune sands would have collapsed upon foot extraction. It is reasonable to expect that the reworking of dry sand by wind would erase the majority of any dry mounds surrounding print impressions.

The deposits of three long-lived pluvial periods have been described at the Coyote Buttes (Loope and Rowe 2003; Loope 2006). The lowermost interdune deposit measured in this study (0 - 7 m, Figure 3.3), likely corresponds to pluvial episode 2 of Loope and Rowe (2003). The middle interdune deposit (61 - 66 m), in which the trample surface is located, likely matches pluvial episode 3 (Loope, 2006, Figure 1). A final, small exposure at the top of the measured section (107 - 108 m) may signal a fourth pluvial episode. Pluvial episodes associated with interdune deposits indicate large climatic shifts were present during the Jurassic in the Navajo erg—a time when terrestrial and marine sedimentary and fossil data suggests that there was a uniform climate throughout the continents during the Jurassic (Schaeffer, 1970; Hallam, 1993).

A change to a wetter climate may have allowed water table recharge to interdunes via local flow cells (Loope and Rowe, 2003). Given the high porosity of eolian sand, it is also reasonable to expect that precipitation into an interdune would quickly infiltrate unless the water table was present subaerially. In one track, a small trough leading to a lower impression (Figure 3.5I) indicates the active draining of water from the higher print—possibly as the animal’s weight exuded interstitial water from the sand. Variations in impression depth may also be linked to sediment water content and track density. Where track density is greater, impressions are deeper, possibly due to the progressive liquefaction of the sediment with increased trampling. Following Lockley’s (1986) assertion that a direct relationship exists between track depth and sediment water content for animals of a given weight in a homogeneous substrate (provided the clean quartz arenite), it is reasonable to expect that future modeling may yield accurate estimations of both the organism’s size and weight, and the interdune’s water content. This relationship may further be elaborated upon through the examination of the soft-sediment mounds surrounding impressions.

### Dinoturbation as a Mechanism for Convolute Bedding

Navajo Sandstone at the Coyote Buttes displays many areas of convolute bedding (in places exceeding 10 m thick); the trample surface offers an explanation for bedding convolution at the smaller, submeter to meter scale. Convolute bedding and soft-sediment deformation in the Navajo can be extensive and has been attributed to factors including earthquake liquefaction, a fluctuating groundwater table, gravity flow, and current shear (e.g., Doe and Dott, 1980; Horowitz, 1982; Bryant, 2003; Loope and Rowe,



2003; Bryant et al., 2006). Bedding convolutions caused by dinosaur tracks would be more localized and at a much smaller scale. Although individually defined tracks may not be visible in an oblique view of smaller deformed beds at the Coyote Buttes, the density, size and spacing of convolutions approximates that of trample surface tracks. Provided that dinosaur tracks are a possible cause for small-scale convolutions, the track record in the Navajo Sandstone may be much more numerous than previously acknowledged. Linking sub-meter to meter scale convolutions to biologic trace-makers significantly increases the potential for identifying large megafauna traces and migration pathways during the Early Jurassic at the Coyote Buttes.

This initial survey documents the presence of a unique, wet interdune trample surface. Future aerial mapping and modeling analyses could also yield accurate estimations of animal size and behavior while assisting in distinguishing individual trackways amongst the high concentration of prints. With this in mind, the trample surface is a valuable tool for elucidating detailed paleobiologic, paleohydrologic, and paleoclimatic proxies for the Jurassic of the Western Interior.

### Conclusions

An unusual ~1 m thick surface showing extensive (> 1000), steep walled impressions linked with soft sediment deformation occurs in an interdune interval of the Jurassic Navajo Sandstone at the Coyote Buttes along the Arizona/Utah border. This distinctive bed is interpreted to preserve a trample surface created by dinosaurs that visited the wetted eolian site. The repeated foot morphologies, evidence of overprinting, angular penetration, west-southwest alignment, abundance of plastic sediment

deformation features (raised rims surrounding impressions and deformation at digit tips), and impression density argue convincingly for a dinosaur origin of the surface. This dinosaur trample surface at the Coyote Buttes is unusual in exhibiting a combination of multiple overlapping track types and sizes, striking footprint features including claws and toes, high track density and rare tail drag marks. Patterns of at least three ichnogenera are present including *Eubrontes*, *Anchisauripus*, *Grallator*, and the tracks of a sauropodomorph.

The well-preserved tracks of the Top Rock trample surface provide several important paleobiology, paleohydrology, and paleoclimate proxies: (1) the dinoturbation is a mechanism for producing sub-meter to meter scale convolute bedding in moist Navajo Sandstone; (2) the southwestern margin of this Jurassic paleodesert provided sufficient resources to support a diverse population of megafauna; and (3) the trample surface provides additional evidence of a pluvial climate episode, during which shallow groundwater flowed into interdune areas.

Finally, the Coyote Buttes area holds significant scientific educational and aesthetic value for resource management. The remarkable cyclic eolian stratification accentuated by vivid diagenetic coloration, a gracefully scoured landscape, and the record of important dinosaur occupation distinguish the Coyote Buttes from many other Navajo Sandstone locales across the Colorado Plateau.

#### Acknowledgments

We gratefully acknowledge John R. Bowman, William T. Parry, Erich U. Petersen, Anthony A. Ekdale, Jessica Allen and Sally Potter at the University of Utah, as

well as Jim Kirkland at the Utah Geological Survey for their input to this study. The Vermilion Cliffs National Monument administration as well Rody Cox and Mike Salamacha at the Bureau of Land Management provided valuable logistical and permitting assistance. Thanks to Brian Parnham and Sara Hanner for help in the field and to David Gillette and Loïc Costeur for critical review of the manuscript.

### References

- BLAKEY, R.C., 2001, Paleogeography through geologic time, updated June 10, 2002, [http://jan.ucc.nau.edu/~rcb7/global\\_history.html](http://jan.ucc.nau.edu/~rcb7/global_history.html). Checked December, 2006.
- BLAKEY, R.C., PETERSON, F., AND KOCUREK, G., 1988, Synthesis of Late Paleozoic and Mesozoic eolian deposits of the Western Interior of the United States, *in* Kocurek, G., ed., Late Paleozoic and Mesozoic Aeolian Deposits of the Western Interior of the United States: Sedimentary Geology, v. 56, p. 3-125.
- BRYANT, G.C., 2003, Intradunal deformation features from the Jurassic Navajo Sandstone: Geological Society of America Abstracts with Programs, v. 35, p. 601.
- BRYANT, G.C., MONEGATO, G., AND MIAL, A.D., 2006, Soft-sediment deformation and dune dynamics in the Jurassic Navajo erg: Geological Society of America Abstracts with Programs, v. 38, p. 145.
- CHAN, M.A., AND ARCHER, A.W., 2000, Cyclic eolian stratification on the Jurassic Navajo Sandstone, Zion National Park; periodicities and implications for paleoclimate, *in* Sprinkel, D.A., Chidsey, T.A., Jr., and Anderson, P.B., eds., Geology of Utah's Parks and Monuments, Utah Geological Association, Publication 28, p. 606-617.
- CHAN, M.A., MOSER, K., DAVIS, J.M., SOUTHAM, G., HUGHES, K., AND GRAHAM, T. 2005, Desert potholes: ephemeral aquatic microsystems: Aquatic Geochemistry, v. 11, p. 279-302.
- CHAN, M.A., PARRY, W. T., AND BOWMAN, J. R., 2000, Diagenetic hematite and manganese oxides and fault-related fluid flow in Jurassic sandstones, southeastern Utah: AAPG Bulletin, v. 84, p. 1281-1310 (with cover photo on v. 84).
- CLARK, J.M. AND FASTOVSKY, D.E., 1986, Vertebrate biostratigraphy of the Glen Canyon Group in northern Arizona, *in* Padian, K. ed., The Beginning of the Age

- of Dinosaurs: Faunal Changes Across the Triassic-Jurassic Boundary: Cambridge University Press, New York, p. 285-301.
- DOE, T.W., AND DOTT, R.H., JR., 1980, Genetic significance of deformed cross bedding with examples from the Navajo and Weber sandstones of Utah: *Journal of Sedimentary Petrology*, v. 50, p. 793-812.
- EISENBERG, L., 2003, Giant stromatolites and a supersurfaces in the Navajo Sandstone, Capitol Reef National Park, Utah: *Geology*, v. 31, p. 111-114.
- FAUL, H. AND ROBERTS, W.A. 1951, New fossil footprints from the Navajo(?) Sandstone of Colorado: *Journal of Paleontology*, v. 25, p. 266-274.
- GILLETTE, D.D., 2007, Personal communication, 1 February.
- HALLAM, A., 1993, Jurassic climates as inferred from the sedimentary and fossil record: *Philosophical Transactions of the Royal Society of London B*, v. 341, p. 287-296.
- HAMBLIN, A.H. AND FOSTER, J.R. 2000, Ancient animal footprints and traces in the Grand Staircase-Escalante National Monument, south-central Utah, *in* Sprinkel, D.A., Chidsey, T.A., Jr., and Anderson, P.B., eds., *Geology of Utah's Parks and Monuments*, Utah Geological Association, Publication 28, p. 557-568.
- HITCHCOCK, E.H. 1845, An attempt to name, classify, and describe the animals that made the fossil footmarks of New England: *Proceedings of the 6<sup>th</sup> Annual Meeting of the Association of American Geologists and Naturalists*, New Haven, Connecticut, v. 6, p. 23-25.
- HITCHCOCK, E.H. 1858, *Ichnology of New England, A Report on the Sandstone of the Connecticut Valley, Especially its Fossil Footprints*: Boston, William White, 220 p.
- HOROWITZ, D.H., 1982, Geometry and origin of large-scale deformation structures in some ancient wind-blown sand deposits: *Sedimentology*, v. 29, p. 155-180.
- IRBY, G.V. AND ALBRIGHT III, L.B. 2002, Tail-drag marks and dinosaur footprints from the Upper Cretaceous Toreva Formation, northeastern Arizona: *Palaaios*, v. 17, p. 516-521.
- IRMIS, R.B., 2005, A review of the vertebrate fauna of the Lower Jurassic Navajo Sandstone in Arizona, *in* McCord, R.D. eds., *Vertebrate Paleontology of Arizona*, Mesa Southwest Museum, Bulletin 11, p. 55-71.
- KIRKLAND, J., 2006, Personal communication, Utah Geological Survey, 6 December.

- KOCUREK, G., 1996, Desert eolian systems, *in* Reading, H.G. ed., *Sedimentary Environments: Processes, Facies, and Stratigraphy*, Oxford, Blackwell Science, p.125-153.
- KOCUREK, G., 2003, Limits on extreme eolian systems; Sahara of Mauritania and Jurassic Navajo Sandstone examples, *in* Chan, M.A., and Archer, A., eds., *Extreme depositional environments; mega end members in geologic time*, Geological Society of America, Special Paper 370, p. 43-52.
- KOCUREK, G., AND DOTT, R.H., JR., 1983, Jurassic paleogeography and paleoclimate of the central and southern Rocky Mountains regions, *in* Reynolds, M.W., and Dolly, E.D., eds., *Mesozoic Paleogeography of the West-Central United States*, SEPM, Rocky Mountain Section, Rocky Mountain Paleogeography Symposium 2, p. 101-116.
- LOCKLEY, M.G., 1986, The paleobiological and paleoenvironmental importance of dinosaur footprints: *Palaios*, v. 1, p. 37-47.
- LOCKLEY, M.G., 1998, The vertebrate track record: *Nature*, v. 369, p. 429-432.
- LOCKLEY, M.G., AND CONRAD, K., 1989, The paleoenvironmental context, preservation and paleoecological significance of dinosaur tracksites in the Western USA, *in* Gillette, D.D., and Lockley, M.G., eds., *Dinosaur Tracks and Traces*: Cambridge Massachusetts, Cambridge University Press, p. 121-134.
- LOCKLEY, M.G., HOUCK, K.J., AND PRINCE, N.K., 1986, North America's largest dinosaur trackway site: implications for Morrison Formation paleoecology: *GSA Bulletin*, v. 97, p. 1163-1176.
- LOOPE, D.B., 2006, Dry-season tracks in dinosaur-triggered grainflows: *Palaios*, v. 21, p. 132-142.
- LOOPE, D.B., AND ROWE, C.M., 2003, Long-lived pluvial episodes during deposition of the Navajo Sandstone: *Journal of Geology*, v. 111, p. 223-232.
- LOOPE, D.B., ROWE, C.M., AND JOECKEL, R.M., 2001, Annual monsoon rains recorded by Jurassic dunes: *Nature*, v. 412, p. 64-66.
- LOOPE, D.B., SEILER, W.M., MASON, J.A., AND CHAN, M.A., 2008, Wind scour of Navajo Sandstone at the Wave (central Colorado Plateau, U.S.A.): *Journal of Geology*, v. 116, p. 173-183.
- LOOPE, D.B., STEINER, M.B., ROWE, C.M., AND LANCASTER, N., 2004, Tropical westerlies over Pangaeian sand seas: *Sedimentology*, v. 51, p. 315-322.

- MARTINELL, J., DE GIBERT, J.M., DOMENECH, R., EKDALE, A.A., AND STEEN, P.P., 2001, Cretaceous ray traces? An alternative interpretation for the alleged dinosaur tracks of La Posa, Isona, NE Spain: *Palaaios*, v. 16, p. 409-416.
- NETOFF, D.I., COOPER, B.J. AND SHROBA, R.R. 1995, Giant sandstone weathering pits near Cookie Jar Butte, southeastern Utah, *in* Riper, C. ed., *Proceeding of the Second Biennial Conference on Research in Colorado Plateau National Parks: Transactions and Proceeding Series NPS/NRNAU/NRTIP-95-11*, US Department of the Interior, National Park Service, p. 25-53.
- OLSEN, P.E. AND GALTON, P.M., 1977, Triassic-Jurassic tetrapod extinctions: are they real?: *Science*, v. 197, p. 983-986.
- OLSEN, P.E., SMITH, J.B., AND McDONALD, N.G. 1998, Type material of the type species of the classic theropod footprint genera *Eubrontes*, *Anchisauripus*, and *Grallator* (Early Jurassic, Hartford and Deerfield basins, Connecticut and Massachusetts, U.S.A.): *Journal of Vertebrate Paleontology*, v. 18, p. 586-601.
- PARRISH, J.T., 1993, Climate of the supercontinent Pangea: *Journal of Geology*, v. 101, p. 215-233.
- PARRISH, J.T., AND PETERSON, F., 1988, Wind directions predicted from global circulation models and wind directions determined from eolian sandstones of the western United States – a comparison: *Sedimentary Geology*, v. 56, p. 261-282.
- PETERSON, F., 1988, Pennsylvanian to Jurassic eolian transportation systems in the western United States: *Sedimentary Geology*, v. 56, p. 207-260.
- RAINFORTH, E.C., 1997, Vertebrate ichnological diversity and census studies, Lower Jurassic Navajo Sandstone: Unpublished M.S. thesis, University of Colorado at Boulder, 48 p.
- SAMPSON, P.J., 1992, Sedimentology of the Navajo Sandstone, southern Utah, USA: Unpublished Ph.D. dissertation, University of Oxford, 291 p.
- SCHAEFFER, B., 1970, Mesozoic fishes and climate: *Proceedings of the North American Paleontological Convention Part D*, September 1969, Chicago, p. 376-388.
- VERLANDER, J.E., 1995, Basin-scale stratigraphy of the Navajo Sandstone: southern Utah, U.S.A.: Unpublished Ph.D. dissertation, University of Oxford, 159 p.
- WILSON, J.A. AND CARRANO, M.T. 1999, Titanosaur and the origin of “wide-gauge” trackways: a biomechanical and systematic perspective on Sauropod locomotion: *Paleobiology*, v. 25, p. 252-267.

WINKLER, D.A., JACOBS, L.L., CONGLETON, J.D., AND DOWNS, W.R., 1991, Life in a sand sea: biota from Jurassic interdunes: *Geology*, v. 19, p. 889-892.

## CHAPTER 4

# HEMATITE “MICROBERRY” WIND RIPPLES: EOLIAN CONDITIONS FOR A TERRESTRIAL MARTIAN ANALOG FROM THE JURASSIC NAVAJO SANDSTONE, UTAH-ARIZONA

Published in 38<sup>th</sup> Lunar and Planetary Science Conference  
(XXXVIII), 2007, Contribution No. 2076, p. 2076-2077.

Winston M. Seiler, Marjorie A. Chan, and Robert J. Sullivan<sup>1</sup>

<sup>1</sup>Department of Astronomy, Cornell University

### Abstract

Small iron oxide cemented micro-concretions within the Jurassic Navajo Sandstone at the Coyote Buttes area of the Vermilion Cliffs National Monument are useful terrestrial analogs to similar features on Mars. These micro-concretions are numerous within Liesegang band reaction fronts formed by diffusion. Weathering releases the micro-concretions from the host rock. These well-cemented spherules are typically 1.5 mm in diameter with an average mass of 0.0056 g.

In localized depressions and alcoves where winds are strong or funneled, the micro-concretions are arranged into transient ripples with an average ripple index of 18.



Similar coarse-grained ripple trains of micro-concretions (“microberries”) have been imaged by the NASA Mars Exploration Rover Opportunity at Meridiani Planum. Strong Martian winds have released the “microberries” from the host rock to create accumulation lags that are reworked at the surface. These terrestrial analogs may be useful to scale and compare to the “microberry” examples to better understand both geologic and atmospheric conditions on Mars where present day ripples appear inactive.

### Introduction

A unique set of conditions produces complex coarse-grained wind ripples that include tiny, iron oxide micro-concretions from eolian Jurassic Navajo Sandstone of the Coyote Buttes area within Vermillion Cliffs at the Utah-Arizona border. Although the micro-concretions occur in many Navajo Sandstone exposures, this local site has the convergence of: contrasting physical conditions between well-cemented concretions and weakly cemented host rock; weathering processes to release the concretions from the host rock; and sufficient wind to concentrate, accumulate, and work the concretions into ripple forms (Figure 4.1). Terrestrial concretions are already established as analogs to the hematite-enriched spherules (blueberries) on Mars (Catling, 2004; Chan et al., 2004, 2005; Ormö et al., 2004), but this special occurrence also shows remarkable morphologic resemblance to wind-blown regolith at Meridiani Planum (Figure 4.2).

### Observations and Results

Micro-concretions typically form by diffusion and where they are well cemented, they can weather out of chemical reaction fronts as discrete solid spherules (Figure 4.3),

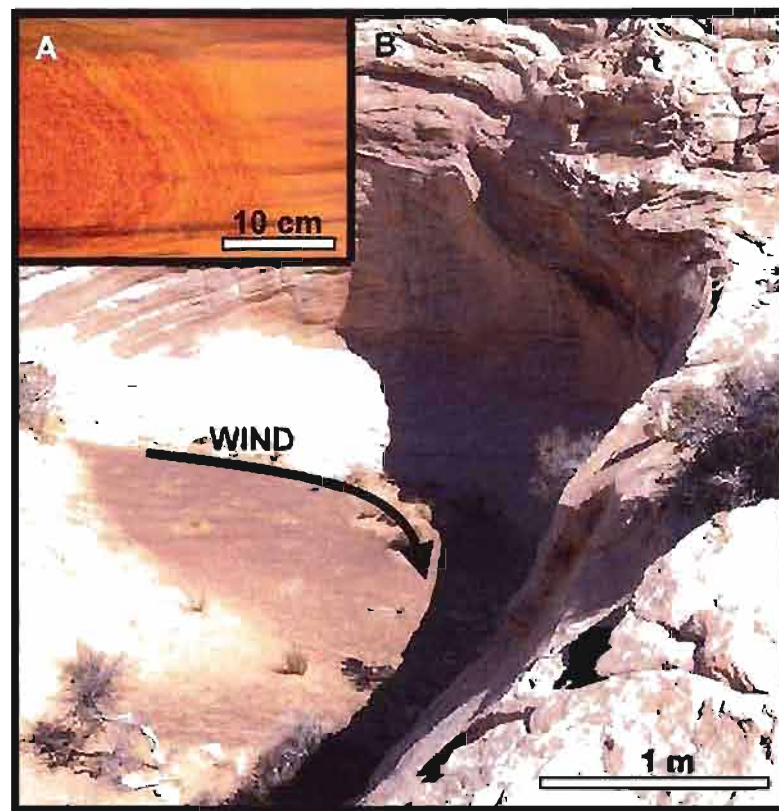


Figure 4.1. Depositional context of micro-concretion ripples. A) Well-cemented micro-concretions weather from chemical reaction fronts within the host rock (Liesegang bands). B) Micro-concretions collect in ripple trains within alcoves where winds are funneled and accelerated.

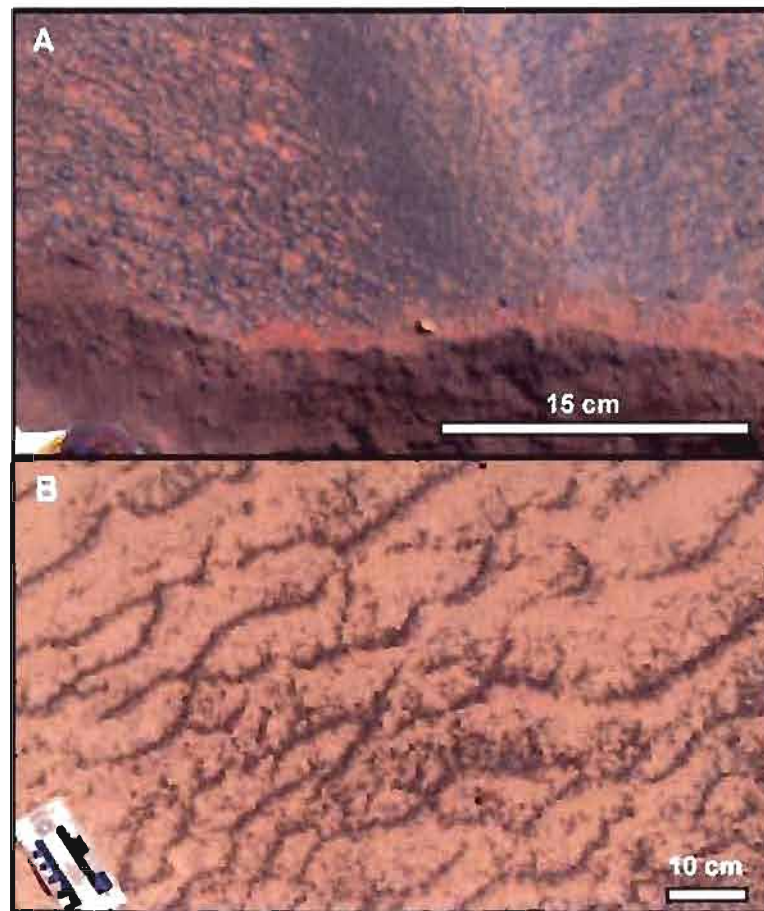


Figure 4.2. Representative micro-concretion ripples from A) Meridiani Planum, Mars imaged by the MER Opportunity (Pancam stretched false color image, Sol 367B, Seq P2550; photo credit: NASA/JPL/Cornell) and B) Jurassic Navajo Sandstone of Northern Arizona.

loosened from the host eolian sandstone. The micro-concretion spherules of this study have an average diameter of 1.5 mm. Micro-concretion grain mass averages 0.0056 g. Average grain mass of medium-grained quartz sand derived from the host rock is  $\sim 0.000075$  g. The grain mass ratio is  $\sim 74:1$  (Figure 4.4).

The micro-concretions can be worked into coarse-grained ripples in shallow depressions and alcoves where winds are strong or funneled. Predominately westerly winds entrain sand to actively abrade sandstone walls to release micro-concretions. These micro-concretions are then organized into trains of straight to sinuous, in-phase, coarse-grained micro-concretion ripples and catenary out-of-phase ripples (Figures. 4.2 and 4.5). These are local, complex, and transient wind ripples that possess irregular and bifurcating crests. Ripple trains extend in pathways up to 14.5 m and are characterized by 5 mm thick accumulations of micro-concretions on the windward/stoss sides and crests of the asymmetric ripples (Figure 4.5). On the leeward faces and in the ripple troughs, micro-concretion accumulations are scattered and generally only a surface coating. The average micro-concretion ripple index (wavelength to height) is 18. Micro-concretions demonstrate reverse grading formed by two likely mechanisms, possibly in combination: (1) a common sieve or “Brazil nut” effect such that the micro-concretions typically “float” on top of the finer-grained quartz sand, or (2) motions typical of coarse-grained ripples in which the larger micro-concretion grains move in creep and are overrun by the ripple itself (Sharp, 1963; Anderson and Bunas, 1993; Figure 4.5). Wind gusts (measured at a height of  $\sim 5$  cm from the air-sediment interface) that move the micro-concretions by low saltation are about 6.6 m/s, although micro-concretions can be moved in creep if sufficient sand is in traction at sustained wind

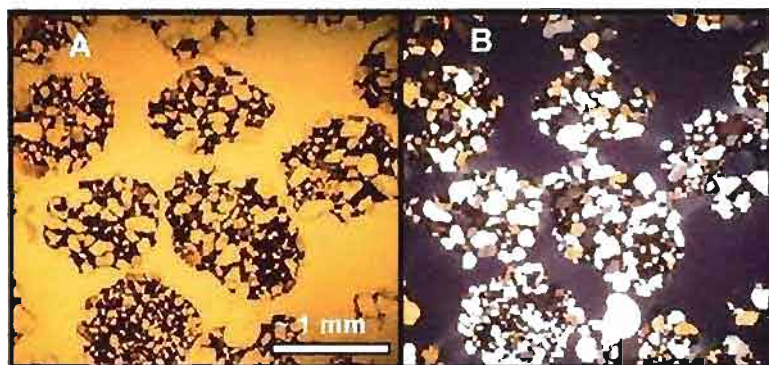


Figure 4.3. Petrographic thin section of spheroidal micro-concretions in plane light A) and crossed nicols B). Dark hematite cement encases eolian quartz (light) grains.

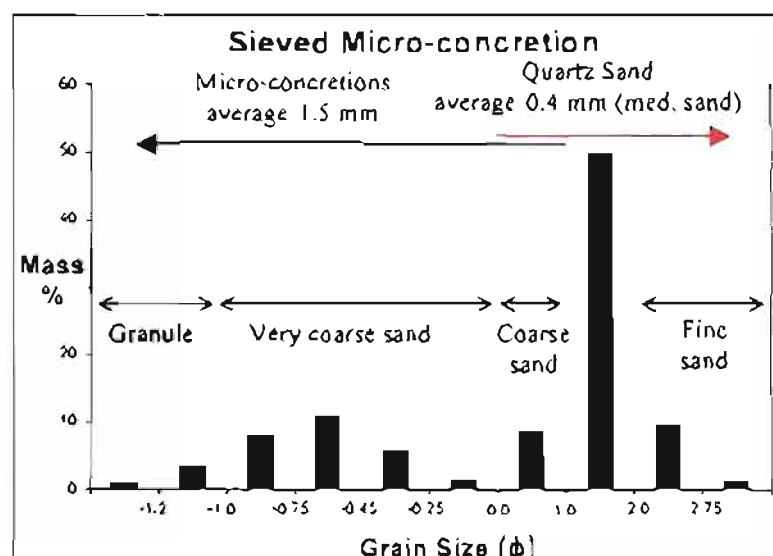


Figure 4.4. Grain size distribution of quartz sand and micro-concretions from sieved samples. Grain size scale is non-linear.

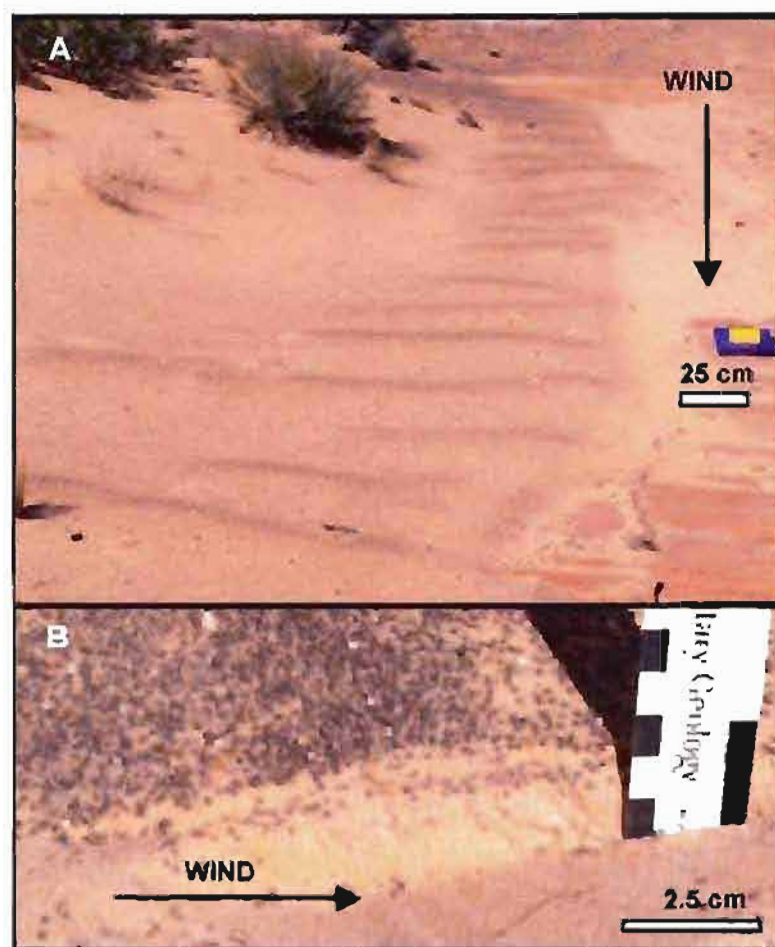


Figure 4.5. Navajo Sandstone micro-concretion ripples. A) Predominately straight crested ripple train. B) Micro-concretions form a thin (~5 mm) veneer on the windward/stoss side of ripples.

speeds of  $\sim 4.5$  m/s. Trenches through the complex concretion ripples reveal distinct, narrow ( $\sim 5$  mm) bands of micro-concretions representing sand burial of previously deposited micro-concretions during periods when wind speeds are sufficient to transport and deposit sand but are unable to mobilize micro-concretions.

### Discussion

Aerodynamics of the terrestrial micro-concretion ripple systems reveal several characteristics:

1. Micro-concretions can be moved by eolian transport (requiring  $\sim 4.5$  m/s wind, 5 cm above the surface). Larger sizes of concretions (e.g., 1+ cm sizes), that are very abundant, are too large for wind transport and hence form deflation lags instead of being reworked and transported.

2. Relatively tight micro-concretion population distribution allows wind to sort out very fine size differences to work the concretions into ripple forms. Inverse grading is enhanced by the density/specific gravity contrast of the coarse-grained micro-concretions vs. the fine-grained quartz sand. The largest micro-concretions mobilized (up to  $\sim 2$  mm) tend to occur on the very crest of the ripples, as is typical of coarse-grained ripples (Sharp, 1963; Anderson and Bunas, 1993).

3. Strong wind gusts (possibly seasonal), eddies, and primary vs. secondary wind regimes give rise to the complex ripple forms in combination with limited area, limited sand supply, and other unusual geomorphic variables.

At Meridiani Planum, the mass ratio between the 1.5 mm Mars spherules (dubbed “microberries” by the NASA Mars Exploration Rover team [Squyres et al., 2006]) and

the basaltic, 100 micron sand likely ranges from 3000:1 to 6000:1, depending on the amount of hematite in the 1.5 mm concretions. This Mars ratio is higher than the terrestrial example, where the micro-concretions contain finer grained hematite and have incorporated quartz grains. However, extremely strong Martian winds (Jerolmack et al., 2006) and very abundant microberries allow for better developed and more pervasive concretion ripples on Mars.

### Conclusions

The remarkable Jurassic Navajo Sandstone micro-concretions in the Coyote Buttes area of Utah-Arizona form complex ripples in areas with loose accumulations of concretions and strong wind gusts. These ripple forms are a useful terrestrial analog to similar features on Mars. This analog demonstrates the history of diagenesis and concretion formation in the host rock, stages of weathering, and final modern wind processes. The limited localized occurrence of these ripples is indicative of the number of environmental conditions required for their formation. These circumstances may be related and scaled to geologic and atmospheric conditions on Mars where similar ripples are far more abundant and exhibit a wider variety of ripple types (e.g., asymmetrical straight, sinuous and catenary ripples) in a stronger wind regime.

### Acknowledgments

This work is supported by the National Aeronautics and Space Administration (to Chan) under grant NNG06GI10G issued through the Mars Fundamental Research Program. We acknowledge the Bureau of Land Management – Vermillion Cliffs National Monument for sampling permission.



### References

- ANDERSON R.S. AND BUNAS K.L., 1993, Grain size segregation and stratigraphy in aeolian ripples modeled with a cellular automation: *Nature*, v. 365, p. 740-743.
- CHAN, M.A., BEITLER, B., PARRY, W.T., ORMÖ, J, AND KOMATSU, G., 2004, A possible terrestrial analogue for haematite concretions on Mars: *Nature*, v. 429, p. 731-734.
- CHAN, M.A., BOWEN, B.B., PARRY, W.T. ORMÖ, J, AND KOMATSU, G., 2005, Red rock and red planet diagenesis: comparisons of Earth and Mars concretions: *GSA Today*, v. 15, p. 4-10.
- CATLING, D.C., 2004, On Earth, as it is on Mars?: *Nature*, v. 429, p. 707-708.
- JEROLMACK, D.J., MOHRIG, D., GROTZINGER, J.P., FIKE, D.A., AND WATTERS, W.A., 2006, Spatial grain size sorting in eolian ripples and estimation of wind conditions on planetary surfaces: Applications to Meridiani Planum, Mars: *Journal of Geophysical Research*, v. 11, p. 1-14.
- ORMÖ, J., KOMATSU, G., CHAN, M.A., BEITLER, B., AND PARRY, W.T., 2004, Geological features indicative of processes related to the hematite formation in Meridiani Planum and Aram Chaos, Mars: A comparison with diagenetic hematite deposits in southern Utah, USA: *Icarus*, v. 171, p. 295-316.
- SHARP, R.P., 1963, Wind Ripples: *Journal of Geology*, v. 71, p. 617-636.
- SQUYRES, S.W., KNOLL, A.H., ARVIDSON, R.E., CLARK, B.C., GROTZINGER, J.P., JOLLIFF, B.L., MCLENNAN, S.M., TOSCA, N., BELL, J.F. III, CALVIN, W.M., FARRAND, W.H., GLOTCH, T.D., GOLOMBEK, M.P., HERKENHOFF, K.E., JOHNSON, J.R., KLINGELHÖFER, G., MCSWEEN, H.Y., AND YEN, A.S., 2006, Two years at Meridiani Planum: Results from the Opportunity Rover: *Science*, v. 313, p. 1403-1407.

## CHAPTER 5

### A COMPARISON OF MINERAL IDENTIFICATION BY REFLECTANCE SPECTROSCOPY AND POWDER X-RAY DIFFRACTION

#### Abstract

Reflectance spectroscopy has been utilized to identify mineralogy responsible for diagenetic coloration of the Navajo Sandstone. However, some questions exist over the accuracy of mineral identification by reflectance spectroscopy compared to powder x-ray diffraction. In particular, reflectance spectroscopy detects minerals in low abundance that may not register by x-ray diffraction. This study examines quartz sand samples with known proportions of hematite and goethite powdered standards to compare the sensitivity of reflectance spectroscopy to x-ray diffraction. This technique also allows the quantitative sensitivity assessment of reflectance spectra features (band minima) used to identify mineral species under conditions where the relative abundance of hematite and goethite are known.

#### Introduction and Objectives

Visible and near infrared (VNIR) reflectance spectroscopy offers a practical means of mineral identification where (1) outcrops are inaccessible for hand sampling (Mars), or (2) coloration patterns exist at regional scales (the Navajo Sandstone in

southern Utah), or (3) the photogenic character of an outcrop necessitates non-scarring, leave-no-trace sampling (the Coyote Buttes Special Permit Area, UT/AZ). In fact, visible and near infrared reflectance spectroscopy has been utilized extensively to determine the mineralogical composition of rocks on both Earth and Mars (Christensen et al., 2001; Bandfield et al., 2003; Beitler et al., 2003; Arvidson et al., 2005; Bowen et al., 2007). However, the accuracy of VNIR reflectance spectroscopy has been questioned in samples where spectral signatures indicate the presence of minerals not detected when analyzed using powder x-ray diffraction (XRD) (Parry, personal communications, 2007; Petersen, personal communications 2007, 2008). To address these discrepancies, a series of experiments were run in which quartz sand samples were combined with powdered hematite and goethite mixtures of known composition and abundance in order to simulate iron oxide grain coatings of Navajo Sandstone diagenetic facies. These samples were analyzed by both VNIR reflectance spectroscopy and powder x-ray diffraction. An analysis of using the two techniques for mineral identification resolves discrepancies between the two and shows that VNIR spectroscopy is very useful and sensitive, and that quantitative mineral abundances can be gleaned from spectral signatures.

This study has three main objectives: (1) to compare the sensitivity and utility of powder x-ray diffraction to visible and near infrared reflectance spectroscopy when determining the mineralogy of iron oxide grain coatings; (2) to determine the position of absorption features recorded by reflectance spectroscopy in samples where a known, homogenized mixture of hematite and goethite are present; (3) to interpret the relative hematite and goethite abundances from samples whose absorption troughs occur between that of hematite (860 nm) and goethite (900-930 nm) (Morris et al., 1985; Townsend,

1987); and (4) to determine whether reflectance values can be used to determine relative quartz abundance in samples with unknown quartz and iron oxide (HFO) mixtures.

## Methods

### Sample Preparation

Thirty-four samples were created from known mineral standards obtained from the University of Utah, Department of Geology and Geophysics mineral collection. Hematite, goethite, and quartz standards were examined by XRD to verify mineral composition and purity. Hematite and goethite standards were crushed and powdered by mortar and pestle to approximately a very fine silt or clay ( $\sim 7\phi - 9\phi$ ) and mixed at 100:0, 90:10, 75:25, and 50:50 weight percent ratios. These powdered hematite-goethite mixtures were thoroughly mixed with a fine-grained quartz sand at 50:50, 75:25, 90:10, 95:5, and 99:1 weight percent ratios to simulate grain coatings.

### Visible and Near Infrared Reflectance Spectroscopy

Samples were analyzed for visible (VIS) and near infrared (NIR) reflectance spectra using an Analytical Spectral Devices Inc. Fieldspec Spectroradiometer (Model FSP350-2500P), analytical spectral device (ASD). The ASD measures reflectance spectra on 2151 channels from 350-2500nm. Measurements were made using calibrated artificial illumination, and a bare fiber foreoptic optimized to a standardized white reference plate. White referencing was repeated between multiple sample batches. These samples were analyzed using the ASD with the foreoptic mounted at 1 cm ( $\sim 0.3$  cm field of view).

## Powder X-Ray Diffraction

Powder x-ray diffraction (XRD) was used to identify the mineral constituents of the known samples. A Rigaku D-2000, powder sample x-ray diffractometer operating at 40 kV and 30 mA with Cu K $\alpha$  radiation was utilized. Samples were analyzed over 15–50 2 $\theta$  (degrees), with hematite/goethite identification performed between 34–37 2 $\theta$  (degrees). Scans were performed at 2°/min. Data were processed by Material Data Inc., Jade software.

Eleven of the 34 samples examined by ASD were also analyzed by XRD. Seven samples were analyzed where a constant weight ratio of 99:1 quartz to hematite/goethite mixture was maintained while the mixture of hematite/goethite was varied. Hematite (Hm) and goethite (Go) mixtures were created at 100 Hm:0 Go, 90 Hm:10 Go, 75 Hm:25 Go, 50 Hm:50 Go, 25 Hm:75 Go, 10 Hm:90 Go, and 0 Hm:100 Go weight percent ratios.

Four additional samples were analyzed with a constant 50:50 hematite:goethite mixture, but with the ratio between quartz (Qtz) and hematite/goethite mixture (HFO<sub>mix</sub>) was varied. These samples included 99 Qtz:1 HFO<sub>mix</sub> (from sample described above), 95 Qtz:5 HFO<sub>mix</sub>, 90 Qtz:10 HFO<sub>mix</sub>, 75 Qtz:25 HFO<sub>mix</sub>, and 50 Qtz:50 HFO<sub>mix</sub>.

## Results

### Visible and Near Infrared Reflectance Spectroscopy

Visible and near infrared reflectance spectra were obtained for all 34 samples and the three standards. Particular attention was paid to spectral bands between 750 and 1300 nm to diagnosis the presence of hematite and goethite. Within this interval, hematite and goethite possesses band minima near 860 nm and 900–930 nm respectively (Morris et al.,

1985; Townsend, 1987). Band minima for each iron oxide mixture were averaged and range from 861 nm for pure hematite mixtures to 918 nm for pure goethite mixtures (Table 5.1). Hematite and goethite mixtures display minima between these end members. Overall reflectance is directly related to Quartz content in the samples—those with the greatest amount of Quartz (99 Qtz:1 HFO<sub>mix</sub>) displayed the greatest reflectance (Figure 5.1).

Continuum removed spectra were also calculated for the iron oxide mixtures. Continuum removed spectra are calculated as  $R' = R_m/R_c$  where  $R_m$  = measured reflectance and  $R_c$  = absorption continuum (a straight line segment from a reflectance shoulder at 750 nm to a reflectance shoulder at 1300nm) (Bowen et al., 2007; Clark and Roush 1984). Continuum removed spectra allows specific absorption features to be examined in isolation—shifts in apparent band minima caused by wavelength dependent scattering, and spectrum slope in multi-mineral systems are removed (Clark and Roush, 1984). Continuum removed spectra display average minima at 867 nm and 991 nm for hematite and goethite end members respectively (Table 5.2).

### Powder X-Ray Diffraction

XRD analysis of hematite, goethite, and quartz standard samples determined that mineral identification can be made between 34-37  $2\theta$  (degrees) (Figure 5.2). In this range, a diagnostic quartz peak is at 36.5  $2\theta$  (degrees), a hematite peak is at 35.5  $2\theta$  (degrees), and a goethite peak is at 34.5  $2\theta$  (degrees).

In 99 Qtz:1 HFO<sub>mix</sub> samples, a hematite peak is visible as a minor, slight bulge at 35.58  $2\theta$  (degrees) in only two of the seven samples—when the iron oxide mix was

Table 5.1

Band Minima (nm) for Measured Reflectance (R<sub>m</sub>) Spectra

Sample Composition	HFO Mixture Composition						
	100 Hm:0 Go	90 Hm:10 Go	75 Hm:25 Go	50 Hm:50 Go	25 Hm:75 Go	10 Hm:90 Go	0 Hm:100 Go
99 Qtz:1 HFO	855	859	854	878	878	894	929
95 Qtz:5 HFO	861	865	864	878	887	898	923
90 Qtz:10 HFO	863	864	864	878	891	898	927
75 Qtz: 25 HFO	863	861	864	878	891	909	904
50 Qtz:50 HFO	864	864	865	878	898	899	909
Avg. Band Minima (nm)	861	863	868	878	889	900	918
Standard Deviation	3.49	2.51	4.60	0	7.31	5.59	11.22

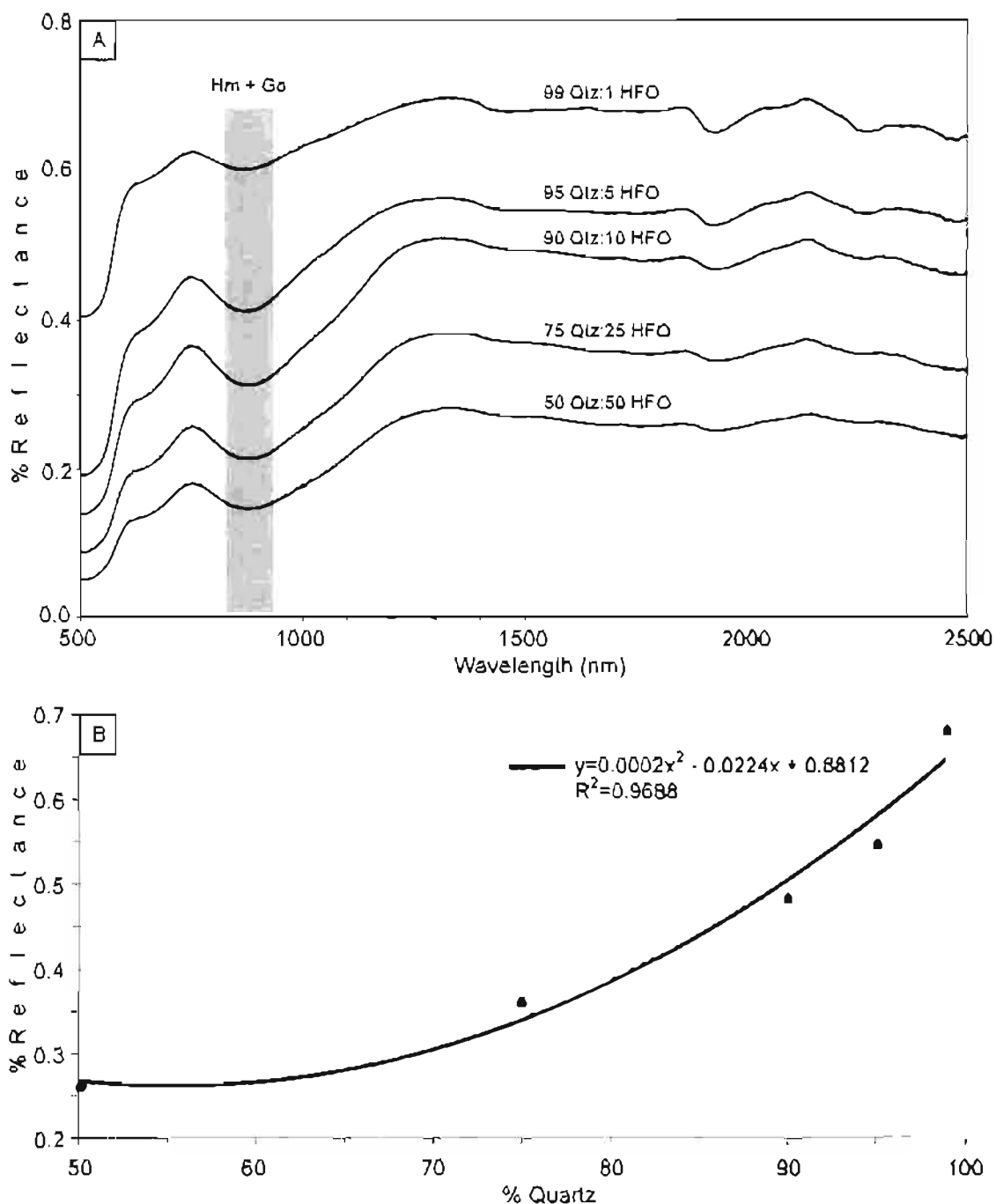


Figure 5.1. Reflectance spectra of samples with varying quartz content. A) Reflectance spectra of 50 Hm:50 Go HFO<sub>mix</sub> mixtures combined with quartz sand at various weight percent ratios. Gray bar marks the expected range of hematite and goethite band minima. Diagnostic band minima for each sample are clearly resolved using ASD while diffraction patterns are unreliable for mineral identification using XRD (Figure 4). B) Average reflectance between 1600 and 1700 nm for the samples with varying quartz content (displayed above). Relative percent quartz in the samples can be determined by reflectance values.



Table 5.2

Band Minima (nm) for Continuum Removed (Rm/Rc) Spectra

Sample Composition	10:0 Mixture Composition						
	100 Hm, 0 Go	90 Hm, 10 Go	75 Hm, 25 Go	50 Hm, 50 Go	25 Hm, 75 Go	10 Hm, 90 Go	0 Hm, 100 Go
99 Qtz, 1 HFO	865	871	874	895	917	970	991
95 Qtz, 5 HFO	867	871	879	891	928	969	991
90 Qtz, 10 HFO	871	871	877	898	915	977	990
75 Qtz, 25 HFO	869	871	875	901	928	972	987
50 Qtz, 50 HFO	864	872	881	898	919	971	994
Avg. Band Minima (nm)	867	871	877	897	930	972	991
Standard Deviation	2.86	0.55	2.86	5.78	13.19	3.11	2.51

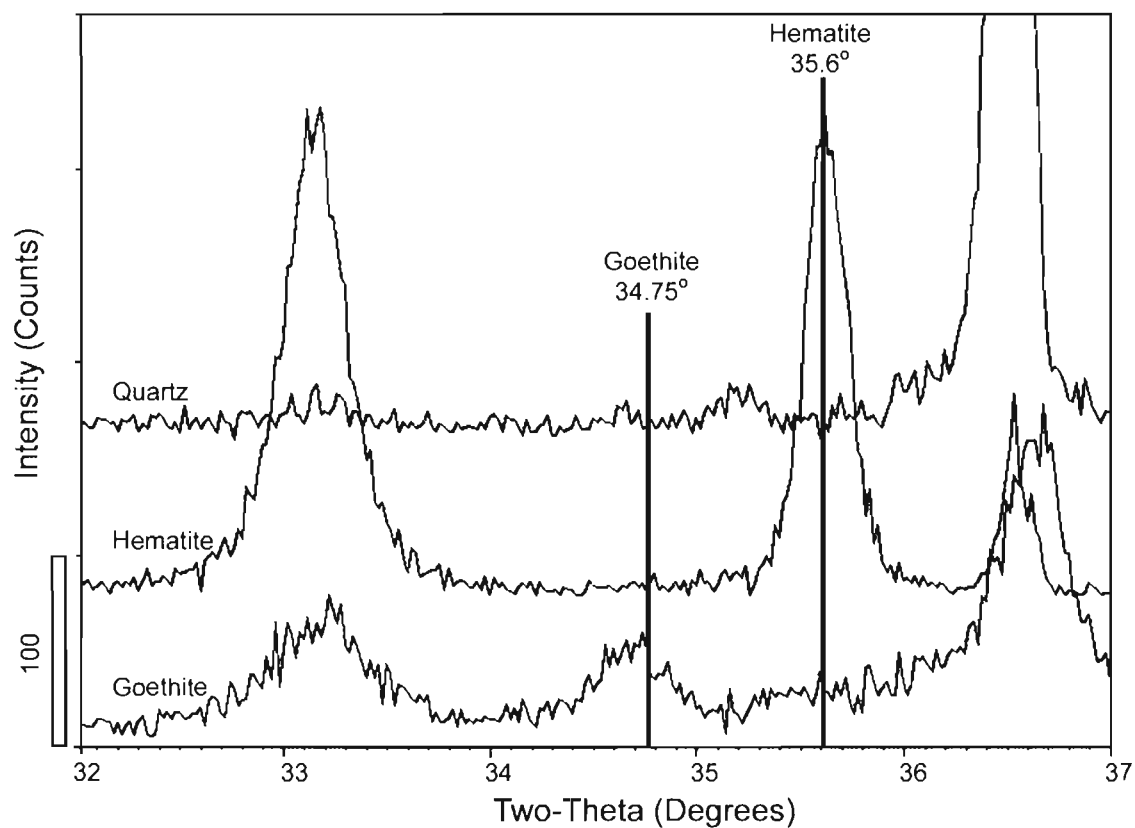


Figure 5.2. X-ray powder diffraction patterns of hematite, goethite, and quartz standards. Distinct, diagnostic peaks for hematite and goethite occur at  $35.6^\circ$  and  $34.75^\circ$  respectively. Relative intensity indicated by scale bar.

composed of 100 Hm:0 Go and 90 Hm: 10 Go (Figure 5.3). Hematite peak area was 1.6% and 0.9% of the quartz peak, for these two respective hematite mixtures. In all samples, a strong quartz peak is visible at  $36.5\ 2\theta$  (degrees). Goethite peaks were not observed in any 99 Qtz:1 HFO<sub>mix</sub> samples though the mineral is present in the samples.

Samples where the hematite/goethite ratio was kept at 50:50 and the weight percent of this HFO mixture was varied with respect to quartz were also analyzed. As noted above, neither hematite nor goethite peaks were observed in the 99 Qtz:1 HFO<sub>mix</sub> sample. However, a minor hematite peak (1.0% peak area) exists in the 95 Qtz:5 HFO<sub>mix</sub> sample (Figure 5.4). As the weight percent of the iron oxide mixture relative to quartz was increased, the hematite peak became more apparent (Figure 5.4). In only the 50 Qtz:50 HFO sample, were both goethite and hematite peaks visible.

### Discussion

#### Hematite and Goethite Detection by ASD vs. XRD

Clear differences in sensitivity to hematite and goethite occur in ASD and XRD data. In all samples—even those at 99 Qtz:1 HFO<sub>mix</sub>—hematite and goethite add distinct, visible hues to the white, quartz sand (red and yellow respectively). Though both hematite and goethite are known to exist in the samples analyzed by XRD (Figures 5.3 and 5.4), diagnostic diffraction patterns are minor if not absent for hematite and are missing for all but one sample of goethite. However, ASD analysis clearly detects iron oxide mixtures with recorded band minima between 855 nm and 930 nm as would be expected from hematite and goethite (Table 5.1). Even at a mere 1% HFO by weight

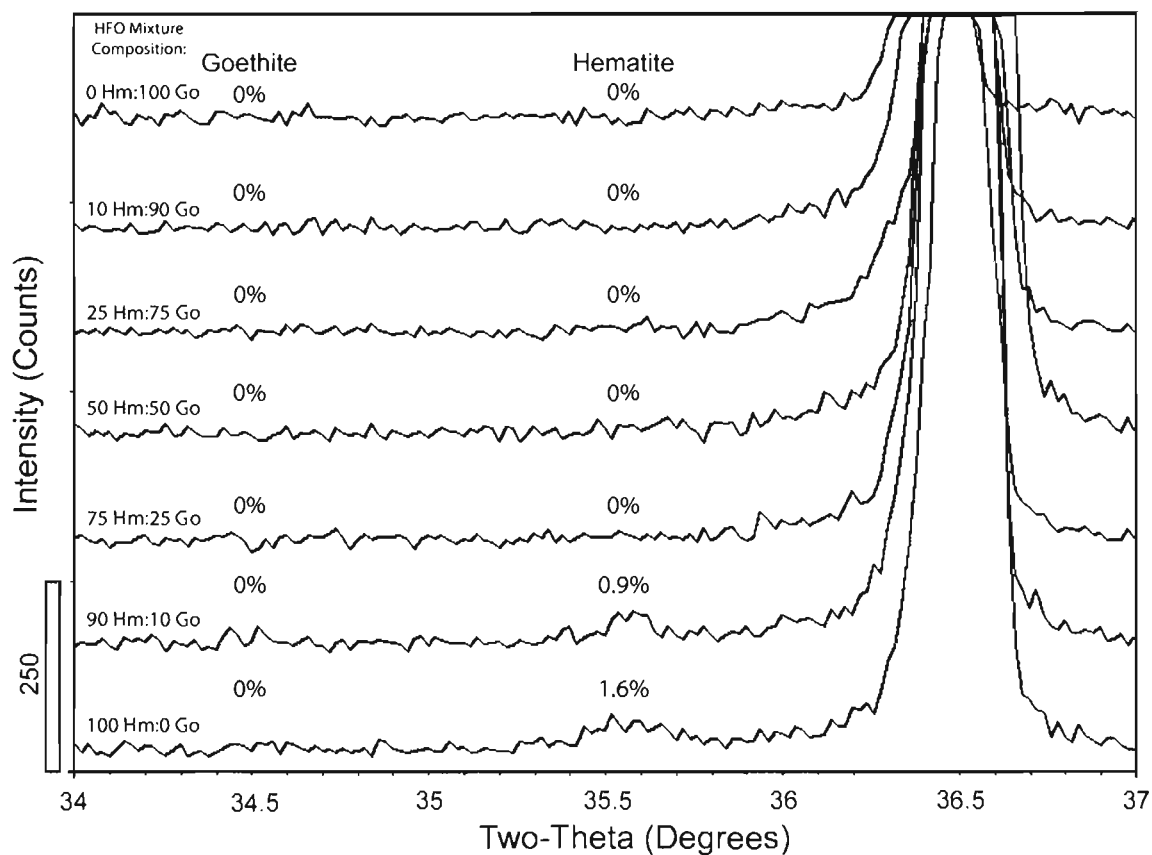


Figure 5.3. X-ray powder diffraction patterns for 99 Qtz:1 HFO<sub>mix</sub> weight percent mixtures. Peak percent area relative to quartz (36.5°) given for both hematite and goethite. Relative intensity indicated by scale bar.

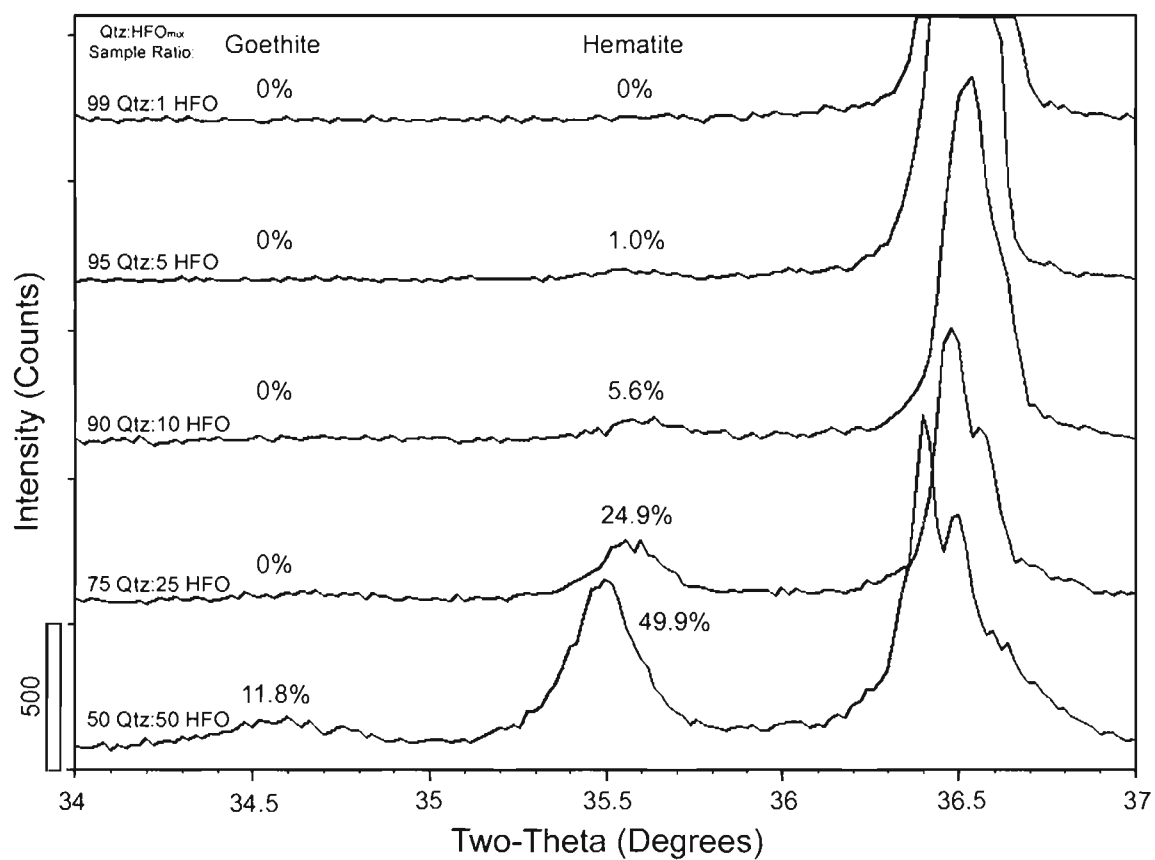


Figure 5.4. X-ray powder diffraction patterns of 50 Hm:50 Go HFO<sub>mix</sub> mixtures combined with quartz sand at various weight percent ratios. Peak percent area relative to quartz (36.5°) given for both hematite and goethite. Goethite is only indicated by XRD in the 50 Qtz:50 HFO<sub>mix</sub> sample. Relative intensity indicated by scale bar.

composition, ASD allows accurate discrimination of hematite and goethite in the samples.

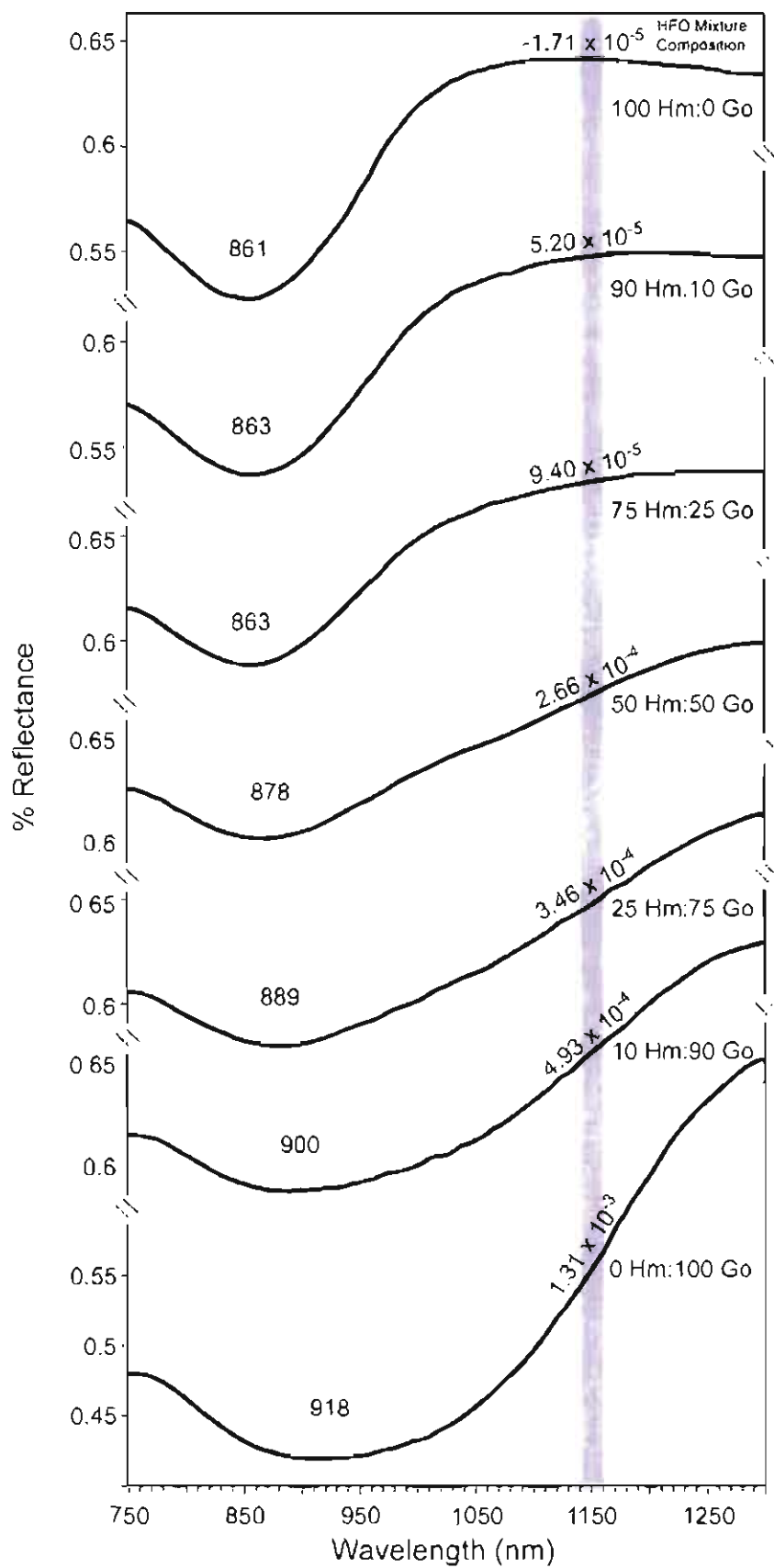
In addition, XRD detection favors hematite over goethite between 34 – 37 2 $\theta$  (degrees). The hematite diffraction pattern over this interval forms a relatively sharp peak, while goethite displays a broad, shallow crest (Figure 5.2). In samples with equal proportions of hematite and goethite in the iron oxide mixture (Figure 5.4), a goethite diffraction pattern is only visible in the 50 Qtz:50 HFO<sub>mix</sub> XRD sample, but is again recorded in each sample by ASD. Not only is the ASD more sensitive than XRD at resolving hematite and goethite in the sand samples, but in its limited capacity at low mineral concentrations, XRD is more capable at detecting hematite than goethite.

Work by Bowen and others (2007), describes a wide range of iron oxide abundance in the Navajo Sandstone, exceeding 35% in iron oxide concretions, but also well below 1% in red and bleached sandstone facies. In these common Navajo Sandstone color facies, ASD provides a reliable means to distinguish between hematite and goethite where mineral abundance falls below the sensitivity of XRD in whole rock.

#### Absorption Minima in Hematite and Goethite Mixtures

By analyzing known mixtures of hematite and goethite, the reflected and continuum removed minima can be determined for varying proportions of the iron oxides (Table 5.1). Examining reflected spectra ( $R_m$ ) at varying hematite:goethite mixtures (Figures 5.5 and 5.6) reveals that hematite has a stronger influence on the position of reflected band minima than does goethite. The addition of 10% (by weight) hematite to goethite results in an 32% shift in band minima towards hematite (a shift from 918 nm for

Figure 5.5. 750-1300 nm absorption features for various hematite:goethite mixtures. Hm:Go added to quartz sand at a 99 Qtz:1 HFO<sub>mix</sub> weight percent ratio. Band minima represent the average of all samples at the stated Hm:Go ratio. Slope of each absorption feature between 1140-1160 nm (thick gray line) displayed. Slope over a known interval may prove diagnostic when comparing absorption features of samples with unknown mineral compositions. Band minima position indicated by thin gray bar.





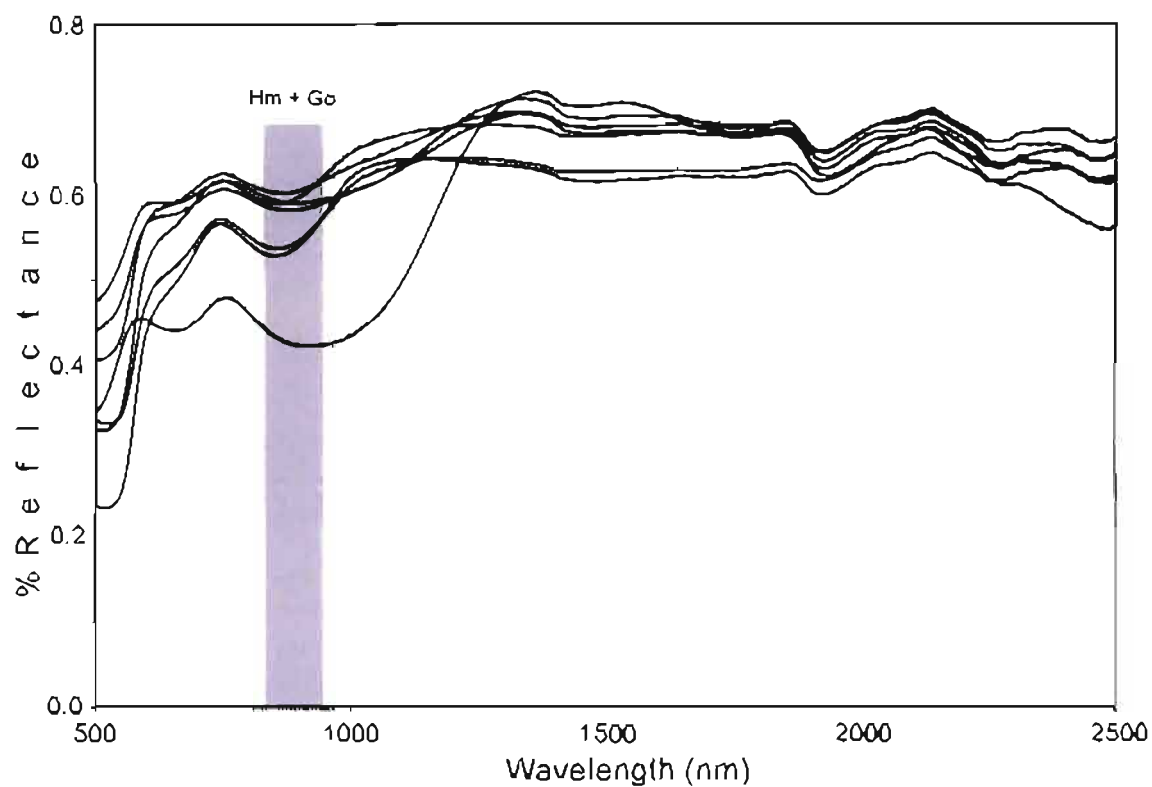


Figure S.6. Reflectance spectra for 99 Qtz:1 HFO<sub>HMX</sub> weight percent mixtures. Gray bar marks the expected range of hematite and goethite band minima. Note that while goethite is not noted and hematite is only faintly visible in two of these samples when measured with XRD (Figure 3), diagnostic band minima between ~855-930 nm are clearly resolved by ASD.

0 Hm:100 Go to 900 nm for 10 Hm:90 Go). In contrast, adding 10% (by weight) goethite to hematite results in only a 4% shift in band minima towards goethite (a shift from 861 nm for 100 Hm:0 Go to 863 nm for 90 Hm:10 Go). Additionally, the presence of hematite in iron oxide mixtures serves to narrow the 750-1300 nm absorption feature.

Similar hematite sensitivity is observed in continuum removed spectra. The addition of 10% (by weight) hematite to goethite results in an 15% shift in continuum removed band minima towards hematite (a shift from 991 nm for 0 Hm:100 Go to 972 nm for 10 Hm:90 Go). In contrast, adding 10% (by weight) goethite to hematite results in only a 3% shift in continuum removed band minima towards goethite (a shift from 867 nm for 100 Hm:0 Go to 871 nm for 90 Hm:10 Go). Sensitivity of both continuum removed and reflectance spectra reveals that the spectral character of iron oxide mixtures is more sensitive to variations in hematite than to variations in goethite.

#### Hematite:Goethite Abundances in Unknown Mixtures

The relative abundance of hematite and goethite in unknown mixtures can be extrapolated from examining the band minima shift observed in this study (Figure 5.7A). Band minima of known iron oxide mixtures are fit with a 2<sup>nd</sup> order polynomial trendline:

Measured Reflectance Spectra:

$$y = 0.02656567x^2 - 48.8962978x + 22499.07 \quad R^2 = 0.978$$

Continuum Removed Spectra:

$$y = 0.00661916x^2 - 13.032005x + 6418.128 \quad R^2 = 0.988$$

Natural variations commonly occur in iron oxides due to the inclusion of elements other than iron into the mineral structure (Ji et al., 2002). However, the quantified shift in

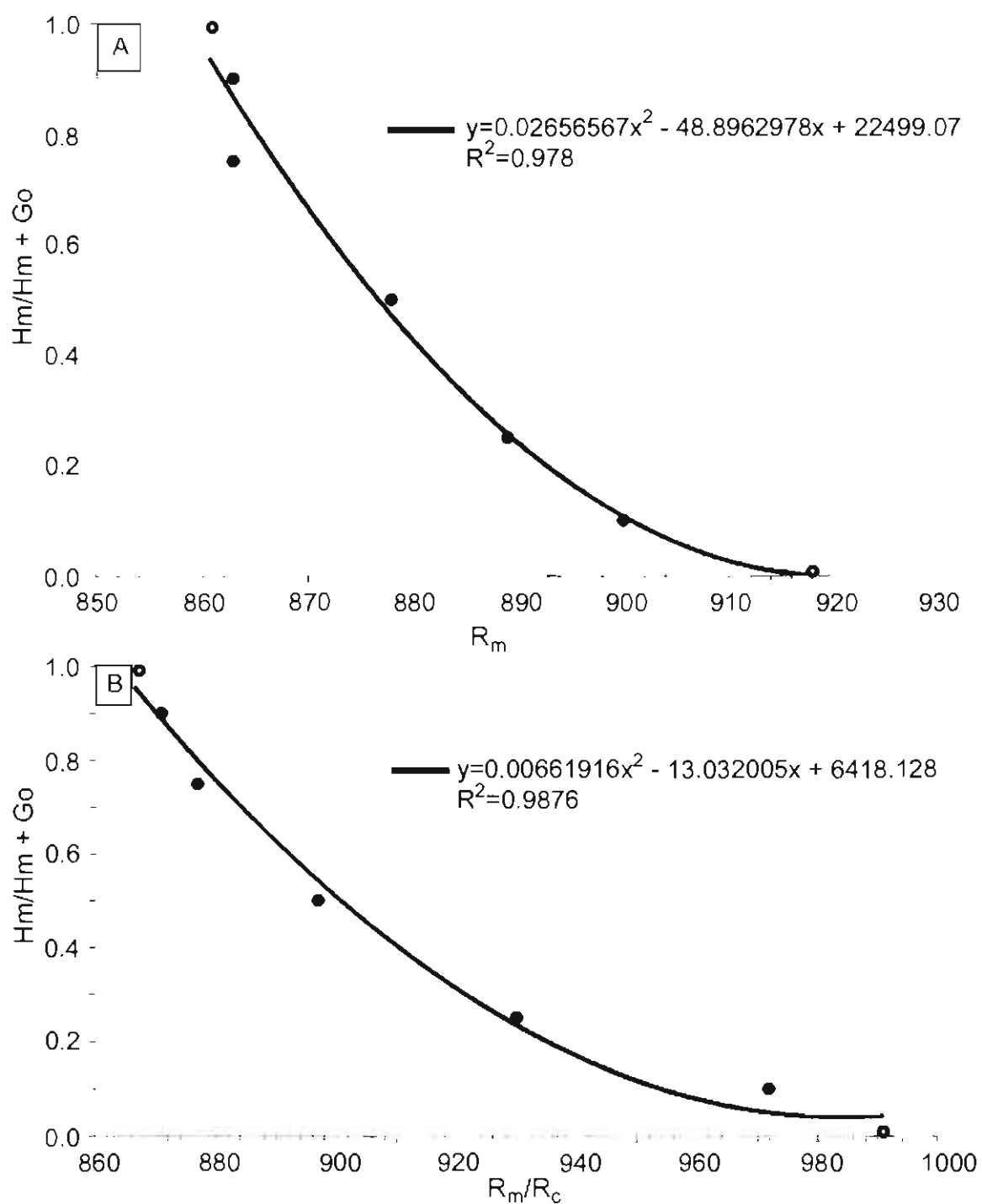


Figure 5.7. Average band minima of 34 Hm:Go mixtures. A) Measured reflectance ( $R_m$ ) band minima. B) Continuum removed ( $R_m/R_c$ ) band minima.

band minima of known iron oxide mixtures allows for an approximation of hematite and goethite abundance in field samples of colored Navajo Sandstone where band minima is intermediate between hematite and goethite.

### Quartz Abundances in Unknown Mixtures

The relative abundance of quartz in an unknown mixture can be derived from examining the average reflectance over an interval where no absorption features are known to occur (Figure 5.7B). Reflectance values were averaged between 1600-1700 nm in samples where a constant Hm:Go mixture was varied with respect to quartz abundance. Average reflectance for given quartz abundance was fit with a second order polynomial trendline:

$$y = 0.0002x^2 - 0.0224x + 0.8812 \quad R^2 = 0.9688$$

By examining the reflectance over an interval without absorption features, the relative abundance of quartz in a sandstone (compared to iron oxide) may be extrapolated.

### Conclusions

Both ASD and XRD analyses provide valuable mineralogical characterization. However, ASD analysis offers several advantages over XRD in evaluating diffuse iron oxide mixtures of hematite and goethite. (1) ASD analysis yields accurate identification of mineral species (hematite and goethite) that are at too low a concentration to be reliably detected by XRD. ASD accurately distinguishes hematite-goethite mixtures at 1 wt %, but XRD generally requires >10 wt % for reliable mineral identification of hematite-goethite mixtures. (2) ASD derived band minima can accurately distinguishing

between hematite and goethite; XRD is able to more readily detect hematite than goethite, particularly at low mineral concentrations. (3) Relative mineral abundances can be derived from band minima positions between those of pure hematite and pure goethite. (4) Relative mineral abundance of quartz compared to iron oxide can be derived from the average reflectance value over an interval lacking absorption features. Comparison of synthetically-derived and field sample band minima allows for a quantitative understanding of Navajo Sandstone mineralogy. Reflectance spectroscopy remains a valuable and quantitative tool in identifying mineralogy associated with diagenetic coloration facies in the Navajo Sandstone.

### References

- ARVIDSON, R.E., POULET, F., BIBRING, J.P., WOLFF, M., GENDRIN, A., MORRIS, R.V., FREEMAN, J.J., LANGEVIN, Y., MANGOLD, N., AND BELLUCCI, G., 2005, Spectral reflectance and morphologic correlations in eastern Terra Meridiani, Mars: *Science*, v. 307, p. 1591-1594.
- BANDFIELD, J.L., GLOTTCH, T.D., AND CHRISTENSEN, P.R., 2003, Spectroscopic identification of carbonate minerals in the Martian dust: *Science*, v. 301, p. 1084-1087.
- BEITLER, B., CHAN, M.A., AND PARRY, W.T., 2003, Bleaching of Jurassic Navajo Sandstone on Colorado Plateau Laramide highs: evidence of exhumed hydrocarbon supergiants?: *Geology*, v. 31, p. 1041-1044.
- BOWEN, B.B., MARTINI, B.A., CHAN, M.A., AND PARRY, W.T., 2007, Reflectance spectroscopic mapping of diagenetic heterogeneities and fluid-flow pathways in the Jurassic Navajo Sandstone: *AAPG Bulletin*, v. 91, p. 173-190.
- CHRISTENSEN, P.R., MORRIS, R.V., LANE, M.D., BANDFIELD, J.L., AND MALIN, M.C., 2001, Global mapping of Martian hematite mineral deposits: remnants of water-driven processes on early Mars: *Journal of Geophysical research*, v. 106, p. 23,873-23,885.

- CLARK, R.N., AND ROUSH, T.L., 1984, Reflectance spectroscopy: quantitative analysis techniques for remote sensing applications: *Journal of Geophysical Research*, v. 89, p. 6329-6340.
- JI, J., BALSAM, W., CHEN, J., AND LIU, L., 2002, Rapid and quantitative measurement of hematite and goethite in the Chinese loess-paleosol sequence by diffuse reflectance spectroscopy: *Clays and Clay Minerals*, v. 50, p. 208-216.
- MORRIS, R.V., 1985, Spectral and other physiochemical properties of submicron powders of hematite, maghemite, magnetite, goethite, and lepidocrite: *Journal of Geophysical Research*, v. 90, p. 3126-3144.
- PARRY, W.T., 2007, Personal Communications: 25 October, 2007.
- PETERSEN, E.U., 2007, Personal Communications: 25 October, 2007.
- PETERSEN, E.U., 2008, Personal Communications: 3 January, 2008.
- TOWNSEND, T.E., 1987, Discrimination of iron alteration minerals in visible and near-infrared reflectance data: *Journal of Geophysical Research*, v. 92, p. 1441-1454.

## APPENDIX A

### SUPPORTING DATA AND FIGURES

#### Introduction

The following pages present supporting data to the preceding chapters and to studies of the Navajo Sandstone at Coyote Buttes resulting in the publications of Chan et al. (2008) and Loope et al. (2007). Samples collected at Coyote Buttes and the analyses performed on each are summarized (Table A.1); an overall characterization of the field area's coloration is provided (Figure A.1). This introduction briefly discusses the data included in these appendices, with further data—including measured reflectance spectra and complete field notes—accompany this manuscript in digital form (see Appendix B).

#### SEM Analysis

Ten samples were imaged and analyzed under a LEO 440i scanning electron microscope equipped with an energy dispersive x-ray (EDAX) analytic tool. Samples from each diagenetic facies were sputtered with gold and imaged at an accelerated current of 20kV under varying magnification. Sandstone grain surface textures were evaluated (Figures A.2 to A.10) and chemical composition recorded with EDAX (Tables A.1 to A.22). SEM imaging reveals several interesting textures:

Table A.1

## Sample Facies, Locality and Analyses

Sample ID	Facies	Location	Elevation (ft)	Spectra	Thin Section	SEM	Sieved
CBN 6.19.06#1	Micro-conc. Ripple Crest	N36 58.994' W112 00.232'	5686				x
CBN 6.19.06#2	Micro-conc. Ripple Trough	N36 58.994' W112 00.232'	5686				x
CBN 6.19.06#3	Micro-conc. Ripple Crest	N36 58.994' W112 00.232'	5686				x
CBN 6.19.06#4	Micro-conc. Ripple Trough	N36 58.994' W112 00.232'	5686				x
CBN 6.19.06#5	Micro-conc. Unrippled Sand	N36 58.994' W112 00.232'	5686				x
CBN 6.20.06#1	Micro-conc. Ripple Crest	N36 59.241' W112 00.429'	5708				x
CBN 6.20.06#2	Micro-conc. Ripple Trough	N36 59.241' W112 00.429'	5708				x
CBN 6.20.06#3	Micro-conc. Ripple Crest	N36 59.241' W112 00.429'	5708				x
CBN 6.21.06#1	Micro-conc. Ripple Crest	N36 59.456' W112 00.339'	5632				x
CBN 6.21.06#2	Micro-conc. Free Sand	N36 59.456' W112 00.339'	5632				x
CBN 6.25.06#1	Variable Lies./Red & White	N36 59.722' W112 00.436'	5270	x			
CBN 6.25.06#2	Variable Lies./Red & White	N36 59.738' W112 00.651'	5266	x	x	x	
CBN 7.13.06#1	Red & White Banded	N36 59.772' W112 00.510'	5230	x			
CBN 7.13.06#2	Bleached	N36 59.772' W112 00.510'	5230	x	x		
CBN 7.13.06#3	Variable Lies./Red & White	N36 59.732' W112 00.417'	5227	x			
CBN 7.13.06#4	Basal Red	N36 59.768' W112 00.416'	5188	x			
CBN 7.13.06#5	Variable Lies./Red & White	N36 59.753' W112 00.373'	5220	x			
CBN 7.13.06#6	Red & White Banded	N36 59.756' W112 00.415'		x	x		
CBN 7.14.06#1	Basal Red	Measured Section 1 - 2m		x	x		
CBN 7.14.06#2	Variable Lies./Red & White	Measured Section 1 - 4.5m		x			
CBN 7.14.06#3	Variable Lies./Red & White	Measured Section 1- 5.5m		x			
CBN 7.14.06#4	Variable Lies./Red & White	Measured Section 1- 18.75m		x			
CBN 7.14.06#5	Red & White Banded	Measured Section 1- 35m		x			
CBN 7.15.06#1	Variable Lies./Red & White	Measured Section 1- 57.5m		x			
CBN 7.15.06#2	Variable Lies./Red & White	Measured Section 1- 57.5m		x			
CBN 7.15.06#3	Bleached	Measured Section 1- 62m		x			
CBN 7.15.06#4	Variable Lies./Red & White	Measured Section 1- 84m		x			
CBN 7.15.06#5	Variable Lies./Red & White	Measured Section 1- 83.5m		x			
CBN 7.15.06#6	Variable Lies./Red & White	Measured Section 2- 2.75m		x			

Micro-conc. = micro-concretion; Hem. = hematite; Variable Lies./Bleached = variable Liesegang facies overprinted atop bleached facies

Variable Lies./Red & White = variable Liesegang facies overprinted atop red and white banded facies



Table A.1 Continued

Sample ID	Facies	Location	Elevation (ft)	Spectra	Thin Section	SEM	Sieved
CBN 7.15.06#7	Variable Lies./Bleached	Measured Section 2- 16.5m		x	x		
CBN 7.15.06#8	Variable Lies./Bleached	Measured Section 2- 16.5m		x	x		
CBN 7.15.06#9	Variable Lies./Bleached	Measured Section 2- 16.5m		x	x		
CBN 7.15.06#10	Orange Hem. & Micro-conc.	Measured Section 2- 17.75m		x			
CBN 7.16.06#1	Variable Lies./Bleached	Measured Section 2- 30.5m		x			
CBN 7.16.06#2	Variable Lies./Bleached	Measured Section 2- 30m		x			
CBN 7.16.06#3	Variable Lies./Bleached	Measured Section 2- 29m		x			
CBN 7.16.06#4	Variable Lies./Bleached	Measured Section 2- 30m		x			
CBN 7.16.06#5	Variable Lies./Bleached	Measured Section 2- 55.5m		x			
CBN 7.16.06#6	Variable Lies./Bleached	Measured Section 2- 55.5m		x			
CBN 7.17.06#1	Deformation Band	Measured Section 2- 71m		x			
CBN 7.17.06#2	Deformation Band	Measured Section 2- 81.75m		x			
CBN 7.17.06#3	Deformation Band	Measured Section 2- 84.25m		x	x		
CBN 7.17.06#4	Deformation Band	Measured Section 2- 91.75m		x			
CBN 7.17.06#5	Deformation Band	Measured Section 2- ~96m		x			
CBN 7.17.06#6	Upper Red	Measured Section 2- 93.25m		x	x		
CBN 7.19.06#1	Basal Red	Measured Section 3- 2.5m		x	x		
CBN 7.19.06#2	Variable Lies./Red & White	Measured Section 3- 11m		x			
CBN 7.19.06#3	Red & White Banded	Measured Section 3- 19m		x			
CBN 7.19.06#4	Variable Lies./Red & White	Measured Section 3- 26.5m		x			
CBN 7.19.06#5	Variable Lies./Red & White	Measured Section 3- 25.25m		x			
CBN 7.19.06#6	Variable Lies./Red & White	Measured Section 3- 31m		x			
CBN 7.20.06#1	Variable Lies./Bleached	Measured Section 3- 37m		x		x	
CBN 7.20.06#2	Variable Lies./Bleached	Measured Section 3- 50m		x		x	
CBN 7.20.06#3	Variable Lies./Bleached	Measured Section 3- 61m		x			
CBN 7.20.06#4	Bleached	Measured Section 3- 63.25m		x			
CBN 7.20.06#5	Variable Lies./Bleached	Measured Section 3- 64.5m		x			
CBN 7.21.06#1	Variable Lies./Bleached	Measured Section 3- 75.25m		x			
CBN 7.21.06#2	Bleached	Measured Section 3- 78m		x	x		
CBN 7.22.06#1	Orange Hem. & Micro-conc.	Measured Section 3- 81.5m		x	x		
CBN 7.22.06#2	Orange Hem. & Micro-conc.	Measured Section 3- 81.5m		x	x	x	

Micro-conc. = micro-concretion; Hem. = hematite; Variable Lies./Bleached = variable Liesegang facies overprinted atop bleached facies  
 Variable Lies./Red & White = variable Liesegang facies overprinted atop red and white banded facies

Table A.1 Continued

Sample ID	Facies	Location	Elevation (ft)	Spectra	Thin Section	SEM	Sieved
CBN 7.22.06#3	Orange Hem. & Micro-conc.	Measured Section 3- 81.5m		x			
CBN 7.22.06#4	Bleached	Measured Section 3- 96.5m		x			
CBN 7.22.06#5	Bleached	Measured Section 3- 105m		x			
CBN 7.22.06#6	Variable Lies./Bleached	Measured Section 3- 107.25m		x			
CBN 7.22.06#7	Orange Hem. & Micro-conc.	N36 59.542' W112 00.294'	5537	x			
CBN 8.22.06#1	Bleached	N36 58.843' W112 00.469'	5718	x	x		
CBN 8.22.06#2	Orange Hem. & Micro-conc.	N36 58.886' W112 00.378'	5730	x	x		
CBN 8.22.06#3	Orange Hem. & Micro-conc.	N36 59.045' W112 00.144'	5703	x	x		
CBN 8.22.06#4	Orange Hem. & Micro-conc.	N36 59.183' W112 00.074'	5670	x		x	
CBN 8.22.06#5	Orange Hem. & Micro-conc.	N36 59.293' W112 00.191'	5678	x			
CBN 8.22.06#6	Bleached	N36 59.208' W112 00.299'	5716	x	x	x	
CBN 8.22.06#7	Bleached	N36 59.238' W112 00.389'		x			
CBN 8.22.06#8	Orange Hem. & Micro-conc.	N36 59.399' W112 00.354'	7677	x	x		
CBN 12.18.06#1	Bleached	N36 59.458' W112 00.500'		x	x		
CBN 12.18.06#2	Orange Hem. & Micro-conc.	N36 59.548' W112 00.430'		x			
CBN 12.18.06#3	Orange Hem. & Micro-conc.	N36 59.574' W112 00.406'	5535	x			
CBN 12.18.06#4	Orange Hem. & Micro-conc.	N36 59.567' W112 00.414'	5537	x			
CBN 12.18.06#5	Bleached	N36 59.567' W112 00.414'	5537	x	x		
CBN 12.18.06#6	Bleached	N36 59.550' W112 00.371'	5615	x			
CBN 12.18.06#7	Orange Hem. & Micro-conc.	N36 59.686' W112 00.275'	5522	x			
CBN 12.18.06#8	Orange Hem. & Micro-conc.	N36 59.682' W112 00.267'	5498				
CBN 12.18.06#9	Bleached	N37 00.284' W112 00.488'	5143	x	x	x	
CBN 12.18.06#10	Red & White Banded	N37 00.759' W112 00.608'	5048	x	x		
CBN 12.20.06#1	Variable Lies./Bleached	N36 59.510' W112 00.584'	5317	x			
CBN 12.20.06#2	Bleached	N36 59.522' W112 00.577'	5335	x			
CBN 12.20.06#3	Variable Lies./Bleached	N36 59.526' W112 00.571'	5339	x			
CBN 12.20.06#4	Variable Lies./Red & White	N36 59.441' W112 00.590'	5275	x			
CBN 12.20.06#5	Variable Lies./Red & White	N36 59.441' W112 00.590'	5275	x	x		
CBN 12.20.06#6	Upper Red	N36 59.183' W112 01.177'	5508	x	x	x	
CBN 12.21.06#1	Variable Lies./Basal Red	N36 59.607' W112 00.216'	5325	x			
CBN 12.21.06#2	Variable Lies./Basal Red	N36 59.506' W111 59.923'	5263	x	x		

Micro-conc. = micro-concretion; Hem. = hematite; Variable Lies./Bleached = variable Liesegang facies overprinted atop bleached facies  
 Variable Lies./Red & White = variable Liesegang facies overprinted atop red and white banded facies

Table A.1 Continued

Sample ID	Facies	Location	Elevation (ft)	Spectra	Thin Section	SEM	Sieved
CBN 12.21.06#3	Basal Red	N36 59.508' W111 59.939'	5233	x	x		
CBN 12.21.06#4	Basal Red	N36 59.665' W112 00.106'	5148	x	x		
CBN 12.21.06#5	Bleached	N36 59.574' W112 00.277'		x			
CBN 12.21.06#6	Variable Lies./Red & White	N36 59.733' W112 00.387'	5269	x	x	x	
CBN 12.21.06#7	Red & White Banded	N36 59.708' W112 00.347'	5262	x			
CBN 12.22.06#1	Basal Red	N37 00.596' W112 00.689'		x	x	x	
CBN 4.25.07#1	Basal Red	N36 58.797' W112 00.787'		x			
CBN 4.25.07#2	Basal Red	N36 58.829' W112 00.812'		x			
CBN 4.26.07#1	Red & White Banded	N37 00.578' W112 00.655'		x			
CBN 4.26.07#2	Red & White Banded	N37 00.624' W112 00.709'		x	x		
CBN 4.29.07#1	Red & White Banded	Measured Section 4- 22m		x			
CBN 4.29.07#2	Red & White Banded	Measured Section 4- 31m		x			
CBN 4.29.07#3	Red & White Banded	Measured Section 4- 35.5m			x		
CBN 4.30.07#1	Variable Lies./Bleached	Measured Section 4- 70.5m		x	x		
CBN 5.1.07#1	Variable Lies./Bleached	Measured Section 4- 139m		x	x		
CBN 5.1.07#2	N/A	N36 59.456' W112 00.339'	5632				
CBN 5.2.07#1	Bleached	N37 00.519' W112 00.511'	5165	x			
CBN 5.2.07#2	Red & White Banded	N37 00.332' W112 00.541'	5138	x	x		
CBN 5.2.07#3	Red & White Banded	N37 00.348' W112 00.551'	5125				
CBN 5.2.07#4	Red & White Banded	N37 00.303' W112 00.555'	5135		x		
CBN 5.2.07#5	N/A	Measured Section 3- 105m					
CBN 5.2.07#6	Bleached	N36 59.717' W112 00.337'	5285	x			
CBN 12.18.07#1	Upper Red	N37 00.393' W112 01.030'	5335	x			
CBN 12.18.07#2	Basal Red	N35 59.679' W111 59.863'	5141	x			
CBN 12.19.07#1	Bleached	N36 39.228' W112 01.250'	5463	x			
CBN 12.19.07#2	Upper Red	N36 59.158' W112 01.197'	5518	x			
CBN 12.19.07#3	Upper Red	N36 59.411' W112 01.114'	5676	x	x		
CBN 12.19.07#4	Upper Red	N36 58.791' W112 00.667'	5801	x	x		
CBN 12.19.07#5	Upper Red	N36 58.615' W112 00.588'	5896	x			
CBN 12.20.07#1	Upper Red	N37 00.015' W112 00.790'	5702	x	x		
CBN 12.20.07#2	Upper Red	N36 59.942' W112 00.847'	5745	x			
CBN 12.20.07#3	Upper Red	N36 59.942' W112 00.847'	5745	x			

Micro-conc. = micro-concretion; Hem. = hematite; Variable Lies./Bleached = variable Liesegang facies overprinted atop bleached facies  
 Variable Lies./Red & White = variable Liesegang facies overprinted atop red and white banded facies

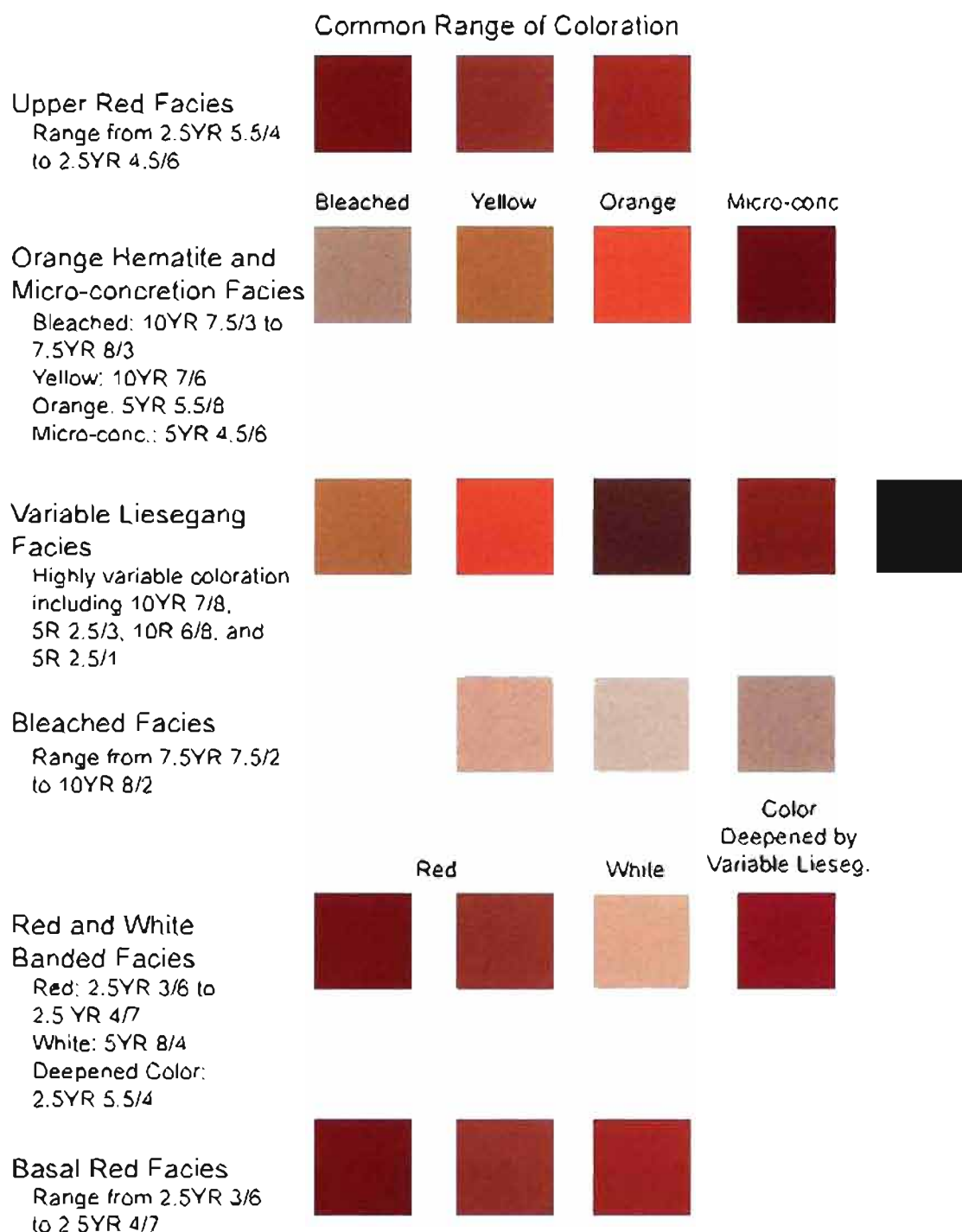


Figure A.1. Common coloration of Coyote Buttes diagenetic facies. Total variation in sandstone coloration exceeds the generalized representative sampling displayed, but the most typical colors are indicated here. Color palette is fairly representative of observed color range and was reproduced from field photographs taken in similar lighting conditions. Munsell coloration is noted beneath each facies. Exact digital conversion of Munsell coloration is difficult due to digital processing and printing variations. Micro-conc. = micro-concretion; Lieseg. = Liesegang.

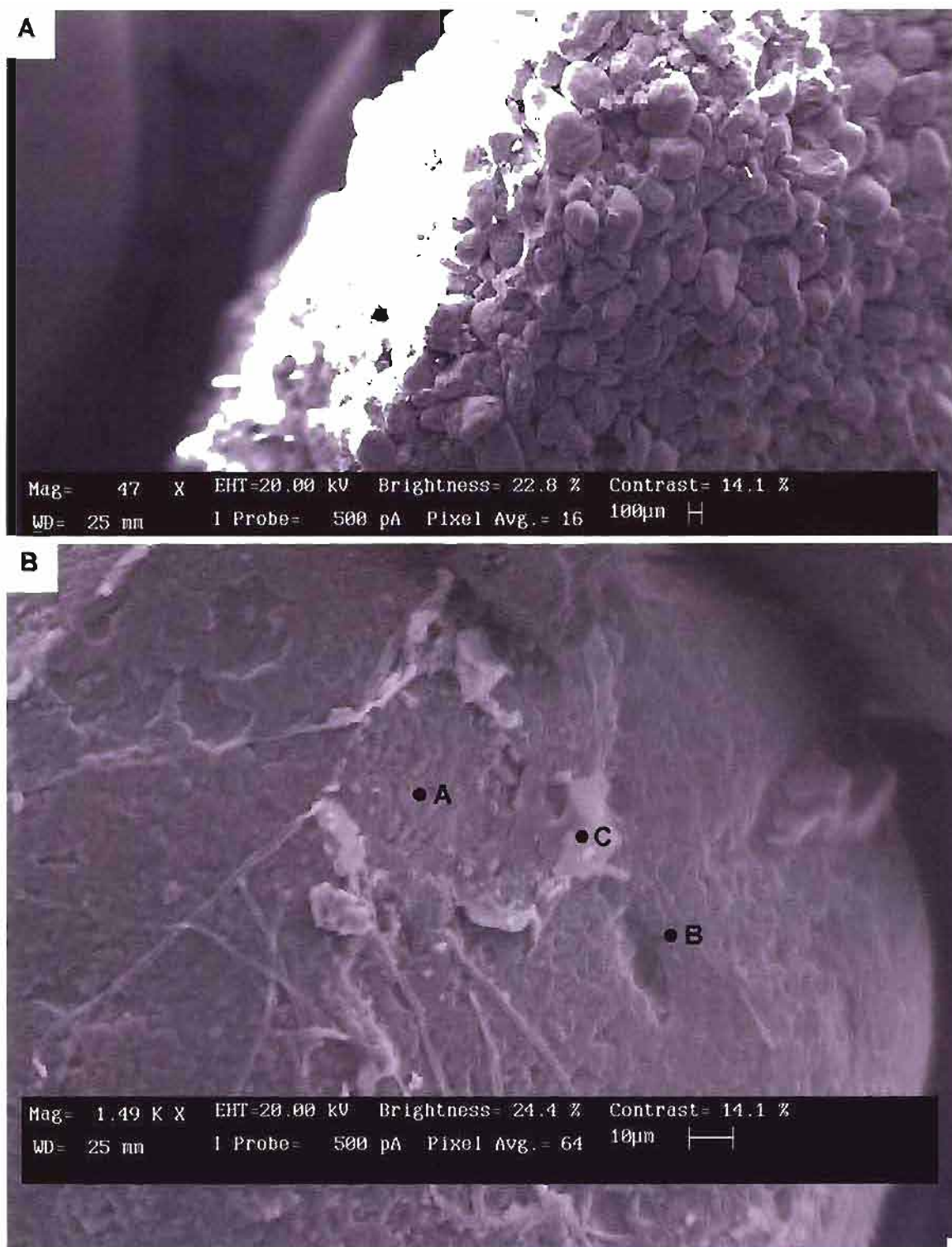


Figure A.2. SEM image of sample CBN 7.20.06#1. A) Overall sandstone texture at 47X magnification. B) Single grain at 1,490X magnification. Letters A, B, and C correspond to location of EDAX analysis reported in Tables A.2 – A.4. Locations A and B mark likely iron oxide graincoats, location C marks remnant intergranular quartz cement.

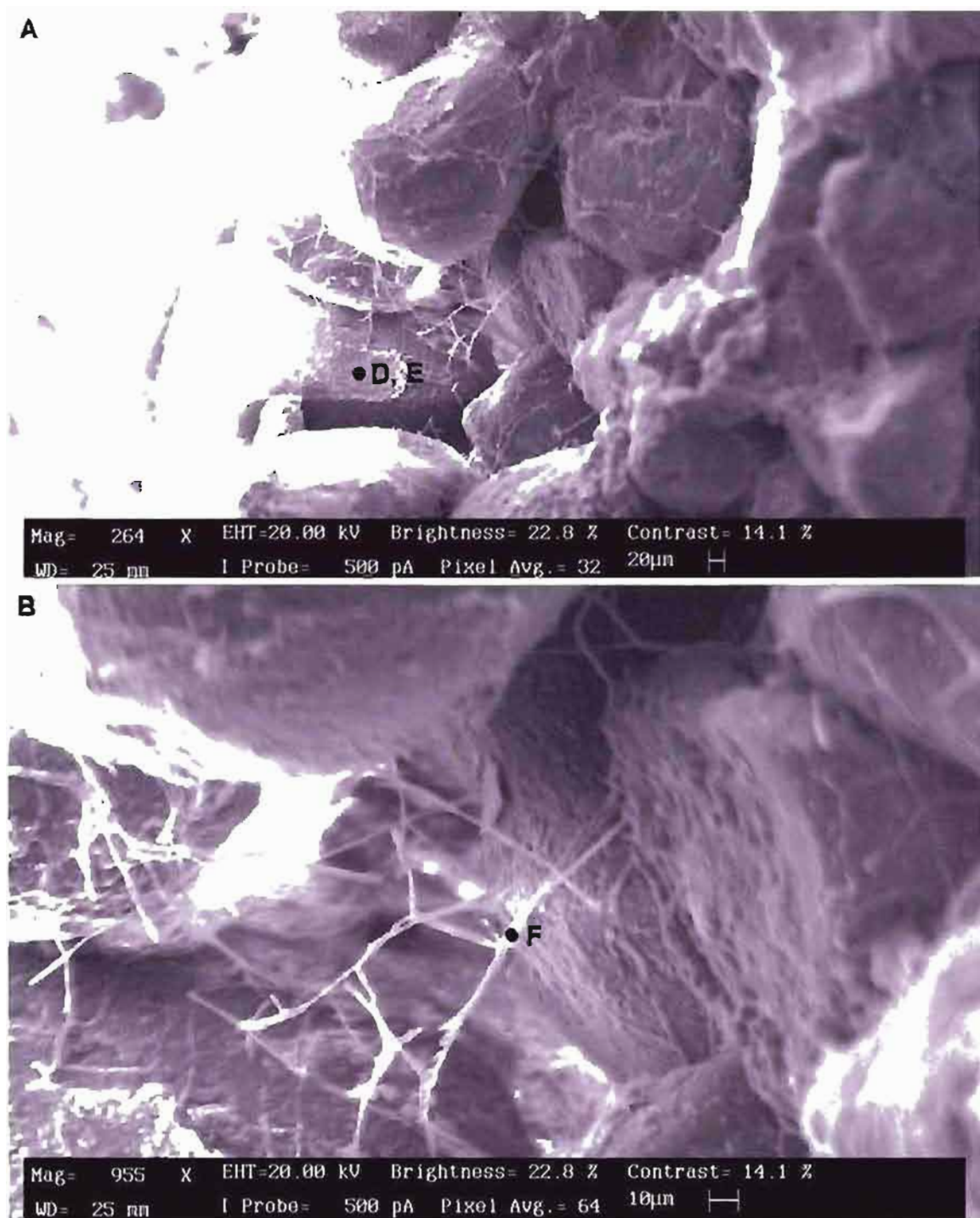


Figure A.3. SEM image of carbon-rich fibers in sample CBN 7.20.06#1. A) Locations D and E correspond with Tables A.5 and A.6. B) Location F corresponds with Table A.7 and is on an organic fiber.



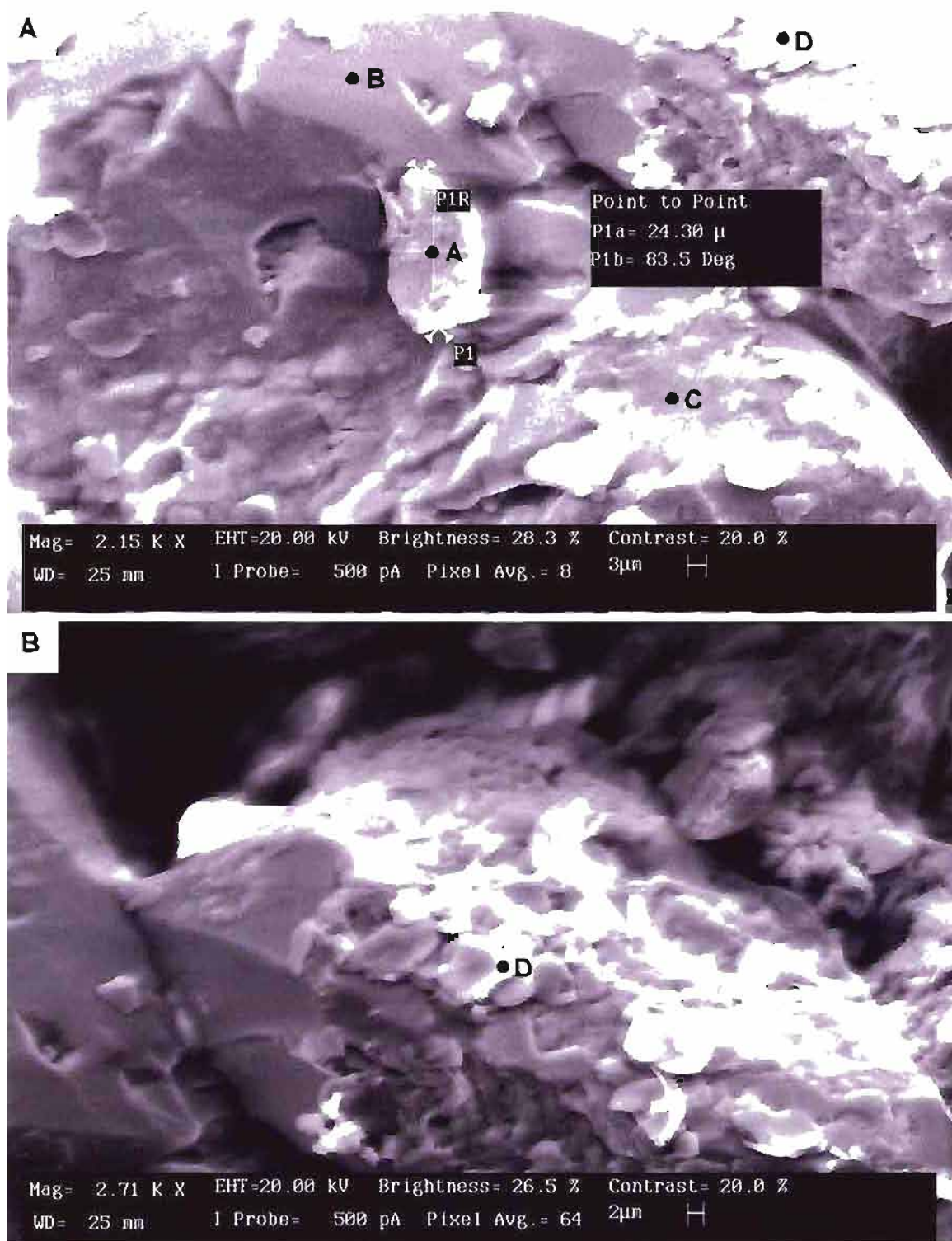


Figure A.4. SEM image of sample CBN 7.22.06#2. A) Letters correspond to locations of EDAX analyses reported in Tables A.8 - A.11. Point B is a clean face of a quartz crystal; Points A, C are quartz overgrowths with minor Aluminum; Point D is a clay overgrowth. B) Location D is on the same grain in both image A and B.

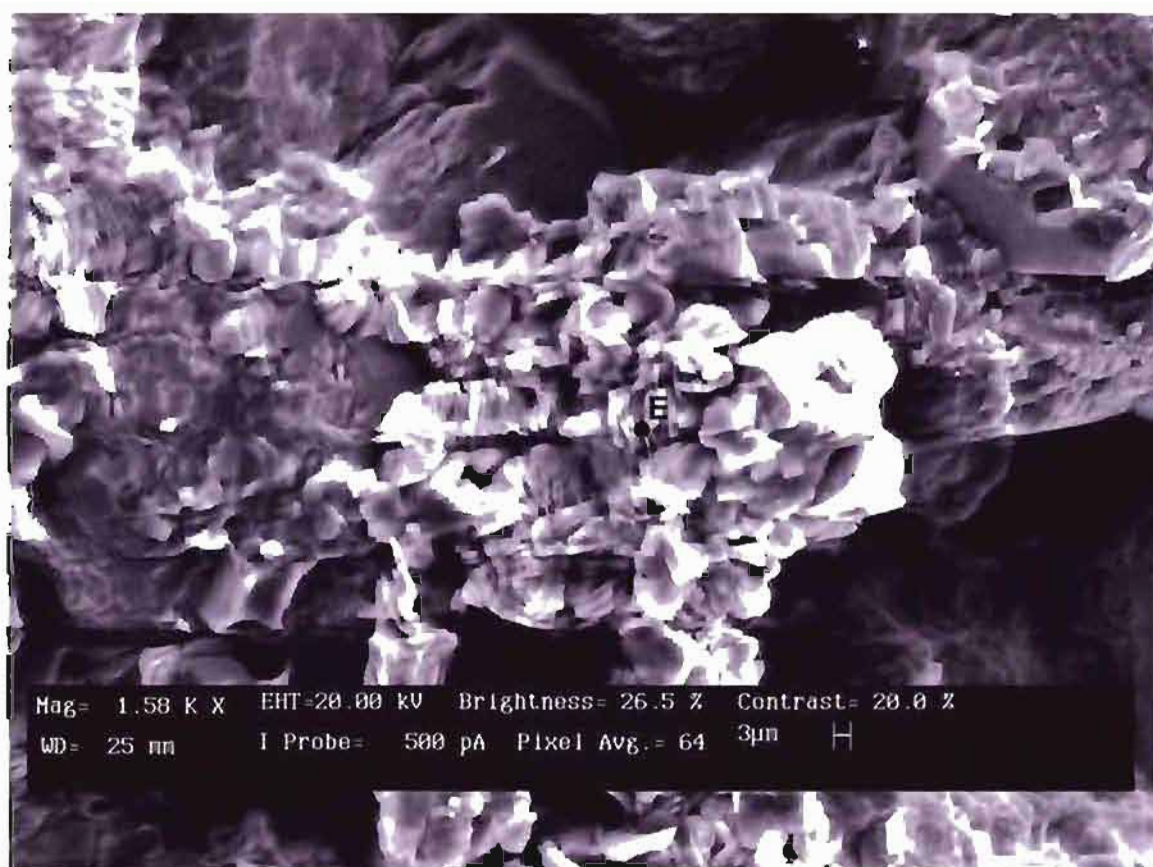


Figure A.5. SEM image of sample CBN 7.22.06#2. Letter E corresponds to EDAX analysis reported in Table A.12. Platelets are likely clay overgrowths atop quartz grains.



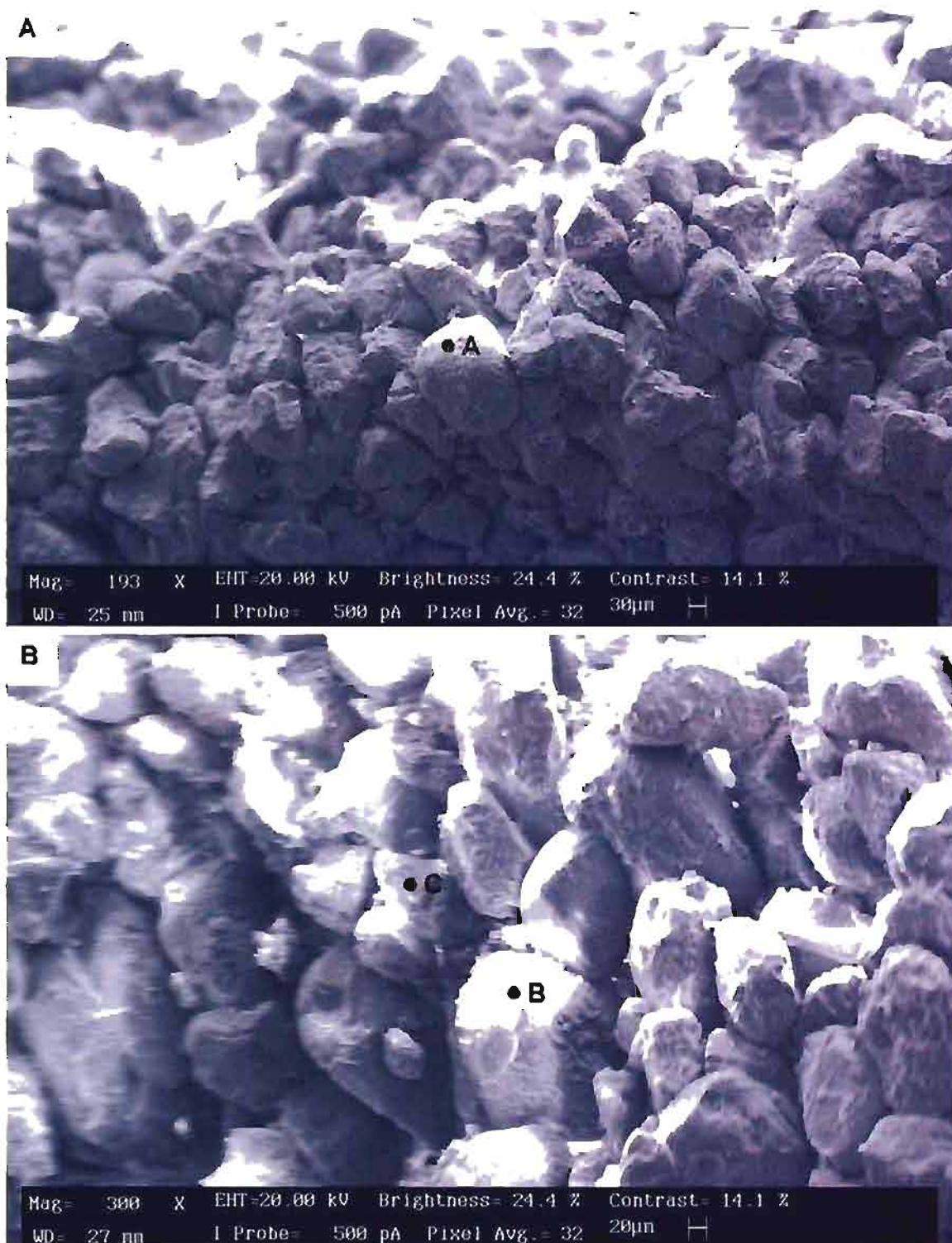


Figure A.6. SEM image of bleached sample CBN 12.18.06#9. A) Frosted quartz grain texture at 193X magnification. Letter A corresponds to EDAX analysis reported in Table A.14. B) Close-up of quartz grains with possible clay grain coats at 300X magnification. Letters B and C correspond to EDAX analyses reported in Tables A.15 and A.16.



Figure A.7. SEM image of variable Liesegang atop red and white banded sample CBN 12.21.06#6. Letter A and B corresponds to EDAX analyses reported in Tables A.17 and A.18. Textured iron oxide grain coating imaged throughout, best viewed at right (arrow).



Figure A.8. SEM image of sample CBN 12.21.06#3.



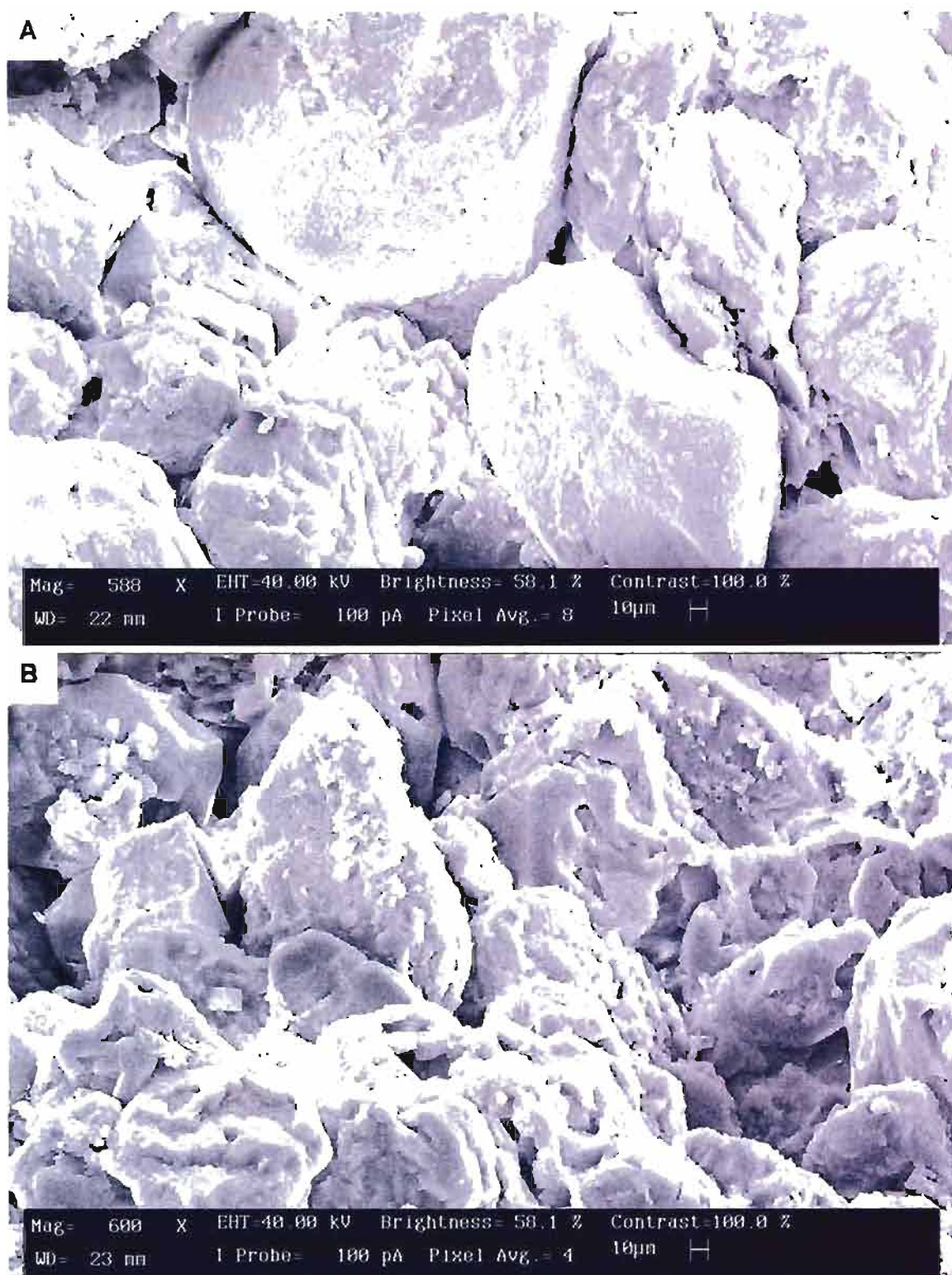


Figure A.9. SEM image of orange hematite and micro-concretion facies sample CBN 8.22.06#4. A) Grains display both euhedral overgrowths (iron oxide?) and overgrowth-free grains. B) Euhedral overgrowths (iron oxide?) are pervasive. EDAX analysis not performed.

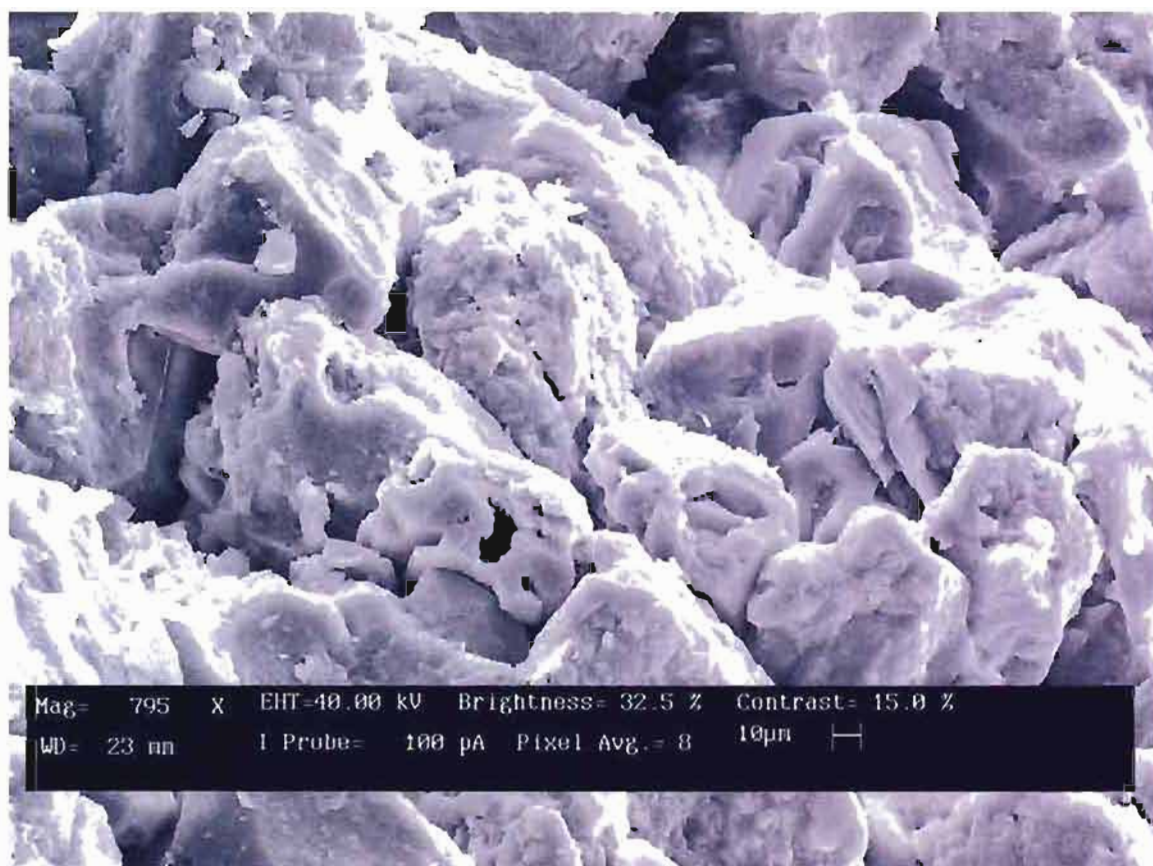


Figure A.10. SEM image of orange hematite and micro-concretion facies sample CBN 8.22.06#4. Euhedral overgrowths (iron oxide?) are pervasive. EDAX analysis not performed.

Table A.2

## EDAX Analysis, Sample CBN 7.20.06#1 Location A

Element	Apparent Conc.	Stat. Sigma	Inten. Corr.	Std. Corr.	Element %	Sigma %	Atomic %
O	5.28	0.27	1.03	0.70	5.13	0.26	56.66
Al	0.09	0.04	0.72	0.94	0.12	0.06	0.78
Si	3.52	0.10	0.81	1.01	4.33	0.12	27.22
K	0.21	0.06	1.01	0.99	0.21	0.06	0.94
Fe	3.98	0.30	0.87	1.00	4.55	0.34	14.40

Conc. = concentration; Stat. = statistical; Inten. Corr. = intensity correction; Std. = standard

Table A.3

## EDAX Analysis, Sample CBN 7.20.06#1 Location B

Element	Apparent Conc.	Stat. Sigma	Inten. Corr.	Std. Corr.	Element %	Sigma %	Atomic %
O	5.83	0.27	1.01	0.70	5.76	0.26	69.93
Al	0.18	0.04	0.81	0.94	0.22	0.05	1.62
Si	2.95	0.09	0.88	1.01	3.37	0.10	23.31
K	0.28	0.05	0.99	0.99	0.28	0.05	1.40
Fe	0.91	0.16	0.85	1.00	1.08	0.18	3.75

Conc. = concentration; Stat. = statistical; Inten. Corr. = intensity correction; Std. = standard

Table A.4

## EDAX Analysis, Sample CBN 7.20.06#1 Location C

Element	Apparent Conc.	Stat. Sigma	Inten. Corr.	Std. Corr.	Element %	Sigma %	Atomic %
O	8.78	0.33	1.09	0.70	8.09	0.31	74.11
Al	0.07	0.04	0.83	0.94	0.08	0.05	0.43
Si	3.96	0.10	0.91	1.01	4.37	0.11	22.79
K	0.18	0.05	0.99	0.99	0.18	0.05	0.69
Fe	0.64	0.15	0.84	1.00	0.76	0.18	1.99

Conc. = concentration; Stat. = statistical; Inten. Corr. = intensity correction; Std. = standard

Table A.5

## EDAX Analysis, Sample CBN 7.20.06#1 Location D

Element	Apparent Conc.	Stat. Sigma	Inten. Corr.	Std. Corr.	Element %	Sigma %	Atomic %
O	145.95	1.72	1.00	0.70	145.89	1.72	69.96
Al	4.14	0.27	0.88	0.94	4.73	0.31	1.34
Si	91.37	0.66	0.92	1.01	98.96	0.72	27.03
K	2.83	0.27	0.97	0.99	2.92	0.28	0.57
Fe	6.62	0.51	0.84	1.00	7.92	0.61	1.09

Conc. = concentration; Stat. = statistical; Inten. Corr. = intensity correction; Std. = standard

Table A.6

## EDAX Analysis, Sample CBN 7.20.06#1 Location E

Element	Apparent Conc.	Stat. Sigma	Inten. Corr.	Std. Corr.	Element %	Sigma %	Atomic %
O	169.99	2.18	1.00	0.70	170.59	2.19	69.92
Al	6.70	0.38	0.88	0.94	7.66	0.43	1.86
Si	103.32	0.84	0.91	1.01	113.04	0.92	26.39
K	4.09	0.36	0.97	0.99	4.21	0.37	0.71
Fe	7.97	0.69	0.84	1.00	9.54	0.82	1.12

Conc. = concentration; Stat. = statistical; Inten. Corr. = intensity correction; Std. = standard

Table A.7

## EDAX Analysis, Sample CBN 7.20.06#1 Location F

Element	Apparent Conc.	Stat. Sigma	Inten. Corr.	Std. Corr.	Element %	Sigma %	Atomic %
C	8.36	0.71	0.34	1.25	24.45	2.09	16.68
O	122.23	1.44	0.94	0.70	130.29	1.53	66.71
Al	8.09	0.26	0.84	0.94	9.62	0.31	2.92
Si	35.30	0.40	0.87	1.01	40.53	0.46	11.82
K	4.74	0.26	1.03	0.99	4.58	0.25	0.96
Fe	5.25	0.43	0.85	1.00	6.21	0.51	0.91

Conc. = concentration; Stat. = statistical; Inten. Corr. = intensity correction; Std. = standard

Table A.8

## EDAX Analysis, Sample CBN 7.22.06#2 Location A

Element	Apparent Conc.	Stat. Sigma	Inten. Corr.	Std. Corr.	Element %	Sigma %	Atomic %
O	268.85	2.19	1.10	0.70	245.11	1.99	72.71
Al	8.74	0.33	0.81	0.94	10.83	0.40	1.91
Si	108.11	0.69	0.87	1.01	124.98	0.80	21.12
K	6.29	0.32	1.00	0.99	6.30	0.32	0.77
Fe	34.87	0.89	0.85	1.00	41.25	1.05	3.51

Conc. = concentration; Stat. = statistical; Inten. Corr. = intensity correction; Std. = standard

Table A.9

## EDAX Analysis, Sample CBN 7.22.06#2 Location B

Element	Apparent Conc.	Stat. Sigma	Inten. Corr.	Std. Corr.	Element %	Sigma %	Atomic %
O	136.66	1.29	0.94	0.70	145.46	1.37	66.19
Al	0.33	0.19	0.92	0.94	0.36	0.21	0.10
Si	125.46	0.59	0.98	1.01	128.53	0.61	33.32
K	0.50	0.19	0.95	0.99	0.53	0.20	0.10
Fe	1.91	0.34	0.83	1.00	2.30	0.41	0.30

Conc. = concentration; Stat. = statistical; Inten. Corr. = intensity correction; Std. = standard

Table A.10

## EDAX Analysis, Sample CBN 7.22.06#2 Location C

Element	Apparent Conc.	Stat. Sigma	Inten. Corr.	Std. Corr.	Element %	Sigma %	Atomic %
O	108.81	1.15	0.91	0.70	119.66	1.26	64.39
Al	5.39	0.23	0.93	0.94	5.82	0.25	1.86
Si	101.92	0.54	0.95	1.01	107.35	0.57	32.91
K	1.92	0.20	0.95	0.99	2.02	0.21	0.45
Fe	2.13	0.35	0.83	1.00	2.57	0.42	0.40

Conc. = concentration; Stat. = statistical; Inten. Corr. = intensity correction; Std. = standard



Table A.11

## EDAX Analysis, Sample CBN 7.22.06#2 Location D

Element	Apparent Conc.	Stat. Sigma	Inten. Corr.	Std. Corr.	Element %	Sigma %	Atomic %
O	131.20	1.24	0.97	0.70	135.58	1.28	67.33
Al	23.91	0.33	0.90	0.94	26.60	0.37	7.83
Si	68.61	0.46	0.84	1.01	81.79	0.55	23.14
K	4.78	0.24	0.97	0.99	4.92	0.25	1.00
Fe	4.08	0.37	0.84	1.00	4.88	0.45	0.69

Conc. = concentration; Stat. = statistical; Inten. Corr. = intensity correction; Std. = standard

Table A.12

## EDAX Analysis, Sample CBN 7.22.06#2 Location E

Element	Apparent Conc.	Stat. Sigma	Inten. Corr.	Std. Corr.	Element %	Sigma %	Atomic %
O	142.01	1.26	1.11	0.70	128.39	1.14	71.53
Al	30.98	0.34	0.88	0.94	35.32	0.38	11.67
Si	37.85	0.35	0.77	1.01	49.13	0.46	15.59
K	2.03	0.19	0.99	0.99	2.06	0.19	0.47
Fe	3.93	0.36	0.84	1.00	4.68	0.43	0.75

Conc. = concentration; Stat. = statistical; Inten. Corr. = intensity correction; Std. = standard

Table A.13

## EDAX Analysis, Sample CBN 7.22.06#2 Bulk Count

Element	Apparent Conc.	Stat. Sigma	Inten. Corr.	Std. Corr.	Element %	Sigma %	Atomic %
O	105.18	1.10	0.99	0.70	106.44	1.12	70.46
Al	6.35	0.20	0.87	0.94	7.33	0.24	2.88
Si	57.11	0.40	0.89	1.01	64.05	0.45	24.15
K	4.42	0.21	0.98	0.99	4.51	0.21	1.22
Fe	5.71	0.36	0.84	1.00	6.82	0.43	1.29

Conc. = concentration; Stat. = statistical; Inten. Corr. = intensity correction; Std. = standard

Table A.14

## EDAX Analysis, Sample CBN 12.18.06#9 Location A

Element	Apparent Conc.	Stat. Sigma	Inten. Corr.	Std. Corr.	Element %	Sigma %	Atomic %
O	234.15	1.67	1.16	0.70	201.96	1.44	77.49
Al	0.48	0.19	0.86	0.94	0.56	0.22	0.13
Si	95.00	0.52	0.93	1.01	101.75	0.56	22.24
K	0.41	0.17	0.99	0.99	0.41	0.18	0.06
Fe	0.58	0.26	0.83	1.00	0.69	0.32	0.08

Conc. = concentration; Stat. = statistical; Inten. Corr. = intensity correction; Std. = standard

Table A.15

## EDAX Analysis, Sample 12.18.06#9 Location B

Element	Apparent Conc.	Stat. Sigma	Inten. Corr.	Std. Corr.	Element %	Sigma %	Atomic %
O	120.29	1.20	0.80	0.70	150.44	1.50	70.93
Al	16.00	0.28	0.87	0.94	18.31	0.32	5.12
Si	59.46	0.43	0.87	1.01	68.64	0.49	18.44
K	27.99	0.40	1.00	0.99	27.90	0.40	5.38
Fe	0.81	0.26	0.83	1.00	0.98	0.32	0.13

Conc. = concentration; Stat. = statistical; Inten. Corr. = intensity correction; Std. = standard

Table A.16

## EDAX Analysis, Sample CBN 12.18.06#9 Location C

Element	Apparent Conc.	Stat. Sigma	Inten. Corr.	Std. Corr.	Element %	Sigma %	Atomic %
O	94.00	1.03	0.77	0.70	118.14	1.29	71.45
Al	11.16	0.23	0.87	0.94	12.81	0.27	4.59
Si	46.25	0.37	0.87	1.01	53.04	0.42	18.27
K	22.63	0.36	1.01	0.99	22.50	0.35	5.57
Fe	0.54	0.26	0.83	1.00	0.65	0.31	0.11

Conc. = concentration; Stat. = statistical; Inten. Corr. = intensity correction; Std. = standard

Table A.17

## EDAX Analysis, Sample CBN 12.21.06#6 Location A

Element	Apparent Conc.	Stat. Sigma	Inten. Corr.	Std. Corr.	Element %	Sigma %	Atomic %
O	323.73	1.97	1.60	0.70	202.98	1.23	79.89
Al	8.09	0.22	0.64	0.94	12.64	0.35	2.95
Si	11.46	0.25	0.73	1.01	15.79	0.34	3.54
K	0.74	0.22	1.09	0.99	0.68	0.20	0.11
Fe	106.03	1.14	0.89	1.00	119.80	1.29	13.51

Conc. = concentration; Stat. = statistical; Inten. Corr. = intensity correction; Std. = standard

Table A.18

## EDAX Analysis, Sample CBN 12.21.06#6 Location B

Element	Apparent Conc.	Stat. Sigma	Inten. Corr.	Std. Corr.	Element %	Sigma %	Atomic %
O	223.45	1.66	1.55	0.70	144.63	1.08	74.03
Al	2.03	0.17	0.61	0.94	3.36	0.28	1.02
Si	9.27	0.23	0.72	1.01	12.96	0.32	3.78
K	1.01	0.22	1.11	0.99	0.91	0.20	0.19
Fe	129.32	1.25	0.90	1.00	143.11	1.39	20.98

Conc. = concentration; Stat. = statistical; Inten. Corr. = intensity correction; Std. = standard

Table A.19

## Sample CBN 12.21.06#3 Bulk Count

Element	Apparent Conc.	Stat. Sigma	Inten. Corr.	Std. Corr.	Element %	Sigma %	Atomic %
O	75.24	0.91	1.07	0.70	70.08	0.85	74.50
Al	1.64	0.13	0.84	0.94	1.95	0.16	1.23
Si	32.81	0.30	0.90	1.01	36.39	0.33	22.04
K	2.00	0.15	0.99	0.99	2.02	0.15	0.88
Fe	3.73	0.28	0.84	1.00	4.46	0.34	1.36

Conc. = concentration; Stat. = statistical; Inten. Corr. = intensity correction; Std. = standard

Table A.20

## Sample CBN 12.21.06#3 Bulk Count

Element	Apparent Conc.	Stat. Sigma	Inten. Corr.	Std. Corr.	Element %	Sigma %	Atomic %
O	158.52	1.33	1.10	0.70	143.78	1.20	76.01
Al	2.63	0.18	0.84	0.94	3.11	0.21	0.98
Si	63.97	0.42	0.91	1.01	70.59	0.46	21.26
K	3.53	0.19	0.99	0.99	3.55	0.19	0.77
Fe	5.44	0.35	0.84	1.00	6.50	0.42	0.98

Conc. = concentration; Stat. = statistical; Inten. Corr. = intensity correction; Std. = standard

Table A.21

## Sample CBN 12.21.06#3 Bulk Count

Element	Apparent Conc.	Stat. Sigma	Inten. Corr.	Std. Corr.	Element %	Sigma %	Atomic %
O	74.26	1.26	0.94	0.70	78.62	1.33	70.05
Al	3.96	0.23	0.85	0.94	4.64	0.27	2.45
Si	41.39	0.46	0.89	1.01	46.48	0.52	23.59
K	5.70	0.29	0.99	0.99	5.78	0.29	2.11
Fe	5.90	0.49	0.84	1.00	7.05	0.59	1.80

Conc. = concentration; Stat. = statistical; Inten. Corr. = intensity correction; Std. = standard

Table A.22

Sample CBN 12.21.06#3 Single Grain

Element	Apparent Conc.	Stat. Sigma	Inten. Corr.	Std. Corr.	Element %	Sigma %	Atomic %
O	137.61	1.28	1.07	0.70	128.37	1.19	74.08
Al	3.92	0.20	0.85	0.94	4.59	0.24	1.57
Si	62.05	0.43	0.90	1.01	68.71	0.47	22.59
K	2.93	0.20	0.99	0.99	2.97	0.20	0.70
Fe	5.39	0.36	0.84	1.00	6.44	0.43	1.06

Conc. = concentration; Stat. = statistical; Inten. Corr. = intensity correction; Std. = standard

1. Variable Liesegang, secondary iron oxide appears as a rough, but regular grain coating (Figures A.2, A.3, and A.7).
2. Orange hematite and micro-concretion facies samples display coating-free euhedral quartz grains (Figure A.4), uneven, anhedral quartz overgrowths (Figure A.4), and clay minerals (Figures A.4 and A.5).
3. Bleached sandstone lacks iron oxide coatings and display minor clays (Figure A.6).
4. Unidentified, well-formed, euhedral crystal growths (iron oxide?) occur in the orange hematite and micro-concretion facies.

The textures revealed in the subset imaged by SEM may be applicable to the larger facies, and requires further investigation.

#### Reflectance Spectra Transects

Visible and near infrared reflectance spectra were measured to record small-scale trends in mineralogy along detailed transects of 18, variably colored samples. These fine-scale transects were performed with the foreoptic mounted 0.5-1 cm from the sample, creating a 0.15-0.30 cm field of view. Figures A.11 to A.28 document spectra measurement locations that correspond to reflectance spectroscopy files in digital format.

#### Thin Section Photomicrographs

Thin sections were created from 38 samples representing each of the six diagenetic facies (Figures A.29 to A.37). These thin sections were examined using transmitted light. Several unique features are revealed:

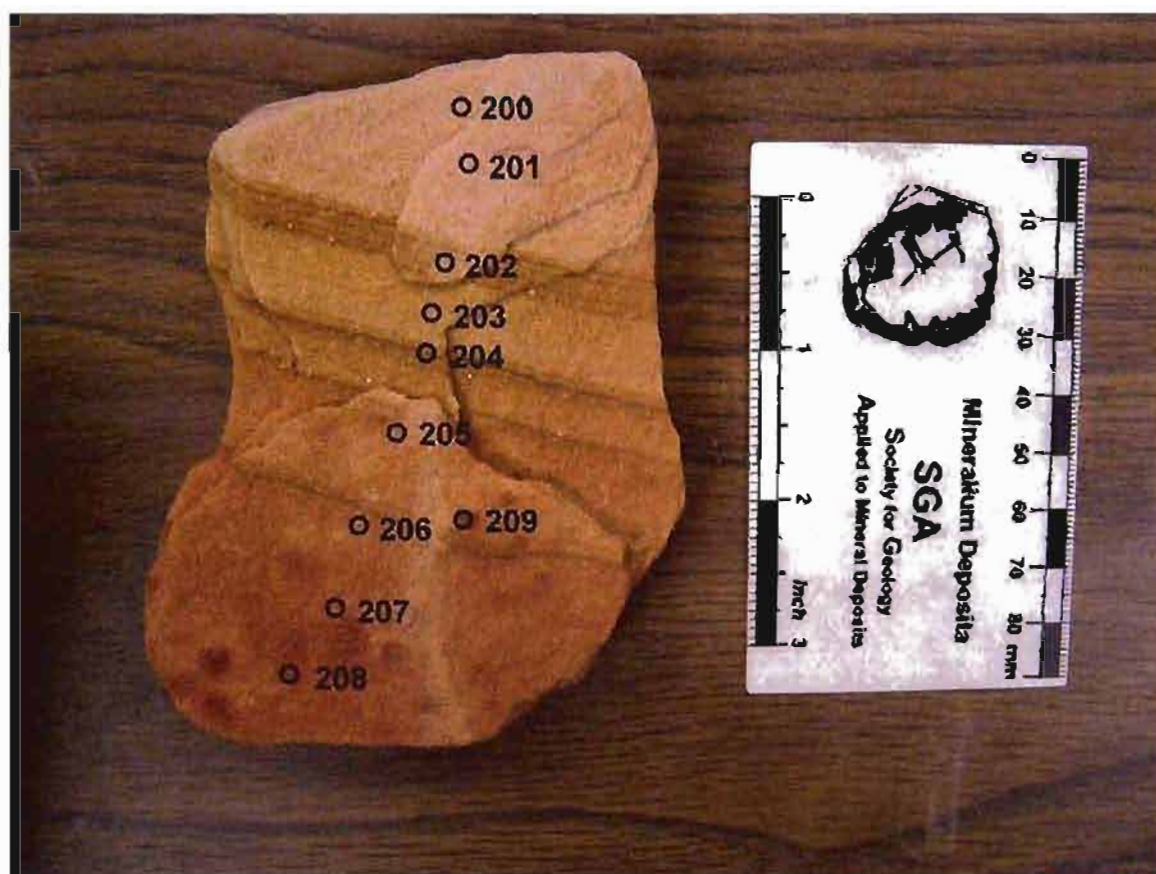


Figure A.11. Reflectance spectra transect across sample CBN 8.22.06#5. Numbers correspond to individual spectral analyses.



Figure A.12. Reflectance spectra transect across sample CBN 7.22.06#2. Numbers correspond to individual spectral analyses.



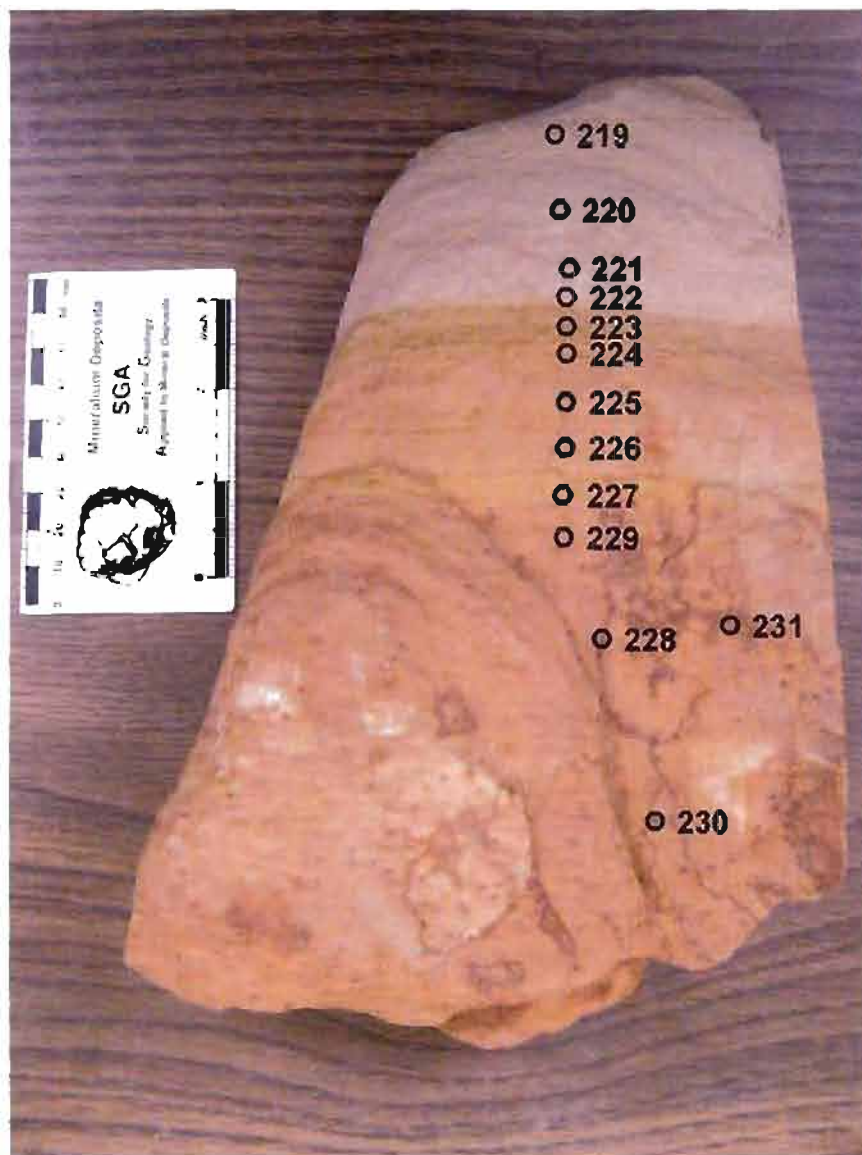


Figure A.13. Reflectance spectra transect across sample CBN 7.22.06#1. Numbers correspond to individual spectral analyses

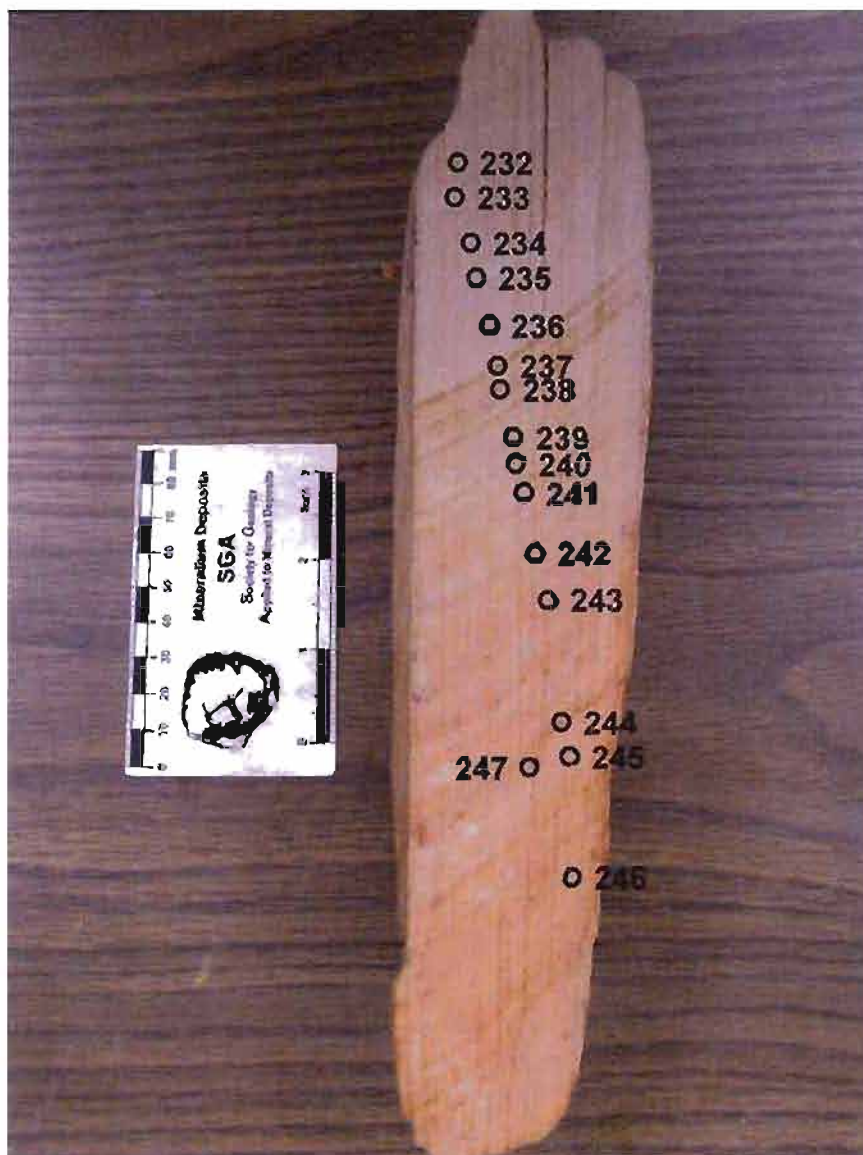


Figure A.14. Reflectance spectra transect across sample CBN 8.22.06#3. Numbers correspond to individual spectral analyses.



Figure A.15. Reflectance spectra transect across sample CBN 12.20.06#5. Numbers correspond to individual spectral analyses.





Figure A.16. Reflectance spectra transect across sample CBN 12.20.06#5. Numbers correspond to individual spectral analyses.



Figure A.17. Reflectance spectra transect across sample CBN 12.20.06#4. Numbers correspond to individual spectral analyses.



Figure A.18. Reflectance spectra transect across sample CBN 12.21.06#2. Numbers correspond to individual spectral analyses.





Figure A.19. Reflectance spectra transect across sample CBN 12.21.06#6. Numbers correspond to individual spectral analyses.

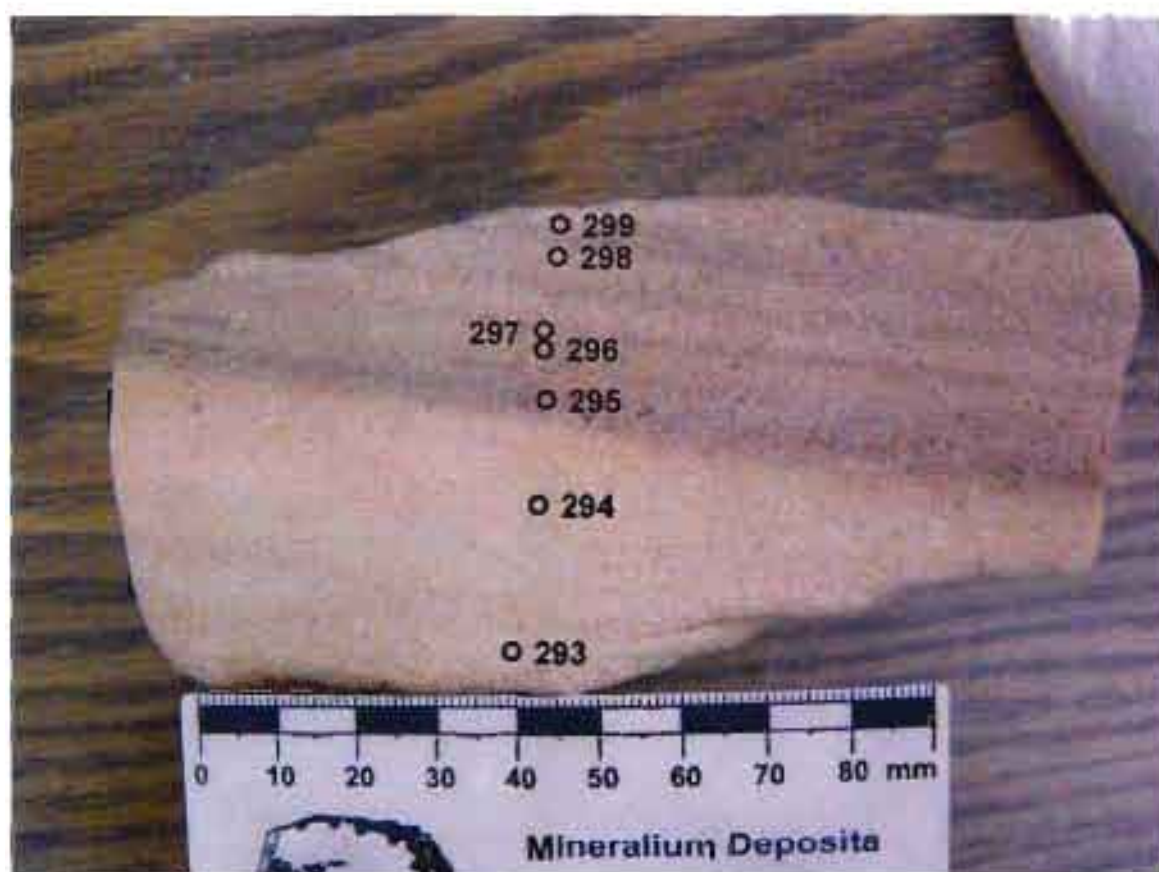


Figure A.20 Reflectance spectra transect across sample CBN 5-1.07#1. Numbers correspond to individual spectral analyses.





Figure A.21. Reflectance spectra transect across sample CBN 7.15.06#9. Numbers correspond to individual spectral analyses.

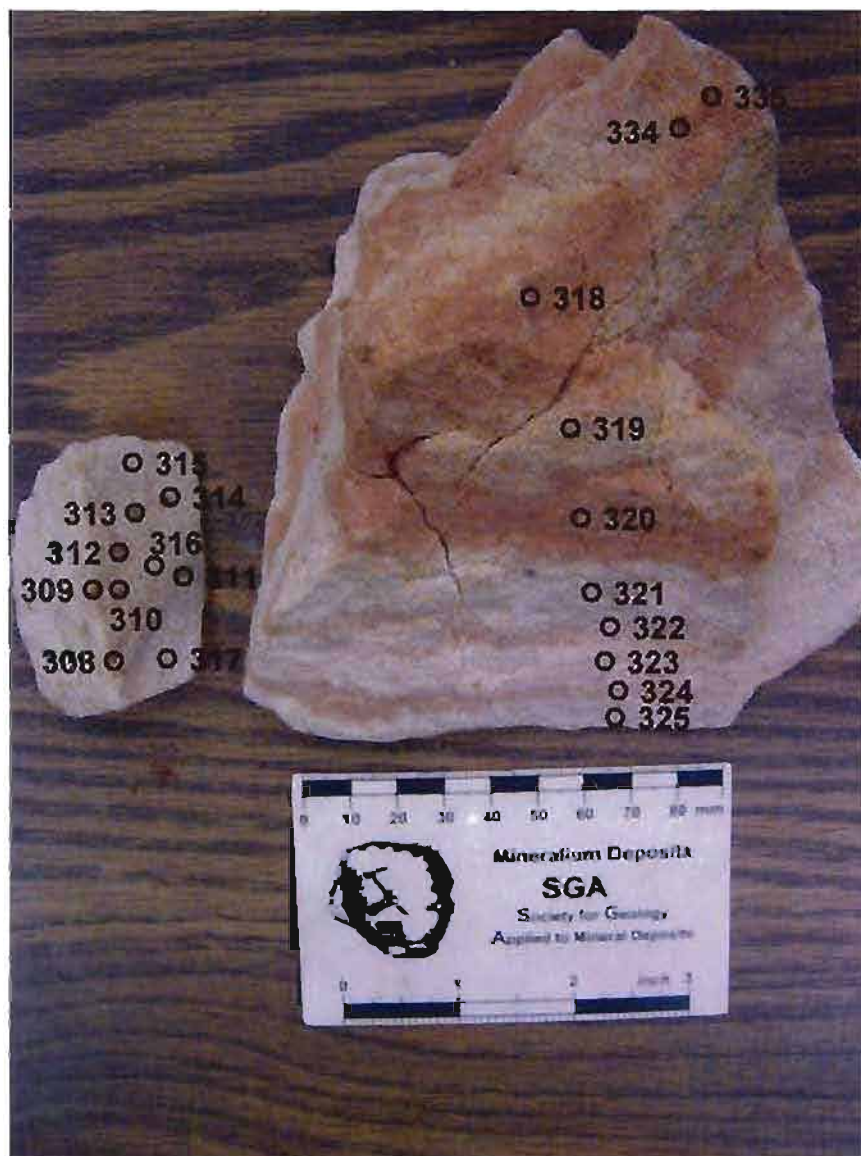


Figure A.22. Reflectance spectra transect across sample CBN 12.18.06#10. Numbers correspond to individual spectral analyses.



Figure A.23. Reflectance spectra transect across sample CBN 7.19.06#2. Numbers correspond to individual spectral analyses.



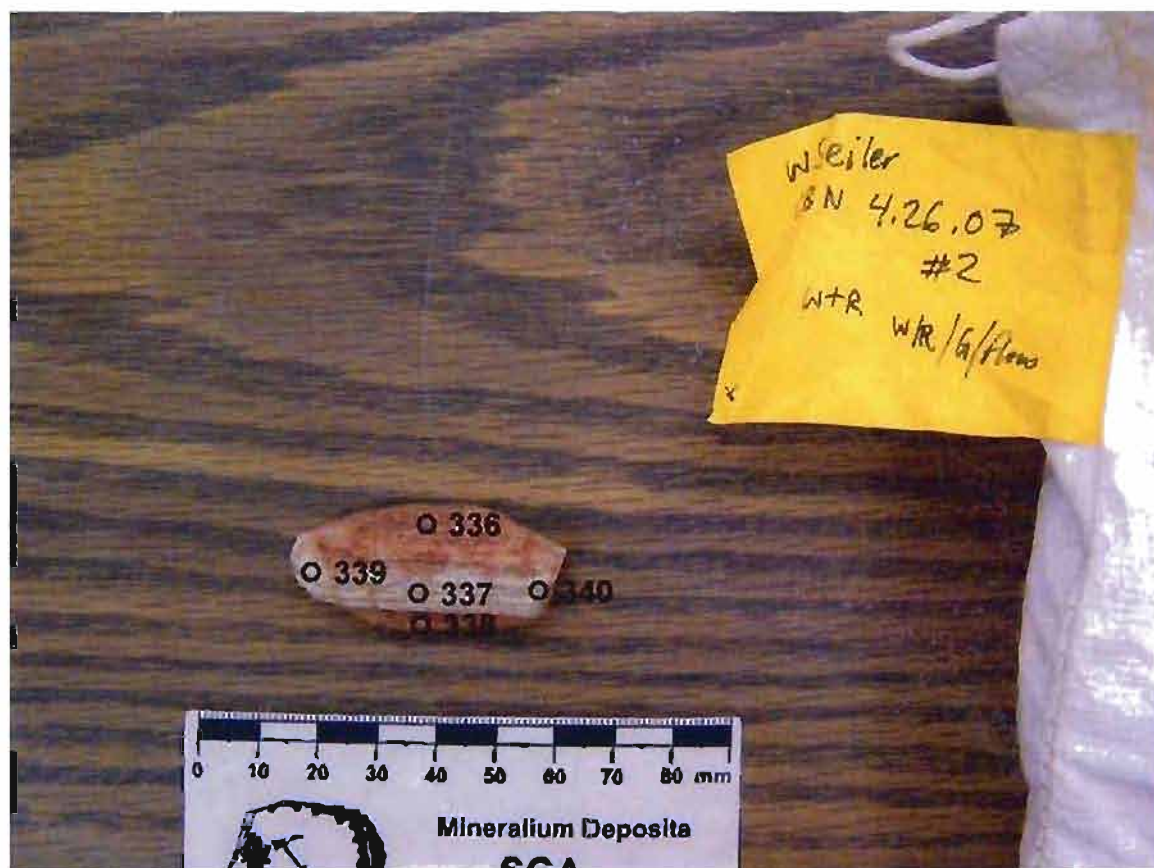


Figure A.24. Reflectance spectra transect across sample CBN 4.26.07#2. Numbers correspond to individual spectral analyses.



Figure A.25. Reflectance spectra transect across sample CBN 7.20.06#4. Numbers correspond to individual spectral analyses.



Figure A.26. Reflectance spectra transect across sample CBN 12.21.06#5. Numbers correspond to individual spectral analyses.





Figure A.27. Reflectance spectra transect across sample CBN 7.14.06#2. Numbers correspond to individual spectral analyses.



Figure A.28. Reflectance spectra transect across sample CBN 5.2.07#2. Numbers correspond to individual spectral analyses.



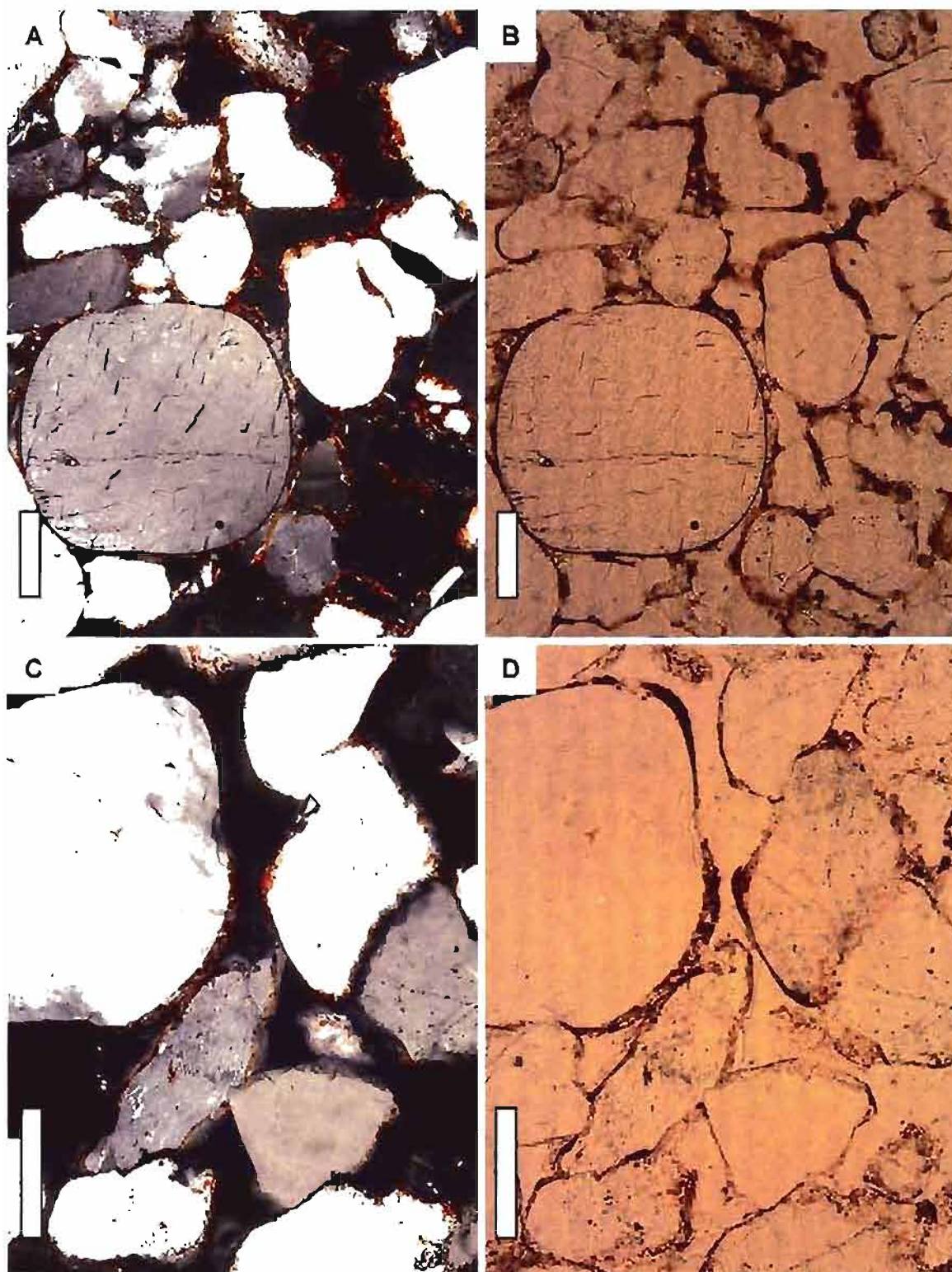


Figure A.29. Photomicrographs of basal red facies. Thin, primary hematite is "trapped" beneath early quartz overgrowths. A) Sample CBN 7.19.06#1 under cross-polarized light (XPL). B) Sample CBN 7.19.06#1 under plane-polarized light (PPL). C) Sample CBN 12.21.06#3 under XPL. D) Sample CBN 12.21.06#3 under PPL. Scale bar = 0.1 mm.



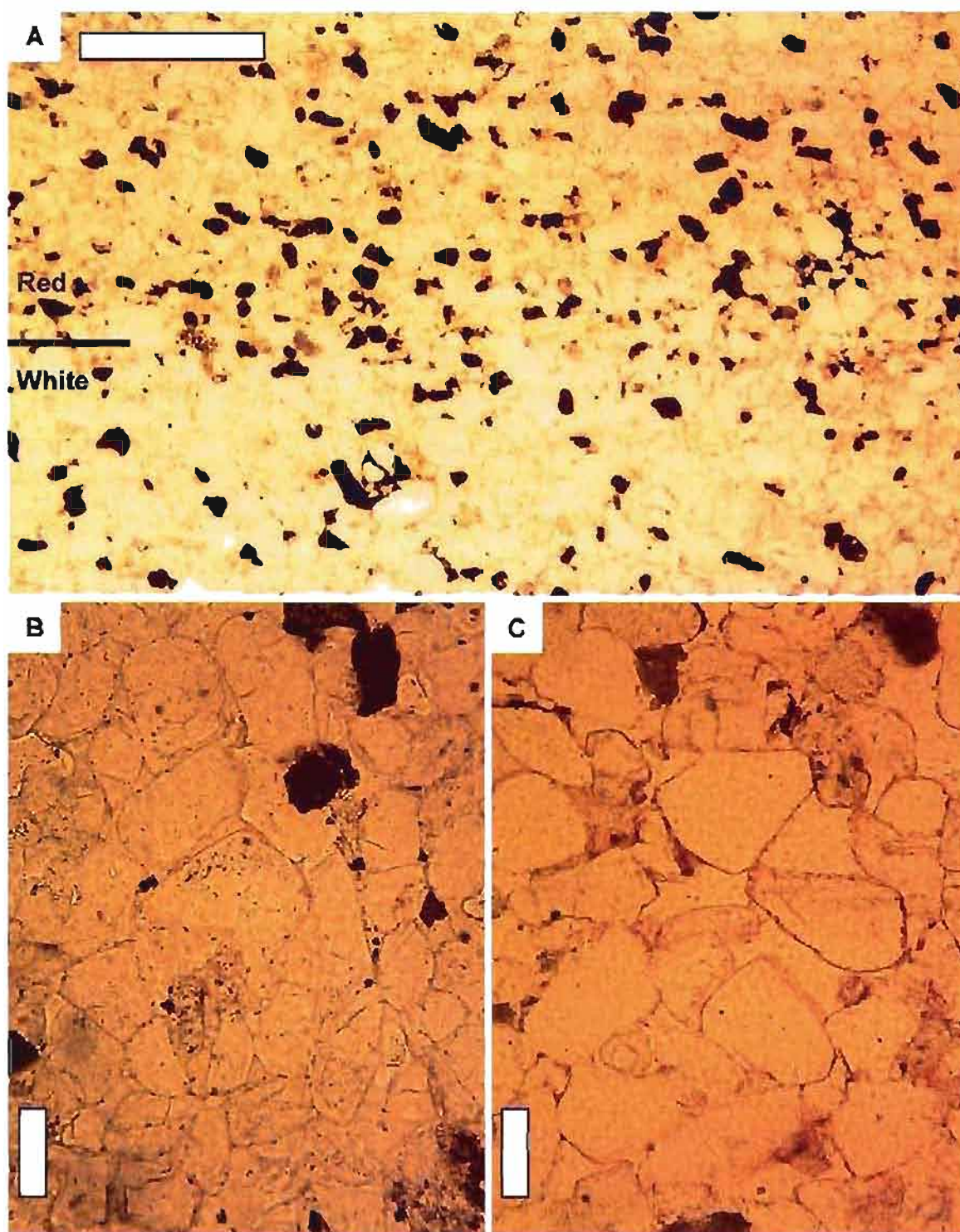


Figure A.30. Photomicrographs of red and white banded facies sample CBN 12.18.06#10. Thin section stained for potassium feldspar. A) Upper half of the thin section is in the red zone, lower half is in the white (bleached) zone. Scale bar = 1 mm. B) Bleached zone; scale bar = 0.1 mm. C) Red zone; scale bar = 0.1 mm.



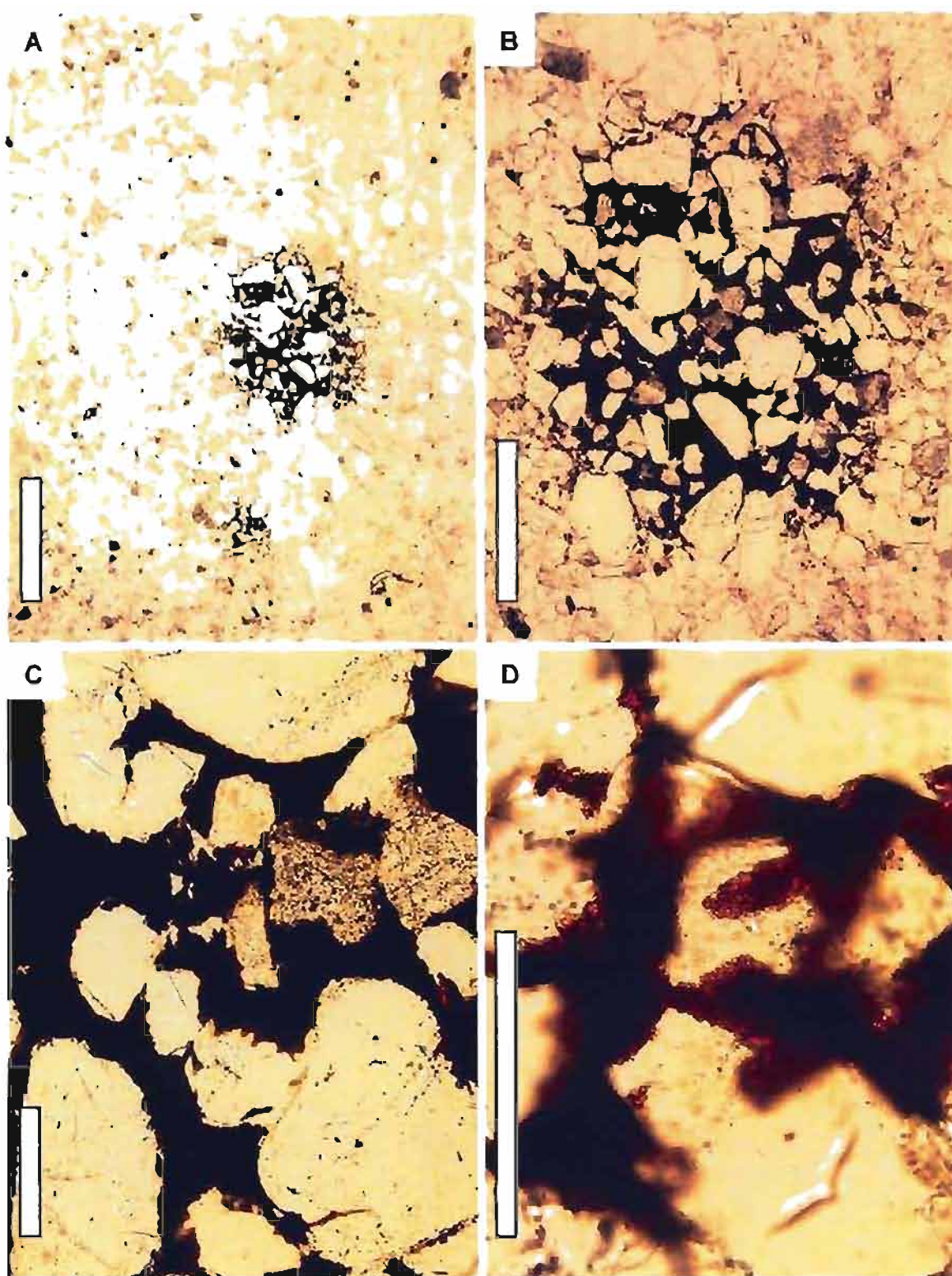


Figure A.31. Photomicrographs of a micro-concretion in the bleached facies. Images A-D successively enlarge the same iron oxide micro-concretion in sample CBN 12.18.06#5 under plane-polarized light. A) Scale bar = 1 mm. B) Scale bar = 0.5 mm. C) Scale bar = 0.1 mm. D) Scale bar = 0.1 mm.



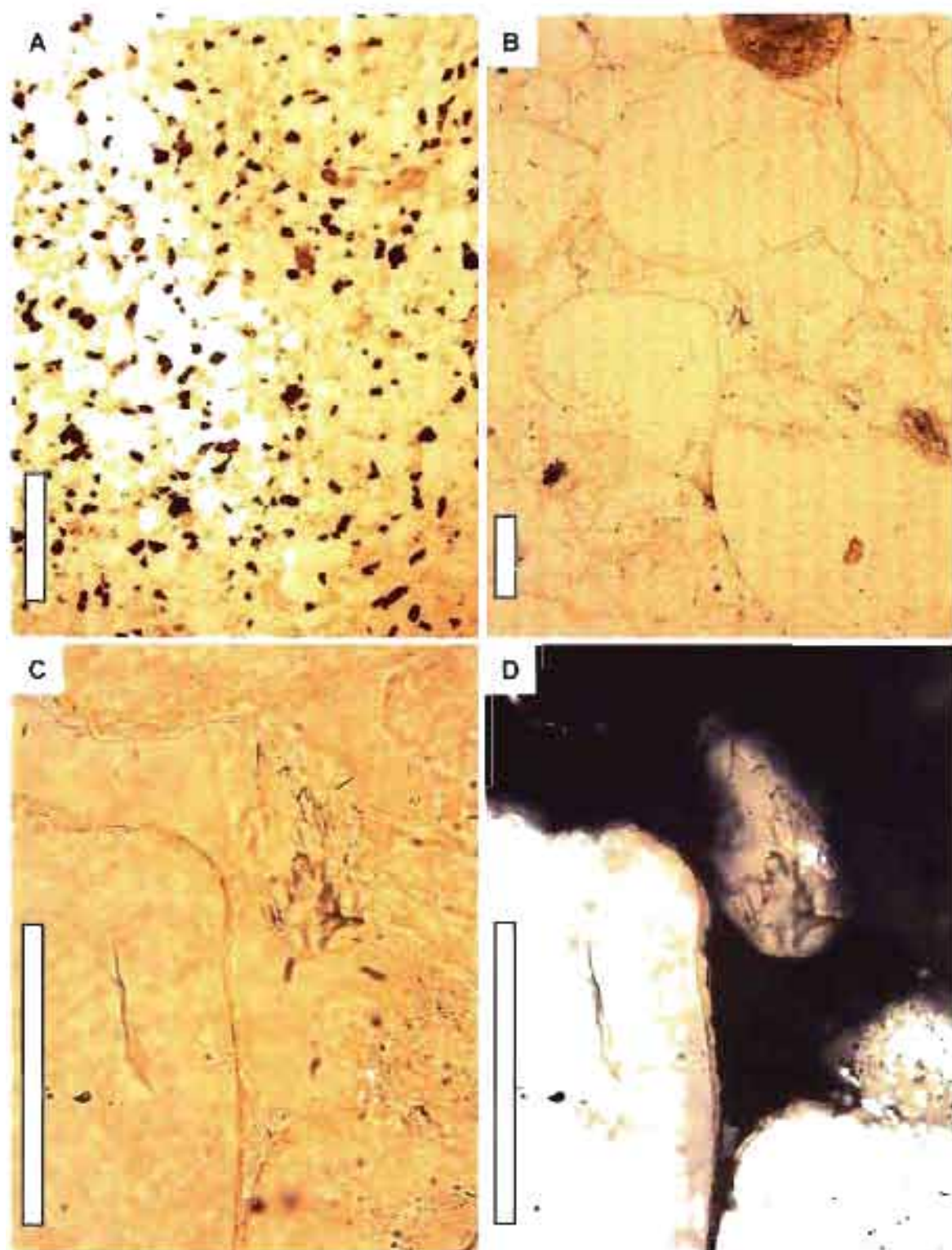


Figure A.32. Photomicrographs of bleached facies samples CBN 12.18.06#5 (A) and CBN 8.22.06#6 (B-D). A) Under plane-polarized light (PPL), stained for potassium feldspar; scale bar = 1 mm. B) Under PPL, stained for potassium feldspar (dark grain at top border); scale bar = 0.1 mm. C) Remnant iron oxide preserved only beneath quartz overgrowth; scale bar = 0.1 mm. D) Under cross-polarized light, scale bar = 0.1 mm.

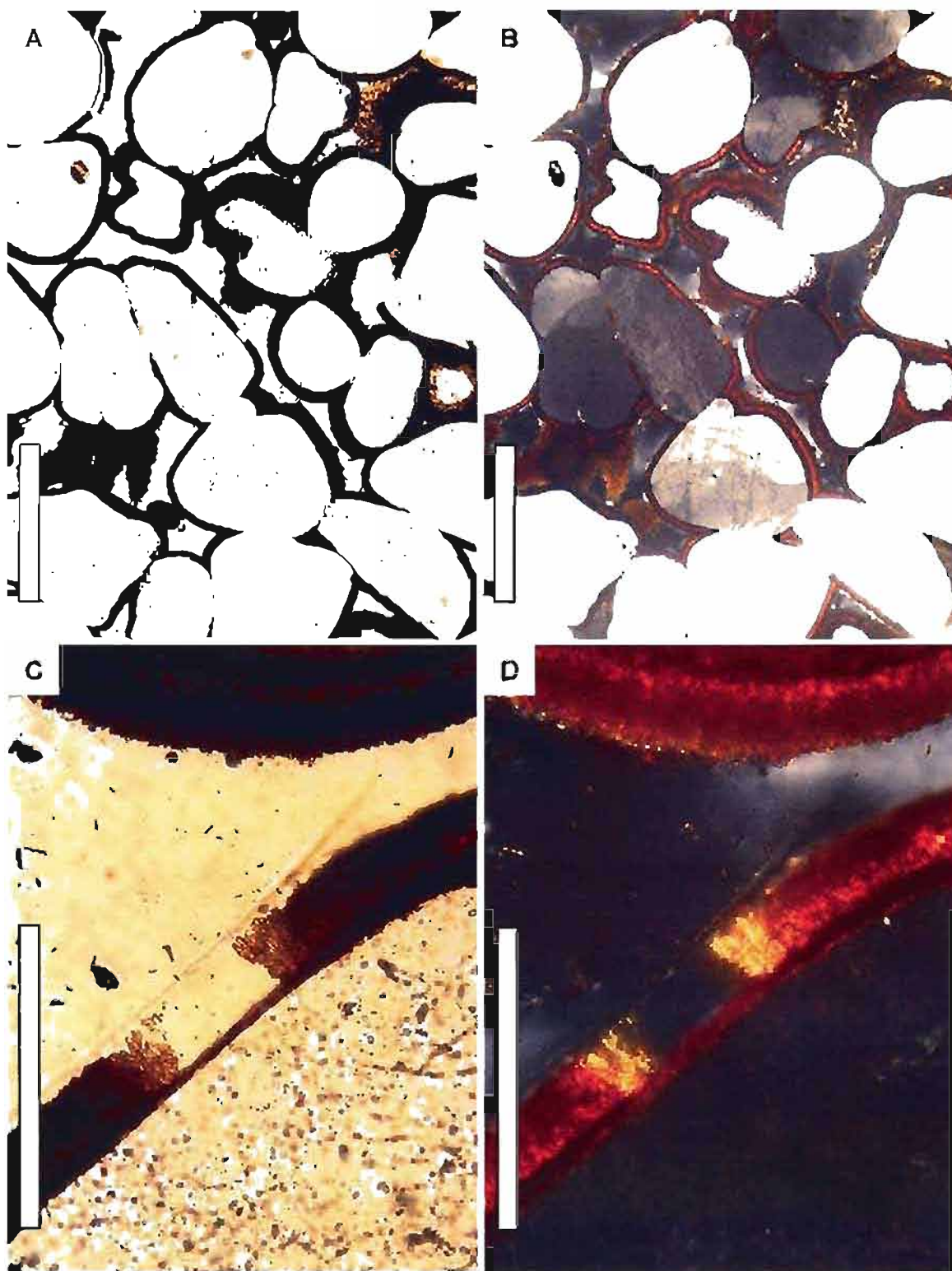


Figure A.33. Photomicrographs of variable Liesegang facies sample CBN 6.25.06#2. Secondary iron oxide occurs as radiating fibers. A) Under plane-polarized light (PPL); scale = 0.5 mm. B) Under cross-polarized light (XPL); scale = 0.5 mm. C) Under PPL; scale = 0.1 mm. D) Under XPL. Scale bar = 0.1 mm.



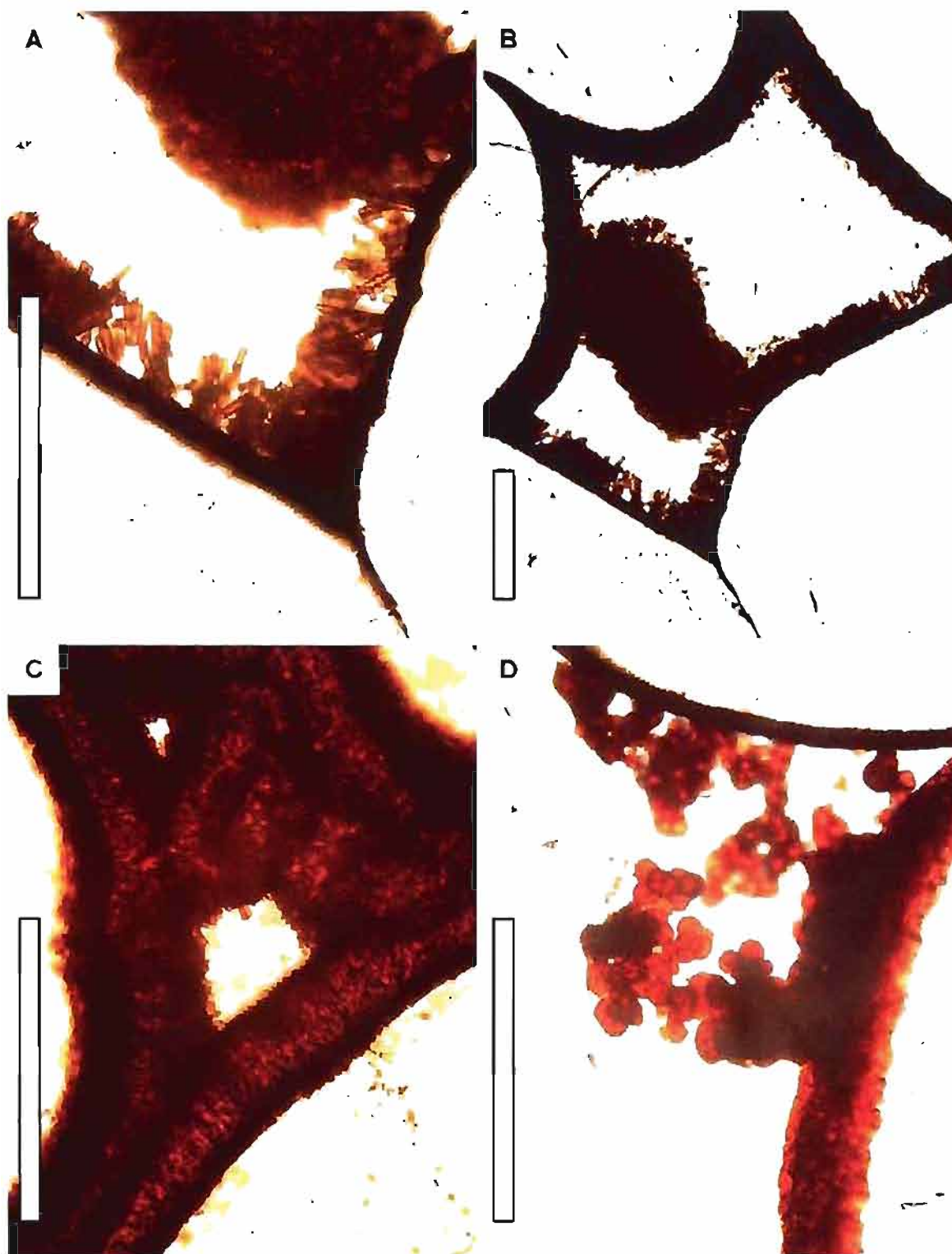


Figure A.34. Photomicrographs of iron oxide crystal growth in variable Liesegang facies samples CBN 6.25.06#2 (A-C) and CBN 12.21.06#6 (D) under plane-polarized light. A) Fibrous growth and a mass of euhedral iron oxide crystals. B) Fibrous crystals and a crystal mass filling pore space. C) Fibrous crystals. D) Euhedral iron oxide crystal platelets. Scale bar = 0.1 mm.



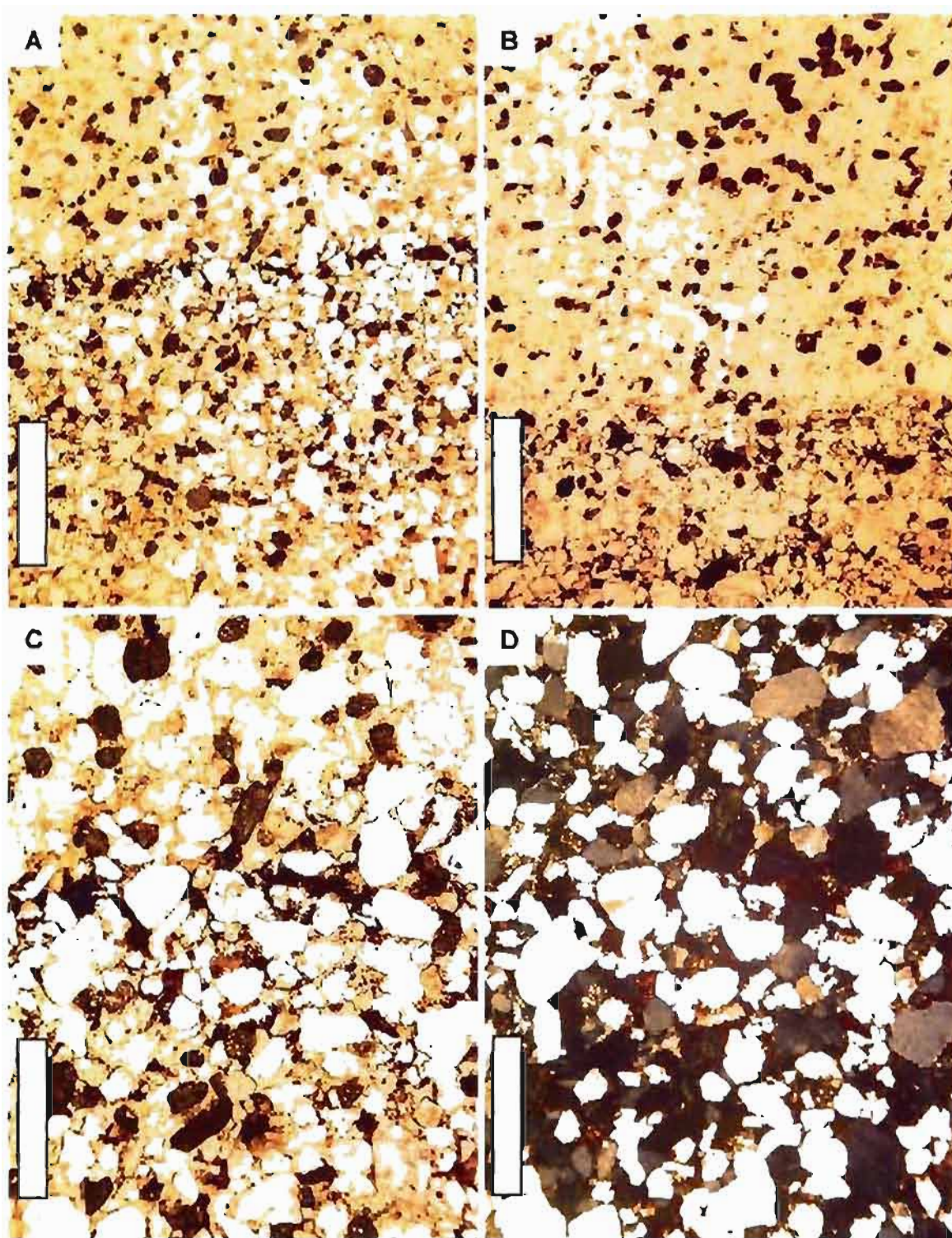


Figure A.35. Photomicrographs of orange hematite and micro-concretion facies samples CBN 8.22.06#2 (A, C, D) and CBN 7.22.06#2 (B). In each image, abrupt Liesegang banding is marked by dark brown to opaque, anhedral to euhedral, porosity filling, iron oxide crystals. Thin sections stained for potassium feldspar. A) Under plane-polarized light (PPL); scale bar = 1 mm. B) Under PPL; scale bar = 1 mm. C) Under PPL; scale bar = 0.5 mm. D) Under cross-polarized light; scale bar = 0.5 mm.



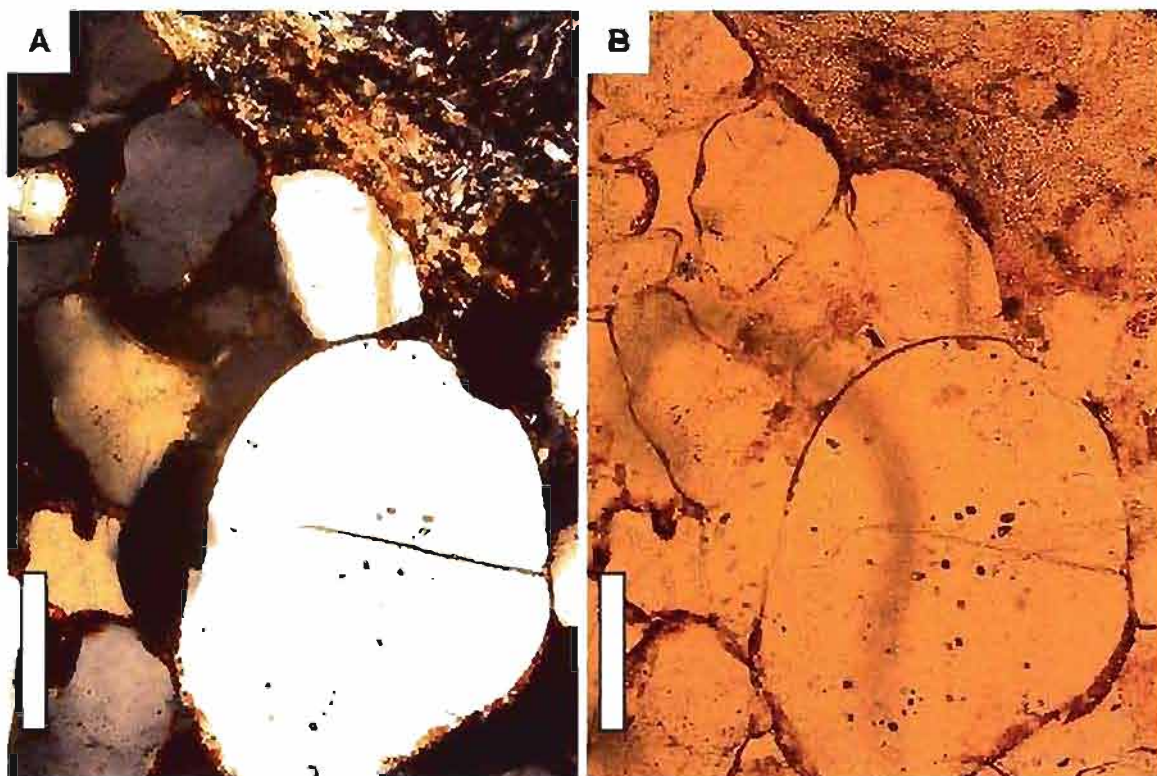


Figure A.36. Photomicrographs of upper red facies sample CBN 12.20.06#6. Thin, primary hematite coats the large quartz grain, and is viewed in two dimensions at the upper portion of the grain. The lower right of the grain shows the hematite coat where the quartz displays some relief. Clay alteration occupies the upper right portion of the images. A) Under cross-polarized light. B) Under plane-polarized light. Scale bar = 0.1 mm.



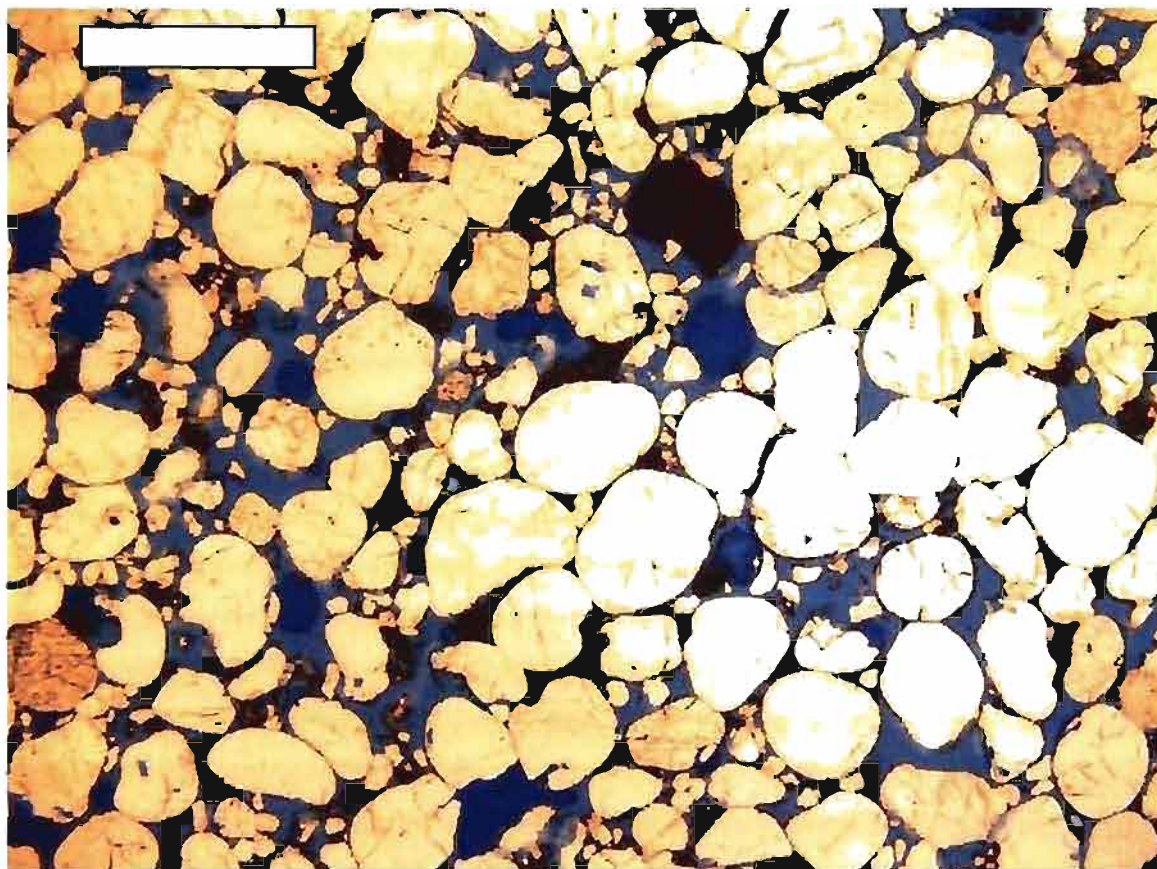


Figure A.37. Photomicrograph of basal red facies showing high (20-30%) porosity. Blue epoxy highlights porosity in sample CBN 7.14.06#1 under plane-polarized light. Scale bar = 1 mm.

1. Thin, primary hematite graincoats are “trapped” beneath early quartz overgrowths.
2. Thoroughly bleached samples display hematite grain coats where preserved beneath quartz overgrowths. Isolated, remnant hematite can occur in narrow pore throats at grain contacts.
3. Well-developed, secondary hematite crystals of the variable Liesegang facies display euhedral fibers, euhedral platelets and porosity filling masses of euhedral crystal growth. Platelets can form colloform assemblages.
4. Liesegang banding at orange hematite and micro-concretion reaction fronts occur abruptly as dark brown to opaque anhedral to euhedral, porosity-filling iron oxide crystals.
5. Interparticle porosity can commonly be as high as 30%.
6. Potassium feldspar can be as high as 30% (Figure 2.5).

#### Dinosaur Trample Surface Characterization

Tables A.23 to A.32 support data presented in Chapter 3. To document the significance of the trample surface, ten field plots (2 x 2 m) totaling 40 m<sup>2</sup> were surveyed as a preliminary means to assess the occurrence of impressions. Plots were chosen randomly (to avoid bias towards the larger, more unusual, or visually exciting impressions), with the stipulation that plots not overlap. In randomly selecting ten plots from within the main trample area, a representative initial characterization could be made of the trample surface as a whole, including impression type, dimensions, morphology, and density. Each plot was photographed along with individual tracks of interest.

Table A.23

## Trample Surface Plot 1, Impression Dimensions and Orientation

Track #	Length (cm)	Width (cm)	Depth (cm)	Md. Width (cm)	Md. Height (cm)	Shape	Orient. (deg.)	Comments
1	80	73	14	13	5	c		
2	100	95	12			c		OP
3	107	78	13			c		
4	6	5	2			c		OP
5	5.5	4.5	2			c		OP
6	8	6	3			c		OP
7	6	4	2.5			c		OP
8	5	4	2			c		OP
9	17	13	4			irreg	180	T, OP
10	5	4	2.5			c		OP
11	7	4	2.5			c		OP
12	10	7	3			c		OP
13	11	15	2			irreg	347	T, OP
14	3	2.5	2			c		OP
15	11	8	8	7	4	c		OP
16	25	30	13	5	6	irreg	100	T, OP
17	8	6	4			c		OP
18	13	5	3.5			c		OP
19	18	7	3			c		OP
20	9	5	3			c		OP
21	5	4	3			c		OP
22	5	4	2			c		OP
23	20	15	11			irreg	21	T
24			4	5	4	c	16	
25	13	13	11.5			c		
26	23	20	15	8	4.5	c		
27	90	83	7			c		

o = ovate; c = circular; irreg = irregular; e = elongate; T=tridactyl; OP=overprinting; Md.=mound; Orient.=orientation

Table A.23 Continued

Track #	Length (cm)	Width (cm)	Depth (cm)	Md. Width (cm)	Md. Height (cm)	Shape	Orient. (deg.)	Comments
28	5	4	3			c		
29	8	7	3			c		
30	20	23	9			c	157	OP
31	43	45	10	10	10	c		
32	23	24	5			c	346	T
33	35	8	5			irreg		
34	6	5	3			c		
35	7	5	2.5			c		
36	6.5	5	2.5			c		
37	6	7	3			c		
38	8	6	4			c		
39	14	12	3			c		
40	10	8	2			c		
41	6	4.5	2.5			c		
42	15	9	8			c	74	
43	30	40	15			c		

o = ovate; c = circular; irreg = irregular; e = elongate; T=tridactyl; OP=overprinting; Md.=mound; Orient.=orientation

Table A.24

## Trample Surface Plot 2, Impression Dimensions and Orientation

Track #	Length (cm)	Width (cm)	Depth (cm)	Md. Width (cm)	Md. Height (cm)	Shape	Orient. (deg.)	Comments
1	25	25	8.5			c/irreg		
2	18	17.5	5.5	4	2	c		
3	42	29	11.5	3	2	o	235	OV
4	25	17	6.5	2	1	c	220	
5	11.5	10	5			c		
6	23	17	6	4	2.5	o	230	OV
7	25	22	6.5	4	2.5	irreg	174	T
8	6	3.5	3			c		
9	15.5	14	5.5			c		
10	7	5.5	5			c		
11	10.5	7.5	18			irreg		
12	7		8.5			irreg		
13	21.5	21	8	5.5	1	c		
14	22.5	19.5	8.5	6.5	2.5	c		
15	9	6	2	2	1	c		
16	3	3	2.5			c		
17	3	3	2.5			c		
18	3	3	2			c		
19	2	2	1			c		
20	2	2	1			c		
21	8.5	5.5	4	3	2	c		
22	6	5	5			irreg		
23	16.5	11.5	9	8	3	c/irreg	145	
24	25.5	14	9.5	3.5	2	irreg	249	T
25	5	3.5	2.5			c		
26	30	27	8.5	4	2	o	255	OV
27	18.5	15	6			c		

o = ovate; c = circular; irreg = irregular; e = elongate; T=tridactyl; OP=overprinting; Md.=mound; Orient.=orientation

Table A.24 Continued

Track #	Length (cm)	Width (cm)	Depth (cm)	Md. Width (cm)	Md. Height (cm)	Shape	Orient. (deg.)	Comments
28	18	11	3.5	2.5	1	c		
29	15	10.5	3.5			c		
30	55	40	10	6	2	o		
31	4	4	2.5			c		
32	4	2	3.5			irreg		
33	6	7	3.5			irreg		
34	2	3	2.5			irreg		

o = ovate; c = circular; irreg = irregular; e = elongate; T=tridactyl; OP=overprinting; Md.=mound; Orient.=orientation

Table A.25

## Trample Surface Plot 3, Impression Dimensions and Orientation

Track #	Length (cm)	Width (cm)	Depth (cm)	Md. Width (cm)	Md. Height (cm)	Shape	Orient. (deg.)	Comments
1	37	32	14.5	15	7	c		
2	25	20	7.5			c		
3	10	7	2.5	2	1.5	irreg	90	T
4	4	4	2.5	1.5	1	c		
5	9	7	2			irreg		T
6	20	15	5.5			c		
7	6	5	3.5			c		
8	4.5	4	3.5			c		
9	3	2	1.5			c		
10	6	6	4	2.5	1.5	c	185	OV
11	23	23	6	9	3	c	94	S w/12&13
12	3	3	2.5			c	167	S w/11&13
13	21	10	4	3	2	irreg	65	S w/11&13
14	10	3	2			irreg		
15	5	2.5	2			irreg		
16	5	5	3			c		
17	2.5	2.5	2			c		
18	4.5	2	2.5			o		
19	5	3	1.5			o		
20	6	3.5	2			o		OP
21	5	2.5	2.5			irreg		S w/22&23
22	5	3	1.5			irreg		S w/21&23
23	8	5	2			irreg		S w/21&22
24	15	14	4	2	2	c	110	OP
25	3	3	1.5			c		
26	4.5	4	2	2	1	c		S

o = ovate; c = circular; irreg = irregular; e = elongate; T=tridactyl; S=Sauropodomorph; OV=ovate w/digit III; OP=overprinting; Md.=mound; Orient.=orientation

Table A.25 Continued

Track #	Length (cm)	Width (cm)	Depth (cm)	Md. Width (cm)	Md. Height (cm)	Shape	Orient. (deg.)	Comments
27	7	5	2.5			c		
28	25	19	8			c		
29	18	13	4.5			irreg		
30	8	6	3.5			c		
31	7	6	3.5			c	285	
32	9	6.5	2.5			c		
33	5	4	2			c		
34	7	7	4.5	2.5	2	c		
35	9	7.5	9	2.5	1	c		
36	2.5	3	1			c		
37	17	14	14			c		
38	105	58	19			irreg		
39	18	10	12			irreg		
40	6	6	3			c		
41	7	6	3.5			c		
42	10	2.5	2			irreg		
43	6	4	3.5			c		
44	4	3	1			c		
45	4	3	2			c		
46	5	3.5	5			c		
47	5	2	1			o		
48	35	27	13			c		
49	30	25	6.5	3.5	1.5	c		
50	15	10	8	4	1.5	c	90	
51	58	50	6.5			irreg		OP
52	9	9	2.5	2.5	2	c		
53	10	8.5	2.5	2	1.5	irreg		
54	10	6	3			irreg		
55	5.5	4.5	2.5			o		

o = ovate; c = circular; irreg = irregular; e = elongate; T=tridactyl; S=Sauropodomorph; OV=ovate w/digit III; OP=overprinting; Md.=mound; Orient.=orientation



Table A.25 Continued

Track #	Length (cm)	Width (cm)	Depth (cm)	Md. Width (cm)	Md. Height (cm)	Shape	Orient. (deg.)	Comments
56	9	6	4.5			irreg		
57	7	4	4.5			c		
58	80	60	14			c		
59	15	15	6.5	2.5	2	c		
60	10	10	5			irreg		
61	22.5	16	7	2.5	3	o		OV
62	20	14	6.5	4	1.5	o		OV
63	15	8	5	2	1	o		OV
64	31	24	10	2.5	1	o		
65	12	8	8.5			irreg		
66	12	9.5	5	4	1	o	194	T
67	75	50	15			irreg		

o = ovate, c = circular; irreg = irregular, c = elongate, T=tridactyl; S=Sauropodomorph; OV=ovate w/digit III; OP=overprinting; Md.=mound; Orient.=orientation

Table A.26

## Trample Surface Plot 4, Impression Dimensions and Orientation

Track #	Length (cm)	Width (cm)	Depth (cm)	Md. Width (cm)	Md. Height (cm)	Shape	Orient. (deg.)	Comments
1	60	52	10	10	5	c		
2	15	7	2.5	3	1.5	o		S w/3
3	14	8	3	2.5	1	o	243	S w/2
4	24	14	4	4	1.5	o		
5	6	3.5	1.5			irreg		
6	5	2.5	2			irreg		
7	5	4	2			irreg		
8	17	9	2.5			irreg		
9	15	6	2			irreg		
10	5.5	5.5	2			c		
11	6	3.5	2			irreg		
12	13	5	2.5			irreg		
13	6.5	6	3	2	1	c		
14	6.5	6.5	1.5	1.5	0.5	c		
15	13	9	5.5			o		
16	22	14	8			c to irreg		
17	35	35	6	8	3	c		
18	23	20	5.5	1.5	0.5	c	262	OP
19	24	20	2.5	5	1.5	c		OP
20	45	32	14	7	3.5	o	66	
21	7	6	1			irreg		
22	30	20	4			irreg		
23	9	6	1.5			o		
24	11	4	2			e		
25	14	8.5	1.5			irreg		
26	7	7	1.5	2.5	1	c		

o = ovate; c = circular; irreg = irregular; e = elongate; T=tridactyl; S=Sauropodomorph; OV=ovate w/digit III; OP=overprinting; Md.=mound; Orient.=orientation

Table A.26 Continued

Track #	Length (cm)	Width (cm)	Depth (cm)	Md. Width (cm)	Md. Height (cm)	Shape	Orient. (deg.)	Comments
27	6.5	6	2	1.5	0.5	c		
28	8	5.5	1	1.5	1	irreg		
29	10	6.5	2.5	2.5	0.5	irreg		T
30	27	11	5			e		
31	31	25	13.5	11	5.5	o	249	
32	16	15	10	9	4	irreg	340	T
33	29	14	2.5			irreg		
34	25	23	5			irreg	330	T
35		33	3	2.5	2	irreg		T
36	7	6	3.5			c		
37	10	5	2	3	2	e		
38	19	12.5	9			c		
39	3	3	1.5			c		
40	25	17	8			o		OP
41	12	12	3.5			c		
42	30	18	4			o		
43	22	20	9			c		
44	22	21	10.5			c		
45	18	20.5	12			irreg	236	S
46	43	35	17	9	5	c		
47	9	5	2.5	2	1	o		
48	8	6	4			c		
49	20.5	23	6			c		
50	30	25	4			irreg		

o = ovate; c = circular; irreg = irregular; e = elongate; T=tridactyl; S=Sauropodomorph; OV=ovate w/digit III; OP=overprinting; Md.=mound; Orient.=orientation

Table A.27

## Trample Surface Plot 5, Impression Dimensions and Orientation

Track #	Length (cm)	Width (cm)	Depth (cm)	Md. Width (cm)	Md. Height (cm)	Shape	Orient. (deg.)	Comments
1	18	13	4.5	3	1.5	o	247	OP
2	32	25	6.5	7.5	1	o		
3	42	27	7			o	232	OV
4	63	40	10.5	3	1	o		OP
5	45	45	10			o		
6	5	4.5	1			irreg		T
7	7	4.5	1			irreg		
8	10	9	1.5	1.5	0.5	c		
9	20	9	3.5			e		
10	6.5	4	2	1.5	0.5	e		
11	3.5	3.5	1.5			c		
12	4.5	3	1			o		
13	4.5	3	0.5			o		
14	4.5	3	0.5			o		
15	7	6.5	2			c		
16	42	35	10.5			o		OP
17	65	54	5.5	5	4	o		
18	38	29	5			o		OP
19	46	33	5	5	1	o		
20	80	30	10			e		
21	28.5	21.5	9	3.5	3	o	60	
22	47.5	40	2.5			irreg		
23	27	17	6.5			o	257	S w/24, OP
24	28	10	4	2	2.5	e		S w/23, OP
25	12	9	5.5	3	1	o	255	OV, OP
26	18	4	3.5			e		OP

o = ovate; c = circular; irreg = irregular; e = elongate; T=tridactyl; S=Sauropodomorph; OV=ovate w/digit III; OP=overprinting; Md.=mound; Orient.=orientation

Table A.27 Continued

Track #	Length (cm)	Width (cm)	Depth (cm)	Md. Width (cm)	Md. Height (cm)	Shape	Orient. (deg.)	Comments
27	12	9	3			irreg		OP
28	7	3.5	2.5			irreg		OP
29	11	5.5	3			irreg	47	T
30	18	5	2			e/irreg		
31	10	7	3			irreg		
32	13	10	3			irreg		
33	2.5	2.5	1.5			c		
34	3	3	3			c		
35	11	9	2.5	4	1.5	o		
36	51	43	12	11	5	irreg		
37	3	3	1.5			c		
38	3	2.5	1			c		
39	20	15.5	4	9.5	2	irreg		
40	23	11	8	8		irreg		
41	4.5	4	2			irreg		
42	12	4	3			e		
43	27.5	23	6.5			o	300	OV
44	35	8	4	5	1	e		
45	20	4.5	3.5	4	3	irreg		S
46	26.5	3.5	3.5	6.5	3	e/irreg		
47	50	7	2.5			e/irreg		
48	19	13	4	3	1	o		
49	76	78	4.5	4.5	2	c		T, OP
50	25	19	6	2.5	1	o	242	OV, OP
51	28	15	4			o		OP
52	23	18	5	2.5	1	o	263	OV, OP
53	11	10	2	4	1	c		OP
54	6.5	4.5	1.5	2	1	o		
55	5	3	1.5	2.5	1	irreg		

o = ovate; c = circular; irreg = irregular; e = elongate; T=tridactyl; S=Sauropodamorph; OV=ovate w/digit III; OP=overprinting; Md.=mound; Orient.=orientation

Table A.27 Continued

Track #	Length (cm)	Width (cm)	Depth (cm)	Md. Width (cm)	Md. Height (cm)	Shape	Orient. (deg.)	Comments
56	7	5	1.5			o		
57	12	5	2			e		
58	12	14	3	3	1	irreg	112	T
59	6.5	3	1.5			e		
60	10	5	2			e		
61	20	11	4	3.5	2	e/o		
62	20	11.5	2.5	3	1	e/o		
63	20	15	2			o		
64	15.5	10.5	2			o		
65	9	8	2.5	2	1	c/o		
66	7.5	6	1.5			o		
67	3.5	3.5	1.5			c		
68	5.5	5	2.5			c		
69	17	12	2.5			irreg		T
70	10	8	2			irreg		
71	5.5	3	1			irreg		
72	6.5	6	3.5			irreg		
73	13	10	3			irreg		
74	12.5	10	2			c		
75	15	7.5	4	2.5	1.5	e		
76	8	5	2			o		
77	11	9	2.5			c		
78	13	11	3.5			c/o		
79	18	6	4			e		
80	14	13	4			irreg		

o = ovate; c = circular; irreg = irregular; e = elongate; T=Iridactyl; S=Sauropodamorph; OV=ovate w/digit III; OP=overprinting; Md.=mound; Orient.=orientation

Table A.28

## Trample Surface Plot 6, Impression Dimensions and Orientation

Track #	Length (cm)	Width (cm)	Depth (cm)	Md. Width (cm)	Md. Height (cm)	Shape	Orient. (deg.)	Comments
1	37	30	7			o	225	
2	17	10.5	7	3	1	o		OV
3	41	32	9.5			o		
4	19	15	8			o	255	
5	13	9	3	2	0.5	o	238	
6	19	15	7			o	241	
7	38	25	8.5			irreg		
8	78	55	15			irreg		T
9	75	75	17			irreg		
10	8	8	5	2.5	1	c	251	
11	27	10	3.5			e		
12	11.5	9	4.5			o		
13	37	27	9			o	50	
14	75	50	18			irreg	40	
15	40	10	8	7	2	e		
16	20	15	4			o		
17	15	12	2			o		
18	53	38	6	1	2	o		
19	15	12	4			o		OP
20	70	50	7			irreg/o		

o = ovate; c = circular; irreg = irregular; e = elongate; T=tridactyl; OV=ovate w/digit III; OP=overprinting; Md.=mound; Orient.=orientation

Table A.29

## Trample Surface Plot 7, Impression Dimensions and Orientation

Track #	Length (cm)	Width (cm)	Depth (cm)	Md. Width (cm)	Md. Height (cm)	Shape	Orient. (deg.)	Comments
1	28	25	6			o		
2	17	13	7			o	244	OV
3	1.5	1.5	1			c		
4	3.5	3	1			o		
5	4.5	4.5	1			irreg		
6	15	5	2.5			e		
7	15	4	1.5			e		
8	15	17	2			irreg	193	T
9	5.5	4	2	1.5	1	c/o		
10	47	35	6			irreg	249	T
11	20	16.5	3	3	1	o		OP
12	35	30	6	5	2	o		
13	7	6.5	5			irreg	52	T
14	10	5.5	2			o		
15	9	6	3	2.5	1.5	o		
16	7	7	2			irreg		
17	7	7	5			c		
18	5	5	2			c		
19	4	3	1.5			irreg		
20	45	37	6			o		
21	22	17	4	3	1.5	o		
22	4	3	1			o		
23	3	3	1			c		
24	20	17	7			o	264	OV
25	27	6	2			irreg		
26	20	5	2			e/irreg		

o = ovate; c = circular; irreg = irregular; e = elongate; T=tridactyl; OV=ovate w/digit III; OP=overprinting; Md.=mound; Orient.=orientation



Table A.29 Continued

Track #	Length (cm)	Width (cm)	Depth (cm)	Md. Width (cm)	Md. Height (cm)	Shape	Orient. (deg.)	Comments
27	14	10	9	7	3	o		
28	20	17	3			irreg		
29	12	10	8	5	2	c/o		
30	65	75	12.5			irreg	132	T
31	10	6	4			o		
32	31	24	6			o/irreg		
33	15	12	4.5	4	0.5	o		
34	73	55	4			o		
35	46	39	9	6	1.5	o	310	OP
36	5.5	5	1	1.5	0.5	c		OV, OP
37	2.5	2.5	1			c		OP
38	6	4.5	2.5			o		OP
39	6	5	2.5			c/o		OP
40	70	20	5			e/irreg		
41	6.5	7	2	2.5	2	o		
42	7	6	1			irreg		
43	7.5	7		2		irreg		T
44	8	7	3			c		
45	11.5	7	2.5	3	1	o/e		
46	10	7.5	2.5	2	0.5	o		
47	15	13	3.5			o		
48	37	36	4			c		
49	22	21	3.5	3	0.5	c		OP
50	2.5	2.5	1.5			c		
51	5.5	4	2	2	0.5	o		
52	4.5	3	1.5			o		
53	2	2	1			c		
54	9	7.5	4	2	0.5	o		
55	11.5	6	3.5	1.5	1.5	o	41	T

o = ovate; c = circular; irreg = irregular; e = elongate; T=tridactyl; OV=ovate w/digit III; OP=overprinting; Md.=mound; Orient.=orientation

Table A.29 Continued

Track #	Length (cm)	Width (cm)	Depth (cm)	Md. Width (cm)	Md. Height (cm)	Shape	Orient. (deg.)	Comments
56	20.5	16.5	4	2	1.5	o		
57	20	20	3			irreg		
58	11	7	3			irreg		
59	6	3	1			o		
60	4.5	3.5	1			o		
61	7	5	1.5			o		

o = ovate; c = circular; irreg = irregular; e = elongate; T=tridactyl; OV=ovate w/digit III; OP=overprinting; Md.=mound; Orient.=orientation

Table A.30

## Trample Surface Plot 8, Impression Dimensions and Orientation

Track #	Length (cm)	Width (cm)	Depth (cm)	Md. Width (cm)	Md. Height (cm)	Shape	Orient. (deg.)	Comments
1	25	19	12.5	6	2	o		OV
2	11	11	3	3	1	c		
3	35	20	6.5			o		OP
4	9	6.5	1			irreg.		
5	11	3.5	2			e/irreg.		
6	25	27	9			c		
7	7	5.5	3	2	1	o		
8	7	5	2			o		
9	13	10	2.5			o		
10	45	30	11			irreg.		
11	31	24	12	5	1	o		
12	20	5	1.5			e		
13	36	27	4.5	1.5	1	irreg.	17	T
14	14	12	7			o		
15	15	14	4			c/o		
16	14	13.5	3	4	1	c		
17	36	24	8.5			o	275	OV
18	5	5	2	2	0.5	c		
19	5	3	1.5	1.5	0.5	o		
20	8	5	1.5			o		
21	25	25	6.5			c		
22	5.5	4.5	2.5			irreg.		T
23	2.5	2.5	1.5			c		
24	45	40	3.5	1.5	1	o		
25	30	27	7	5	1.5	o		OP
26	55	7	3	4.5	1.5	e	28	

o = ovate; c = circular; irreg = irregular; e = elongate; T=tridactyl; OV=ovate w/digit III; OP=overprinting; Md.=mound; Orient.=orientation

Table A.30 Continued

Track #	Length (cm)	Width (cm)	Depth (cm)	Md. Width (cm)	Md. Height (cm)	Shape	Orient. (deg.)	Comments
27	37	28	6			o		
28	32	28	6			o		
29	20	17	4.5	5.5	1	o		
30	7.5	6.5	2			o		
31	8	7	5			o		
32	20.5	19.5	4.5			o/irreg.		
33	5	3	1.5			o		
34	160					tail		

o = ovate; c = circular; irreg = irregular; e = elongate; T=tridactyl; OV=ovate w/digit III; OP=overprinting; Md.=mound; Orient.=orientation

Table A.31

## Trample Surface Plot 9, Impression Dimensions and Orientation

Track #	Length (cm)	Width (cm)	Depth (cm)	Md. Width (cm)	Md. Height (cm)	Shape	Orient. (deg.)	Comments
1	14	14	6.5	7	2	triang (irreg)		OP
2	29	25	12	6	1.5	o		
3	40	35	5.5	3	1.5	c		
4	12	10	5			o		OP
5	20	20	4			c		
6	8	5	3			irreg.		
7	19	19	4.5			c		
8	25	20	8			o	40	OV
9	25	25	4.5			c		OP
10	29	25	9			o		
11	7	6.5	3	2.5	1.5	o		OP
12	35	30	13	2.5	1	o		OV
13	4	3	2	1	0.5	o		
14	6.5	6	2.5			irreg.		T
15	5	4	2			o		
16	19	19	6			c		
17	21.5	19	6.5			o		
18	39	25	11			o		
19	11	10	2			c		
20	9	7	5	3.5	2.5	c/o		
21	4	4	1.5			c		
22	10	5	1.5			e		T w/23
23	4.5	4	2			o		T w/22
24	4	4	1.5			c		
25	10	6	4	3	1.5	e		
26	10	13	5	3	2	irreg.		

o = ovate; c = circular; irreg = irregular; e = elongate; T=tridactyl; OV=ovate w/digit III; OP=overprinting; Md.=mound; Orient.=orientation

Table A.31 Continued

Track #	Length (cm)	Width (cm)	Depth (cm)	Md. Width (cm)	Md. Height (cm)	Shape	Orient. (deg.)	Comments
27	7	5	0.5			o		
28	9	8	2.5			o		
29	16.5	14	2.5			o		
30	18	13	2.5			o		
31	20	16	3.5	1.5	1	o/irreg	333	T
32	12	10.5	3			o/irreg		
33	6	7.5	2			irreg.		T
34	5	3.5	1.5			o		
35	4	3.5	1			o		
36	7	6	1.5			irreg.		
37	8	7	1.5			irreg.		
38	12.5	4	1.5			e		
39	3.5	3	1			irreg.		
40	5.5	3.5	0.5			irreg.		
41	14	12	4	2	3	o		
42	8	6	3	3.5	1	o		
43	19	10	3.5	5	2	o		
44	6	5	1			irreg.		
45	22	20	3			o		
46	15	5.5	1			e		
47	18	4	1	1.5	0.5	e		
48	12	5	2.5			e		
49	6	2	1			e		
50	7	3	1.5			e		
51	12	10	3.5			irreg.		
52	20	12	5	3	0.5	o	247	
53	7	7	1			irreg.	315	T
54	5	4.5	1			irreg.		
55	4	2.5	1			o		

o = ovate; c = circular; irreg = irregular; e = elongate; T=tridactyl; OV=ovate w/digit III; OP=overprinting; Md.=mound; Orient.=orientation

Table A.31 Continued

Track #	Length (cm)	Width (cm)	Depth (cm)	Md. Width (cm)	Md. Height (cm)	Shape	Orient. (deg.)	Comments
56	4.5	4.5	1	1.5	0.5	c		
57	20	16	7	6.5	3	o	245	
58	21	20	5	3.5	2	o	180	
59	19	13	7	3	2	o	250	OV
60	144	14.5	5.5	4	1.5	Tail	186	OP
61	10	8	5.5	1	0.5	o	62	OV
62	26.5	20	10	8	1	o	140	
63	15	8	2.5			o		
64	18	14	2.5			o		
65	32	9	3			e		
66	6.5	6.5	1			c		

o = ovate; c = circular; irreg = irregular; e = elongate; T=tridactyl; OV=ovate w/digit III; OP=overprinting; Md.=mound; Orient.=orientation

Table A.32

## Trample Surface Plot 10, Impression Dimensions and Orientation

Track #	Length (cm)	Width (cm)	Depth (cm)	Md. Width (cm)	Md. Height (cm)	Shape	Orient. (deg.)	Comments
1	10	8.5	4.5			o		
2	40	27	6.5	2	1.5	o		
3	8	8	4			c		
4	4	4	1.5	2	1	c		
5	45	5	4			e		OP
6	20	15	9.5			o		
7	35	25	10			o		OV
8	130	12.5	15	10		tail		
9	61	45	5			o		
10	7.5	5	1			o		
11	46	18	9	8	2.5	o	61	OV
12	52	28	20			o		OV
13	12	8	3.5			o		
14	30	23	10.5			o		
15	17	9	2.5	2.5	1	irreg		
16	34	5	2			tail		
17	17	9	10.5			o	242	OV
18	10	8	4			o		

o = ovate; c = circular; irreg = irregular; e = elongate; T=tridactyl; OV=ovate w/digit III; OP=overprinting; Md.=mound; Orient.=orientation



Individual impressions were measured, inclusive of those only partially entering a given plot. Measurements include impression length, width and depth, the width and height of surrounding soft-sediment mounds, impression orientation, and any notable features (shape, overprinting, toe and claw prints, morphology).

### Terrestrial Analogs to Mars

Data supporting Chapter 4 is presented in Tables A.33 to A.40. Micro-concretions were sieved to reveal grain size fractionation. Ripple trains are characterized to include individual ripple measurements and to determine a wind ripple index.

Modern surface weathering fractures were measured at four Coyote Buttes sites. These polygonal joint sets serve as terrestrial analogs to “Wopmay” style weathering observed by the Mars Exploration Rover Opportunity at Meridiani Planum,, Mars. Tables A.41 to A.46 present data used to discuss these features by Chan et al. (2008)

### Characterization of The Wave

Tables A.47 and A.48 support discussions of The Wave in Chapter 2. Wind velocity was measured using a Kestral hand-held anemometer. Velocity and step and riser measurements contributed to Loope et al. (2008).

Table A.33

## Sieved Fractions of Micro-concretion Bearing Sand

Sieve Range [sieve # (μm)]	Sample ID, Description and Mass (g)								
	6.19.06#1 ripple crest	6.19.06#2 ripple trough	6.19.06#3 ripple crest	6.19.06#4 ripple trough	6.19.06#5 non rippled sand	6.20.06#1 ripple crest	6.20.06#2 ripple trough	6.20.06#3 ripple crest	6.21.06#1 ripple crest
larger than #8 (2360)	0.59	0.32	0.5	0.93	1.6	1.17	0.65	0.27	0
#10 (2000) - #8 (2360)	1.35	0.29	2.41	2.11	1.72	9.06	5.65	1.92	0.05
#12 (1700) - #10 (2000)	2.43	0.26	4.63	2.92	2.8	17.73	13.76	7.19	2.6
#14 (1400) - #12 (1700)	2.24	0.21	3.35	1.99	0.73	15.77	13.38	12.37	15.97
#16 (1180) - #14 (1400)	0.98	0.08	0.74	0.43	0.1	3.99	2.91	6.75	17.33
#18 (1000) - #16 (1180)	0.34	0.05	0.16	0.1	0.03	1	0.54	1.18	4.62
#35 (500) - #18 (1000)	4.01	1.94	2.63	0.95	0.25	14.48	10.51	10.26	11.25
#60 (250) - #35 (500)	88.43	88.94	67.14	62.34	29.21	72.09	64.99	73.29	68.46
#100 (150) - #60 (250)	22.73	50.42	27.95	43.1	31.34	16.05	13.6	29	10.23
smaller than #100 (150)	3.4	11.54	6.6	9.76	14.79	2.78	1.69	7.63	1.23

Table A.34

## Characterization of Micro-concretion Site 1

Ripple #	Orientation	Height (mm)	Dip (N)	Dip (S)	Crest Length (cm)	Width of Concs. (cm)	Ripple #'s	$\lambda$ (mm)	Ripple Index
1	116		4	8	110	7	1-2	830	46
2	110	18	6	7	170	6	2-3	420	30
3	102	14	8	10	70	4	3-4	470	39
4	90	12	8	5	70	7	4-5	500	29
5	95	17	10	5	230	8	5-6	570	29
6	90	20	13	9	130	8	6-7		
7	83	10	10	8	110	7	7-8		
8	109	10	8	8	60	6	8-9	770	77
9	80	10	11	10	80	6	9-10	350	29
10	100	12	8	9	60	6	10-11	440	44
11	82	10	10	7	45	7	11-12		
12	73	10	11	10	40	7	12-13	420	42
13	79	10	10	8	100	6	13-14	590	23
14	76	26	14	8	100	6	14-15	400	22
15	92	18	10	8	45	5	15-16		
16	85	12	9	6	60		16-17	500	20
17	91	25	14	13	80	7	17-18	200	50
18	90	4			40	4	18-19	500	33
19	93	15	8	8	95	6	19-20	190	16
20	80	12	1	6	50		20-21	400	31
21	82	13	6	7	100	8	21-22	610	32
22	86	19	7	5	90	10	22-23	2170	
23	92		7	3	150	8	23-24	360	
24	99		6	2	60		24-25	730	73
25	98	10	4	8	100	5	25-26	270	18
26	90	15	4	6	100	5	26-27	300	30
27	82	10					27-28	350	35
28	90	10							
29	curved	16	9	7					

Location: N36 58.992' W112 00.232' 5686'; 29 ripples in train: 14.5 m long, 0.7-2.2 m wide zone; wind from 198°.

Table A.35

## Characterization of Micro-concretion Site 2

Ripple #	Orientation	Description	Height (mm)	Dip (W)	Dip (E)	Crest Length (cm)	Width of Concs. (cm)	Ripple #'s	$\lambda$ (mm)	Ripple Index
1	33		7	5	11	30	4	1-2	170	24
2	14		7	8	8	30	4	2-3		
3	39		9w 3e	7	5	38	2.5	3-4	250	
4	36		5 to 10	8	12	40	3.5	4-5	250	
5	30		5	8	8	25	3	5-6	300	60
6	4	branching	3w 35e	4	16	44	4	6-7	680	
7A	350		7 to 10	10	12	39	4.5	7-8	160	
7B	30		5	5	5	38	3	8-9	430	215
8	42		2	14	4	36	2	9-10		
9	30	arcuate	2.5	11	4	40	1.5	10-12	250	167
10	238	arcuate	1.5	20	0	43	2	11-13	400	57
11	355		7	9	6	23	2	12-13		
12	270		6	12N	5S	128	3.5	13-14		
13	327		3	11	4	22	3	14-15	240	30
14	358	arcuate	8	15	7	45	4	15-16	130	26
15	25	arcuate	5	9	7	25	2	16-17	230	23
16	12	arcuate	10	4	9	18	2	17-18	100	20
17	347	arcuate	5	3	8	10	1			
18	8	arcuate	7	1	11	10	1.5			

Location: N36 59.241' W 112 00.429' 5708'; 18 ripples in train: 8.5 m long, 1.7 m wide zone; wind from 275°.

Table A.36

## Characterization of Micro-concretion Site 3A

Ripple #	Orientation	Description	Height (mm)	Dip (W)	Dip (E)	Crest Length (cm)	Width of Lee Concs. (cm)	Width of Stoss Concs. (cm)
1	38		33	28	9W	25	3	6
2	35		40	29	4	75	4	7
3	40		18	26	8	26	2	4
4	35		19	21	5	69	3	7
5	10		10	16	6	37	3	5
6	27		12	20	7	58	3	5
6B	19		5	15	7	23	2	7
7	27	arcuate	12	23	7	30	2.5	10
8	2	arcuate	10 to 15	26	9	75	2.5	7.5
9	18		10	24	4	32	1.5	5
10	23		13	29	2	33	1.5	5
10B	20		8	25	10	23	2	3
11	10		13	28	2	22	4	5
12	5		8	30	3	64	1.5	5
13	355		10	21	4	40	2	9

Location: N36 59.456' W 112 00.339' S 632'; 13 ripples in train: 3.1 m long, 0.9 m wide zone; wind from 125° (with some bidirectional flow).

Table A.37

## Wind Ripple Index of Micro-concretion Site 3A

Ripple #'s	Height (mm)	$\lambda$ (mm)	Ripple Index
1-2	33	390	12
2-3	40	170	4
2-4	30	430	14
3-4	18	250	14
4-5	19	230	12
4-6	15	370	25
5-6	10	190	19
6-6B	12	120	10
6B-7	5	250	50
7-8	12	210	18
8-9	12.5	330	26
8-10B	8	160	20
10-11	13	330	25
11-12	13	240	18
12-13	8	390	49

Location: N36 59.456' W112 00.339' 5632'

13 ripples in train: 3.1 m long, 0.9 m wide zone

Wind from 125° (with some bidirectional flow)

Table A.38

## Wind Ripple Index of Site 3B (No Micro-concretions)

Height (mm)	$\lambda$ (mm)	Ripple Index
1	45	45
2	70	35
1	45	45
1	35	35
1	40	40
1	43	43
2	73	37
3	75	25
1.5	55	37
1	40	40
2	55	28
1	65	65
2	58	29
2	68	34
2	55	28
3	70	23
1	45	45
2	48	24
2	60	30
2	60	30

Location: N36 59.456' W112 00.339' 5632'

Straight Crests, Few Bifurcations; Oriented 10°-35°

Crests avg. 1.5 m long; wind variable

Table A.39

## Wind Ripple Index of Sand Ripple Site 3C (No Micro-concretions)

Height (mm)	$\lambda$ (mm)	Ripple Index
2	80	40
2	80	40
2	75	38
1	60	60
1	78	78
1	65	65
2	85	43
2	75	38
2	75	38
2	80	40
2	80	40
2	75	38
2	75	38
1	65	65
2	65	33
2	75	38
1	75	75
2	70	35
2	75	38
2	80	40

Location: N36 59.456' W112 00.339' 5632'

Straight Crests; Oriented 310°-315°; Crests Avg. 1.5 m long

Wind from 220°-250°



Table A.40

## Wind Ripple Index of Micro-concretion Site 3D

Height (mm)	$\lambda$ (mm)	Ripple Index
Short Period Ripples		
3	50	17
4	60	15
2	35	18
2	45	23
3	50	17
4	85	21
4	75	19
3	85	28
3	75	25
4	40	10
2	45	23
3	55	18
2	45	23
4	60	15
3	65	22
4	40	10
4	80	20
3	50	17
3	45	15
5	70	14
Long Period Ripples		
10	120	12
6	140	23
11	150	14
7	160	23
14	170	12
15	160	11
12	150	13

Location: N36 59.456' W112 00.339' 5632'

Straight to Arcuate Crests; Oriented 265°-315°

7.5 m long, 6.5 m wide zone; wind from 200° (variable)

Table A.41

Intersection Angles and Analysis of Polygonal  
Fractures Measured from Wopmay Rock,  
Meridiani Planum, Mars

Angle	Angle	Angle
150	139	83
117	100	138
94	142	83
115	153	107
119	100	128
140	145	112
93	137	131
95	92	150
104	139	134
145	110	146
110	110	123
109	113	107
120	133	114
96	125	110
120	135	85
147	123	134
116	119	132
122	130	139
119	113	96
122	127	126
119	116	141
115	109	105
141	90	115
122	110	122
140	130	127
74	97	150
94	105	123
129	145	125
148	112	91
102	113	133
45	126	90
90	80	138
136	92	115
124		

Table A.42

Intersection Angles and Fracture Lengths of Large (>2.0 m dia.) Polygonal Fractures  
Measured from Navajo Sandstone

Angle	Angle	Angle	Length (m)	Length (m)	Length (m)
155	122	102	3.5	1.1	3.08
145	135	165	4.7	2.7	1.75
105	113	112	2.23	1.15	0.9
114	133	160	3.9	2.5	1.3
134	140	124	4.1	2.1	2
90	135	163	2.87	1.4	1.78
85	114	133	3.3	4.2	3.6
144	92	88	2.22	1.4	4.14
106	137	105	2	1.2	4.1
127	106	119	2.93	2.93	1.47
80	110	107	4.47	3.43	1
101	160	138	4.78	2.1	0.6
162	112	145	2.1	1.53	1.5
132	162	148	3.5	1.82	1
160	107	84	3.3	2.9	1.27
96	130	128	0.93	1.98	0.36
152	120	87	2.6	2.4	1.1
135	131	137	1.8	2.4	1.78
97	125	164	2.14	1.75	0.6
163	162	136	1.86	2	2.24
136	119	157	2.08	1.37	1.1
102	170	106	3.32	1.2	0.83
119	131	174	1.53	1.7	2.13
119	119	136	1.44	1.38	1.53
152	109	157	2.87	3.91	0.9
94	132	106	2.73	2.44	0.9
162	119	174	2.32	0.8	2.67
96	162	136	2.5	2.22	3.03
158	166	91	2.96	1.87	1.5
162	125	105	2.77	4.56	1.3
148	152		4.14	2.1	1
111	71		3.47	1.66	2.55
115	143		1.2	1.77	1.3
143	94		1.7	1.1	1.51
114	140		2.3	1.6	0.95
155	131		1.02	4.27	0.76
126	145		2.5	1.26	0.83
105	94		0.92	3.45	1.7
96	134		2.1	1.12	1.69
150	114		0.57	1.8	3.5
120	104		3.6	1.86	1.9
127	96		0.82	0.93	1
119	89		0.62	0.6	1.26

Location: N36° 59' 39.26" W112° 0' 12.61"

Table A.43

Intersection Angles of Small (<2.0 m  
dia.) Polygonal Fractures Measured from  
Navajo Sandstone

Angle	Angle	Angle
150	140	131
103	135	136
110	135	114
112	149	131
132	115	118
126	124	132
120	123	112
116	117	129
110	132	110
132	117	106
121	138	148
107	124	123
115	110	109
131	125	
Location: N36° 59' 30.79" W 112° 0' 33.93"		

Table A.44

## Bulbous Polygonal Weathering Fractures

Width N/S (m)	Width E/W (m)	Height (m)
5.5	3.08	1.3
6.5	5.06	1.96
7.39	4.75	1.7
3.05	2.8	0.9
3.5	4.02	0.63
8	3.6	0.54

Location: N36° 59' 32.28" W112° 0' 34.27"

Table A.45

## Vertical Faces Accompanying Polygonal Weathering Fractures

Strike	Dip	Dip Direction	Height (cm)	Facing Direction	Comments
251	90		88	N	Regional Joint
271	85	S	28	N	
234	75	N	8	N	
237	71	N	19.5	N	
261	86	N	6.5	N	
340	90		3	E	
245	85	N	12	N	
310	78	E	8.5	E	
228	76	N	8	S	
319	70	W	14.5	E	
262	81	N	8	N	
257	53	N	24	N	
250	78	N	7	N	
280	90		4.5	N	
274	73	N	15	N	
253	88	N	10	N	
268	87	N	5	N	
360	87	W	12	E	
292	84	N	10.5	N	
259	63	N	8	N	
305	84	E	6.5	NE	

Location: N36° 59' 39.26" W 112° 0' 12.61"

Table A.46

## Checkerboard Weathering Fractures

Orientation	Spacing (m)
290	
297	1.05
295	0.58
291	0.5
296	0.63
300	0.59
305	0.5
291	0.65
295	0.73
298	0.52
300	0.55
303	0.5
300	0.39
305	0.6
305	0.42
310	0.6
305	0.62
322	0.55
314	0.76
313	0.65
312	0.57
316	0.49
311	0.63
310	0.43
315	0.35
306	0.55
310	0.61
309	0.55
307	0.69
307	0.6
300	0.66
302	0.82
305	0.74
296	0.75
296	0.76
302	0.61
295	0.58
302	0.44
296	0.59
300	0.59
N36° 59' 31.59" W   12° 0' 31.00"	

Table A.47

## Step and Riser Orientation and Inferred Wind Direction at The Wave

Step and Riser Orient. (Deg.)	Wind Direction	Step and Riser Orient. (Deg.)	Wind Direction	Step and Riser Orient. (Deg.)	Wind Direction
227	137	210	120	233	143
231	141	239	149	232	142
234	144	204	114	233	143
252	162	216	126	236	146
245	155	246	156	232	142
220	130	264	174	242	152
222	132	216	126	237	147
235	145	208	118	230	140
264	174	232	142	225	135
231	141	245	155	209	119
228	138	230	140	235	145
235	145	218	128	241	151
242	152	135	45	241	151
233	143	215	125	225	135
215	125	186	96	245	155
244	154	186	96	245	155
245	155	183	93	242	152
242	152	183	93	233	143
230	140	190	100	239	149
247	157	185	95	220	130
205	115	190	100	215	125
200	110	200	110	214	124
215	125	180	90	227	137
190	100	135	45	131	41
230	140	214	124	238	148
232	142	235	145	235	145
219	129	222	132	187	97
220	130	275	185	247	157
221	131	262	172	273	183
238	148	273	183	226	136
220	130	275	185	242	152
242	152	230	140	215	125
230	140	235	145	230	140

Location: N36° 59.753' W112° 00.373'



Table A.48

## Wind Velocity Measured at The Wave

$V_c$ (ft/sec)	$V_i$ (ft/sec)	$(V_c - V_i)/V_i$ (%)
2.2	1.8	22
3.9	3.3	18
	2	
3.7	3.5	6
3.9	3	30
3.4	2.4	42
2.1	2.7	-22
6.4	4.7	36
3.6	3.4	6
3.9	3.2	22
4.5	5.4	-17
4.7		
8.4	6.4	31
1.7	1.4	21
3.5	3.2	9
3.5	3.8	-8
2.4	2.9	-17
3	3.6	-17
2.6	1.5	73
2.8	4.2	-33
2.7	3	-10
1.8	2.1	-14
2.9	3.1	-6
3.1	3.1	
2.2	2.4	-8
2.8	2.1	33
2.6	2.9	-10
4.4	2.1	110
3.1	3.1	
4.4	2.1	110
3.1	2.7	15
4.3	2.5	72
4.9	4.5	9
4.9	3.9	26
5.3	5.1	4
6	7.1	-15
3	3.3	-9
4.4	5	-12
4.8	4.5	7
4.9	4.8	2
5.4	5.4	
5.9	6	-2
4.6	3.7	24

$V_c$  = Velocity at Constriction N36° 59' 45.11" W112° 0' 22.69"

$V_i$  = Velocity in South Trough N36° 59' 44.74" W112° 0' 22.01"

$V_n$  = Velocity at North Trough Exit N36° 59' 46.58" W112° 0' 22.61"

$V_s$  = Velocity at South Trough Exit N36° 59' 44.32" W112° 0' 21.65"

Table A.48 Continued

$V_c$ (ft/sec)	$V_t$ (ft/sec)	$(V_c - V_t)/V_t$ (%)
4.2	4.7	-11
3.7	4	-8
2.2	2.6	-15
2	1.8	11
2.5	3.8	-34
4.3	3.9	10
3.7	1.9	95
3.9	3.7	5
3	2	50
4.2	3.6	17
5	3.8	32
4.8	4.5	7
4	3.3	21
4.5	3.9	15
3.3	3.2	3
3.2	2.7	19
3.4	2.8	21
3.4	4.2	-19
3.3	2.9	14
5.6	6.8	-18

$V_c$ (ft/sec)	$V_s$ (ft/sec)	$(V_c - V_s)/V_s$ (%)
3	2.2	36
2.4	2.4	
5	5.7	-12
4.3	3	43
3.1	5.2	-40
2.1	4.6	-54

$V_c$ (ft/sec)	$V_n$ (ft/sec)	$(V_c - V_n)/V_n$ (%)
3.5	3.2	9
3.8	3.6	6
3.7	3	23
3.2	3	7
3.9	4.8	-19
3.9	3.3	18
1.7	2	-15

$V_c$  = Velocity at Constriction N36° 59' 45.11" W112° 0' 22.69"

$V_t$  = Velocity in South Trough N36° 59' 44.74" W112° 0' 22.01"

$V_n$  = Velocity at North Trough Exit N36° 59' 46.58" W112° 0' 22.61"

$V_s$  = Velocity at South Trough Exit N36° 59' 44.32" W112° 0' 21.65"

### References

- CHAN, M.A., YONKEE, W.A., NETOFF, D.I., SEILER, W.M., AND FORD, R.L., 2008, Polygonal cracks in bedrock on Earth and Mars: Implications for weathering: *Icarus*, v.194, p. 65-71.
- LOOPE, D.B., SEILER, W.M., MASON, J.A., AND CHAN, M.A., 2008, Wind scour of Navajo Sandstone at the Wave (central Colorado Plateau, U.S.A.): *Journal of Geology*, v. 116, p. 173-183.

## APPENDIX B

### DATA IN DIGITAL FORMAT (CD)

#### Introduction

The bound volume of this thesis is accompanied by supporting data in digital format on CD entitled “Jurassic Navajo Sandstone of the Coyote Buttes, Utah/Arizona: Coloration and Diagenetic History, Preservation of a Dinosaur Trample Surface, and Terrestrial Analogs to Mars: Supporting Data.” Contents include the thesis in its entirety and files too large or impractical for inclusion in print form. Contents are listed by file name followed by a brief description:

- WSeilerConcRipples.xls  
Characterization of eolian micro-concretion ripples. Presented in Tables A.33 to A.40.
- WSeilerFieldNotebook.pdf  
A scan of the field notebook compiled at the Coyote Buttes.
- WSeilerPolygons.xls  
Characterization of modern weathering polygonal fractures. Presented in Tables A.42 to A.46.
- WSeilerReflSpectra.xls  
Reflectance spectra from 107 samples.

- WSeilerReflSpectraTransects.xls  
Reflectance spectra from transects documented by Figures A.11 to A.28.
- WSeilerSampleList.pdf  
A list of collected samples including analyses performed on each;  
presented in Table A.1.
- WSeilerSEMEDX.xls  
SEM/EDAX analysis of various samples. Presented in Tables A.2 to A.22  
and corresponding to Figures A.2 to A.10.
- WSeilerThesis.pdf  
A digital copy of the thesis in its entirety.
- WSeilerTrample.xls  
Data collected from the analysis of 10 plots from the dinosaur trample  
surface (Tables A.23 to A.32). Supports data presented in Tables 3.1 to  
3.3.
- WSeilerWave.xls  
Data collected from a characterization of The Wave. Presented in Tables  
A.47 to A.48.